Contorted Organic Semiconductors for Molecular Electronics

Yu Zhong

Submitted in partial fulfillment of the requirements

for the degree of Doctor of Philosophy in the

Graduate School of Arts and Sciences

COLUMBIA UNIVERSITY

2017

Abstract

Contorted Organic Semiconductors for Molecular Electronics

Yu Zhong

This thesis focuses on the synthesis, properties and applications of two types of contorted organic molecules: contorted molecular ribbons and conjugated corrals. We utilized the power of reaction chemistry to writing information into conjugated molecules with contorted structures and studied "structure-property" relationships. The unique properties of the molecules were expressed in electronic and optoelectronic devices such as field-effect transistors, solar cells, photodetectors, etc.

In Chapter 2, I describe the design and synthesis of a new graphene ribbon architecture that consists of perylenediimide (PDI) subunits fused together by ethylene bridges. We created a prototype series of oligomers consisting of the dimer, trimer, and tetramer. The steric congestion at the fusion point between the PDI units creates helical junctions, and longer oligomers form helical ribbons. Thin films of these oligomers form the active layer in n-type field effect transistors. UV−vis spectroscopy reveals the emergence of an intense long-wavelength transition in the tetramer. From DFT calculations, we find that the HOMO−2 to LUMO transition is isoenergetic with the HOMO to LUMO transition in the tetramer. We probe these transitions directly using femtosecond transient absorption spectroscopy. The HOMO−2 to LUMO transition electronically connects the PDI subunits with the ethylene bridges, and its energy depends on the length of the oligomer.

In Chapter 3, I describe an efficiency of 6.1% for a solution processed non-fullerene solar cell using a helical PDI dimer as the electron acceptor. Femtosecond transient absorption spectroscopy revealed both electron and hole transfer processes at the donor−acceptor interfaces, indicating that charge carriers are created from photogenerated excitons in both the electron donor and acceptor phases. Light-intensity-dependent current−voltage measurements suggested different recombination rates under short-circuit and open-circuit conditions.

In Chapter 4, I discuss helical molecular semiconductors as electron acceptors that are on par with fullerene derivatives in efficient solar cells. We achieved an 8.3% power conversion efficiency in a solar cell, which is a record high for non-fullerene bulk heterojunctions. Femtosecond transient absorption spectroscopy revealed both electron and hole transfer processes at the donor-acceptor interfaces. Atomic force microscopy reveals a mesh-like network of acceptors with pores that are tens of nanometers in diameter for efficient exciton separation and charge transport. This study describes a new motif for designing highly efficient acceptors for organic solar cells.

In Chapter 5, I compare analogous cyclic and acyclic π-conjugated molecules as n-type electronic materials and find that the cyclic molecules have numerous benefits in organic photovoltaics. We designed two conjugated cycles for this study. Each comprises four subunits; one combines four electron-accepting, redox-active, diphenyl-perylenediimide subunits, and the other alternates two electron-donating bithiophene units with two diphenyl-perylenediimide units. We compare the macrocycles to acyclic versions of these molecules and find that, relative to the acyclic analogs, the conjugated macrocycles have bathochromically shifted UV-vis absorbances and are more easily reduced. In blended

films, macrocycle-based devices show higher electron mobility and good morphology. All of these factors contribute to the more than doubling of the power conversion efficiency observed in organic photovoltaic devices with these macrocycles as the n-type, electron transporting material. This study highlights the importance of geometric design in creating new molecular semiconductors.

In Chapter 6, I describe a new molecular design that enables high performance organic photodetectors. We use a rigid, conjugated macrocycle as the electron acceptor in devices to obtain high photocurrent and low dark current. We directly compare the macrocyclic acceptor devices to an acyclic control device; we find that the superior performance of the macrocycle originates from its rigid, conjugated, and cyclic structure. The macrocycle's rigid structure reduces the number of charged defects originating from deformed sp^2 carbons and covalent defects from photo/thermo-activation. With this molecular design we are able to suppress dark current density while retaining high responsivity in an ultra-sensitive non-fullerene organic photodetector. Importantly, we achieve a detectivity of ~10^{14} Jones at near zero bias voltage. This is without the need for extra carrier blocking layers commonly employed in fullerene-based devices. Our devices are comparable to the best fullerene-based photodetectors, and the sensitivity at low working voltages (< 0.1 V) is a record for non-fullerene OPDs.

Table of Contents

List of Figures

List of Tables

Acknowledgements

First and foremost, I would like to heartily thank my advisor, Prof. Colin Nuckolls, for his constant guidance, encouragement and support throughout my Ph.D. study. He always gave me freedom and motivated me to explore exciting projects. His immense knowledge, innovation and foresight were instrumental in making these projects feasible. I admire his enthusiasm for chemistry, his ability of applying chemistry principles to solving practical scientific questions, his leadership that empowers the team to overcome difficulties and his vision of transforming molecules into materials with functions and applications. The valuable training I received from him is my great treasure for my academic career. It has been a wonderful experience working with him in the past five years.

I deeply feel indebted to Prof. Xiaoyang Zhu, Dr. Fay Ng and Dr. Michael Steigerwald, whom I think of as my second advisors, for their help and support from different aspects. Prof. Xiaoyang Zhu brought me into the world of spectroscopy. I have been fascinated by his elegant methods and experiments to study fundamental chemistry problems. Without his help, I could not gain insight into the underlying mechanisms in all of my research projects. I also got educated a lot from the discussion and his comments during their group meetings, which is like a classical physical chemistry course to me. Dr. Fay Ng is an amazing synthetic chemist. The excellent perylenediimide molecules she synthesized were the base of my Ph.D. research. It was my great fortune and pleasure working with her to study the structure and property of the molecules. I am very grateful for all her support on my projects and encouragement during my hard times. Dr. Michael Steigerwald is a mentor, a teacher and a scientist whom I respect very much and from

whom I have learnt a lot. He taught me basics of quantum chemistry and guided me how to use computational methods to understand the properties of molecules. His extensive knowledge and insightful viewpoints have made me think differently. I deeply appreciate him passing on the knowledge to me.

I would like to express my gratitude to all of my collaborators in and out of the Nuckolls group. Dr. M. Tuan Trinh in the Zhu group is my closest collaborator on all of my projects. I deeply appreciate all of his work on the transient absorption that made my projects happen. I also want to thank Melissa Ball, Dr. Brandon Fowler and Dr. Bharat Kumar for synthesizing the materials for my study. I thank Dr. Seok Ju Kang and Dr. Chul-Ho Lee for their mentorship when I started in the lab. They taught me how to grow crystals and make electronic devices. I am also grateful to Wei Wang, Boyuan Zhang, and Prof. Rongsheng Chen for giving me a lot of help on device fabrication and their significant contributions to my projects. I thank Prof. Lynn Loo at Princeton University and Geoffrey E. Purdum, Dr. Petr Khlyabich and Melda Sezen in her research group for collaborating on the non-fullerene solar cell projects. I thank Dr. Chang-Yong Nam, Dr. Charles Black and Dr. Matthew Sfeir at the Brookhaven National Laboratory for their assistance on transient absorption and device characterization. I would like to thank my collaborators for all of their efforts and help, especially Prof. Shengxiong Xiao, Seokjoon Oh, Dr. Ying Wu, Dr. Tracy Chen, Dr. Bumjung Kim, Qizhi Xu, Panpan Li, Dr. Haiming Zhu, Jue Wang, Katherine Elbert, Dr. Daniel W. Paley, Grisha Etkin, Prof. Omer Yaffe and Prof. Yi Rao at Temple University. I would also like to thank Prof. Luis Campos, Prof. Ioannis Kymissis and Prof. Xavier Roy for taking the time to serve on my defense committee.

Last but not least, I would like to thank my parents for their unfailing love, support and encouragement. I would also like to thank my wife, Jinchao Huang for her understanding and love through the years. The happiest time with her has made my life in New York. The past five-year time was a critical stage in my life. I started this journey with full passion for science, expecting for gains from my research and wonderful memories with my friends, colleagues and advisors. However, I never expected everything to be smooth during the process. Sometimes I lost my direction when I did not see anything promising; sometimes I got hesitated about whether I should persist in my dreaming academic career. It was her faithful support that encouraged me, made me determined to carry on when I met obstacles. I could not have accomplished many work in my study without her encouragement. We share the passion and interest in research work. I am proud of her work in designing batteries that will potentially change the world. She is always proud of what I achieved, what I am doing now and what I am going to do in the future. She believes that my efforts will pay off someday. She likes listening to me about what is happening in the lab. She was just as excited as me when I made some progress. What's more, she loves life so much and makes our life colorful. I am truly thankful for her endless love.

— Yu Zhong

This work is dedicated to my parents and my wife.

Chapter 1 Introduction to Contorted Organic semiconductors

1.1 Background

This thesis describes a body of research in the design, synthesis, and study of contorted organic semiconductors. The contorted structure has several important ramifications on the inherent physical behavior of these materials. The intermolecular contacts in crystals and polycrystalline films are versatile relative to those available to flat aromatics, and, consequently, their charge transport properties in organic materials-based devices can be improved. In addition, the nonplanar structures provide concave surfaces that recognize the convex surfaces of fullerenes. This mode of self-assembly makes them useful in creating atomically-defined p-n junctions in organic photovoltaics. Finally, these materials are more soluble and less likely to spontaneously aggregate compared to flat aromatics, allowing for solution-based processing of devices.

It is important to put this body of research into context within organic materials research. The molecules described below are elements of nanostructured carbon-based materials. They are model systems and potential seeds for the synthesis of nanotubes, graphene, and fullerenes.[1-5] These molecules and the understanding of their properties inform and provide a counterpoint to studies on flat aromatics.[2] Moreover, the molecules described here are influenced by plastic electronic materials, but, in this case, molecular

recognition events and self-assembly processes transform them from molecules to materials.[6]

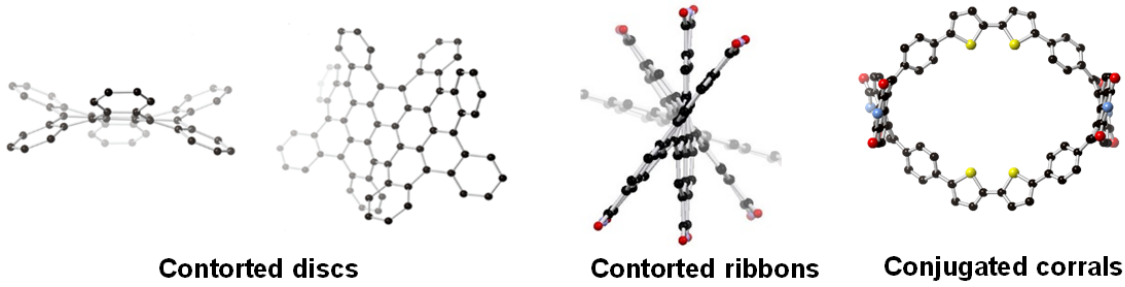

Figure 1.1. DFT models of contorted organic semiconductors.

1.2 Molecular structures

1.2.1. Contorted discs

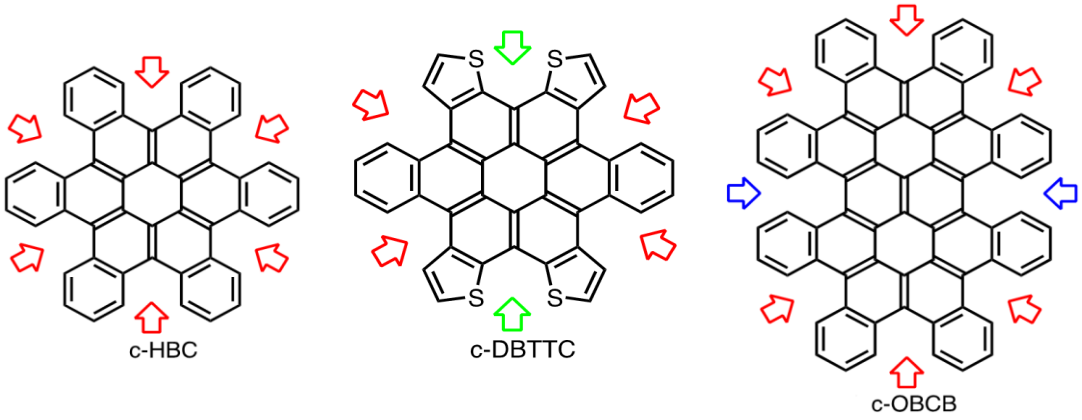

Figure 1.2. Molecular structures of c-HBC, c-DBTTC and c-OBCB. Red arrows show the cove regions benzophenanthrene subunits; green arrows for similar interactions with thiophene rings.

The molecular feature incorporated into the design of the contorted discs is benzophenanthrene, also known as [4]-helicene, which is the smallest helicene[7]. A highly non-planar molecule results from the steric congestion in the cove positions. Benzophenanthrene has a splay angle of 19.9°, and a barrier for inversion between the two helicenes of 7.6 kcal/mol.[8] The contorted hexabenzocoronene (c-HBC) shown in Figure

1.2 is conceptually the superposition of six benzophenanthrene subunits into a hexagonal array.[9] Substituting four benzo groups with thiophenes creates the heteroaromatic contorted dibenzotetrathienocoronene (c-DBTTC, Figure 1.2).[10] Extending the core along one axis generates the contorted octabenzocircumbiphenyl (c-OBCB, Figure 1.2).[11]

1.2.2. Contorted ribbons

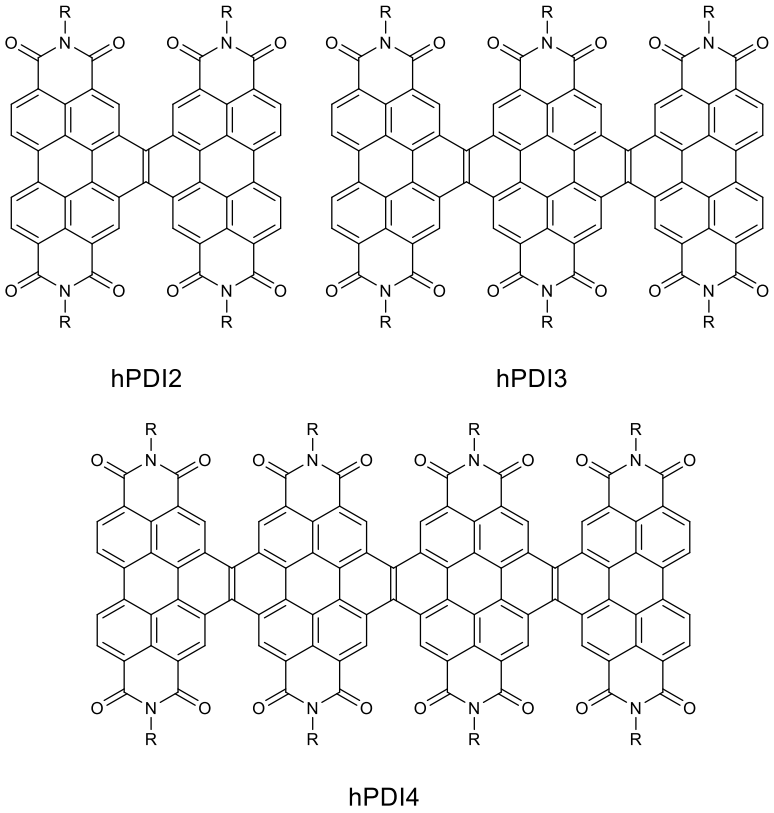

Figure 1.3. Molecular structures of helical ribbons, hPDI2, hPDI3 and hPDI4.

The ribbon-shaped, contorted molecules can be conceptualized as ultra-narrow pieces of graphene. The contortion causes them to wind into helical ribbons. We created versions of these contorted molecules whose cores can be extended in one direction to make one-dimensional contorted ribbons. We fused perylenediimides (PDIs) together to make atomically-defined, helical graphene ribbons, the h-PDI family (Figure 1.3). Our approach allows for exquisite structural control and versatility to synthesize oligomeric

derivatives.[12] Figure 1.3 shows the three oligomers we synthesized: the dimer (hPDI2), trimer (hPDI3), and tetramer (hPDI4).

1.2.3. Conjugated corrals

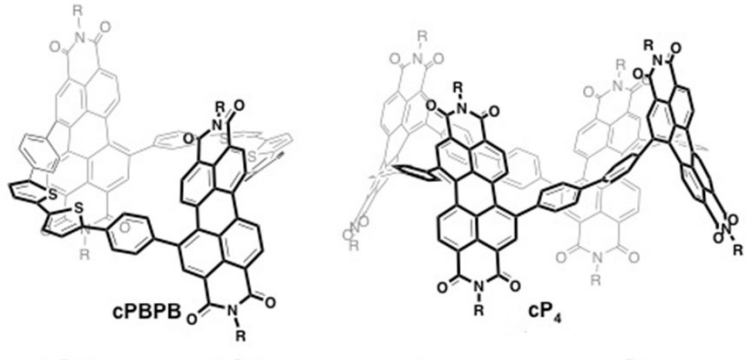

Figure 1.4. Molecular structures of **cPBPB** and **cP4**.

The last design motif for contorted molecules is building conjugated, cyclic structures. There are two examples of conjugated cycles that incorporate multiple repeated units of the redox-active, diphenyl-perylenediimide (**P**) subunit. One macrocycle alternates a bithiophene (**B**) unit with a **P** unit to form the **-P-B-P-B-** cyclic pattern, denoted here **cPBPB**, where "**c**" denotes cyclic. A second macrocycle (**cP4**) directly links the diphenyl-perylenediimide subunits into a tetrameric structure (Figure 1.4).[13]

1.3 Self-assembled materials from contorted aromatics.

Adding alkoxyl chains to the periphery of the c-HBC creates structures that self-assemble. With 4-dodecycloxy chains (Figure 1.5A), c-HBC forms a hexagonally-ordered columnar liquid-crystalline phase (Figure 1.5B).[9] These stacks are interesting because the co-axial aromatic core of the stack can act as a conduit for charge and the exterior of the molecule can behave as an insulating sheath. The formation of self-assembled wires from the tetra-dodecyloxy c-HBC was robust, and we could cast films that contained these columnar phases. In these films, the columns align themselves parallel to the surface (over

macroscopic distances) with the discs oriented edge-on to the substrate (Figure 1.5C).

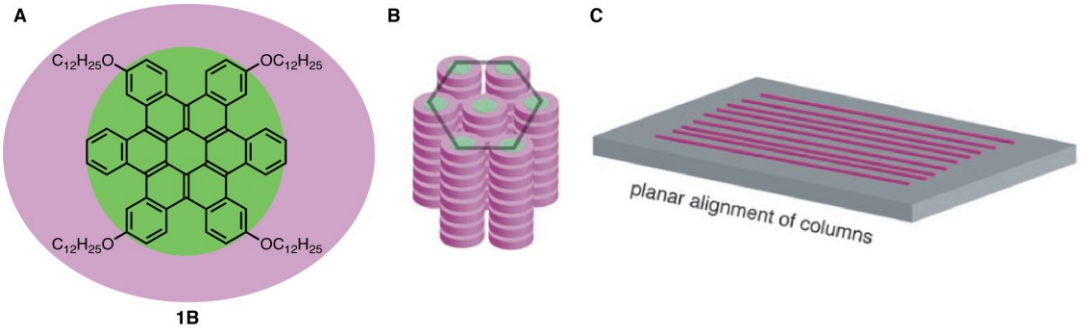

Figure 1.5. (A) c-HBC (**1B**) with 4-dodecycloxy chains. (B) Columnar, hexagonal arrangement of c-HBC. (C) The columns of c-HBC align themselves parallel to the substrate. Reproduced from reference 9.

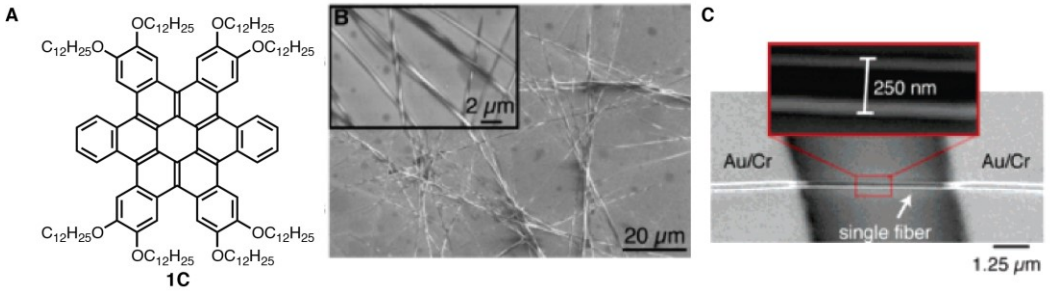

Figure 1.6. (A) c-HBC (**1C**) with 8-dodecyloxy chains**.** (B) Scanning electron microscopy image of the c-HBC organized into nanoscale cables. The inset shows a higher magnification view. (C) Individual cables could be put into devices by using an elastomeric stamp to pick and place cables out of the mat. Reproduced from reference 14.

The mode of self-assembly changes when we substitute the c-HBC with 8-dodecyloxy chains (Figure 1.6A). It shows no mesophase but forms crystalline fibers that stack in an orthorhombic fashion.[14] Nanoscale versions of these can be manipulated with an elastomeric stamp to pick individual cables out of tangled mats to place them into electrical devices (Figure 1.6B,C). This pick-and-place procedure elucidates a general

method to manipulate and position highly-ordered, self-assembled nanostructured materials to elucidate their materials' properties. These individual cables act as p-type semiconducting cables.

Based on the OFET experiments detailed above, our hypothesis was that contorted aromatic molecules' properties were limited by defects, grain boundaries, and other extrinsic factors. To test this assertion, we devised a method to measure properties on an individual stack of molecules composed of only a few molecules. The contacts we used were from an individual single-walled carbon nanotube, wired into a device, that had a section excised using lithography.[15-18] The carbon nanotube point contacts formed the source and drain electrodes and were separated by only a few nanometers (see Figure 1.7A). At most 20 molecules can span the gap between the point contacts. We made a film by spin-casting c-HBC with 4-dodecycloxy chains and annealing to form an ordered columnar liquid crystalline phase.[17] This device shows record mobility (>1 $cm^2V^{-1}s^{-1}$) for an OFET from columnar liquid crystalline materials.[17]

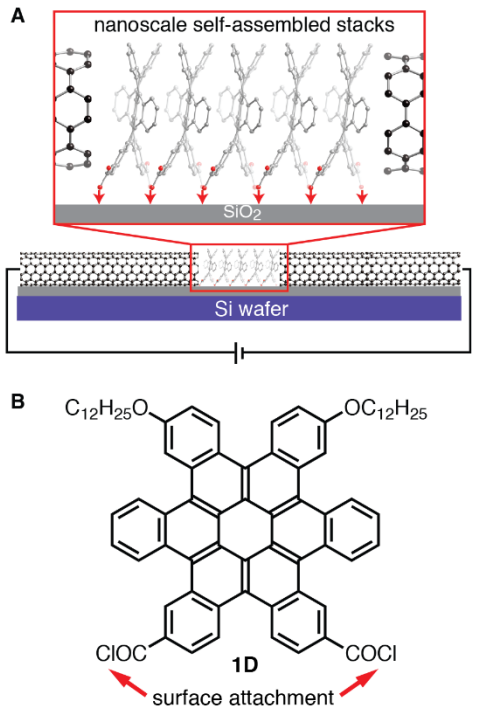

Figure 1.7. (A) Stack of c-HBC molecules between the carbon nanotube point contacts. (B) **1D** with acid chlorides to form a monolayer transistor channel between the carbon nanotube contacts. Reproduced from reference 18.

1.4 Photovoltaics

Given their unusual shapes and facile charge transport, we were interested in studying these contorted molecules in OPVs. As mentioned above, the contorted disk shaped molecules are good hole-transporting materials through their supramolecular columns.[10,19] Controlled annealing of solution-processed c-DBTTC thin films yields a crystalline donor layer comprised of a supramolecularly-assembled, three-dimensional network of cables. This scaffold not only facilitates charge transport, but also provides a template for a reticulated heterojunction with C_{60}.[20] The nanostructured active layer provides a three to fourfold increase in the power conversion efficiency compared to active layers based on the flat, thermally evaporated analog.[21]

Self-assembly of the donor and the acceptor at the molecular-scale has been proposed to control morphology and improve device performance in the polymer bulkjunctions,[22-25] although molecular examples are rare.[26-28] c-HBC is a perfect partner for molecular self-assembly and co-crystallization with fullerenes because they are complementary to each other in size and shape. Indeed, co-crystallization occurs both from solution and the vapor phase to form a 'ball-and-socket' arrangement (Figure 1.8A).[29] We found that a derivative of c-DBTTC also co-crystallizes with C_{60} to produce a 2:1 ratio of C_{60} to c-DBTTC (Figure 1.8B).[10] This supramolecular arrangement of ball-shaped, n-type semiconductor and bowl-shaped p-type semiconductor arranges them to communicate electronically and imparts the good photovoltaic properties discussed below.

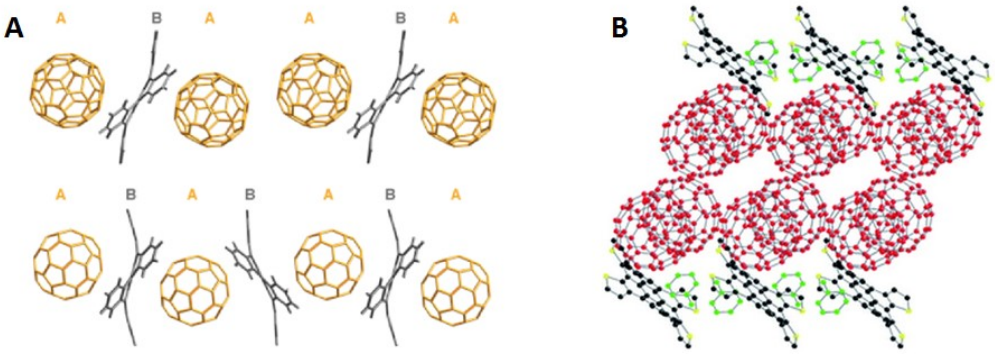

Figure 1.8. (A) Co-crystals of c-HBC and C_{60} from solution (top) and from vapor phase (bottom). (B) Co-crystals of a derivative of c-DBTTC with C_{60} (red carbon atoms). Toluene molecules are shown in green. Reproduced from reference 10 and 29.

To test whether shape complementarity was important, we constructed two devices utilizing c-HBC and a completely planar HBC derivative.[2] Both molecules share similar electronic and physical properties, with the notable difference being shape. We found devices made from c-HBC were more efficient relative to the non-contorted derivative by about two orders of magnitude greater photon conversion efficiency (PCE).[29] We were able

to conclude that the c-HBCs form a shape complementary complex with n-type acceptors like fullerenes, yielding an intimate donor-acceptor interface that results in enhanced electronic properties.

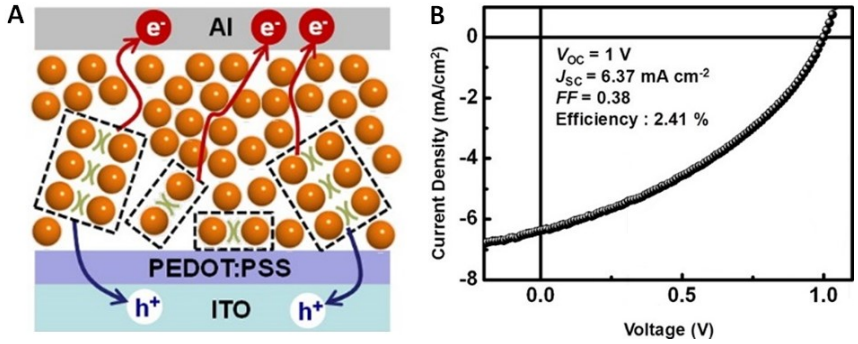

Figure 1.9. (A) Self-assembled p−n junction of a **1B**:$PC_{70}BM$ blended film. (B) J−V characteristics of a 10/90 wt% **1B**/$PC_{70}BM$ device under illumination. Reproduced from reference 30.

The supramolecular 'ball-and-socket' complex also exists in the blended films of both c-HBC:$PC_{70}BM$,[30] c-DBTTC:$PC_{70}BM$,[31] and c-OBCB:$PC_{70}BM$.[11] Formation of this supramolecular complex directly affects charge separation in the active layer (Figure 1.9A), leading to efficient organic solar cells from solution. **1B** in the blend film achieves a maximum PCE of 2.41% (Figure 1.9B). This is high considering the absorption profile of the **1B** is largely confined to the UV range. We observed improved efficiency of a (**3**):$PC_{70}BM$ solar cell.[11] The bathochromic shift (~80 nm) is responsible for the higher PCE for c-OBCB relative to the smaller contorted aromatics. Further red-shifting of the absorbance will likely improve the performance of these materials in OPVs. These results suggest a new design strategy for solution-processed solar cells to improve device performance by molecular scale self-assembly via non-covalent interaction between a

concave donor and a ball-shape acceptor.

We find that the 'ball and socket' arrangement persists for the range of the materials discussed above. This interface between c-HBC and its derivatives with n-type materials demonstrate their ability to transport holes and electrons in a new design for organic solar cells. This type of interaction would be difficult to achieve within polymer chemistry. We can increase the strength of the association between these contorted molecules and fullerenes by making them more tightly curved. For example, the bowl-shaped hydrocarbons mentioned above exhibit an increase in the association constant when there are two 5-membered rings formed and further increases when there are four 5-membered rings formed.[32]

1.5 References and notes

(1) Akasaka, T; Wudl, F; Nagase, *Chemistry of Nanocarbons.*Wiley: Chichester, West Sussex, 2010.

(2) Wu, J.; Pisula, W.; Müllen, K. *Chem. Rev.* 2007, *107*, 718-747.

(3) Omachi, H.; Segawa, Y.; Itami, K. *Acc. Chem. Res.* 2012, *45*, 1378-1389.

(4) Jasti, R.; Bhattacharjee, J.; Neaton, J. B.; Bertozzi, C. R. *J. Am. Chem. Soc.* 2008, *130*, 17646-17647.

(5) Petrukhina, M. A.; Scott, L. T.; Kroto, H. W. Fragments of Fullerenes and Carbon Nanotubes: Designed Synthesis, Unusual Reactions, and Coordination Chemistry; Wiley: Chichester, West Sussex, 2011.

(6) Bendikov, M.; Wudl, F.; Perepichka, D. F. *Chem. Rev.* 2004, *104*, 4891-4945.

(7) Gingras, M. *Chem. Soc. Rev.* 2013, *42*, 968-1006.

(8) Grimme, S.; Peyerimhoff, S. D. *Chem. Phys.* 1996, *204*, 411-417.

(9) Xiao, S.; Myers, M.; Miao, Q.; Sanaur, S.; Pang, K.; Steigerwald, M. L.; Nuckolls, C. *Angew. Chem. Int. Ed.* 2005, *44*, 7390-7394.

(10) Chiu, C. Y.; Kim, B.; Gorodetsky, A. A.; Sattler, W.; Wei, S.; Sattler, A.; Steigerwald, M. ; Nuckolls, C. *Chem. Sci.* 2011, *2*, 1480-1486.

(11) Xiao, S.; Kang, S. J.; Wu, Y.; Ahn, S.; Kim, J. B.; Loo, Y. L.; Siegrist, T.; Steigerwald, M. L.; Li, H. X.; Nuckolls, C. *Chem. Sci.* 2013, *4*, 2018-2023.

(12) Zhong, Y.; Kumar, B.; Oh, S.; Trinh, M. T.; Wu, Y.; Elbert, K.; Li, P.; Zhu, X.; Xiao, S.; Ng, F.; Steigerwald, M. L.; Nuckolls, C. *J. Am. Chem. Soc.* 2014, *136*, 8122-8130.

(13) Ball, M.; Fowler, B.; Li, P.; Joyce, L. A.; Li, F.; Liu, T.; Paley, D.; Zhong, Y.; Li, H.; Xiao, S.; Ng, F.; Steigerwald, M. L.; Nuckolls, C. *J. Am. Chem. Soc.* 2015, *137*, 9982.

(14) Xiao, S.; Tang, J.; Beetz, T.; Guo, X.; Tremblay, N.; Siegrist, T.; Zhu, Y.; Steigerwald, M.; Nuckolls, C. *J. Am. Chem. Soc.* 2006, *128*, 10700-10701.

(15) Guo, X.; Small, J. P.; Klare, J. E.; Wang, Y.; Purewal, M. S.; Tam, I. W.; Hong, B. H.; Caldwell, R.; Huang, L.; O'Brien, S.; Yan, J.; Breslow, R.; Wind, S. J.; Hone, J.; Kim, P.; Nuckolls, C. *Science* 2006, *311*, 356-359.

(16) Feldman, A. K.; Steigerwald, M. L.; Guo, X.; Nuckolls, C. *Acc. Chem. Res.* 2008, *41*, 1731-1741.

(17) Guo, X.; Xiao, S.; Myers, M.; Miao, Q.; Steigerwald, M. L.; Nuckolls, C. *Proc. Natl. Acad. Sci. U. S. A.* 2009, *106*, 691-696.

(18) Guo, X..; Myers, M.; Xiao, S.; Lefenfeld, M.; Steiner, R.; Tulevski, G. S.; Tang, J.; Baumert, J.; Leibfarth, F.; Yardley, J. T.; Steigerwald, M. L.; Kim, P.; Nuckolls, C. *Proc. Natl. Acad. Sci. U. S. A.* 2006, *103*, 11452-11456.

(19) Xiao, S.; Tang, J.; Beetz, T.; Guo, X.; Tremblay, N.; Siegrist, T.; Zhu, Y.;

Steigerwald, M.; Nuckolls, C. *J. Am. Chem. Soc.* 2006, *128*, 10700-10701.

(20) Schiros, T.; Mannsfeld, S.; Chiu, C. Y.; Yager, K. G.; Ciston, J.; Gorodetsky, A. A.; Palma, M.; Bullard, Z.; Kramer, T.; Delongchamp, D.; Fischer, D.; Kymissis, I.; Toney, M. F.; Nuckolls, C. *Adv. Funct. Mater.* 2012, *22*, 1167-1173.

(21) Gorodetsky, A. A.; Chiu, C. Y.; Schiros, T.; Palma, M.; Cox, M.; Jia, Z.; Sattler, W.; Kymissis, I.; Steigerwald, M.; Nuckolls, C. *Angew. Chem. Int. Ed.* 2010, *49*, 7909-7912.

(22) Miller, N. C.; Sweetnam, S.; Hoke, E. T.; Gysel, R.; Miller, C. E.; Bartelt, J. A.; Xie, X.; Toney, M. F.; McGehee, M. D. *Nano Lett.* 2012, *12*, 1566-1570.

(23) Mayer, A. C.; Toney, M. F.; Scully, S. R.; Rivnay, J.; Brabec, C. J.; Scharber, M.; Koppe, M.; Heeney, M.; McCulloch, I.; McGehee, M. D. *Adv. Funct. Mater.* 2009, *19*, 1173-1179.

(24) Cates, N. C.; Gysel, R.; Beiley, Z.; Miller, C. E.; Toney, M. F.; Heeney, M.; McCulloch, I.; McGehee, M. D. *Nano Lett*. 2009, *9*, 4153-4157.

(25) Kennedy, R. D.; Ayzner, A. L.; Wanger, D. D.; Day, C. T.; Halim, M.; Khan, S. I.; Tolbert, S. H.; Schwartz, B. J.; Rubin, Y. *J. Am. Chem. Soc.* 2008, *130*, 17290-17292.

(26) Bürckstümmer, H.; Tulyakova, E. V.; Deppisch, M.; Lenze, M. R.; Kronenberg, N. M.; Gsänger, M.; Stolte, M.; Meerholz, K.; Würthner, F. *Angew. Chem. Int. Ed.* 2011, *50*, 11628-11632.

(27) Troshin, P. A.; Sariciftci, N. S. Supramolecular Chemistry for Organic Photovoltaics. In *Supramolecular Chemistry: From Molecules to Nanomaterials*; Gale, P. A.; Steed, J. W., Eds.; John Wiley & Sons: Hoboken, 2012.

(28) Loser, S.; Bruns, C. J.; Miyauchi, H.; Ortiz, R. P.; Facchetti, A.; Stupp, S. I.; Marks, T. J. *J. Am. Chem. Soc.* 2011, *133*, 8142-8145.

(29) Tremblay, N. J.; Gorodetsky, A. A.; Cox, M. P.; Schiros, T.; Kim, B.; Steiner, R.; Bullard, Z.; Sattler, A.; So, W. Y.; Itoh, Y.; Toney, M. F.; Ogasawara, H.; Ramirez, A. P.; Kymissis, I.; Steigerwald, M. L.; Nuckolls, C. *Chemphyschem* 2010, *11*, 799-803.

(30) Kang, S. J.; Ahn, S.; Kim, J. B.; Schenck, C.; Hiszpanski, A. M.; Oh, S.; Schiros, T.; Loo, Y. L.; Nuckolls, C. *J. Am. Chem. Soc.* 2013, *135*, 2207-2212.

(31) Kang, S. J.; Kim, J. B.; Chiu, C. Y.; Ahn, S.; Schiros, T.; Lee, S. S.; Yager, K. G.; Toney, M. F.; Loo, Y. L.; Nuckolls, C. *Angew. Chem. Int. Ed.* 2012, *51*, 8594-8597.

(32) Whalley, A. C.; Plunkett, K. N.; Gorodetsky, A. A.; Schenck, C. L.; Chiu, C. Y.; Steigerwald, M. L.; Nuckolls, C. Bending contorted hexabenzocoronene into a bowl. *Chem. Sci.* 2011, *2*, 132-135.

Chapter 2 Helical Perylene Diimide Ribbons for Molecular Electronics

Chapter 2 is reproduced with permission from the authors: Zhong, Y.; Kumar, B.; Oh, S.; Trinh, M. T.; Wu, Y.; Elbert, K.; Li, P. P.; Zhu, X. Y.; Xiao, S. X.; Ng, F.; Steigerwald, M. L.; Nuckolls, C. *J. Am. Chem. Soc.* **2014**, *136*, 8122; Copyright 2014 American Chemical Society. Device fabrication and characterization were performed by myself with assistance from Ying Wu and Katherine Elbert. Synthesis was carried out by Fay Ng, Bharat Kumar and Panpan Li. DFT calculations were performed by Michael L. Steigerwald. Transient absorption measurements were conducted by M. Tuan Trinh.

2.1 Introduction

This chapter describes the design, synthesis and electrical characterization of electron deficient graphene nanoribbons. Graphene, the atomically thin two-dimensional crystal of graphite, has an unusual set of qualities that make it useful for both fundamental research[1-3] and numerous applications[4-6]. However, graphene is limited for many electronic applications because it is a zero-band-gap semiconductor. It was predicted that narrow nanoribbons exhibit different electronic states.[7] In order to open a sufficient electronic gap, narrow graphene nanoribbons with sub-10nm widths are required to yield acceptable on/off transistor operation at room temperature.[8-10] There are several top-down methods to create thin graphene ribbons,[11-17] but the usefulness of the resulting ribbons is limited by the width not being atomically defined and the functional groups on the edge being uncontrolled.[13] A number of bottom-up approaches to synthesize graphene nanoribbons also exist.[18-22] The bottom-up approach is advantageous because it provides an atomically precise synthesis of nanoribbons without any structural defects. It also gives access to chemical modification

along the edges to tune solubility, electrical characteristics, and conformation of the ribbons. Müllen and coworkers have reported several methods for synthesis of graphene nanoribbons either in solution[19,20,22] or on metal surfaces.[21] Despite these studies, there is a dearth of methods to produce n-type, electron transporting ribbons.[18] The present study fills that void by providing a synthetic method to make atomically defined graphene nanoribbons comprising perylene-3,4,9,10-tetracarboxylic acid diimide (PDI, **1** in Figure 2.1) subunits bridged with C=C subunits. We describe a new synthetic procedure to fuse PDIs together with an ethylene bridge forming dimer **2**, trimer **3**, and tetramer **4** (Figure 2.1). The physical and electronic structure of this series of oligomers is a consequence of the unusual fusion in the ribbon backbone. The steric congestion introduced by the fusion between the PDIs causes the ribbons to become severely contorted into helical superstructures.

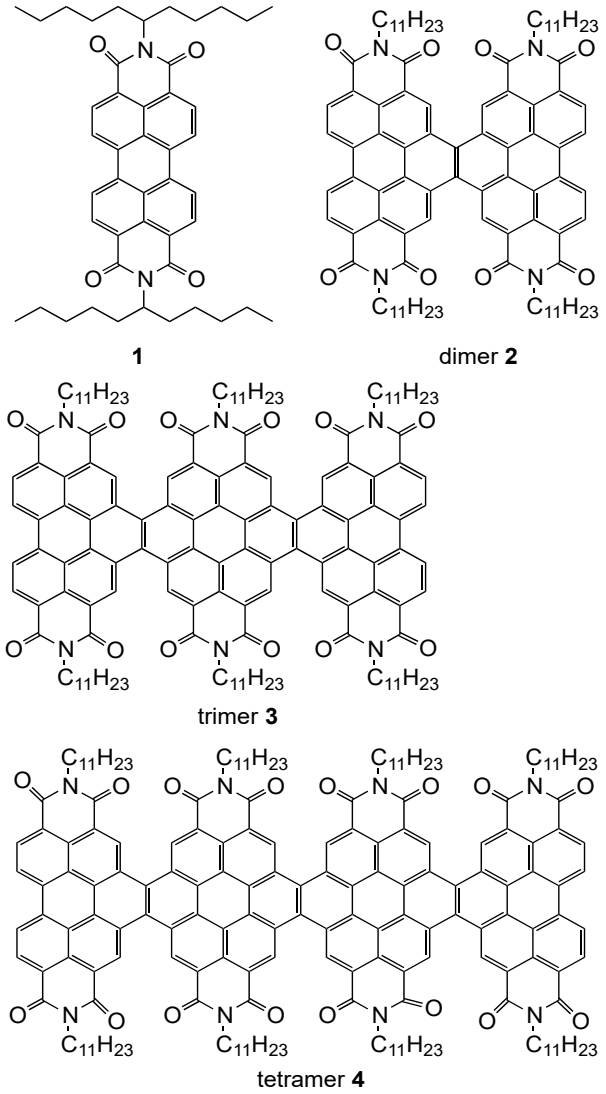

Figure 2.1. PDI monomer **1**, dimer **2**, trimer **3**, and tetramer **4**.

The PDI core has been heavily investigated as a chromophore and as an n-type organic semiconductor. The PDI subunit has found many applications in field effect transistors (FETs),[23] light-emitting diodes (LEDs)[24] and organic photovoltaics (OPVs).[25,26] PDI is a versatile building block for the synthesis of graphene nanoribbons because many synthetic routes have been developed to functionalize the bay positions of the aromatic core.[25,27-29] Pi-conjugated oligomers with PDI units have been reported.[18,30] Notably, Wang and coworkers have prepared graphene nanoribbons with a zig-zag fusion of PDI building

blocks by means of a copper-mediated coupling of a tetrachloro-substituted PDI.[18] However, their approach suffers from low yields and the lack of structural control for the synthesis of higher oligomers. The dimer **2** was synthesized recently from a step-intensive synthesis in an overall yield that is less than 1%.[30] Here we describe a new strategy to synthesize n-type graphene nanoribbons from PDI subunits. Our approach gives the precise control over the final structure and can be extended to the synthesis of higher oligomers.

Scheme 2.1. Synthesis of dimer **2**.[a]

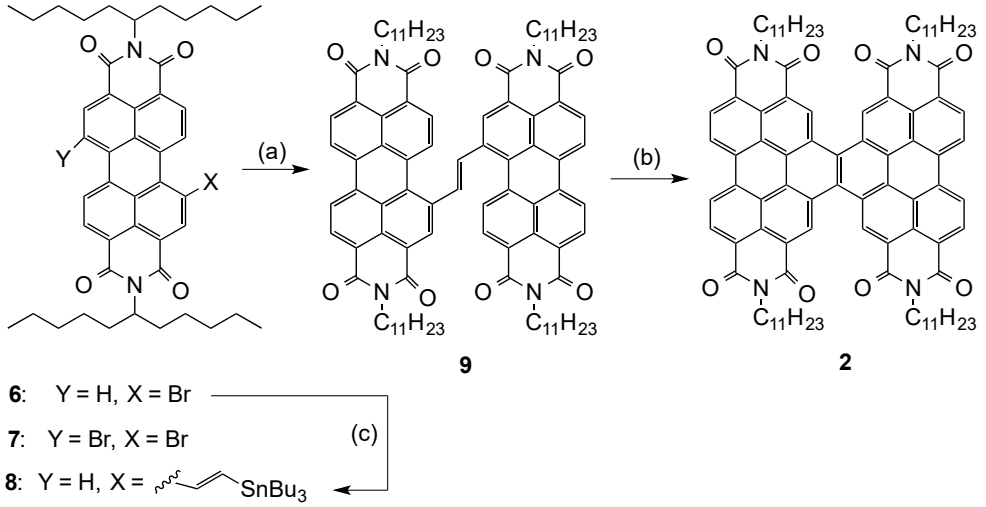

[a]key: (a) **5**, $Pd(PPh_3)_4$, PhMe, reflux, 88%; (b) I_2, air, hν, PhH, 83%; (c) **5**, $Pd(PPh_3)_4$, PhMe, reflux, 70%.

2.2 Oligomer Synthesis

Scheme 2.1 summarizes the synthesis of the dimer **2**. Experimental details are contained in the Supporting Information. We couple trans-1,2-bis(tributylstannyl)ethene (**5**) to the monobromo-PDI (**6**)[31] via a Stille coupling in 88% yield.[27] We then oxidatively cyclized the ethylene-bridged PDI **9** using Mallory photocyclization.[32,33] Optimum conditions for the photocyclization to **2** required both I_2 and purging with air under irradiation with a 450 W Hanovia medium pressure mercury lamp. Under these conditions

high yields (~83%) could be obtained for the dimer **2**.

Scheme 2.2. Synthesis of trimeric PDI **3**.[a]

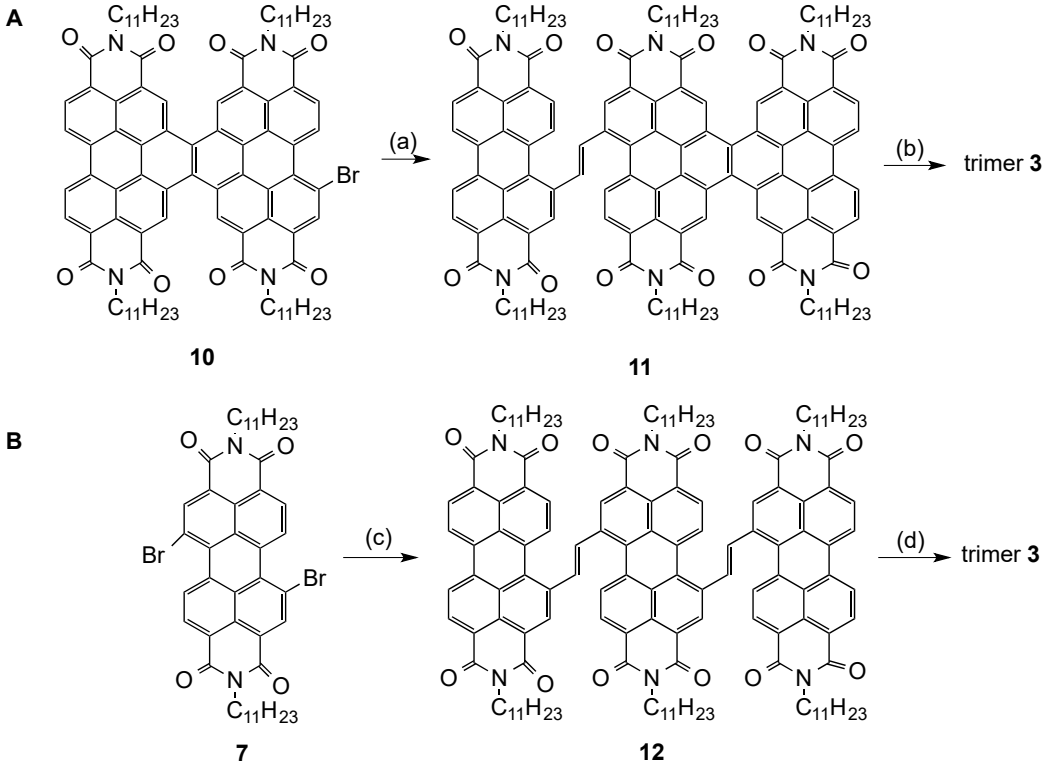

[a]key: (a) **8**, $Pd(PPh_3)_4$, PhMe, reflux, 93%; (b) I_2, air, hν, PhMe, 63%; (c) **8**, $Pd(PPh_3)_4$, PhMe, reflux, 47%; (d) I_2, air, hν, PhMe, 62%

We also found a method to create the important PDI monostannane building block **8**, shown in Scheme 2.1. This building block is essential for the higher oligomer syntheses. We show two alternative syntheses of the trimeric PDI **3** in Scheme 2.2. Coupling monostannane **8** with either the monobrominated dimer **10**, in Scheme 2.4 (see Section 2.7.5 for synthesis of **10**) or with the dibrominated parent PDI[34] (**7**, in Scheme 2.5) furnishes the substrates for the photocyclization. Again we applied the Mallory conditions developed for the dimer; both substrates yield the trimer **3** in >60% yield. The yield of **3** (from **11** or **12**) is in actuality much higher, but it is difficult to chromatograph the cyclized

PDI oligomers due to their tendency to bind to the silica during chromatography.

Scheme 2.3. Synthesis of the tetrameric PDI **4**.[a]

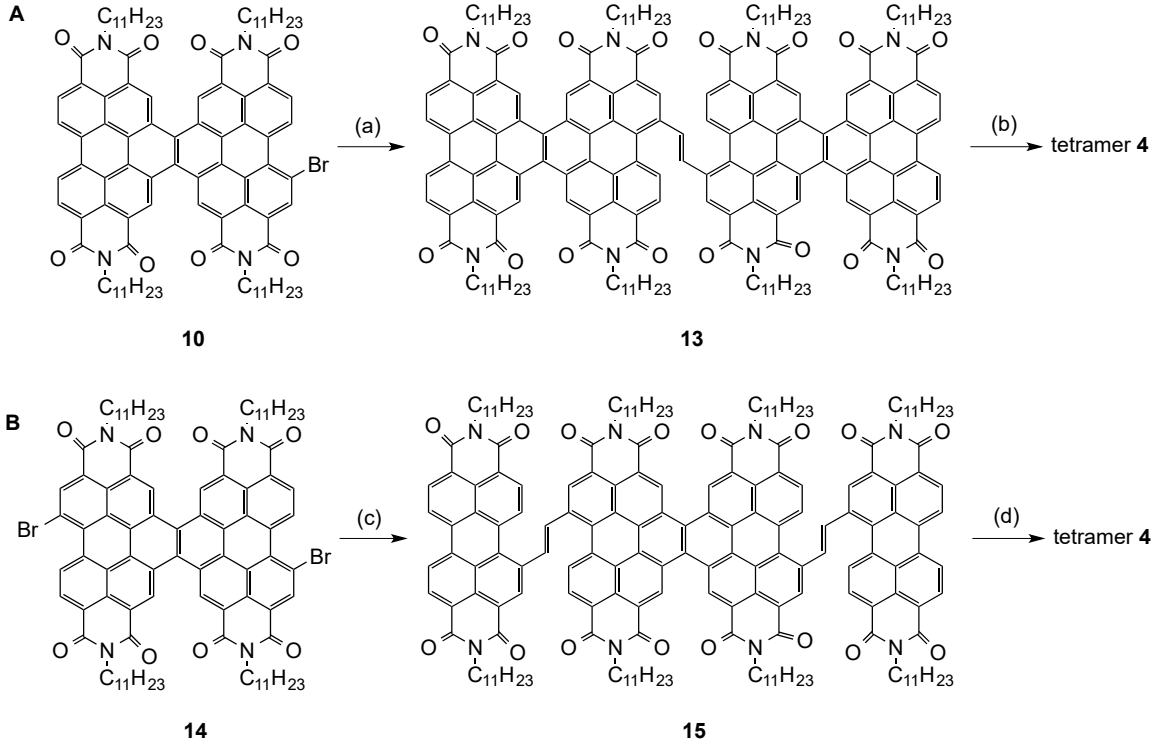

[a]key: (a) **5**, $Pd(PPh_3)_4$, PhMe, reflux, 65%; (b) I_2, air, hν, PhMe; (c) **8**, $Pd(PPh_3)_4$, PhMe, reflux, 72%; (d) I_2, air, hν, PhMe, 45%.

Two analogous routes were developed for the tetrameric PDI **4** shown in Scheme 2.3. In Scheme 2.6 we couple the monobrominated dimer **10** with 1,2-bis(tributylstannyl)ethene (**5**) to yield **13.** In Scheme 2.7, we couple monostannane **8** with the di-brominated dimer **14** (see Section 2.7.5 for synthesis of **14**).[35] Each of these substrates produced the tetramer **4** upon photocyclization. It is perhaps ironic that the reaction mixture resulting from the double photocyclization in Scheme 2.7 was much cleaner than that resulting from the apparently intimately related single photocyclization in Scheme 2.6. The mixture in Scheme 2.6 contains partially cyclized products that are

difficult to separate from the desired product. Therefore we synthesize the tetramer according to Scheme 2.7. Given the high yields, the solubility of the products, and the generality of this method, it is likely that this method can yield substantially longer oligomers.

All oligomers (from dimer to tetramer) are isolated as dark red solids having a metallic sheen. The oligomers are soluble in common organic solvents including toluene, chloroform and dichloromethane. They are insoluble in methanol and ethanol. One advantage of a nonplanar core is that it maintains its solubility and processibility for the longer oligomers. The oligomers are thermally robust; TGA (see Figure 2.9-2.11 in Section 2.8.1) does not show any detectable decomposition below 400 $^{\circ}$C. The oligomers are also resistant to oxidation as evident by absence of any oxidation peak in CV up to +1 V in Bu_4NPF_6 solution (0.1 M) as the electrolyte in dichloromethane (*vide infra*).

2.3 Conformation of the Ribbons

We have been unable to grow single crystals of these materials of sufficient quality for x-ray structure determination, so we relied on DFT optimized structures to gain insight into molecular conformations of the oligomers. To simplify the calculations, we replaced the $C_{11}H_{23}$ side chain attached to each nitrogen atom with a single H. The influence of alkyl N-substituents on the electronic structures is negligible due to the nodes of frontier orbitals at the imide nitrogens.[36,37] The non-planar conformation of the ribbons is a consequence of repulsion between the two C-H bonds on the inner bay position of adjacent PDI units. This steric repulsion causes them to twist away from planarity. This can be seen clearly for the model of the dimer shown in Figure 2.2A. The dimer has a helical twist along ribbon axis meaning that the dimer exists as mixture of enantiomers.[30] The Appendix B contains the

atomic coordinates from the DFT calculations. We performed variable temperature ^{1}H-NMR (between –5 to 100 °C) to determine if there was conformational interchange on the NMR timescale, however the only detectable dynamics for the **2**, **3**, or **4** were due to the hindered rotation of the amide N-CHR bond (Figure2.16-S2.18).[31,34] The broadening of the ^{1}H-NMR resonances due to these rotational isomers obscure details about which conformer exists at room temperature.

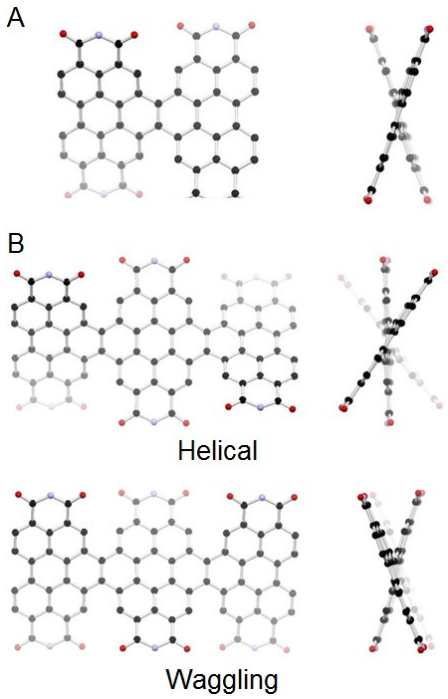

Figure 2.2. DFT models of (A) dimer **2** and (B) trimer **3**.

The trimer structure consists of two conformational options (Figure 2.2B). When the helicity at each of the fusion points has the same handedness, the ribbon is helical. The pitch of this helix is 7.0 nm/turn. We call this the 'Helical' conformation in Figure 2.2B. If the helical sense in the first junction between PDIs is opposite to that of the second junction, then the ribbon is achiral. We call this the "Waggling" conformation in Figure 2.2B.

DFT calculations reveal that the tetramer **4** has three possible conformers. Two of

these conformations are directly analogous to those from the trimer, the helical and waggling conformers (Figure 2.3). Now having three ring junctions, the tetramer can adopt a conformation that is a mixture of helical and waggling. We refer to this as the 'Mixed' conformer. We calculated the relative energies of each of the conformers, and for both the trimer and tetramer all of the competing conformations are isoenergetic.

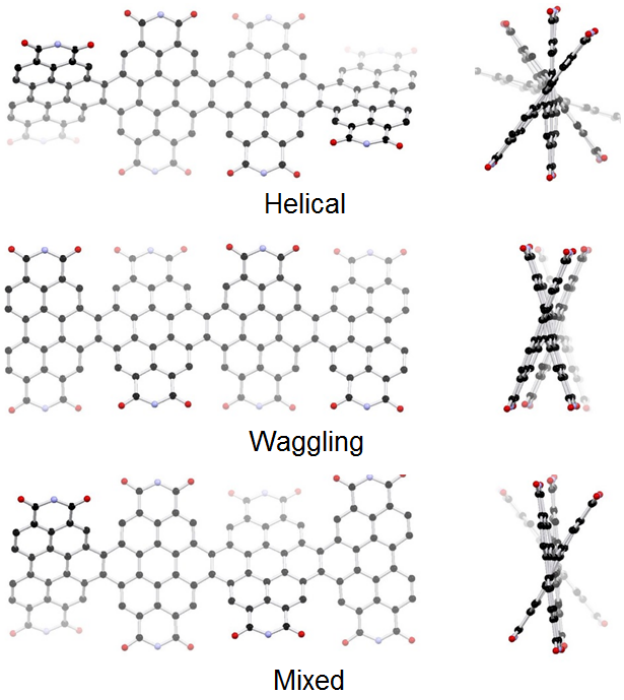

Figure 2.3. DFT models of tetramer **4**.

2.4 Electrical measurements

Electrochemical measurements in CH_2Cl_2 with Bu_4NPF_6 (0.1 M) as the supporting electrolyte reveal that **2**-**4** can accept electrons (Figure 2.13).[38] The trimer **3** and tetramer **4** can accept up to five electrons. From the potential of the first reduction peak, the LUMO was estimated to be -3.77eV, -3.82eV and -3.84eV for **2**, **3** and **4**, respectively. These values are slightly lower than the LUMO level of PDI monomer[18,30] and close to that of common n-type materials such as [6,6]-phenyl-C_{61}-butyric acid methyl ester ($PC_{61}BM$).[39,40]

Table 2.1. FET performance of **2**, **3**, and **4.** [a]Measured in nitrogen-filled glove box. [b]Annealed at 160 °C for 10 min. [c]Annealed at 240 °C for 10 min. [d]Annealed at 200 °C for 10 min. Annealing temperatures reported here are the optimal annealing conditions for the corresponding materials.

	Mobility[a]/$cm^2V^{-1}s^{-1}$	Log(I_{On}/I_{off})	V_{th}/V
2	0.02 [b]	~6	11
3	0.04 [c]	~5	10
4	0.05 [d]	~5	8

We constructed field-effect transistors (FETs) using **2**, **3**, and **4** as the semiconductor to compare their ability to transport electrons. We first treat the substrate (300nm of SiO_2 on a Si wafer) with octadecyltrichlorosilane (OTS) in order to passivate traps on the SiO_2 surface.[41,42] We then spin cast films of **2**, **3**, and **4** onto this surface. The thickness of the organic films is 15-20nm. Transistors made from thicker films (40-60 nm) exhibit nonlinear characteristic at low bias voltage. Au source and drain electrodes are deposited on the film to make a bottom-gate and top-contact configuration with W=105μm and L=15μm. The schematic of the FET device structure is shown in Figure 2.4A. The samples were annealed (under inert atmosphere) to optimize device performance. All of the oligomers form n-type, electron-transporting semiconductors. The typical transfer and output curves for **3** are shown in Figure 2.4C and 2.4D. The FET characteristics for **2** and **4** are similar to those of **3** (See Table 2.1); Figure 2.14 contains the I-V curves for **2** and **4**. The mobility was calculated in the saturation regime[43,44] using $\mu = (W/2L)C_i(V_G-V_T)^2/I_{DS}$, where W and L are the width and length of the channel, C_i (11.5 $nFcm^{-2}$), μ , and V_T

correspond to the capacitance per unit area of the gate insulator, the field effect mobility, and the threshold voltage, respectively. The mobility increases from dimer **2** to tetramer **4**. The FETs for compound **4** exhibits the highest electron mobility, 0.05 $cm^2V^{-1}s^{-1}$. The average threshold voltage varies from 11 V to 8V.[45-48]

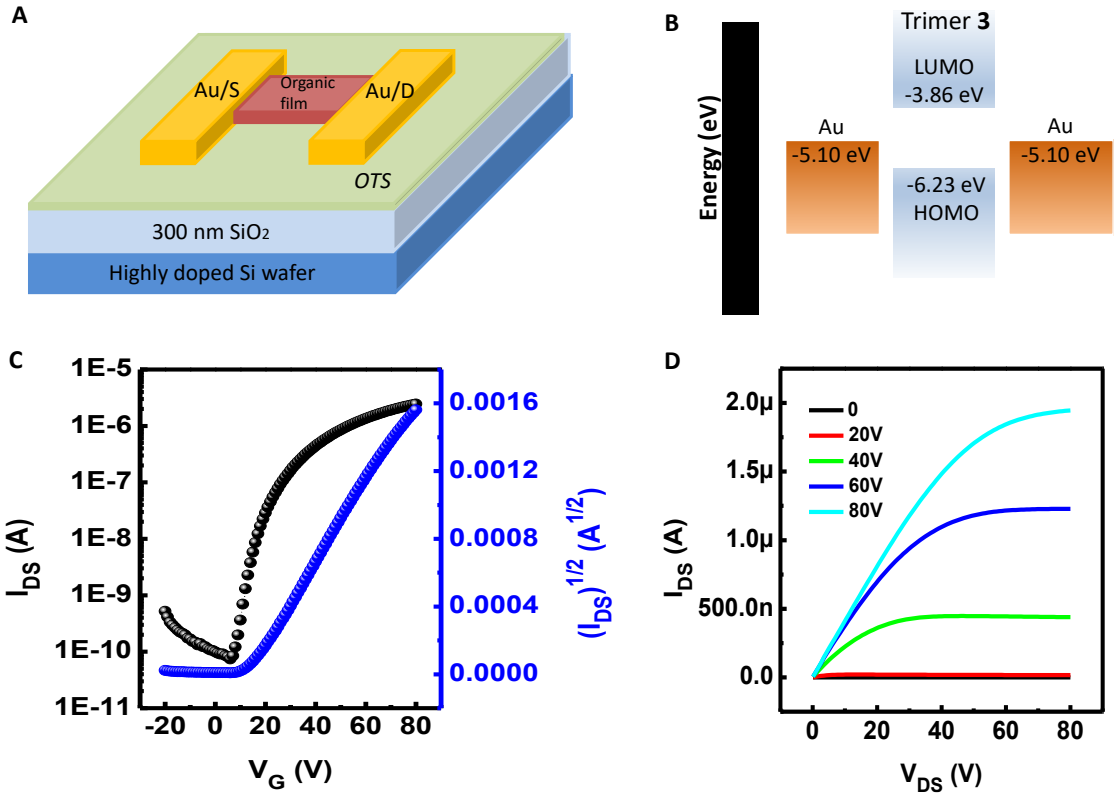

Figure 2.4. (A) Schematic of a FET device structure. (B) Energy diagram for Au/trimer **3**/Au. (C)Transferand (D) Output characteristics of FET for **3**.

The previously reported mobility for PDI monomers with similar structure to **1** range from 0.1 to 2 $cm^2V^{-1}s^{-1}$.[46-49] PDIs featuring planar structure show strong self-aggregation, which facilitates intermolecular charge carrier transport.[47,48] Here, all of the compounds **2-4** formed very smooth films as evident from their AFM images (Figure 2.15) with RMS of 0.32nm, 0.34 nm and 0.27 nm, respectively. No significant crystalline grains were observed. This is probably due to the twisted structures of **2-4** that reduces long range

crystallinity.

2.5 Electronic Structure

We show the absorption and emission spectra for **1** through **4** in Figure 2.5. Comparison of these spectra through the series raised several questions we sought to answer. The first is simple: what is the source of the shift to the red of the lowest energy excitation? The second is less well defined: while the series of absorptions in the monomer has been assigned to a vibrational progression[50,54], the spectra of **2**, **3**, and **4** do not appear as simple, are other higher-energy absorptions present in addition to (or in place of) any vibrational signatures? The third question focuses on the tetramer; why is its lowest-energy absorption so intense? The fourth question is more evident: what is the source of the shorter-wavelength absorptions (~350 nm to ~450 nm) that show up in the oligomers but are absent in the monomer?

The calculated physical structures of **1**-**4** show that we may idealize the PDI-oligomers as individually flat PDI units that are linked by contorted C=C moieties. (In each case the C-C-C-C dihedral angle around the C=C subunits that link the PDI subunits is roughly 155°.) One of our goals was to determine how these subunits interact to yield the electronic behavior of the ultimate nanoribbon. We performed quantum chemical (ground-state DFT and excited state TD-DFT) calculations on the PDI oligomers to better understand these effects and answer the question posed above. We show the computed absorption spectra for **1**-**4** as Figures 2.19-2.25 in Section 2.8.6.

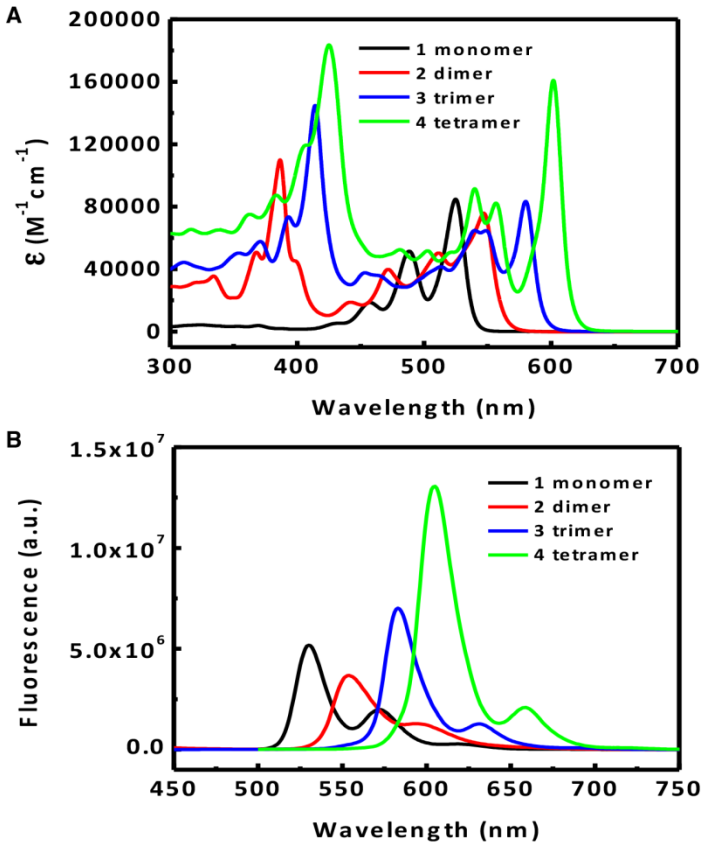

Figure 2.5. (A) UV-vis absorption spectra of monomer **1**, dimer **2**, trimer **3** and tetramer **4** (1 x 10^{-5} M concentration in dichloromethane with a path length l = 1cm) (B) Fluorescence spectra of **1** excited at 488 nm, **2** excited at 386 nm, **3** excited at 414 nm and **4** excited at 425 nm (1 x 10^{-7} M in dichloromethane).

In Table 2.2 we compare the optical HOMO-LUMO gap with the computed HOMO-LUMO gap for **1**–**4.** In each molecule the HOMO is formed primarily from the C-C π orbitals arrayed in alternating phase around the central six-membered rings (Figure 2.6A),[51] and in each molecule the LUMO may be viewed as a similar combination of the corresponding C-C π* orbitals (Figure 2.6B). Excited-state (TD-DFT) calculations show that in the monomer, dimer, and trimer the lowest-energy electronic excitation moves one electron from the HOMO to the LUMO. The energy of this HOMO-LUMO excitation

decreases with increasing oligomer length due to quantum confinement similar to that seen in conjugated molecules or semiconductor clusters.[18,52,53] We also note that the calculated absorption spectrum for **1** is quite simple, showing only a single peak in the visible region; this is in agreement with the previous assignment of the set of equally spaced absorptions as a vibrational progression.[54] Therefore our first question above has a simple answer (at least in elementary, single-electron terms): the lowest-energy optical absorption effectively moves one electron from the HOMO to the LUMO, and as one moves from **1** to **4** both the HOMO and LUMO energies are lowered, but that of the LUMO lowers faster.

Table 2.2. Computational and optical data for **1**, **2**, **3**, and **4**. [a] Calculations were performed at the B3LYP/6-31G** level. [b] Optical band gap were estimated from the wavelength of the absorption peak.

	Computational[a]			Optical[b]	
	E_{HOMO}/eV	E_{LUMO}/eV	E_{gap}/eV	λ_{max}/nm	E_{gap}/eV
1	-6.11	-3.58	2.53	525	2.36
2	-6.19	-3.77	2.41	547	2.27
3	-6.23	-3.86	2.37	580	2.14
4	-6.26	-3.91	2.35	602	2.06

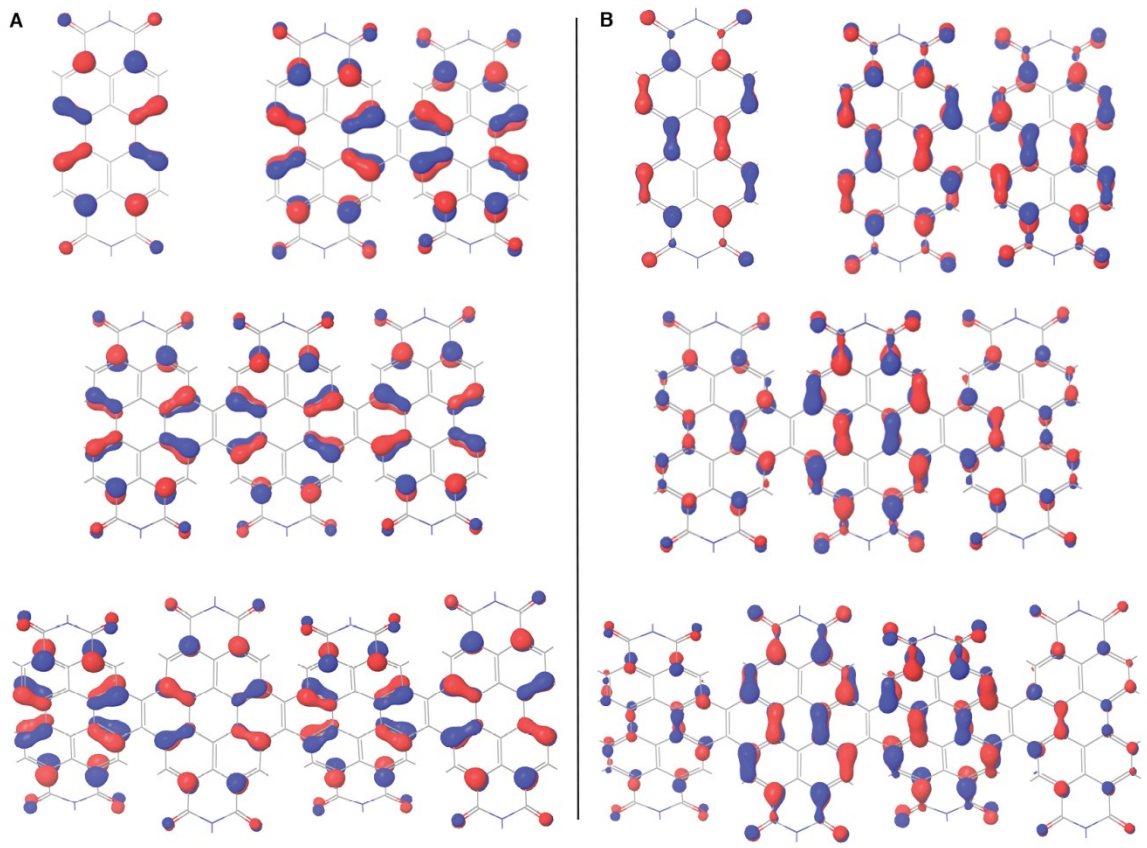

Figure 2.6. (A) Highest occupied molecular orbitals for PDI oligomers. (B) Lowest unoccupied molecular orbitals of PDI oligomers.

While the calculated absorption spectrum of **1** is very simple, the spectra of **2**, **3**, and **4** are more complex. For example, while the calculated spectrum of **1** shows only one peak for wavelengths longer than 350 nm, that of **2** shows at least five, and that of **3** at least seven. These facts, along with the definite non-planarity of the oligomers, suggest an answer to our second question above: that their higher-energy absorptions are not due exclusively to vibronic effects. Further, according to our TD-DFT calculations in **2** and **3**, the second-lowest-energy allowed transition promotes an electron from the HOMO-2 to the LUMO. In each case the HOMO-2 is the highest-energy occupied orbital that can be associated with C=C bonds that bridge the PDI units. Since the LUMO in each molecule

is associated with the PDI subunits, we view this (HOMO-2)-to-LUMO transition as promoting an electron from the bridging C=C subunit array to the PDI subunit array. As with the HOMO-LUMO transition, this excitation also shifts to lower energy with increasing oligomer size. The shift of this (HOMO-2)-to-LUMO to increasingly lower energy with degree of oligomerization is also the source of the very intense longest-wavelength absorption in **4** (Figure 2.5A). This (HOMO-2)-to-LUMO transition also answers our third question above: it is important to note that the energy of this transition in the tetramer is calculated to be essentially the same as that of the HOMO-to-LUMO transition. In fact, the calculated oscillator strength for the (HOMO-2)-to-LUMO transition is much larger than that of the HOMO-LUMO transition. The energy of the HOMO-2 is only slightly lower (~ 4 mh = 0.1 eV) than that of the HOMO, so the C=C and PDI subunits are close to degenerate in the tetramer; this hints that the longer oligomers will provide an even richer photophysics. Our calculations on **2**, **3**, and **4** show a third important type of electronic transition. In these, an electron is promoted from the molecular HOMO (situated primarily on the PDI subunits) to an orbital that is best characterized as a π^* orbital of the bridging olefin (Figure 2.7B). This transition is quite strong and occurs at higher energies. This type of transition accounts for the families of shorter-wavelength absorptions in the oligomers, and answers the fourth of the questions we posed above.

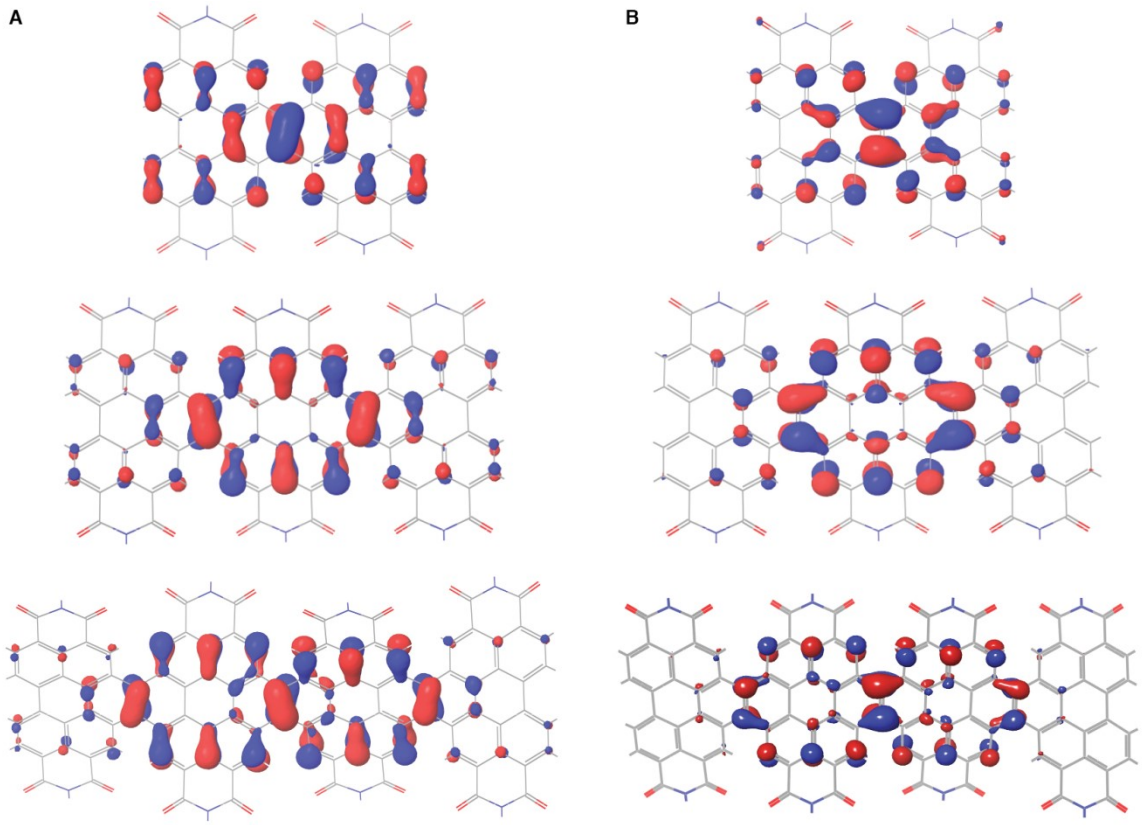

Figure 2.7. (A) HOMO-2 for PDI oligomers. (B) Lowest energy antibonding orbital of the bridging olefin.

To probe these transitions directly we use femtosecond transient absorption spectroscopy; the technique was described elsewhere.[55] We excite the sample of **4** with a 450 nm laser pulse and probe with a white light supercontinuum. Figure 2.8 shows transient absorption spectra as a function of probe photon energy for **4** at different delay times between pump and probe pulses. The negative signals at 550 and 605 nm are due to photo bleaching from the absorption peaks at the same wavelengths. The positive signals are due to photo-induced absorption in the transitions from S_1 to higher lying singlet states. The bleaching peaks are spectrally better resolved than corresponding features in the static spectrum. In particularly, the bleaching features at 605 nm and 550 nm are well separated;

this confirms that the absorption at 550 nm is not vibrational progression associated with the transition centered at 605 nm. Figure 2.8B presents the dynamics at the red side (615 nm) and the blue side (598 nm) of the absorption peak centered at 605 nm. It is clear that the dynamics are very different. These dynamics can be fitted well by a biexponential function. While the decay constants for the dynamics at 598 nm are 2.5 ps and 28 ps, the dynamics at 615 nm are 8 ps and 48 ps. This result is in line with the DFT calculation in which the lowest-energy allowed transition is combination of the (HOMO–2)-to-LUMO and the HOMO-to-LUMO transitions in the tetramer. According to the calculation the difference in energy for these two transitions is ~0.1 eV. We note that the bleaching dynamics for **1** are similar at different probe wavelengths. Section 2.8.7 contains a comparison of the transient absorption spectra for **1**, **2**, and **4** and the dynamics for **1** at different probe wavelengths. This transient absorption data experimentally answers the above questions 2 and 3.

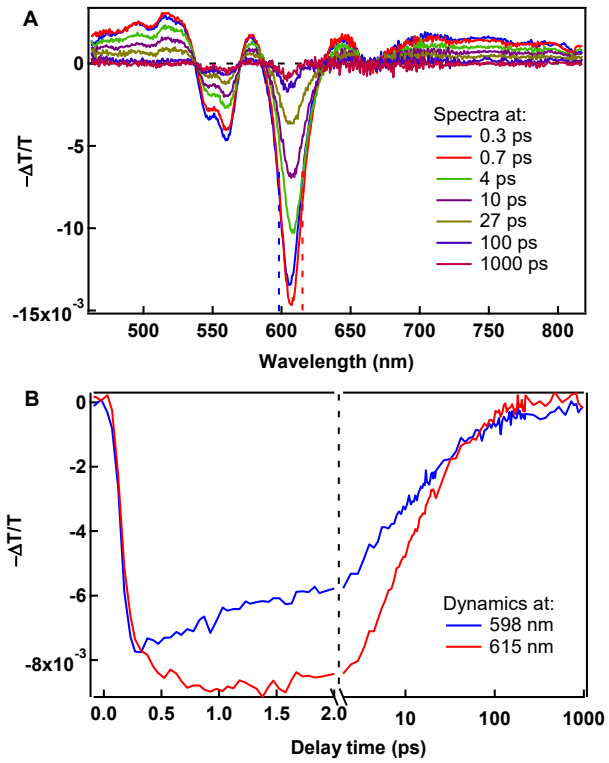

Figure 2.8. (A) Different transmission, -ΔT/T, as a function of probe photon energy at different delay time between pump and probe pulses. (B) Exciton dynamics probing at the red side (615 nm) and blue side (598 nm) of the absorption peak at 605 nm (red and blue dashed lines in the Figure 2.8A).

Therefore we can at least partially assign the optical spectra (Figure 2.5) by citing three families of electronic transition. The first is the HOMO-LUMO transition, and it is roughly similar in the monomer, dimer, trimer, and tetramer. These transitions involve orbitals confined to the PDI subunits; there is little orbital density on the bridging olefins. Only the monomer shows a vibrational progression.[54] In the higher oligomers that are distorted away from planarity, the vibronic effects are absent. In the second family of optical transitions, an electron is promoted from a C=C bonding level in the bridging olefin(s) (Figure 2.7A) to the LUMO. Since the LUMO is situated on the PDI subunits,

this transition is from the olefinic bridges to the PDI framework. These transitions are slightly higher in energy than the HOMO-LUMO transitions in the dimer and trimer, but in the tetramer the two transitions are essentially degenerate. The third family of transitions promotes an electron from the HOMO to antibonding levels of the bridging olefins. Since the HOMO is situated on the PDI subunits, this transition is from the PDI framework to the olefinic bridges. These transitions are all higher in energy, accounting for the shorter wavelength absorptions we see in the dimer, trimer, and tetramer spectra (Figure 2.5).

2.6 Conclusion

In summary, we report here synthesis of a new series of n-type graphene nanoribbons based on PDI oligomers. As the ribbons increase in size their band gaps narrow, and in consequence they show a red-shift of their absorption edge relative to that of the PDI monomer. Their photophysical behavior and electronic structure suggests a bifurcation into PDI and bridging olefin subsystems, and these subsystem merge energetically in the longer oligomers, giving rise to intense, long-wavelength absorbances. Their strong absorption in the 400nm to 600nm range forms a complement to the absorption spectra of low-band-gap electron donor polymers used in solar cells. The newly synthesized oligomers are good electron acceptors and form n-type field effect film transistors. Taken, together, the optical, electronic and charge-transport properties of the oligomers show that they are promising candidates for the OLED and photovoltaic applications.[25,56,57]

2.7 Experimental Section

2.7.1. General Information

All reactions were performed in oven-dried or flame-dried round bottom flasks,

unless otherwise noted. The flasks were fitted with rubber septa and reactions were conducted under a positive pressure of nitrogen, unless otherwise noted. Anhydrous and anaerobic solvents were obtained from a Schlenk manifold with purification columns packed with activated alumina and supported copper catalyst (Glass Contour, Irvine, CA). Automated flash chromatography was performed using a Teledyne Isco Combiflash R_f200 and Redisep R_f Gold Silica columns.

2.7.2. Materials.

Perylene-3,4,9,10-tetracarboxylicbisimides,1-bromoperylene-3,4,9,10 tetracarboxylic bisimides, 1,6 and 1,7-dibromoperylene-3,4,9,10-tetracarboxylicbisimides were synthesized using known procedures.[58] All chemicals were purchased from commercial sources and used without further purification unless otherwise specified.

2.7.3. Instrumentation.

^{1}H, and ^{13}C NMR spectra were recorded on a Bruker DRX300 (300 MHz), Bruker DRX400 (400 MHz) or a Bruker DMX500 (500 MHz) spectrometer. Chemical shifts for protons are reported in parts per million downfield from tetramethylsilane and are referenced to residual protium in the NMR solvent ($CHCl_3$: δ 7.26; C_6H_6 δ 7.15). Chemical shifts for carbon are reported in parts per million downfield from tetramethylsilane and are referenced to the carbon resonances of the solvent ($CDCl_3$ δ 77.0; C_6D_6 δ 128.5). Data are represented as follows: chemical shift, multiplicity (s = singlet, d = doublet, t = triplet, m = multiplet), coupling constants in Hertz, and integration. The mass spectroscopic data were obtained at the Columbia University mass spectrometry facility using a JEOL JMSHX110A/110A tandem mass spectrometer. Absorption spectra were obtained on Shimadzu UV 1800 UV-Vis spectrophotometer and emission spectra were recorded in a

Fluorolog-3 spectrophotometer. Cyclic voltammograms (CVs) were recorded on a CH166 electrochemical workstation using Ag/AgCl electrode as the reference electrode. 0.1 M solution tetrabutylammonium hexafluorophosphate ($TBAPF_6$) in dichloromethane was used as the supporting electrolyte. The thin film transistors were tested on the Agilent 4155C semiconductor parameter analyzer. Atomic force microscopy (AFM) was performed by a PSIA XE100.

2.7.4. Transient absorption.

The pump laser light (~100 fs pulse width, ~200 nJ pulse energy) comes from an optical parametric amplifier pumped by a Ti:sapphire femtosecond regenerative amplifier (800 nm, 1 kHz rep-rate). The probe light is a white-light supercontinuum (450-900 nm, ~100 fs pulse width). The pump and probe beams overlapped under a small angle. The detection consists of a pair of high-resolution multichannel detector arrays coupled to a high-speed data acquisition system.

2.7.5. Synthetic Details.

Synthesis of uncyclized dimer 9

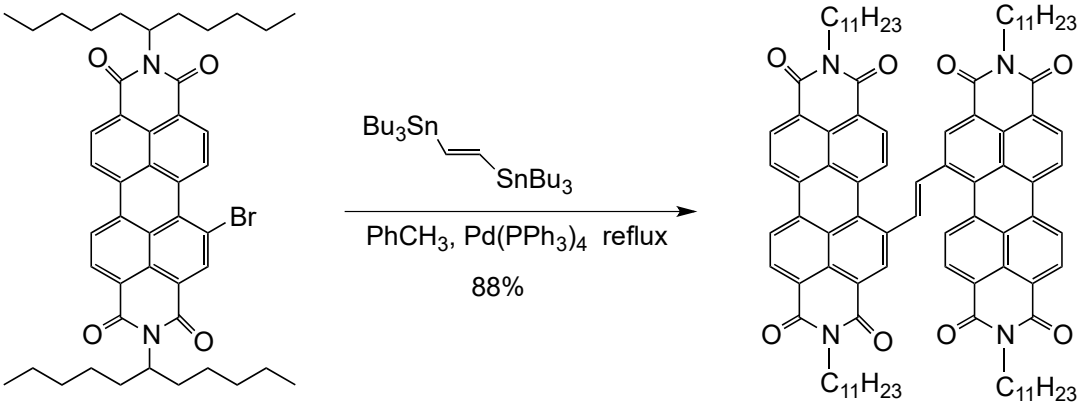

6 **9**

A solution of **6** (2.55 g, 3.28 mmol) and *trans*-1,2-bis(tributylstannyl)ethene **5** (0.90 mL, 1.68 mmols) in toluene (30 mL) was degassed under Argon for 30 minutes. Tetrakis(triphenylphosphine)palladium(0) (100 mg, 0.09 mmol) was added, and the resultant solution was degassed for 20 minutes. The mixture was refluxed for 16 h under Argon. The black reaction mixture was filtered through celite. The solvent was removed under reduced pressure and the product was purified using neutral alumina column chromatography (DCM:hexane 6:4) to yield dark purple crystalline solid **9** (2.1 g, 1.48 mmol, 88%).

^{1}H NMR (400 MHz, $CDCl_3$, 323K): δ 8.97 (s, 2H), 8.76-8.66 (m, 12H), 8.18 (s, 2H), 5.20-5.16 (m, 4H), 2.26-2.23 (m, 8H), 1.88-1.83 (m, 8H), 1.29-1.24 (m, 48H), 0.83-0.79 (m, 24H).

^{13}C NMR (100 MHz, $CDCl_3$, 323K): δ 164.2, 136.0, 134.9, 134.6, 134.3, 133.3, 130.0, 129.4, 128.8, 128.0, 127.4, 123.8, 123.1, 55.1, 55.0, 32.5, 31.9, 26.8, 22.6, 14.1.

IR (ATR) [cm $^{-1}$] 3025, 2966, 2929, 2909, 2842, 2723, 2244, 1628, 1427, 1371.

HRMS (FAB+) m/z (M^+) calcd for $C_{94}H_{108}N_4O_8$ = 1420.82; found 1420.26.

Synthesis of stannyl-PDI 8

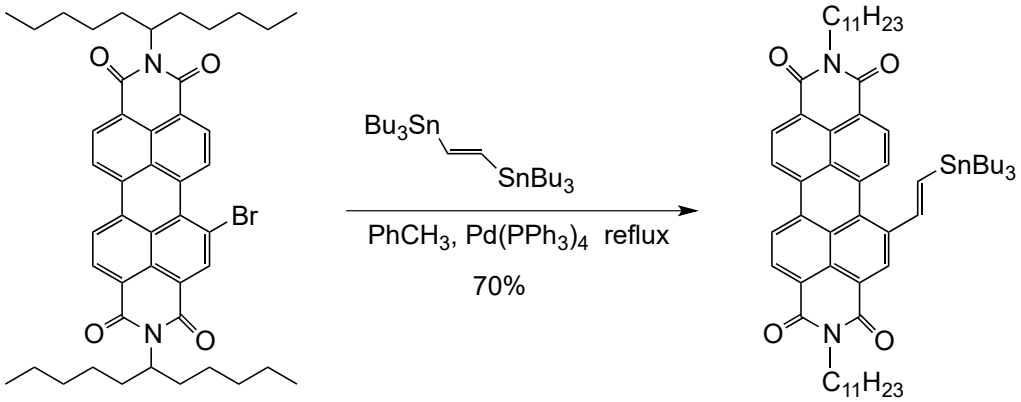

6 **8**

A solution of **6** (1.67 g, 2.15 mmol) and *trans*-1,2-bis(tributylstannyl)ethene (3.0 mL, 5.6 mmols) in toluene (40 mL) was degassed under Argon for 45 minutes. Tetrakis(triphenylphosphine)palladium(0) (65 mg, 0.06 mmol) was added. It was further degassed for 30 minutes. The mixture was refluxed for 3 h under Argon. The black reaction mixture was filtered through celite, solvent was removed under reduced pressure. The residue was purified by neutral alumina column chromatography (gradient mobile phase: DCM:hexane 2:8 to DCM:hexane 6:4) to yield **8** as red solid (1.53 g, 1.51 mmol, 70%).

^{1}H NMR (500 MHz, $CDCl_3$): δ 8.83-8.63 (m, 7H), 7.46 (s, 2H), 5.21-5.17 (m, 2H), 2.27-2.23 (m, 4H), 1.85 (m, 4H), 1.65-1.62 (m, 6H), 1.42-1.25 (m, 30H), 1.11-1.09 (m, 6H), 0.95-0.92 (m, 9H), 0.83-0.81 (m, 12H).

^{13}C NMR (100 MHz, $CDCl_3$): δ 165.0, 163.9, 147.4, 139.5, 138.7, 134.5, 131.2, 130.0, 129.3, 128.3, 127.7, 127.4, 123.5, 122.8, 54.9, 54.8, 32.5, 31.9, 29.4, 27.5, 26.8, 22.7, 14.2, 13.9, 10.0, 1.2.

IR (ATR) [cm $^{-1}$] 2958, 2923, 2852, 1695, 1655, 1588, 1459, 1397, 1330, 1254, 1179, 809, 738.

HRMS (FAB+) m/z (M^+) calcd for $C_{60}H_{82}SnN_2O_4$ = 1014.01; found 1014.50.

Synthesis of cyclized dimer 2

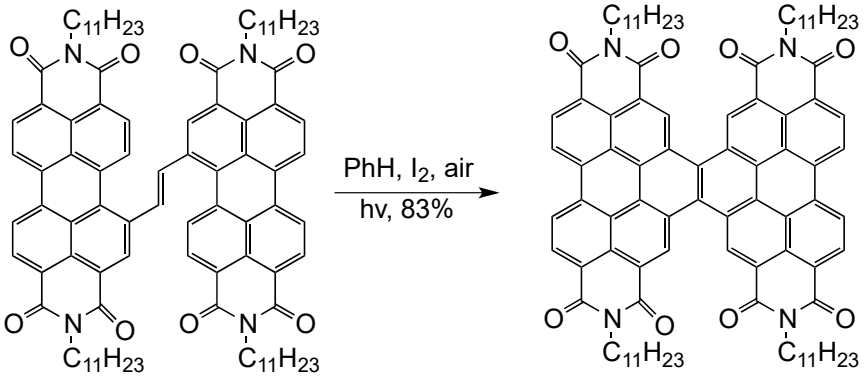

9 **2**

In standard photocyclization glassware, uncyclized dimer **9** (1.0 g, 0.71mmol) was dissolved in 450 mL benzene and iodine (100 mg) was added. The resultant purple solution was photoirradiated using 450W mercury lamp for 36 hours with slow bubbling of air through the solution. The resultant pink reaction mixture extracted with saturated sodium bicarbonate (2 X 400 mL), brine (400 mL) and concentrated under reduced pressure. The residue was treated with 50 mL methanol to crash out red solid. The red solid was purified using column chromatography (gradient mobile phase: DCM:hexane 2:8 to DCM:hexane 6:4) to yield **2** as dark red crystalline solid (0.84 g, 0.59 mmol, 83 %).

^{1}H NMR (500 MHz, $CDCl_3$, 323K): δ 10.31 (s, 4H), 9.47-9.45 (d, J = 8 Hz, 4H), 9.21 (d, J = 8 Hz, 4H), 5.34 (m, 4H), 2.38-2.34 (m, 8H), 1.98 (m, 8H), 1.37-1.31 (m, 48H), 0.87-0.85 (m, 24H).

^{13}C NMR (100 MHz, $CDCl_3$, 323K): δ 164.5, 134.2, 130.5, 127.6, 127.0, 126.8, 126.0, 124.5, 124.1, 123.9, 123.8, 123.3, 123.1, 55.3, 32.7, 31.9, 26.9, 22.7, 14.1.

IR (ATR) [cm $^{-1}$] 2957, 2921, 2854, 1699, 1653, 1591, 1447, 1316, 1258, 1168, 912, 809, 737.

HRMS (FAB+) m/z (M^+) calcd for $C_{94}H_{104}N_4O_8$ = 1417.89; found 1417.30.

Bromination of PDI-dimer 2:

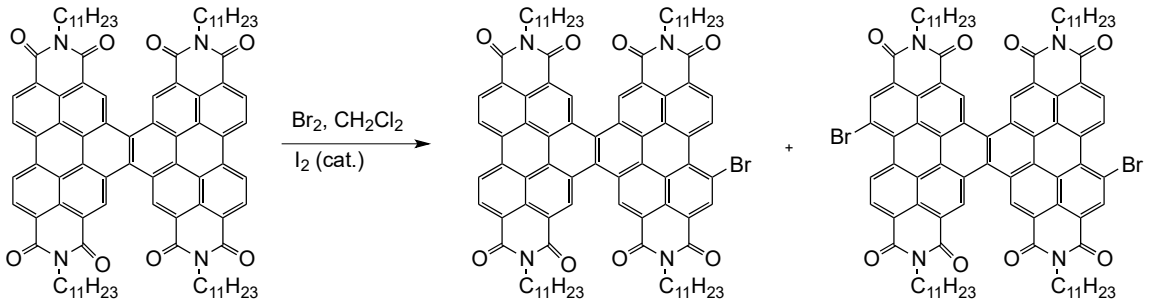

2 **10** **14**

PDI-dimer **2** (1.0 g, 0.71 mmol) was dissolved in 50 mL of dichloromethane.

Excess bromine (10 mL) was added, followed by few crystal of iodine. The solution was capped with a rubber septum and stirred at room temperature for 3 days. Bromine was quenched with saturated solution of sodium thiosulfate (300 mL) and extracted with CH_2Cl_2 (2 x 400 mL). The combined organic layer was dried over anhydrous magnesium sulfate and concentrated under reduced pressure. The crude mixture was purified by silica gel column chromatography (gradient mobile phase: DCM:hexane 2:8 to DCM:hexane 6:4). Dibromide **14** (highest rf, 330 mg, 0.21 mmol), monobromide **10** (lower rf, 480 mg, 0.32 mmol) and starting material **2** (lowest rf, 250 mg, 0.18 mmol) were isolated in 30, 45 and 25% yield, respectively.

DiBr-dimer (14)

^{1}H NMR (500 MHz, $CDCl_3$, 323K): δ 10.75-10.73 (d, J = 8 Hz, 2H), 10.34 (s, 2H), 10.28 (s, 2H), 9.47 (s, 2H), 9.20-9.18 (d, J = 8 Hz, 2H), 5.31 (m, 4H), 2.35 (m, 8H), 1.97 (m, 8H), 1.42-1.32 (m, 48H), 0.85 (m, 24H).

^{13}C NMR (100 MHz, $CDCl_3$, 323K): δ 164.1, 138.5, 134.0, 133.3, 132.8, 129.5, 128.5, 127.3, 127.1, 126.9, 126.6, 126.2, 125.7, 125.6, 125.5, 125.4, 123.7, 121.7, 55.6, 55.4, 32.7, 32.6, 31.9, 26.9, 22.7, 14.1.

IR (ATR) [cm $^{-1}$] 2953, 2928, 2863, 1705, 1662, 1597, 1446, 1321, 1242, 1185, 819, 808, 762.

HRMS (FAB+) m/z (M^+) calcd for $C_{94}H_{102}Br_2N_4O_8$ = 1575.67; found 1575.20.

MonoBr-dimer 10

^{1}H NMR (500 MHz, $CDCl_3$): δ 10.73-10.71 (d, J = 8 Hz, 1H), 10.33 (m, 4H), 9.47-9.45 (d, J = 8 Hz, 3H), 9.20 (m, 3H), 5.32 (m, 4H), 2.34 (m, 8H), 1.96 (m, 8H), 1.43-1.30 (m, 48H), 0.85 (m, 24H).

^{13}C NMR (100 MHz, $CDCl_3$, 323K): δ 164.4, 134.2, 133.3, 132.8, 130.6, 128.4, 127.6, 127.5, 127.1, 127.0, 126.9, 126.8, 126.6, 126.2, 126.1, 126.0, 125.6, 125.5, 125.4, 124.5, 124.2, 124.0, 121.7, 55.6, 55.3, 32.7, 32.6, 31.9, 26.9, 22.7, 14.1.

IR (ATR) [cm $^{-1}$] 2953, 2931, 2863, 1708, 1669, 1590, 1443, 1328, 1256, 1181, 811, 747, 761.

HRMS (FAB+) m/z (M^+) calcd for $C_{94}H_{103}BrN_4O_8$ = 1496.78; found 1496.21.

Synthesis of trimer 3

Scheme 2.4. Method A for synthesis of trimer **3**.

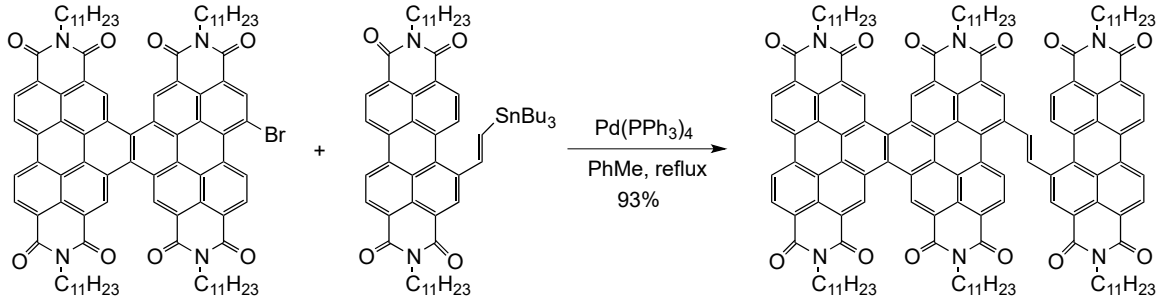

10 **8** **11**

Using PDI-dimer 10

A solution of Br-PDI-dimer **10** (0.26 g, 0.17 mmol) and stannyl-PDI **8** (0.26 g, 0.26 mmol) in toluene (10 mL) was degassed under Argon for 30 minutes. Solid tetrakis(triphenylphosphine)palladium(0) (30 mg, 0.03 mmol) was added, and the solution was further degassed for 15 minutes. The mixture was refluxed overnight (16 h) under Argon. The black reaction mixture was filtered through celite, and the solvent was removed under reduced pressure. The black residue was purified using neutral alumina column chromatography (gradient mobile phase: DCM:hexane 2:8 to DCM:hexane 6:4) to yield **11** as purple crystalline solid (0.35 g, 93%).

^{1}H NMR (500 MHz, $CDCl_3$): δ 10.37 (s br, 4H), 9.52-9.40 (m, 4H), 9.22-9.12 (m, 4H),

8.84-8.77 (m, 6H), 8.70-8.67 (d, J = 16Hz, 1H), 8.45-8.42 (d, J = 16 Hz, 1H), 5.35-5.22 (m, 6H), 2.37-2.28 (m, 12H), 1.96-1.86 (m, 12H), 1.32-1.28 (m, 72H), 0.88-0.81 (m, 36H).

^{13}C NMR (100MHz, $CDCl_3$, 323K): δ 164.3, 137.1, 136.1, 135.3, 134.8, 134.6, 134.2, 134.1, 134.0, 133.5, 132.3, 131.2, 130.1, 129.3, 128.8, 128.0, 127.4, 127.1, 126.7, 126.6, 126.5, 126.0, 125.9, 125.8, 125.3, 124.4, 123.8, 123.1, 55.2, 55.0, 54.9, 32.6, 32.5, 32.4, 31.8, 26.8, 26.7, 26.6, 22.6, 22.5, 14.0.

IR (ATR) [cm $^{-1}$] 2939, 2925, 2858, 1698, 1657, 1593, 1448, 1411, 1320, 1250, 1182, 1122, 811

HRMS (MALDI-TOF) m/z (M^+) calcd for $C_{142}H_{158}N_6O_{12}$ = 2140.81, ($M+H^+$) = 2141.8; found 2141.1.

Synthesis of trimer 3

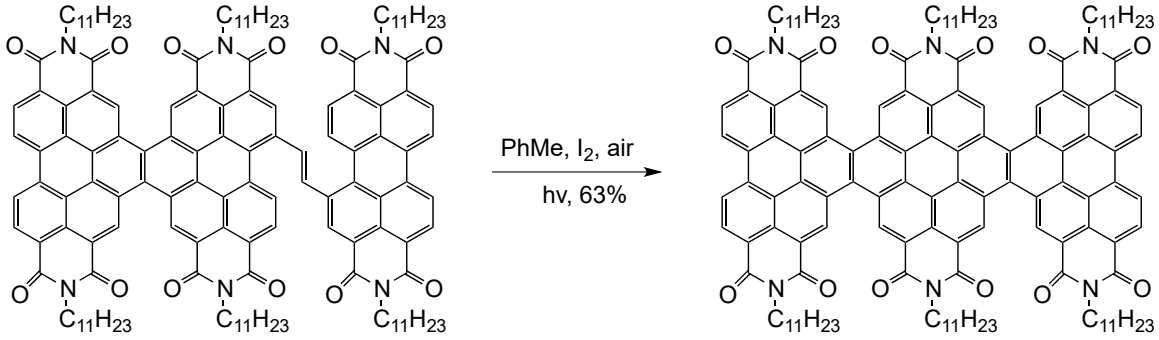

11 **3**

In standard photocyclization glassware, uncyclized trimer **11** (0.4 g, 0.19 mmol) was dissolved in 420 mL anhydrous toluene, followed by addition of iodine (120 mg). The resultant purple solution was photoirradiated using 450W mercury lamp for 20 hours with slow bubbling of air through the solution. Heat was applied to the reaction mixture by minimal cooling of the inner jacketed glass tubing that houses the lamp. The resultant reddish reaction mixture extracted with saturated sodium bicarbonate (2 x 400 mL), and

brine (400 mL). The organic layer was concentrated under reduced pressure. The black residue treated with methanol (40 mL) to crash out dark red solid that was purified using column chromatography (gradient mobile phase: DCM:hexane 0:10 to DCM:hexane 6:4) to yield **3** as dark red crystalline solid (0.26 g, 0.12 mmol, 63 %).

^{1}H NMR (400 MHz, $CDCl_3$, 323K): δ 10.96 (s, 4H), 10.65 (s, 4H), 9.55-9.54 (d, J = 8 Hz, 4H), 9.26 (d, J = 8 Hz, 4H), 5.52 (m, 2H), 5.40 (m, 4H), 2.53-2.42 (m, 12H), 2.12-2.02 (m, 12H), 1.41-1.39 (m, 72H), 0.89 (m, 36H).

^{13}C NMR (100MHz, $CDCl_3$, 323K): δ 164.7, 134.1, 132.7, 130.4, 127.5, 127.4, 127.1, 127.0, 126.0, 125.0, 124.6, 124.5, 123.9, 123.1, 122.2, 55.6, 55.2, 32.7, 32.6, 31.8, 26.9, 26.8, 22.6, 14.0.

IR (ATR) [cm $^{-1}$] 2952, 2928, 2856, 1708, 1597, 1450, 1177.

MS (MALDI-TOF) m/z (M^+) calcd for $C_{142}H_{154}N_6O_{12}$ = 2136.8, ($M+H^+$) = 2137.8; found 2137.7.

Scheme 2.5. Method B for synthesis of trimer **3** using diBr-PDI **7**.

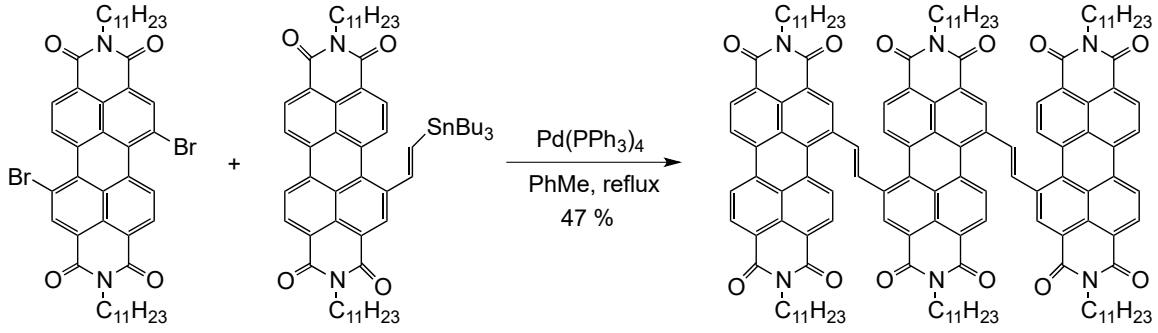

7 **8** **12**

A solution of diBr-PDI **7** (0.10 g, 0.12 mmol) and stannyl-PDI **8** (0.28 g, 0.28 mmol) in toluene (6 mL) was degassed under Argon for 30 minutes. Solid tetrakis(triphenylphosphine)palladium(0) (30 mg, 0.03 mmol) was added, and the solution

was further degassed for 20 minutes. The mixture was refluxed overnight (16 h) under Argon. The black reaction mixture was filtered through celite, and the solvent was removed under reduced pressure. The residue was purified using neutral alumina column chromatography (gradient mobile phase: DCM:hexane 1:9 to DCM:hexane 8:2) to yield **12** as purple crystalline solid (120 mg, 0.056 mmol, 47%).

^{1}H NMR (500 MHz, $CDCl_3$): δ 9.09-9.05 (m, 4H), 8.78-8.67 (m, 16H), 8.27 (s, H), 5.22-5.19 (m, 6H), 2.27-2.25 (m, 12H), 1.86-1.85 (m, 12H), 1.30-1.28 (m, 72H), 0.84-0.82 (m, 36H).

^{13}C NMR (100MHz, $CDCl_3$, 323K): δ 164.2, 136.0, 135.5, 134.8, 134.7, 134.6, 134.5, 134.4, 134.2, 134.0, 133.3, 132.8, 130.2, 130.1, 129.9, 129.3, 128.8, 128.7, 128.2, 128.0, 127.9, 127.3, 123.7, 123.1, 55.0, 54.9, 32.4, 31.7, 26.6, 22.5, 13.9.

IR (ATR) [cm^{-1}] 2924, 2856, 1698, 1655, 1590, 1455, 1409, 1329, 1249, 811.

MS (MALDI-TOF) m/z (M^+) calcd for $C_{142}H_{162}N_6O_{12}$ = 2144.84; found 2144.80.

Cyclized Trimer 3

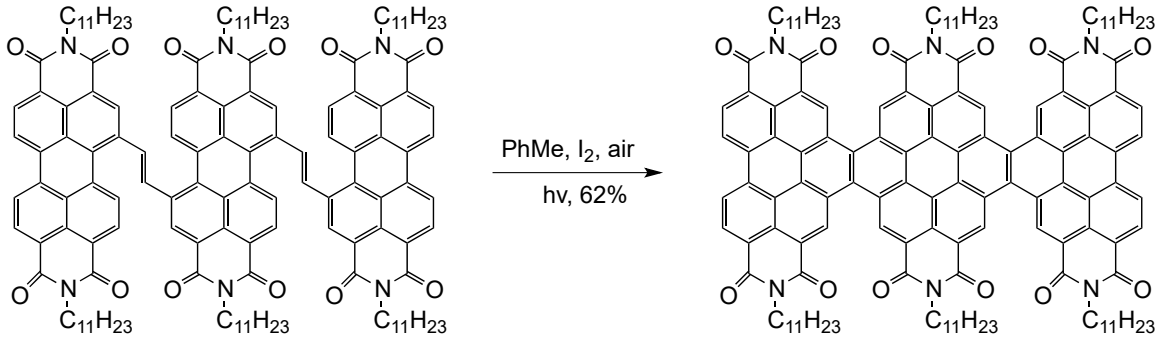

12 **3**

In standard photocyclization glassware, uncyclized trimer **12** (84 mg, 0.04 mmol) was dissolved in 300 mL anhydrous toluene, followed by addition of iodine (15 mg, 0.10 mmol). The resultant purple solution was photoirradiated using 450W mercury lamp for 9

hours with slow bubbling of air through the solution. Heat was applied to the reaction mixture by minimal cooling of the inner jacketed glass tubing that houses the lamp. The resultant reddish reaction mixture was extracted with saturated sodium bicarbonate (2 x 300 mL) and brine (300 mL). The organic layer was concentrated under reduced pressure. The resultant solid was treated with methanol (15 mL) to crash out dark red solid that was purified using silica gel column chromatography (gradient mobile phase: DCM:hexane 2:8 to DCM:hexane 6:4) to isolate **3** as dark red crystalline solid (54 mg, 0.025 mmol, 62 %).

Scheme 2.6. Synthesis of uncyclized-tetramer **13** (Mehtod A).

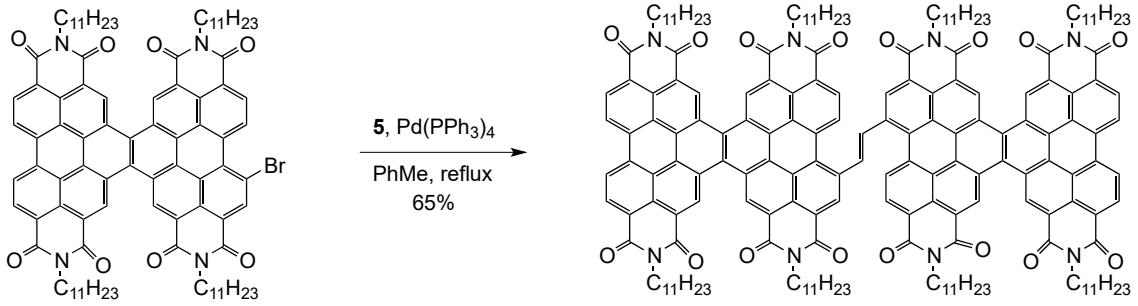

10 **13**

A solution of Br-dimer **10** (410 mg, 0.274 mmol) and *trans*-1,2-bis(tributylstannyl)ethene **5** (100 mg, 0.165 mmols) in toluene (8 mL) was degassed under Argon for 30 minutes. Tetrakis(triphenylphosphine)palladium(0) (20 mg, 0.02 mmol) was added. It was further degassed for 20 minutes. The mixture was refluxed overnight under Argon. The black reaction mixture was filtered through celite, solvent was removed under reduced pressure. The residue was purified by column chromatography using neutral alumina as stationary phase (gradient mobile phase: DCM:hexane 1:9 to DCM:hexane 7:3) to yield **13** as purple crystalline solid (306 mg, 0.107 mmol, 65%).

^{1}H NMR (400 MHz, $CDCl_3$, 323K): δ 10.45-10.41 (m, 8H), 9.76-9.73 (d, J = 8 Hz, 2H), 9.64 (br s, 2H), 9.50-9.47 (d, J = 8 Hz, 4H), 9.32-9.30 (d, J = 8 Hz, 2H), 9.25-9.23 (d, J =

8 Hz, 4H), 8.93 (s, 2H), 5.38-5.37 (m, 8H), 2.42-2.40 (m, 16H), 2.01-2.00 (m, 16H), 1.41-1.34 (m, 98H), 0.91-0.86 (m, 48H).

^{13}C NMR (100 MHz, $CDCl_3$, 323K): δ 164.6, 137.1, 135.5, 134.2, 134.1, 132.6, 130.2, 127.5, 127.1, 126.8, 126.6, 126.0, 125.9, 125.4, 124.5, 123.9, 123.0, 55.2, 32.6, 31.8, 26.8, 22.6, 14.0.

IR (ATR) [cm $^{-1}$] 2955, 2923, 2854, 1698, 1660, 1594, 1448, 1318, 1258, 1179, 808.

HRMS (FAB+) m/z (M^+) calcd for $C_{190}H_{208}N_8O_{16}$ = 2859.73, ($M+H^+$) = 2860.73; found 2860.74.

Scheme 2.7. Synthesis of uncyclized-tetramer **15** (Method B).

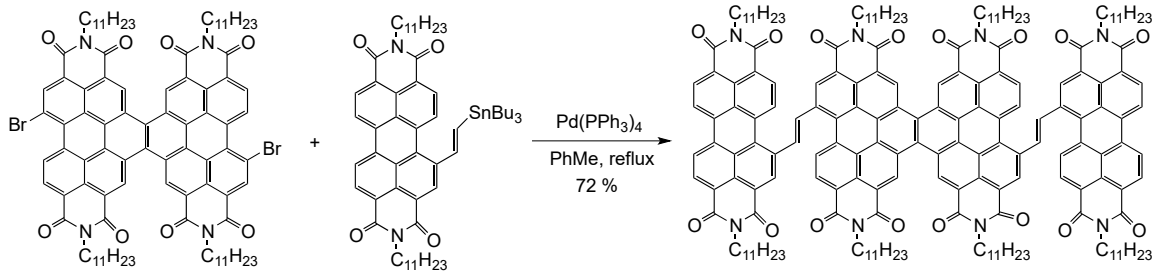

14 **8** **15**

A solution of diBr-dimer **14** (250 mg, 0.16 mmol) and stannyl-PDI **8** (400 mg, 0.39 mmol) in toluene (10 mL) was degassed under Argon for 30 minutes. Solid tetrakis(triphenylphosphine)palladium(0) (20 mg, 0.02 mmol) was added, and the solution was further degassed for 20 minutes. The mixture was refluxed overnight (20 h) under Argon. The black reaction mixture was filtered through plug of celite, and the solvent was removed under reduced pressure. The residue was purified using neutral alumina column chromatography (gradient mobile phase: DCM:hexane 0:10 to DCM:hexane 7:3) to yield **15** as purple crystalline solid (330 mg, 0.115 mmol, 72%).

^{1}H NMR (500 MHz, $CDCl_3$): δ 10.45 (s, 4H), 9.54-9.52 (d, J= 8 Hz, 2H), 9.42(s, 2H), 9.23-

9.14 (m, 4H), 8.85-8.75 (m, 12H), 8.72-8.68 (d, *J* = 15Hz, 2H), 8.47-8.44 (d, *J* = 15Hz, 2H), 5.36 (m, 4H), 5.24 (m, 4H), 2.39-2.28 (m, 16H), 1.97-1.89 (m, 16H), 1.30 (m, 96H), 0.85 (m, 48H).

^{13}C NMR (100MHz, $CDCl_3$, 323K): δ 164.2, 137.1, 136.0, 135.2, 134.9, 134.8, 134.7, 134.3, 134.1, 133.6, 132.3, 130.1, 130.0, 129.4, 128.8, 128.0, 127.4, 127.3, 127.1, 126.7, 126.6, 126.5, 126.0, 125.9, 125.3, 123.8, 123.1, 55.3, 55.0, 54.9, 32.5, 32.4, 31.8, 26.7, 26.6, 22.5, 14.0.

IR (ATR) [cm $^{-1}$] 2957, 2925, 2854, 1699, 1657, 1592, 1447, 1409, 1321, 1246, 1179, 811, 749.

MS (MALDI-TOF) m/z (M^+) calcd $C_{190}H_{212}N_8O_{16}$ = 2863.76; ($M+H^+$) = 2864.7; found 2864.2

Synthesis of Cyclized tetramer 4

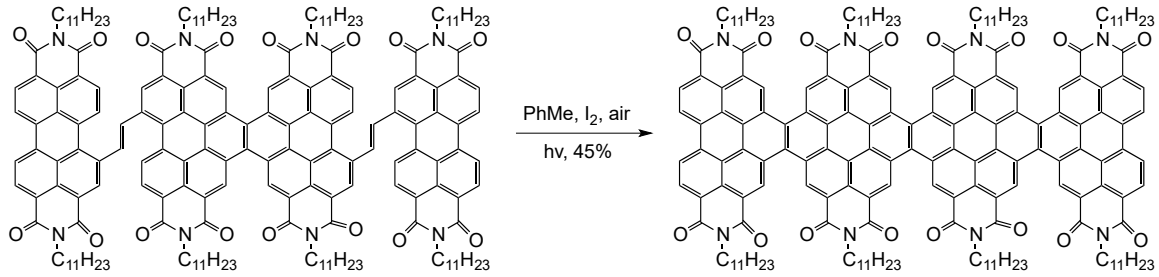

15 **4**

In standard photocyclization glassware, uncyclized tetramer **15** (50 mg, 0.017 mmol) was dissolved in 250 mL toluene, followed by addition of iodine (15 mg, 0.10 mmol). The resultant purple solution was photoirradiated using 450W mercury lamp for 9 hours with slow bubbling of air through the solution. Heat was applied to the reaction mixture by minimal cooling of the inner jacketed glass tubing that houses the lamp. The resultant reddish reaction mixture was extracted with saturated sodium bicarbonate (300

mL) and brine (300 mL). The organic layer was concentrated under reduced pressure. The residue was treated with methanol (15 mL) to crash out dark red solid that was purified using silica gel preparative column chromatography (chloroform:hexane 7:3) to give **4** as dark red crystalline solid (22 mg, 0.007mmol, 45 %).

^{1}H NMR (400 MHz, $CDCl_3$, 323K): δ 11.28 (s, 4H), 11.01 (s, 4H), 10.70 (s, 4H), 9.57-9.55 (d, J = 8 Hz, 4H), 9.31-9.29 (d, J = 8 Hz, 4H), 5.59 (m, 4H), 5.42 (m, 4H), 2.59-2.57 (m, 8H), 2.46-2.44 (m, 8H), 2.17 (m, 8H), 2.05 (m, 8H), 1.61-1.27 (m, 94H), 0.92-0.90 (m, 48H).

^{13}C NMR (100 MHz, $CDCl_3$, 323K): δ 164.8, 134.2, 132.9, 130.5, 127.8, 127.6, 127.4, 127.1, 126.0, 125.1, 124.7, 124.5, 123.9, 123.1, 122.3, 55.7, 55.3, 32.7, 32.6, 31.9, 26.9, 26.8, 22.6, 14.0.

IR (ATR) [cm $^{-1}$] 2953, 2924, 2863,1705, 1662, 1597, 1447, 1317, 1235, 1181, 927, 811.

MS (MALDI-TOF) m/z (M^+) calcd for $C_{190}H_{204}N_8O_{16}$ = 2855.7; found 2855.9

2.7.6 Computational methods.

All quantum chemical calculations were performed using Jaguar, version 8.2, Schrodinger, Inc., New York, NY, 2013. (See A. D. Bochevarov, E. Harder, T. F. Hughes, J. R. Greenwood, D. A. Braden, D. M. Philipp, D. Rinaldo, M. D. Halls, J. Zhang, R. A. Friesner, "Jaguar: A High-Performance Quantum Chemistry Software Program with Strengths in Life and Materials Sciences", *Int. J. Quantum Chem.*, **2013**, *113(18)*, 2110-2142).

All geometries were optimized using the B3LYP functional and the 6-31G** basis set. In the cases of the trimer and tetramer, the energies of the different conformations were compared by performing additional calculations at the several optimized geometries using

the larger cc-pvtz basis set. We observe no significant energy differences between the different local minima in either case.

At the optimized geometry for each local minimum we calculated the associated absorption spectrum using the TD-DFT method that is included in the Jaguar package. We used the 6-31G** basis in these calculations. In the absorption spectra we plot below we have presented the absorption peaks as lorentzians (including an arbitrary 10 nm line broadening), although we calculate only the "stick" spectra. For all of the molecules we present at least the twenty lowest-energy roots determined by the TD-DFT calculations.

In the following pages we include for each molecule (or conformation) its optimized geometry and total energy followed by the results of the TD-DFT excited state calculations.

2.8 Supplementary materials

2.8.1. Thermal Gravimetric Analysis

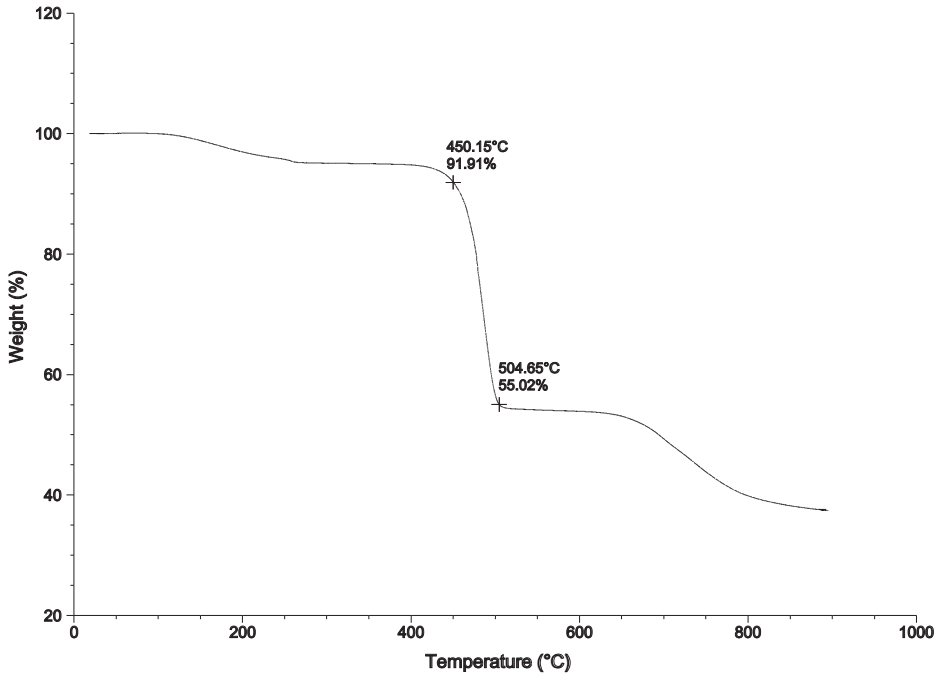

Figure 2.9. TGA analysis of cyclized dimer **2**.

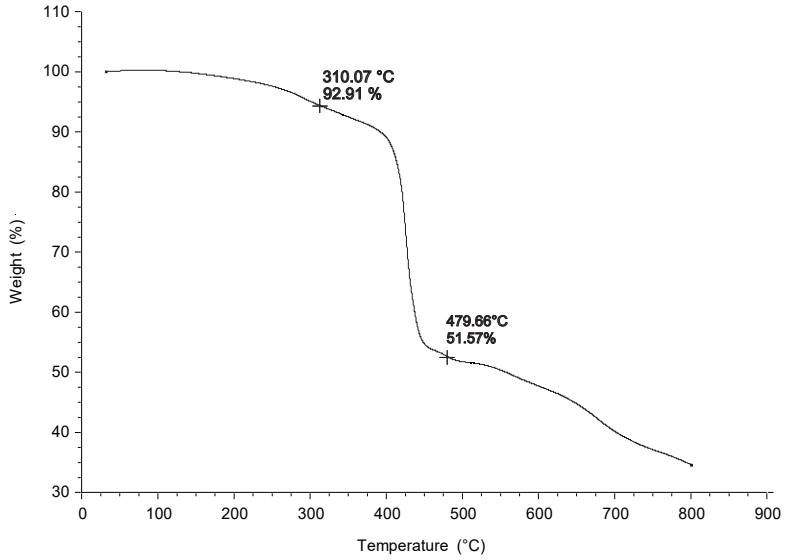

Figure 2.10. TGA analysis of cyclized trimer **3**.

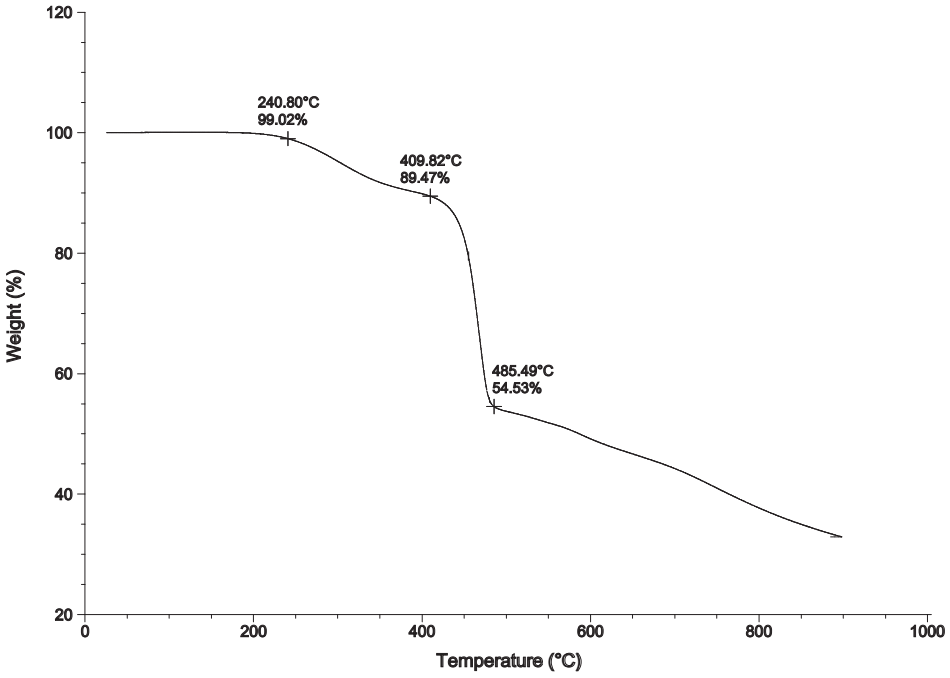

Figure 2.11. TGA analysis of cyclized tetramer **4**.

2.8.2. UV-Vis, fluorescence, and cyclic voltammetry

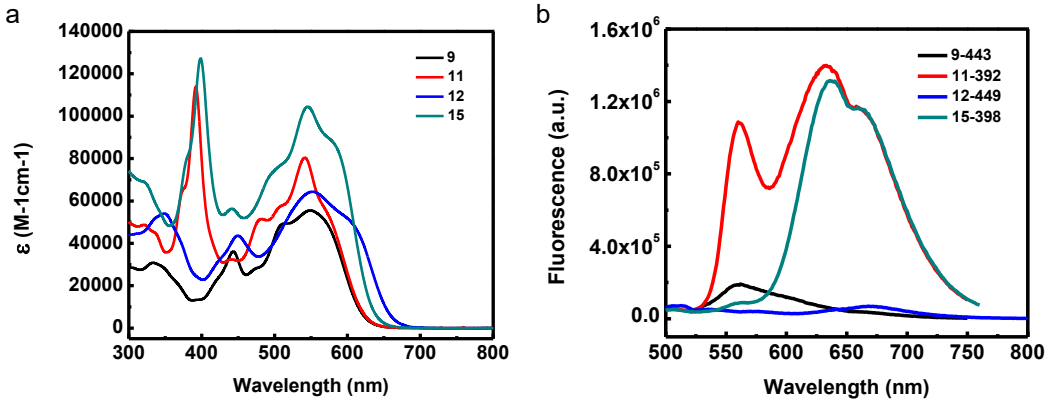

Figure 2.12. (a) UV-vis absorption spectra of **9**, **11**, **12** and **15**. (1 x 10^{-5} M concentration in dichloromethane with a path length l = 1cm) (b)Fluorescence spectra of **9** excited at 443 nm, **11** excited at 392 nm, **12** excited at 449 nm and **15** excited at 398 nm. Concentration of each solution is 10^{-7} M.

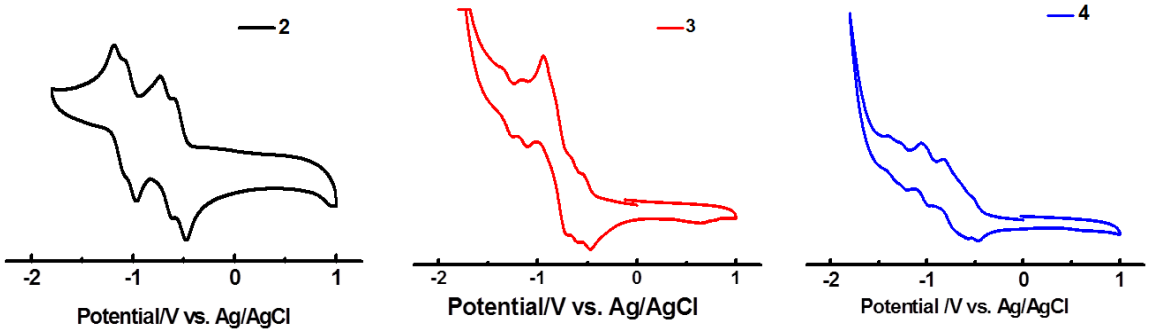

Figure 2.13. Cyclic voltammograms for **2**(black), **3**(red) and **4**(blue).

Table 2.3. Reversible reduction potentials of **2**-**4** with reference to Ag/AgCl electrode[a].

Compound	Reduction potential/V vs. Ag/AgCl				
	E_{1r}/V	E_{2r}/V	E_{3r}/V	E_{4r}/V	E_{5r}/V

2	-0.60	-0.73	-1.09	-1.19	-
3	-0.55	-0.67	-0.94	-1.16	-1.35
4	-0.53	-0.82	-1.06	-1.28	-1.40

Ferrocene/ferrocenium (Fc/Fc^+) was used for calibration. The redox potential of Fc/Fc^+ was located at 0.43V to Ag/AgCl reference electrode under the same condition. It is assumed that the absolute energy level for Fc/Fc^+ redox potential is -4.80eV to vacuum level. Then the energy levels of the lowest unoccupied molecular orbitals (LUMO) were calculated according to the following equation: $E_{LUMO}=-e(E_{red}+4.37)$ (eV).

2.8.3. Transfer and output curves of TFTs

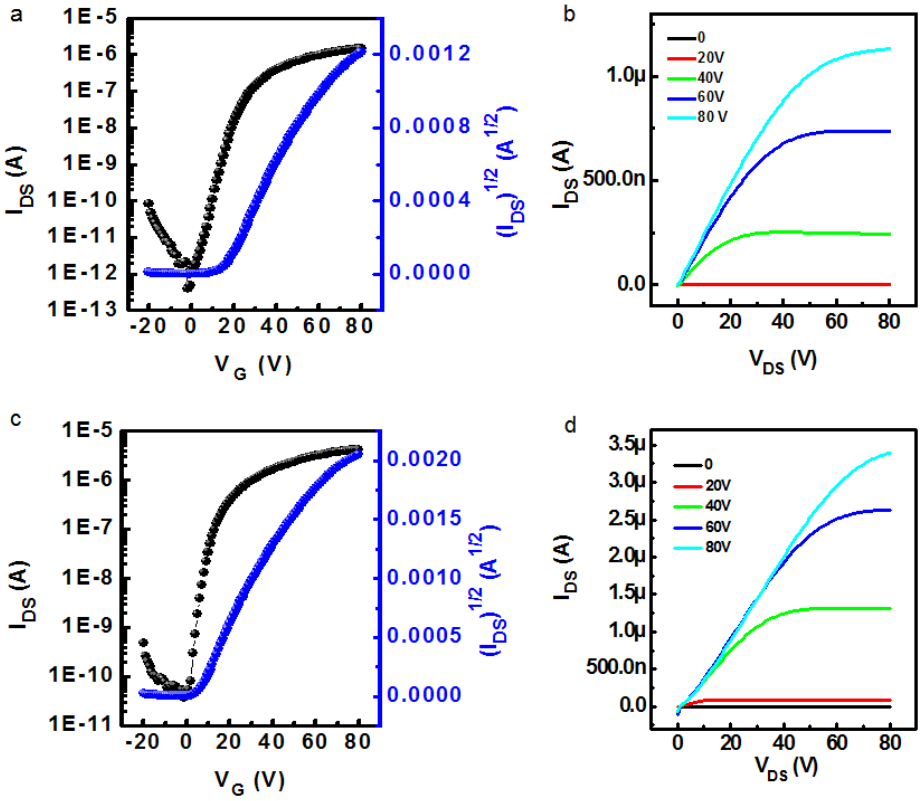

Figure 2.14. Transfer (a and c) and output (b and d) characteristics of TFTs for **2**(a-b) and **4**(c-d).

2.8.4. AFM height images of spin-cast films

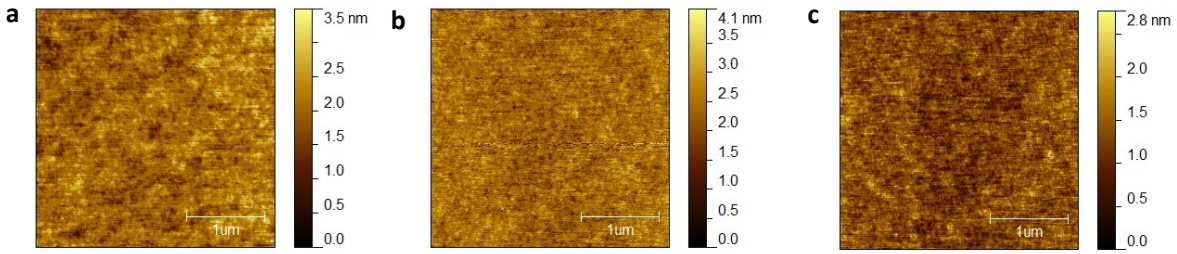

Figure 2.15. AFM height images of spin-cast films from (a) **2** (annealed at 160˚C), (b) **3** (annealed at 240˚C) and (c) **4** (annealed at 200˚C).

2.8.5. VT-NMR spectra of **2**, **3**, and **4**

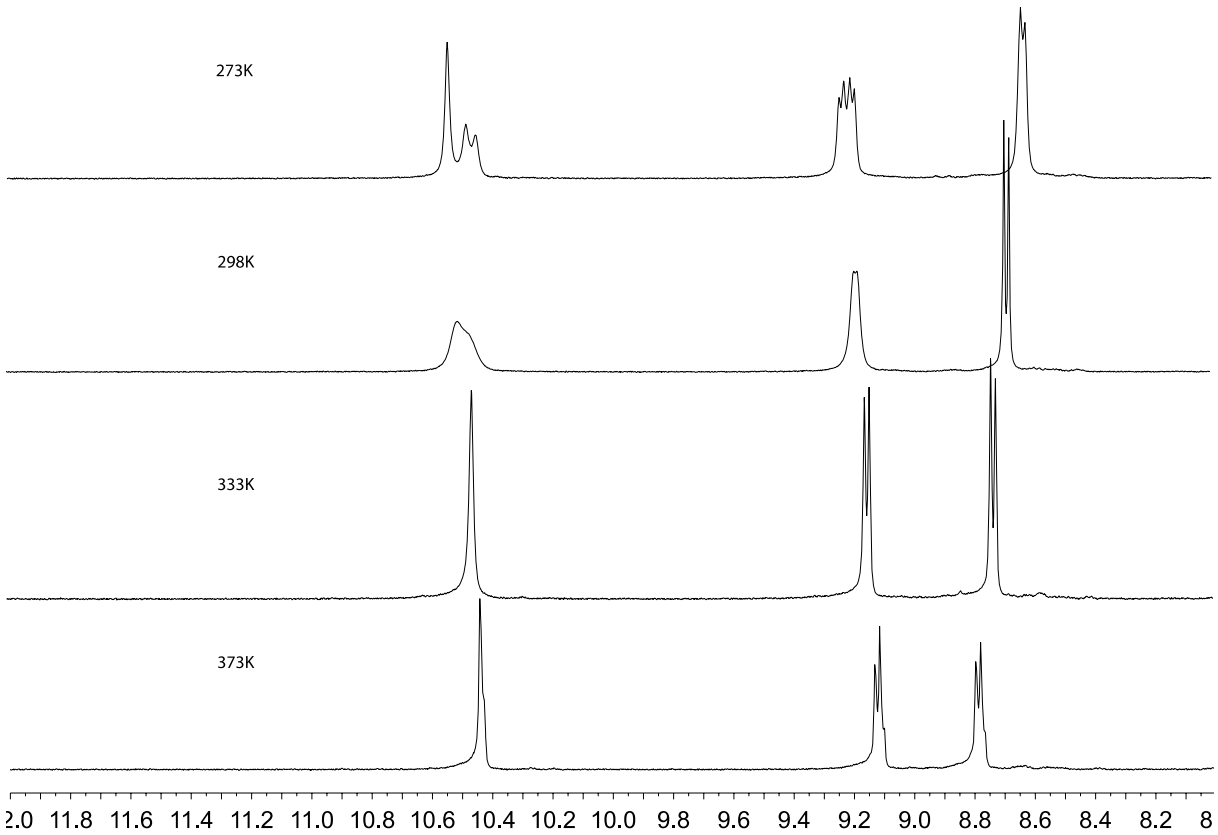

Figure 2.16. VT-NMR of **2**.

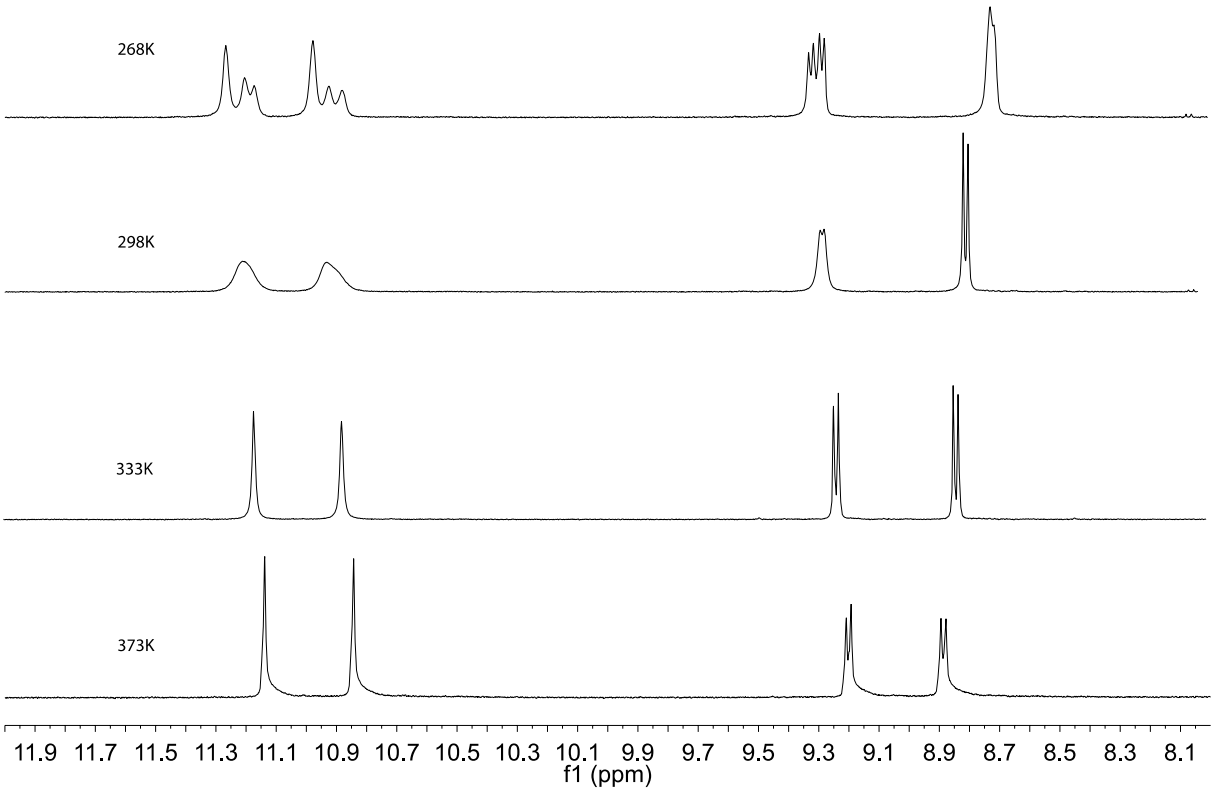

Figure 2.17. VT-NMR of **3**.

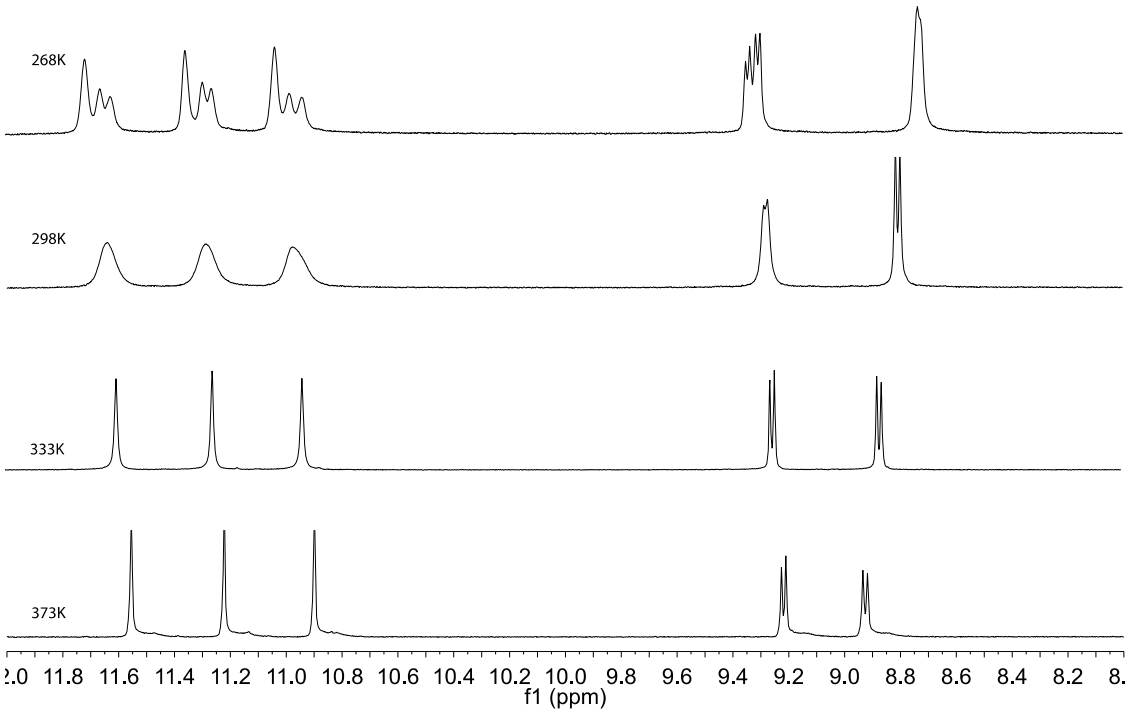

Figure 2.18. VT-NMR of **4**.

2.8.6. Computed absorption spectra

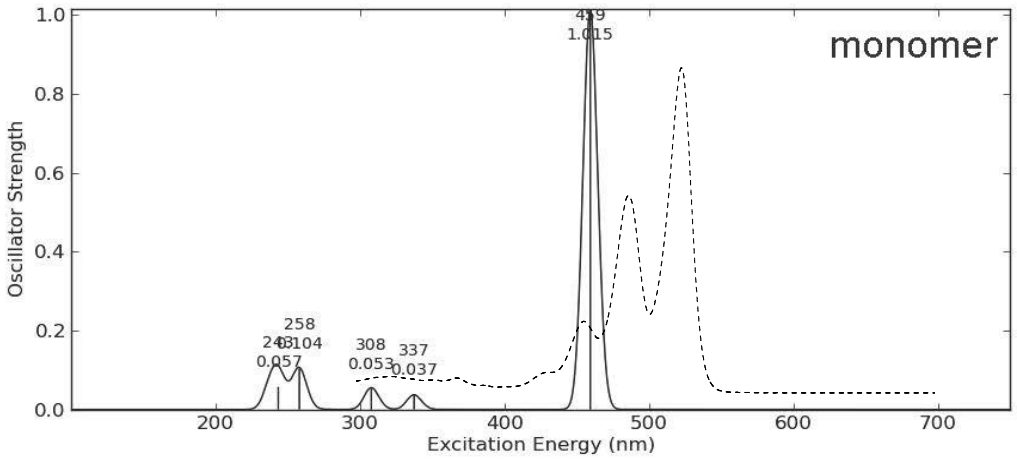

Figure 2.19. Computed absorption spectrum of **1**. The dash line is the observed absorption spectrum of **1**.

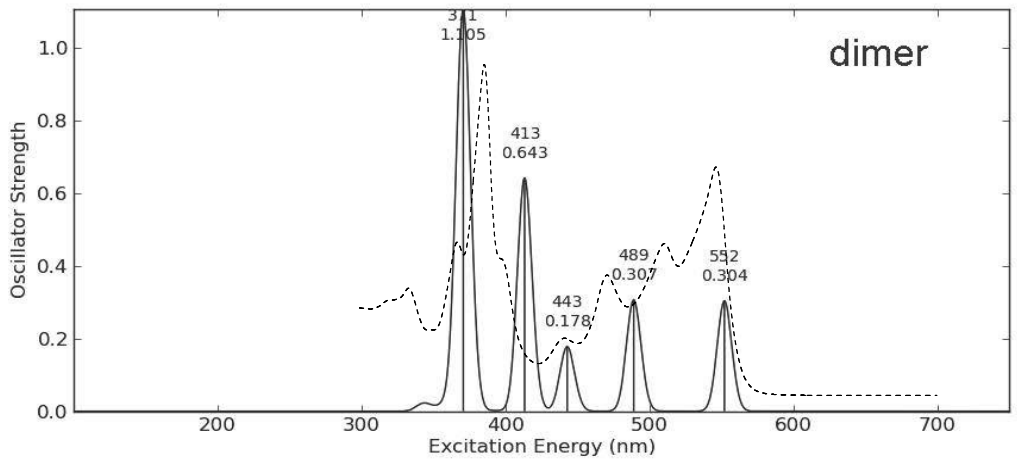

Figure 2.20. Computed absorption spectrum of **2**. The dash line is the observed absorption spectrum of **2**.

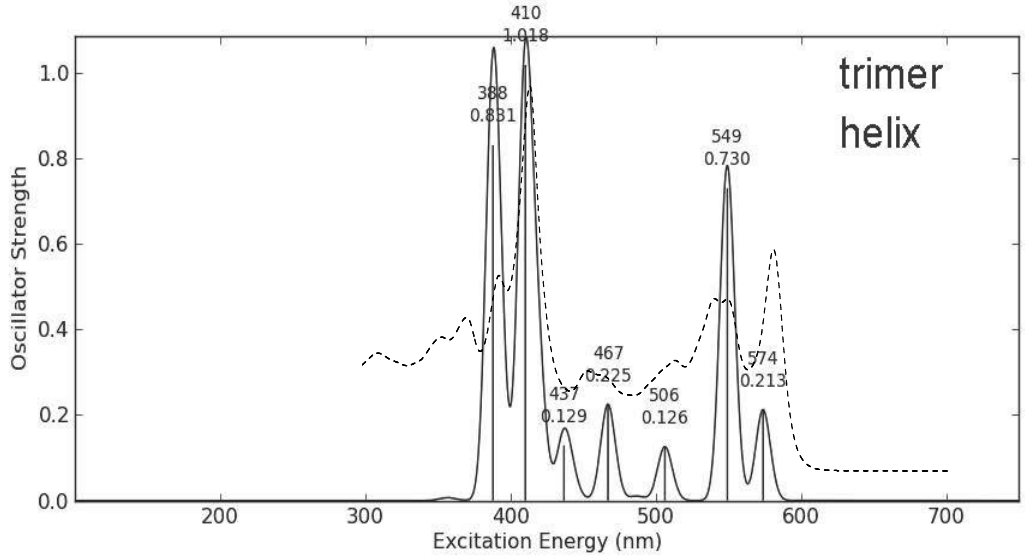

Figure 2.21. Computed absorption spectrum of **3** with 'Helical' conformation. The dash line is the observed absorption spectrum of **3**.

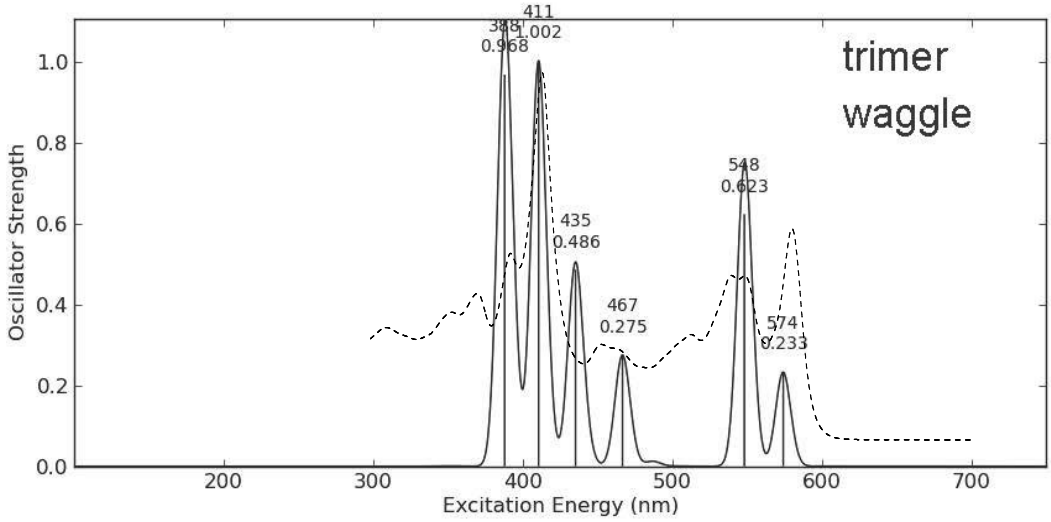

Figure 2.22. Computed absorption spectrum of **3** with 'Waggling' conformation. The dash line is the observed absorption spectrum of **3**.

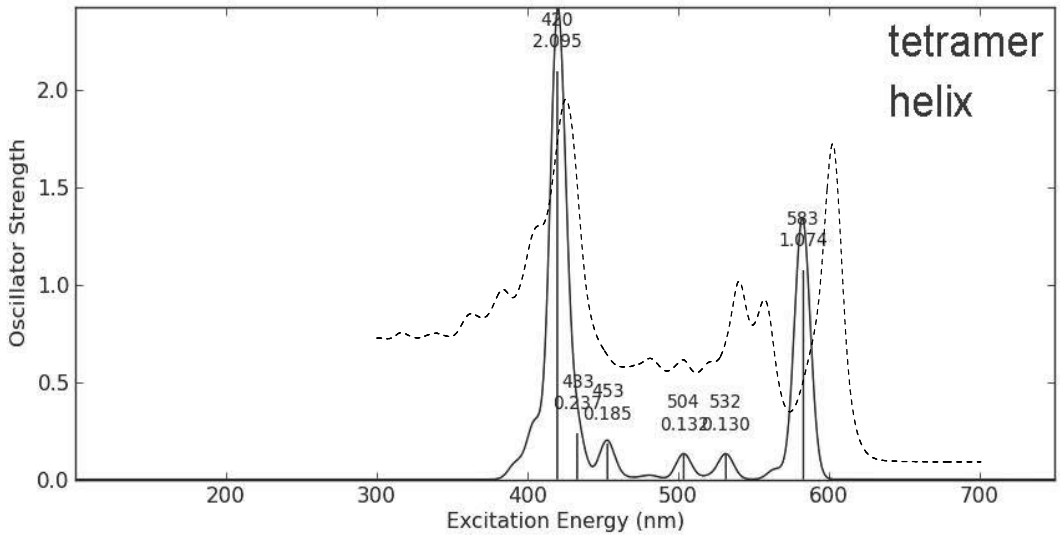

Figure 2.23. Computed absorption spectrum of **4** with 'Helical' conformation. The dash line is the observed absorption spectrum of **4**.

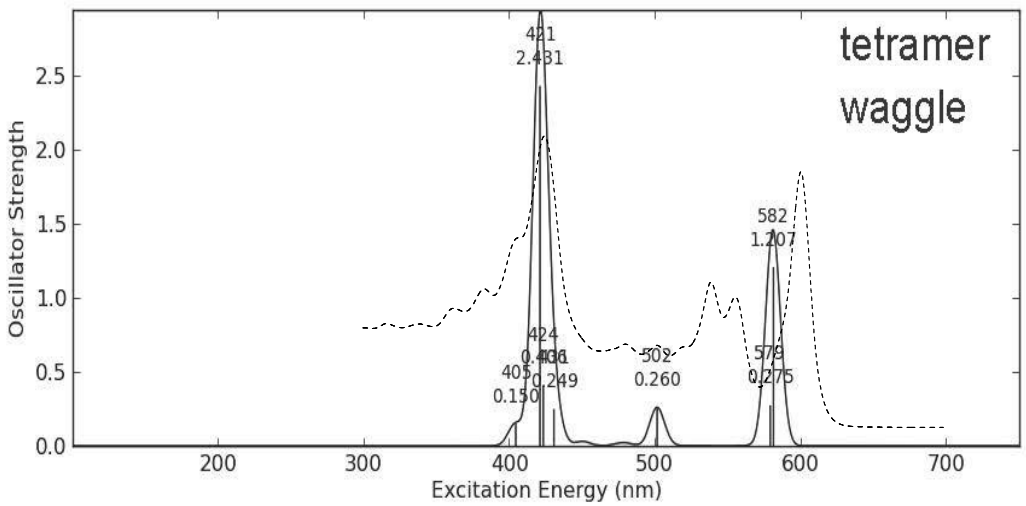

Figure 2.24. Computed absorption spectrum of **4** with 'Waggling' conformation. The dash line is the observed absorption spectrum of **4**.

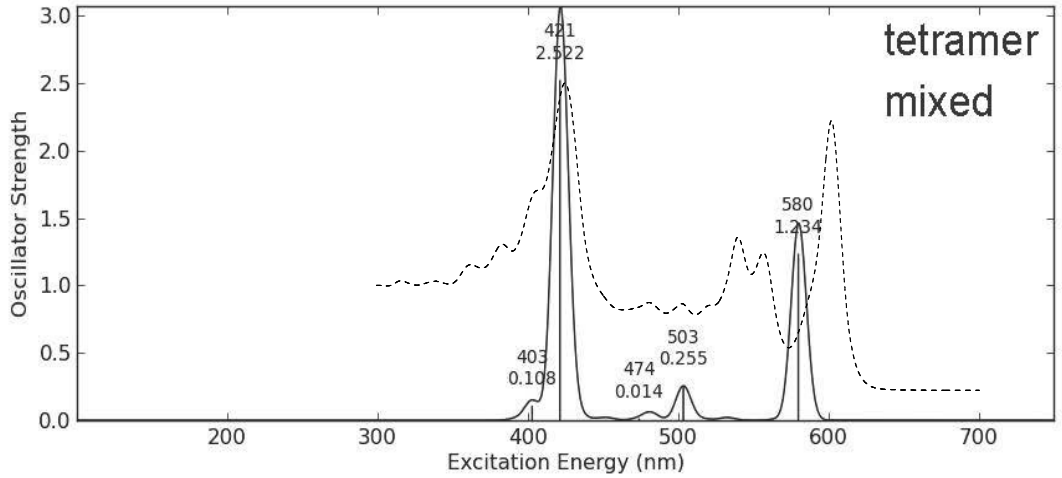

Figure 2.25. Computed absorption spectrum of **4** with 'Mixed' conformation. The dash line is the observed absorption spectrum of **4**.

2.8.7. Femtosecond transient absorption spectra

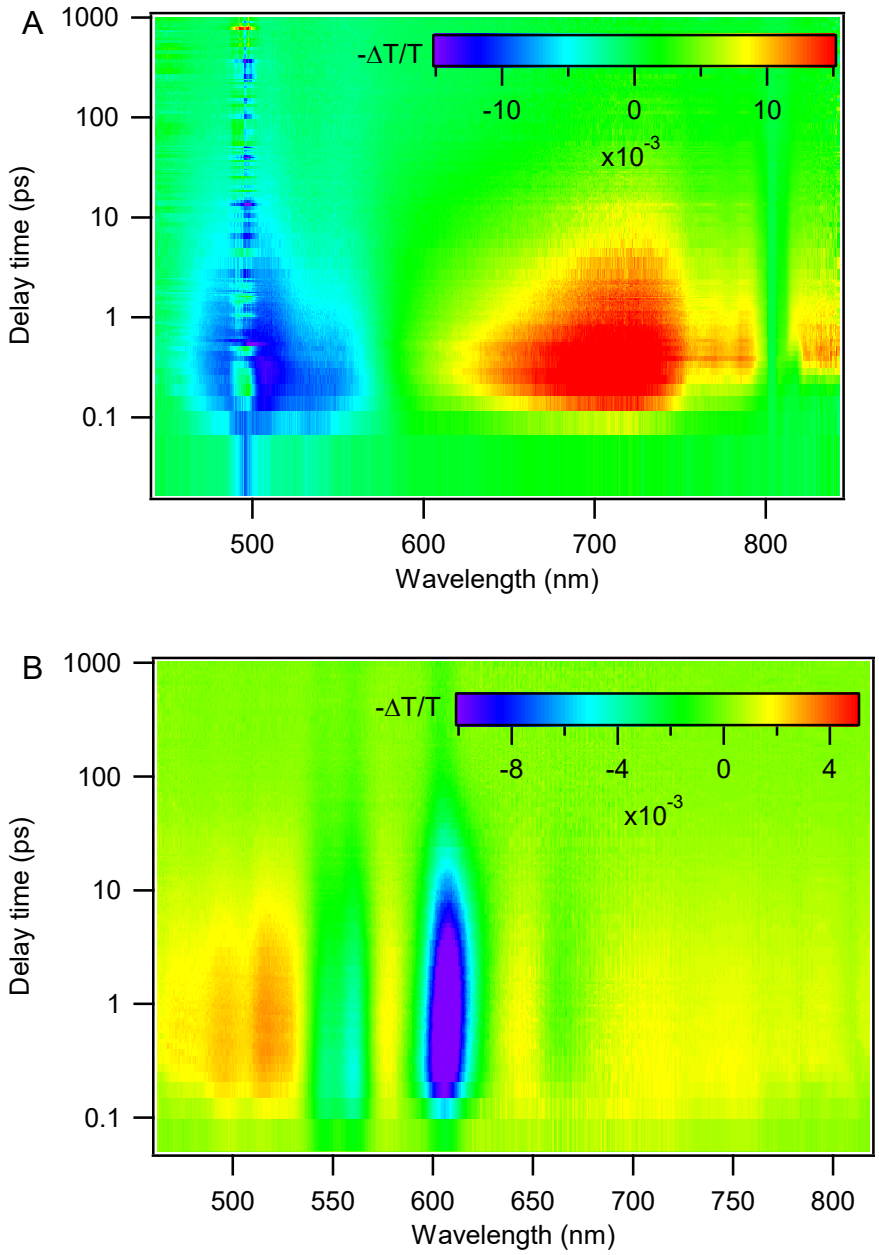

Figure 2.26. Two-dimensional pseudo-color (-ΔT/T) representation of transient absorption spectra as functions of probe photon energy (X) and pump-probe delay time (Y) for monomer **1** (A) pumped at 487 nm and tetramer **4** (B) pumped at 450 nm. The noisy signal around 490 nm at the panel A is due to scattering light from the pump pulse. The samples

were prepared in films by drop cast.

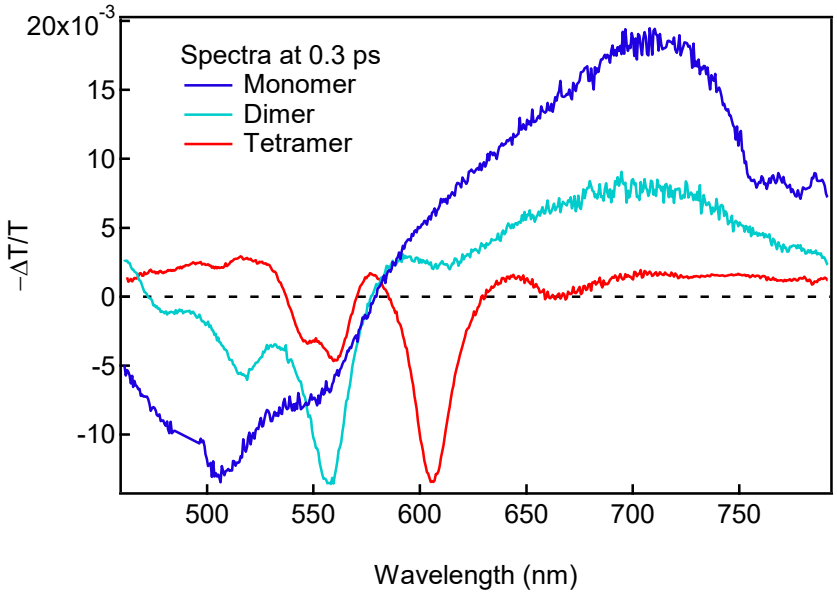

Figure 2.27. Comparison of the transient absorption spectra for monomer **1**, dimer **2**, and tetramer **4** at 0.3 ps delay time between pump and probe pulses. The samples were prepared in films by drop cast. The planar structure in Monomer **1** results in strong aggregation, which facilitates intermolecular interaction that gives rise to broadening of the absorption for the film in comparison to the solution form. The broadening in the absorption displays in the broadening of the bleaching signal at wavelength from 450 to 580 nm. The twist along ribbon in **2** and **4** prevents samples from aggregation that shows clear distinct and sharp features in bleaching signal for **2** and **4**.

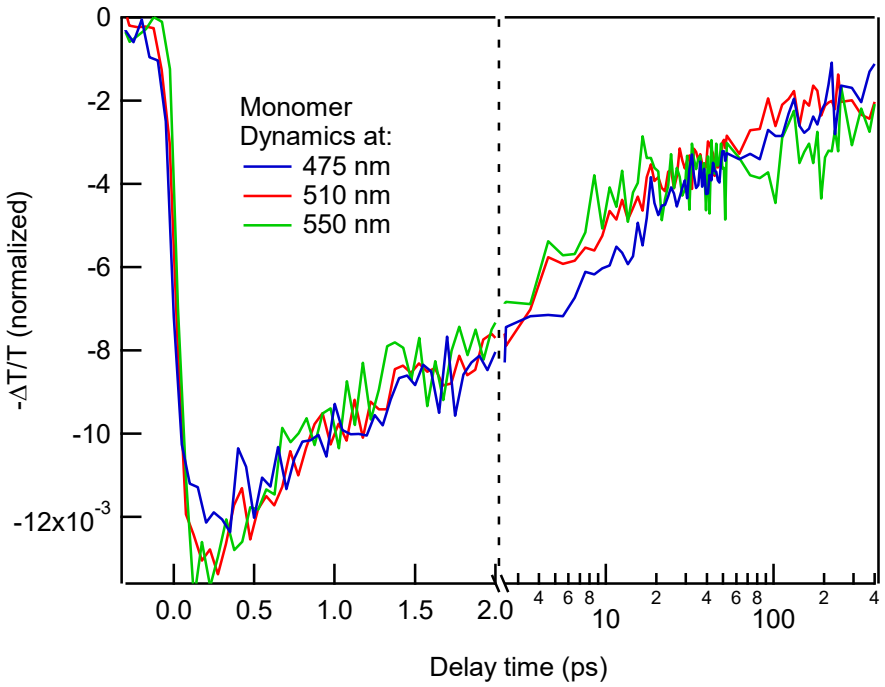

Figure 2.28. Exciton dynamics at different probe wavelengths for monomer **1**.

2.9 References and Notes

(1) Novoselov, K. S.; Geim, A. K.; Morozov, S. V.; Jiang, D.; Zhang, Y.; Dubonos, S. V.; Grigorieva, I. V.; Firsov, A. A. *Science* **2004**, *306*, 666.

(2) Novoselov, K. S.; Geim, A. K.; Morozov, S. V.; Jiang, D.; Katsnelson, M. I.; Grigorieva, I. V.; Dubonos, S. V.; Firsov, A. A. *Nature* **2005**, *438*, 197.

(3) Zhang, Y. B.; Tan, Y. W.; Stormer, H. L.; Kim, P. *Nature* **2005**, *438*, 201.

(4) Eda, G.; Fanchini, G.; Chhowalla, M. *Nat. Nanotechnol.* **2008**, *3*, 270.

(5) Bunch, J. S.; van der Zande, A. M.; Verbridge, S. S.; Frank, I. W.; Tanenbaum, D. M.; Parpia, J. M.; Craighead, H. G.; McEuen, P. L. *Science* **2007**, *315*, 490.

(6) Chung, K.; Lee, C. H.; Yi, G. C. *Science* **2010**, *330*, 655.

(7) Fujita, M.; Wakabayashi, K.; Nakada, K.; Kusakabe, K. *J. Phys. Soc. Jpn.* **1996**, *65*, 1920.

(8) Son, Y.-W.; Cohen, M. L.; Louie, S. G. *Phys. Rev. Lett.* **2006**, *97*, 216803.

(9) Barone, V.; Hod, O.; Scuseria, G. E. *Nano Lett.* **2006**, *6*, 2748.

(10) Wang, X.; Ouyang, Y.; Li, X.; Wang, H.; Guo, J.; Dai, H. *Phys. Rev. Lett.* **2008**, *100*, 206803.

(11) Top-down approach includes chemical or plasma etching graphene sheets, laterally unzipping carbon nanotubes (CNTs), patterning graphene by nanowire mask and direct growth of graphitic nanoribbon from a DNA template. See ref. 12-17.

(12) Li, X.; Wang, X.; Zhang, L.; Lee, S.; Dai, H. *Science* **2008**, *319*, 1229.

(13) Wei, D. C.; Xie, L. F.; Lee, K. K.; Hu, Z. B.; Tan, S. H.; Chen, W.; Sow, C. H.; Chen, K. Q.; Liu, Y. Q.; Wee, A. T. S. *Nat. Commun.* **2013**, *4,* 1374.

(14) Xie, L.; Jiao, L.; Dai, H. *J. Am. Chem. Soc.* **2010**, *132*, 14751.

(15) Jiao, L.; Zhang, L.; Wang, X.; Diankov, G.; Dai, H. *Nature* **2009**, *458*, 877.

(16) Bai, J. W.; Duan, X. F.; Huang, Y. *Nano Lett.* **2009**, *9*, 2083.

(17) Sokolov, A. N.; Yap, F. L.; Liu, N.; Kim, K.; Ci, L.; Johnson, O. B.; Wang, H.; Vosgueritchian, M.; Koh, A. L.; Chen, J.; Park, J.; Bao, Z. *Nat. Commun.* **2013**, *4,* 2402.

(18) Qian, H. L.; Negri, F.; Wang, C. R.; Wang, Z. H. *J. Am. Chem. Soc.* **2008**, *130*, 17970.

(19) Yang, X.; Dou, X.; Rouhanipour, A.; Zhi, L.; Räder, H. J.; Müllen, K. *J. Am. Chem. Soc.* **2008**, *130*, 4216.

(20) Fogel, Y.; Zhi, L. J.; Rouhanipour, A.; Andrienko, D.; Rader, H. J.; Mullen, K. *Macromolecules* **2009**, *42*, 6878.

(21) Cai, J.; Ruffieux, P.; Jaafar, R.; Bieri, M.; Braun, T.; Blankenburg, S.; Muoth, M.; Seitsonen, A. P.; Saleh, M.; Feng, X.; Müllen, K.; Fasel, R. *Nature* **2010**, *466*, 470.

(22) Schwab, M. G.; Narita, A.; Hernandez, Y.; Balandina, T.; Mali, K. S.; De Feyter, S.; Feng, X. L.; Mullen, K. *J. Am. Chem. Soc.* **2012**, *134*, 18169.

(23) Anthony, J. E.; Facchetti, A.; Heeney, M.; Marder, S. R.; Zhan, X. W. *Adv. Mater.* **2010**, *22*, 3876.

(24) Ego, C.; Marsitzky, D.; Becker, S.; Zhang, J.; Grimsdale, A.; Müllen, K.; MacKenzie, J.; Silva, C.; Friend, R. *J. Am. Chem. Soc.* **2003**, *125*, 437.

(25) Zhou, E. J.; Cong, J. Z.; Wei, Q. S.; Tajima, K.; Yang, C. H.; Hashimoto, K. *Angew. Chem. Int. Ed.* **2011**, *50*, 2799.

(26) Sharenko, A.; Proctor, C. M.; van der Poll, T. S.; Henson, Z. B.; Nguyen, T.-Q.; Bazan, G. C. *Adv. Mater.* **2013**, *25*, 4403.

(27) Huo, L. J.; Zhou, Y.; Li, Y. F. *Macromol. Rapid Commun* **2008**, *29*, 1444.

(28) Yan, Q. F.; Zhao, D. H. *Org. Lett.* **2009**, *11*, 3426.

(29) Li, C.; Wonneberger, H. *Adv. Mater.* **2012**, *24*, 613.

(30) Li, Y.; Wang, C.; Li, C.; Di Motta, S.; Negri, F.; Wang, Z. *Org. Lett.* **2012**, *14*, 5278.

(31) Schmidt, C. D.; Lang, N.; Jux, N.; Hirsch, A. *Chem. Eur. J.* **2011**, *17*, 5289.

(32) Mallory, F. B.; Mallory, C. W. In *Organic Reactions*; John Wiley & Sons, Inc.: Hoboken, **1984**; Vol. 30.

(33) Mallory, C. W. M., F. B. *Org. Photochem. Synth.* **1971**, *1*, 55.

(34) Rajasingh, P.; Cohen, R.; Shirman, E.; Shimon, L. J. W.; Rybtchinski, B. *J. Org. Chem.* **2007**, *72*, 5973.

(35) Dibrominated dimer **14** was synthesized by electrophilic bromination of dimer 2, the mixture was used without separation as the both isomers (1,6 or 1,7) will give same product.

(36) Sang Kwon, L.; Yanbing, Z.; Andreas, H.; Yves, G.; Kläus, M.; Allen, J. B. *J. Am. Chem. Soc.* **1999**, *121,* 3513.

(37) Wurthner, F. *Chem. Commun.* **2004**, 1564.

(38) Details of the electrochemical measurements can be found in the Supporting Information Figure S5.

(39) He, Y.; Li, Y. *Phys. Chem. Chem. Phys.* **2011**, *13*, 1970.

(40) Yan, Z.; Yunlong, G.; Yunqi, L. *Adv. Mater.* **2013**, *25*, 5372

(41) Rozlosnik, N.; Gerstenberg, M. C.; Larsen, N. B. *Langmuir* **2003**, *19*, 1182.

(42) Chua, L.-L.; Zaumseil, J.; Chang, J.-F.; Ou, E. C. W.; Ho, P. K. H.; Sirringhaus, H.; Friend, R. H. *Nature* **2005**, *434*, 194.

(43) Zaumseil, J.; Sirringhaus, H. *Chem. Rev.* **2007**, *107*, 1296.

(44) Newman, C. R.; Frisbie, C. D.; da Silva, D. A.; Bredas, J. L.; Ewbank, P.

C.; Mann, K. R. *Chem. Mater.* **2004**, *16*, 4436.

(45) The threshold voltages are in the similar range of reported PDI transistors. See ref. 46-48.

(46) Chesterfield, R. J.; McKeen, J. C.; Newman, C. R.; Ewbank, P. C.; da Silva, D. A.; Bredas, J. L.; Miller, L. L.; Mann, K. R.; Frisbie, C. D. *J. Phys. Chem. B* **2004**, *108*, 19281.

(47) Chen, F. C.; Liao, C. H. *Appl. Phys. Lett.* **2008**, *93,* 103310.

(48) Tatemichi, S.; Ichikawa, M.; Koyama, T.; Taniguchi, Y. *Appl. Phys. Lett.* **2006**, *89,* 112108.

(49) Malenfant, P. R. L.; Dimitrakopoulos, C. D.; Gelorme, J. D.; Kosbar, L. L.; Graham, T. O.; Curioni, A.; Andreoni, W. *Appl. Phys. Lett.* **2002**, *80*, 2517.

(50) Türkmen, G.; Erten-Ela, S.; Icli, S. *Dyes Pigm.* **2009**, *83*, 297.

(51) Xiao, S.; Myers, M.; Miao, Q.; Sanaur, S.; Pang, K.; Steigerwald, M. L.; Nuckolls, C. *Angew. Chem. Int. Ed.* **2005**, *44*, 7390.

(52) Nolde, F.; Pisula, W.; Müller, S.; Kohl, C.; Müllen, K. *Chem. Mater.* **2006**, *18*, 3715.

(53) Steigerwald, M. L.; Alivisatos, A. P.; Gibson, J. M.; Harris, T. D.; Kortan, R.; Muller, A. J.; Thayer, A. M.; Duncan, T. M.; Douglass, D. C.; Brus, L. E. *J. Am. Chem. Soc.* **1988**, *110*, 3046.

(54) Sadrai, M.; Bird, G. R. *Opt. Commun.* **1984**, *51*, 62.

(55) Trinh, M. T.; Sfeir, M. Y.; Choi, J. J.; Owen, J. S. Zhu, X.-Y. *Nano. Lett.* **2013**, 13, 6091.

(56) Zhang, X.; Lu, Z.; Ye, L.; Zhan, C.; Hou, J.; Zhang, S.; Jiang, B.; Zhao, Y.; Huang, J.; Zhang, S.; Liu, Y.; Shi, Q.; Liu, Y.; Yao, J. *Adv. Mater.* **2013**, *25*, 5791.

(57) Yan, Q.; Zhou, Y.; Zheng, Y.-Q.; Pei, J.; Zhao, D. *Chem. Sci.* **2013**, *4*, 4389.

(58) Rajasingh, P.; Cohen, R.; Shirman, E.; Shimon, L. J. W.; Rybtchinski, B. *J. Org. Chem.* **2007**, *72*, 5973-5979.

Chapter 3 Efficient Organic Solar Cells with Helical Perylene Diimide Electron Acceptors

Chapter 3 is reproduced with permission from the authors: Zhong, Y.; Trinh, M. T.; Chen, R. S.; Wang, W.; Khlyabich, P. P.; Kumar, B.; Xu, Q. Z.; Nam, C. Y.; Sfeir, M. Y.; Black, C.; Steigerwald, M. L.; Loo, Y. L.; Xiao, S. X.; Ng, F.; Zhu, X. Y.; Nuckolls, C. *J. Am. Chem. Soc.* **2014**, *136*, 15215.; Copyright 2014 American Chemical Society. Device fabrication and characterization were performed by myself with assistance from Rongsheng Chen, Wei Wang, Qizhi Xu, Petr P. Khlyabich and Chang-Yong Nam. Transient absorption measurements were conducted by M. Tuan Trinh. Synthesis was carried out by Fay Ng and Bharat Kumar. DFT calculations were performed by Michael L. Steigerwald.

3.1 Introduction

We describe here the device performance, charge transfer dynamics, and recombination mechanisms in a highly efficient fullerene-free organic bulk-heterojunction (BHJ) solar cell. The majority of organic solar cells utilize fullerene and its derivatives ($PC_{61}BM$, $PC_{71}BM$, etc.) as the electron acceptors.[1] Despite their wide spread use, fullerene acceptors have some drawbacks. For example, it is difficult to tune the optical properties and electronic structure of fullerenes over a wide range of energy.[2a-2c] Furthermore, there are no general methods to enhance the absorption of the fullerene backbone in the visible and NIR region of the spectrum. Finally, the cost of the fullerene derivatives limits their practical use on a large scale.[2d] The acceptor molecule we test here is based on the commercial dye, perylene diimide (PDI). PDI and its derivatives have attracted a great deal of attention as an alternative electron acceptor because of their good mobility in OFETs,

high molar absorptivity, ease of functionalization, and economical starting materials. Unfortunately PDIs and other electron acceptors have not fulfilled their potential in solar cells. Alternatives to fullerenes typically have photon conversion efficiency (PCE) in the range of 1% - 6%.[3-5] In this study we present the first solar cells that incorporate the helical PDI dimer (denoted as **1** in this chapter) (Figure 3.1) as the electron acceptor. We find that solar cells using **1** with either of two commercial donor polymers (Figure 3.1a), exhibit PCE greater than 5%. We further characterize these devices by studying their charge carrier recombination processes with incident light-intensity-dependent performance measurements. Using transient absorption spectroscopy, we demonstrate that excitons generated in both donor and acceptor phases contribute to the photocurrent by effectively splitting at donor/acceptor interfaces.

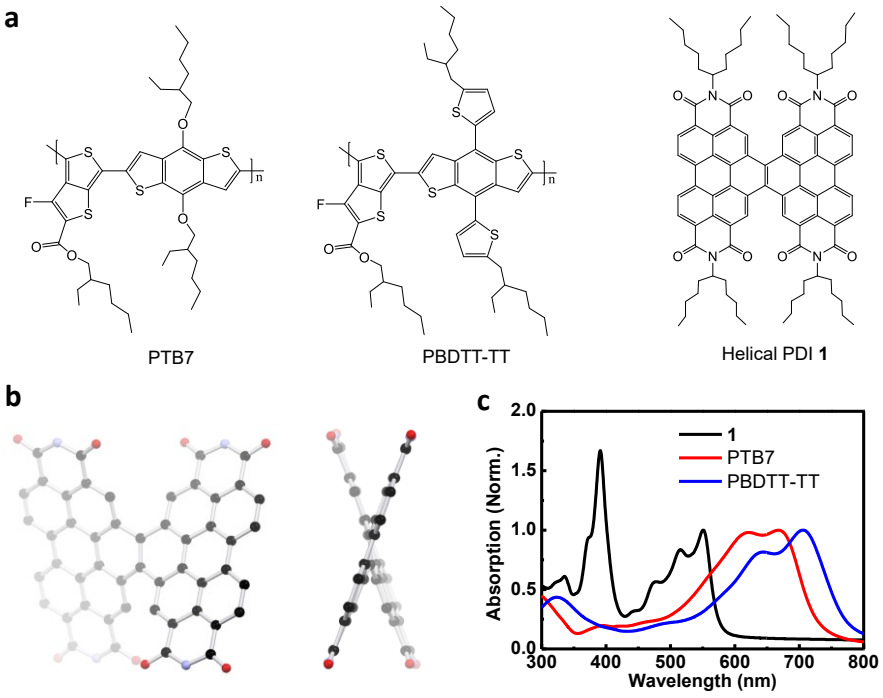

Figure 3.1 (a) Chemical structures of PTB7, PBDTT-TT and helical PDI **1**. (b) Molecular model of **1** from DFT calculation. Hydrogens and alkyl sidechains have been removed for

clarity. Black = carbon; red = oxygen; blue = nitrogen. (c) Film absorption spectra of PTB7, PBDTT-TT and **1,** normalized at their low energy λ_{max}.

3.2 Results and Discussion

Helical **1** is a dimer formed by the fusion of two PDI units with a two carbon bridge.[6] Figure 3.1b shows a molecular model of **1**. We recently described a general synthetic route to this material and higher oligomers.[7] Helical **1** has a relatively high electron mobility, good electron accepting ability and a LUMO level (~4 eV) similar to that of $PC_{61}BM$ or $PC_{71}BM$.[7] Because of the twisted molecular conformation of **1** (Figure 3.1b), it does not aggregate strongly.[8] The branched alkyl chains connected to the imide nitrogen atoms assure good solubility in common organic solvents.[9] **1** absorbs light strongly from 350 nm and 550 nm with a maximum molar extinction coefficient of 1.1×10^5 $M^{-1}cm^{-1}$ (see Figure 3.6 in Section 3.5.1.).[6-7] For these reasons and the high molar absorptivity, we decided to test **1** as an electron acceptor in solar cells. To fabricate BHJs based on **1**, we chose the narrow-bandgap semiconducting polymer polythieno[3,4-b]thiophene-co-benzodithiophene (PTB7)[10] and poly[4,8-bis(5-(2-ethylhexyl)thiophen-2-yl)benzo[1,2-b;4,5-b']dithiophene-2,6-diyl-alt-(4-(2-ethylhexyl)-3-fluorothieno[3,4-b]thiophene-)-2-carboxylate-2-6-diyl)] (PBDTT-TT, also known as PTB7-Th)[11] (shown in Figure 3.1a) as the electron donors. The absorption bands of the PTB7 and PBDTT-TT are red-shifted relative to those of **1** (Figure 3.1c); as a result, blended films of **1** and the donor polymers have broad and intense absorptions that span 350 nm to 800 nm.

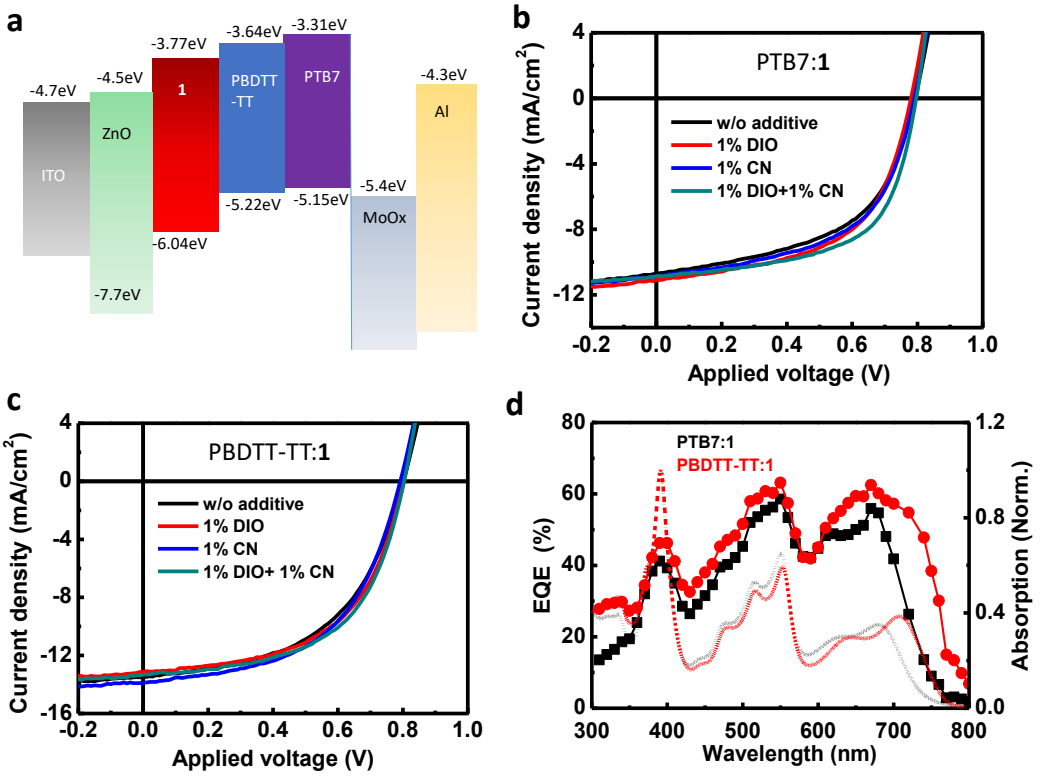

Figure 3.2. (a) Schematic of the energy levels of ITO, ZnO, **1**, PBDTT-TT, PTB7, MoO_x and Al. (b) J-V curves for PTB7:**1** solar cells with different additives. (c) J-V curves for PBDTT-TT:**1** solar cells with different additives. (d) EQE spectra (symbols) of PTB7: **1** (black) and PBDTT-TT:**1** (red) devices with 1% DIO and 1% CN solvent additive and absorption spectra (dashed lines) for the PTB7:**1** (black) and PBDTT-TT:**1** (red) blend films (3:7 D/A mass ratio).

We first varied the mass ratio of PTB7 and **1** in solution to optimize device performance. We fabricated devices in both a conventional structure with a configuration of ITO/PEDOT:PSS(40nm)/PTB7:**1**/BCP(7nm)/Al(100nm) and an inverted structure with a configuration of ITO/ZnO(20nm)/PTB7:**1**/MoO_x(5nm)/Al(100nm). A 3:7 mass ratio of PTB7 and **1** provides the highest PCE: 3.5 % in a conventional structure and 4.5 % in an inverted structure. This data is displayed in Figure 3.7 and 3.8 in Section 3.5.2. Therefore,

we chose the inverted structure for further optimization. A schematic of the energy levels in these inverted devices is shown in Figure 3.2a. Next, we use the di-iodooctane (DIO) and 1-chloronaphthalene (CN) solvent additive to improve overall morphology.[12] Typical J-V curves for PTB7:**1** solar cells with different additives are shown in Figure 3.2b. Compared to devices without additive, those devices with 1% DIO and 1% CN show higher PCEs, mainly due to an improved fill factor from 53.1% without additive to 55.6% with DIO and 54.5% with CN. Furthermore, when 1% DIO and 1% CN were used as co-additive in the solution, the fill factor increased to 60.0%, resulting in an average PCE of 5.14%. The highest PCE we achieved from a PTB7:**1** solar cell is 5.21%. This cell had the following characteristics: J_{sc} of 10.9 mA/cm^2, V_{oc} of 0.791 V and fill factor of 60.0%. We observe a similar effect of DIO and CN with PBDTT-TT:**1** solar cells (shown in Figure 3.2c). Overall, the solar cells containing PBDTT-TT exhibit larger J_{sc} values than PTB7 solar cells because of their more red-shifted absorption. The average PCEs from six devices without any additives is 5.52%; with various additives the average PCE is 5.63% with DIO, 5.70% with CN and 5.94% with DIO and CN co-additive, respectively. A champion PBDTT-TT:**1** solar cell shows the following characteristics: J_{sc} of 13.3 mA/cm^2, V_{oc} of 0.803 V, fill factor of 56.6% and PCE of 6.05%. We summarize the parameters of the solar cells in Table 3.1. These properties are excellent for a PDI based solar cell[4] and competes with the highest PCEs reported for solution-processed non-fullerene BHJs.[3-4] These values are lower than the corresponding cells with fullerenes as the acceptor,[10,11] but these partners were optimized for each other. This highlights the enormous potential of **1** in solar cells by creating tailored donor materials for them.

Table 3.1. Summary of device parameters of PTB7:**1** and PBDTT-TT:**1** solar cells.

	J_{sc} (mA/cm^2)	V_{oc} (V)	FF (%)	PCE (%)[a]
PTB7:**1** -no additive	10.5 ± 0.2	0.796 ± 0.006	53.6 ± 0.5	4.47±0.03 (4.50)
PTB7:**1** -1% DIO	10.9 ± 0.2	0.782 ± 0.004	56 ± 1	4.74 ± 0.05 (4.81)
PTB7:**1** 1% CN	10.7 ± 0.4	0.787 ± 0.009	54.1 ± 0.8	4.54 ± 0.18 (4.70)
PTB7:**1** 1% DIO + 1% CN	11.0 ± 0.1	0.789 ± 0.005	59 ± 1	5.14 ± 0.04 (5.21)
PBDTT-TT:**1** no additive	13.6 ± 0.1	0.796 ± 0.005	51.1 ± 0.7	5.52 ± 0.05 (5.59)
PBDTT-TT:**1** 1% DIO	13.2 ± 0.1	0.794 ± 0.005	54 ± 1	5.63 ± 0.11 (5.81)
PBDTT-TT:**1** 1% CN	13.7 ± 0.2	0.790 ± 0.005	53 ± 1	5.70 ± 0.11 (5.86)
PBDTT-TT:**1** 1% DIO + 1% CN	13.5 ± 0.2	0.796 ± 0.005	55 ± 1	5.94 ± 0.07 (6.05)

[a]Average PCE values were calculated from six devices for each condition; highest PCE values in parentheses.

We measured the electron and hole mobilities in the optimal blend films by the space-charge limited current (SCLC) method.[13] For PTB7:**1** blend film, the hole and electron mobilities are calculated to be 6.7×10^{-5} $cm^2V^{-1}s^{-1}$ and 2.2×10^{-4} $cm^2V^{-1}s^{-1}$, respectively (Figure 3.12). This hole mobility is smaller than that of a PTB7:$PC_{71}BM$ blend film,[10a] probably due to different components and the different mass ratios in the two active layers. For PBDTT-TT:**1** blend film, the hole and electron mobilities are calculated to be 2.9×10^{-4} $cm^2V^{-1}s^{-1}$ and 3.4×10^{-4} $cm^2V^{-1}s^{-1}$, respectively. The hole mobility of PBDTT-TT:**1** blend film is higher than that of PTB7:**1** because of the improved π-stacking of these 2-dimensional conjugated polymer chains.[11] In both kinds of devices, helical PDI **1** exhibits an electron mobility one order of magnitude higher than that of PTB7:$PC_{71}BM$ or PBDTT-TT:$PC_{71}BM$ BHJs.[11b,14]

Figure 3.2d displays the external quantum efficiency (EQE) spectra of the optimal PTB7:**1** and PBDTT-TT:**1** devices. Compared to the PTB7:**1** solar cell, the PBDTT-TT:**1** solar cell shows slightly higher EQE values in the range of 300nm to 700nm, and a

significant increase from 700nm to 800nm due to the red-shifted absorption of PBDTT-TT. The integrated J_{sc} is 10.2 mA/cm^2 for PTB7:**1** solar cell and 12.8 mA/cm^2 for PBDTT-TT:**1** solar cell, respectively, giving an estimate of the PCEs of 4.9% for the former and 5.8% for the latter. These values agree well with the PCEs in Table 3.1, and it should be noted that the EQE values are not zero at 300nm, resulting in a slight underestimation of the PCE when using the EQE spectra. Unlike those solar cells made from fullerene derivatives and other non-fullerene acceptors, both of the EQE curves show three transitions instead of a featureless transition. These peaks arise from the sharp and strong absorption bands of **1** (Figure 3.1c). This feature is unique among PDI-based non-fullerene BHJs because **1** has a rigid conformation that is different when compared to other PDI acceptors.[4] The important point is that we are able to distinguish the photoresponse peaks of the donor polymers and that of **1**. We note that the shape of EQE spectrum is similar to the absorption spectrum of the blend film. Since the absorption from 350 nm to 550 nm for the blend film is mainly from **1**, photo-generated excitons from **1** largely contribute to the photocurrent in these solar cells.

A particular advantage of helical PDI **1** over fullerenes as electron acceptor is the higher optical absorption cross section of the former. To unambiguously establish that light absorption in both donor and acceptor contribute to photocurrent in a PDI **1** based bulk-heterojunction and to establish the charge generation mechanisms, we use transient absorption (TA) spectroscopy. Figure 3.3 shows the differential transmission spectra and dynamics for a film of neat **1** excited at 390 nm. The negative features with peaks at 480, 516 and 556 nm (Figure 3.3a) result from the bleaching of ground state absorption as charges and excitons are created in **1**. The positive signals in the wavelength range < 470

nm and > 570 nm are the excited state absorption (ESA) of the photo-generated charges or excitons in the film. The ESA feature for **1** film centered at 700 nm can be assigned to the singlet $S_1 \rightarrow S_N$ transitions.[15] It decays with a single exponential lifetime of $\tau_{S1} = 8.6 \pm 0.4$ ps (red curve in Figure 3.3b).

Unlike the simple S_1 decay, the dynamics of ground state recovery (green curve in Figure 3.3b, probed at 555 nm) is more complex and can be described by three distinct time constants (tri-exponential fit in Figure 3.3b), with relative populations in parenthesis: $\tau_1 = 0.81 \pm 0.07$ ps (39%) ; $\tau_2 = 8.6 \pm 0.7$ ps (35 %), and $\tau_3 = 800 \pm 50$ ps (26%). The intermediate component ($\tau_2 = 8.6 \pm 0.7$ ps) has a time constant identical to that of singlet decay and is assigned to S_1. Both the faster (0.81 ps) and the slower (800 ps) components do not correspond to S_1 and must be attributed to different species. Since initial photo-excitation in molecular semiconductors is known to generate both excitons and free charge carriers,[16] we assign ground state recovery with $\tau_1 = 0.81 \pm 0.07$ ps and $\tau_3 = 800 \pm 50$ ps to the recombination of charge carriers: the faster component to geminate recombination of the nascent electron-hole pairs and the slower one to two body recombination of individual electron and hole carriers (bimolecular recombination). Evidence for the generation of photocarriers can also be found in the ESA; the fast ESA feature at 590 nm with a decay time constant of 0.7 ± 0.1 ps (blue curve in Figure 3.3b) which is very much close to the fast decay component of bleaching recovery thus is assigned to geminate recombination. There is a broad ESA feature in the TA spectrum at 400 ps spanning from 580 to 850 nm (Figure 3.3a). This recovery occurs on the 800 ps time scale and can be assigned to bimolecular recombination of the individual electron and hole carriers (Figure 3.3a).[16b,16c] From the above fit to the bleaching dynamics at 555 nm, we assign the direct charge

generation yield of 26 % in the in film of **1** upon photoexcitation. Note that we do not assign the slow component to triplets because the triplet absorption in PDI derivatives is known to give a sharp feature at the wavelength range < 600 nm.[15c,17] These features are absent in the TA spectrum (green-yellow curve in Figure 3.3a).

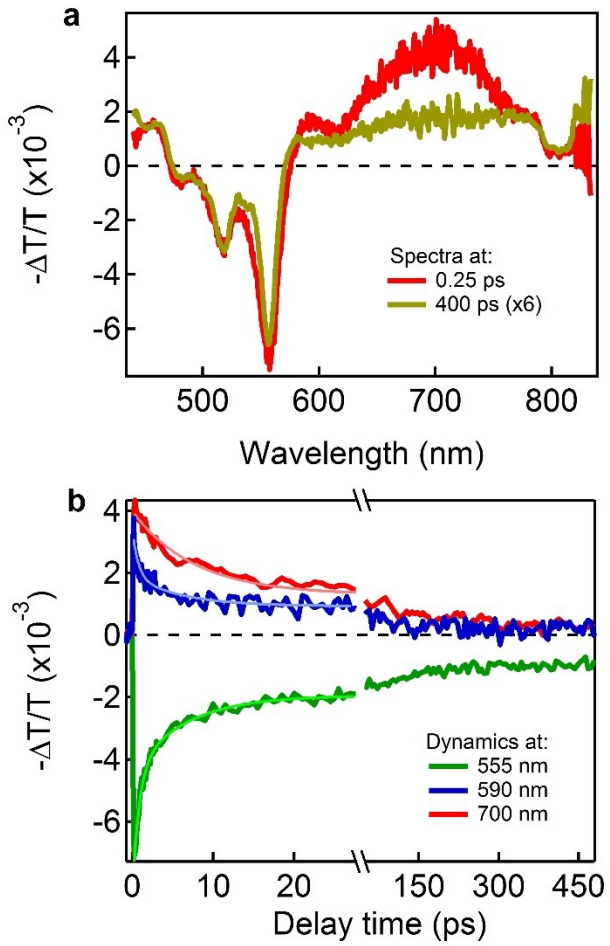

Figure 3.3. (a) Differential transmission spectra (-ΔT/T) as a function of probe wavelength pumping at 390 nm for neat **1** at 0.25 ps and 400 ps. The excited state absorption (ESA) centered at 700 nm at 0.25 ps is due to $S_1 \rightarrow S_N$ transitions. A dip at 800 nm is due to saturation caused by high probe intensity. (b) Dynamics at probe wavelength of 555nm, 590nm and 700 nm.

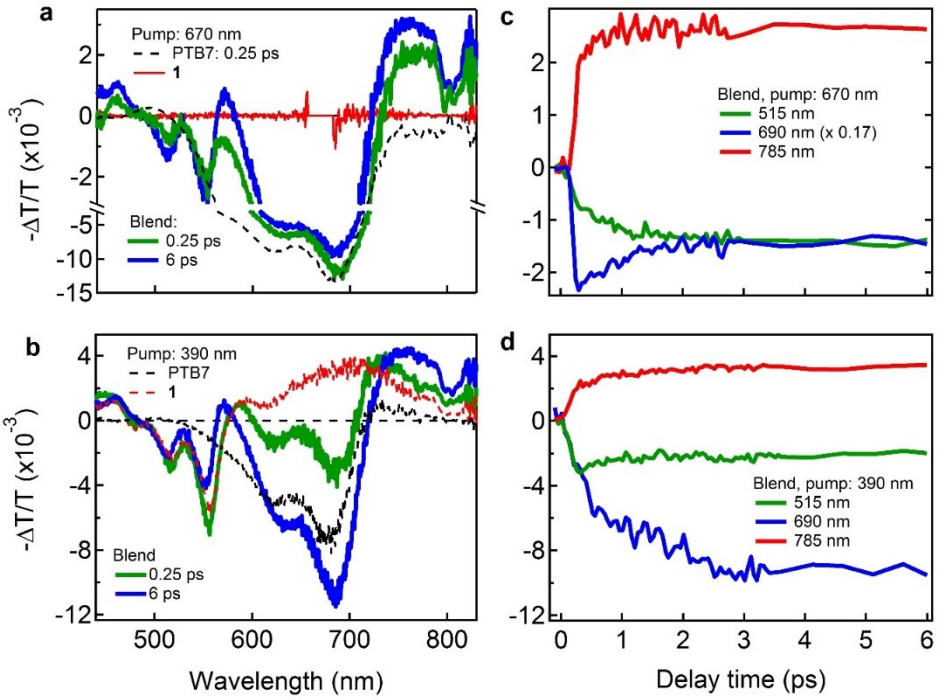

Figure 3.4. (a, b) Differential transmission spectra (-ΔT/T) as a function of probe wavelength pumping at 670 nm, (a), and 390 nm, (b), for neat **1** and neat PTB7: at 0.25 ps, and a blend of **1** and PTB7 films. (c, d) Decay dynamics at the different probe wavelengths pumping at 670 and 390 nm. The dynamics at 690 nm probe wavelength in figure (c) was scaled by a factor 0.17. The pump density is ~20 μJ/cm^2/pulse.

Having investigated the photophysics in neat **1**, we next explored the exciton generation and dissociation in a blend of **1** and PTB7 at a mass ratio of 3:7. Figure 3.4a shows the differential transmission spectra for three films: neat **1**, neat PTB7, and a blend of PTB7 and **1**. At a pump wavelength of 670 nm, we excite only PTB7, not **1** (red solid curve). The black dashed curve represents TA spectrum for neat PTB7 at a probe-delay of 0.25 ps. The negative features with maxima at 625 and 680 nm result from the bleaching of ground state absorption as excitons are created in PTB7. TA spectrum for the blended film at the same excitation wavelength shows, in addition to ground state bleaching of

PTB7, new features at 515 and 555 nm that we attribute to ground state bleaching of PDI. The TA spectrum of neat **1** excited at 390 nm (the red-dashed curve in Figure 3.4b is reproduced from Figure 3.3a) verifies this assignment. The appearance of ground state bleaching of **1** when only PTB7 is photoexcited in the blend is evidence of charge (electron) transfer from the photoexcited donor, PTB7, to the electron acceptor, **1**.

Similar results on photo-induced charge transfer are obtained when we preferentially excite **1** in the blend at 390 nm. At this wavelength, most of the incident light is absorbed by **1**, but a small fraction of light is also absorbed by PTB7 (see absorption spectra in Figure 3.2c). As shown in Figure 3.3b, the spectra at a short time (0.25 ps) show ground bleaching for both PTB7 and **1**. At longer times (6 ps) the bleaching signal in the wavelength range from 600 to 720 nm increases indicating more charge (hole) transfer from **1** into PTB7.

In addition to ground state bleaching and excitonic peaks assigned to PTB7 and **1**, we also observe a broad and strong induced absorption feature that is most evident at > 700 nm (Figure 3.4a and 3.4b) where overlap with the GB and ESA are at a minimum. For pumping at 670 nm, the carriers are only generated in the blend, not in neat PTB7 or **1**. At the shorter excitation wavelength of 390 nm, we observe photo carrier generation in both blend and neat PTB7 or **1**, with the amount of photocarrier generation enhanced in the blend films.

With the above assignment of photophysical processes, we now turn to their dynamics. We present the time evolution of the photo-bleaching and the induced absorption features from the blended film in Figure 3.4c and 3.4d for photo-excitation at 670 nm and 390 nm, respectively. When we excite only PTB7 in the blend (at 670 nm), the induced

absorption at 785 nm rises very fast (within the experimental resolution, <150 fs), indicating ultrafast electron transfer from PTB7 to **1**. This time scale is consistent with ultrafast electron transfer in other reported heterojunctions of conjugated polymers with fullerenes.[18] In addition to the ultrafast rise, there is a slower rise that is 23 % of the total induced absorption amplitude with a time constant of 0.4 ps. We attribute this slower rise to exciton diffusion in PTB7 towards interfaces prior to exciton dissociation.[19] The recovery of PTB7 ground state bleaching probed at 690 nm (blue curve in Figure 3.4c) occurs clearly on two very different time scales; bi-exponential fit gives a fast decay channel with a time constant of 0.7 ps accounting for 40% of the total bleaching amplitude and a slower one with a constant of 1 ns accounting for the remaining 60% (see Figure 3.13 in Section 3.5.5.). The fast decay is a loss channel via exciton recombination in PTB7. This fast decay is similar to that of neat PTB7 during the first 3 ps. The remaining 60% of photo-excited PTB7 leads to efficient charge separation at the donor/accepter interface; the charge carriers subsequently undergo bimolecular recombination (on the 1 ns time scale) in the absence of charge extraction. This decay time constant is consistent with the decay dynamics of excited state absorption probed at 785 nm (Figure 3.13) that we attribute to charge carriers. Similar to that of charge induced absorption at 785 nm, the bleaching signal of **1** at 515 nm (green curve in Figure 3.4c), consists of two components resulting from the ultrafast interfacial electron transfer and exciton diffusion. This bleaching signal also recovers on the ~1 ns time scale attributed to bimolecular recombination.

When both **1** and PTB7 are excited in the blend at 390 nm, the PTB7 ground-state bleaching probed at 690 nm (blue curve in Figure 3.4d) consists of two components: the initial fast and the slower rises with the time constants of 0.2 and 1.2 ps, respectively. The

former with 62 % in amplitude is attributed to direct photo-excitation of PTB7 and hole transfer from **1** into PTB7, the latter with 38 % in amplitude to exciton diffusion in **1** towards interfaces prior to the exciton dissociation. At 390 nm excitation, the recovery of the bleaching signal at 690 nm and the decay dynamics of excited state absorption probed at 785 nm are ~1 ns in consistent with charge recombination when pumped at 670 nm (Figure 3.13).

Based on the transient absorption results presented above, we conclude that both electron and hole transfer, from photo-excited donor and acceptor respectively, occur efficiently at the donor-acceptor interfaces in the blended film. Scheme 3.1 summarizes the competition amongst the different channels.

Scheme 3.1. Summary of the exciton generation and charge separation in the blend of **1** and PTB7 at high excitation energy. (*) denotes the exciton, (-) and (+) denote molecules with the positive and negative charge.

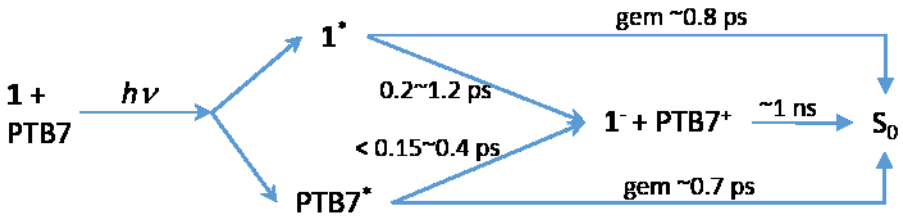

The transient absorption measurements presented above reveal bimolecular recombination of charge carriers in the blend film in the absence of charge extraction. To establish the relative importance of the recombination channels in the solar cell configuration, we measured the J-V characteristics of our devices as a function of incident light intensity from 1 mW/cm^2 to 100 mW/cm^2.[20] Figure 3.14 displays the J-V curves for a typical optimized PTB7:**1** solar cell under different incident light intensities. We extracted

J_{sc} and V_{oc} values from each curve to evaluate the recombination process at short circuit and open circuit, respectively. Figure 3.5a shows the J_{sc} as a function of the light intensity on a Log-Log scale. By fitting the curve to the power law dependence of the J_{sc} on the light intensity expressed as $J_{sc} \propto I^{\alpha}$, we determined the value α to be 0.99 ± 0.01. This near-unity exponent indicates a monomolecular recombination is active.[20b] The bimolecular recombination or space charge effects are very weak at short-circuit conditions.[22] The V_{oc} as a function of the light intensity on a semi-logarithmic scale is shown in Figure 3.5b. We fitted the experimental data to give the slope of the V_{oc} versus the natural logarithm of the light intensity. From 100 mW/cm^2 (1 sun) to 1 mW/cm^2 (0.01 sun), the slope is calculated to be 1.17±0.02 kT/q, suggesting that recombination is a combination of monomolecular and bimolecular processes.[20b] The same experiment carried on the PBDTT-TT:**1** solar cell gives similar results (Figure 3.15). The extracted slopes for log(J_{sc}) vs. log(I) and V_{oc} vs. log(I) are 0.96 ± 0.01 and 1.20 ± 0.03 kT/q, respectively (Figure 3.16). We note that these experimental results are very similar to those of classical P3HT:PCBM solar cells,[20b] indicating that the same level of recombination loss may account for the high performance of our solar cells. More recently, Zang et el. reported a highly efficient non-fullerene solar cell,[4g] but the specific types of monomolecular recombination that occur in these cells are unknown. Sharenko and coworkers have proposed trap-dominant device performance in a PDI monomer based solar cell.[4b] However, geminate recombination may also contribute to charge carrier loss as proposed in the PTB7:fullerene solar cell[22] and the PDI-based solar cells.[4b]

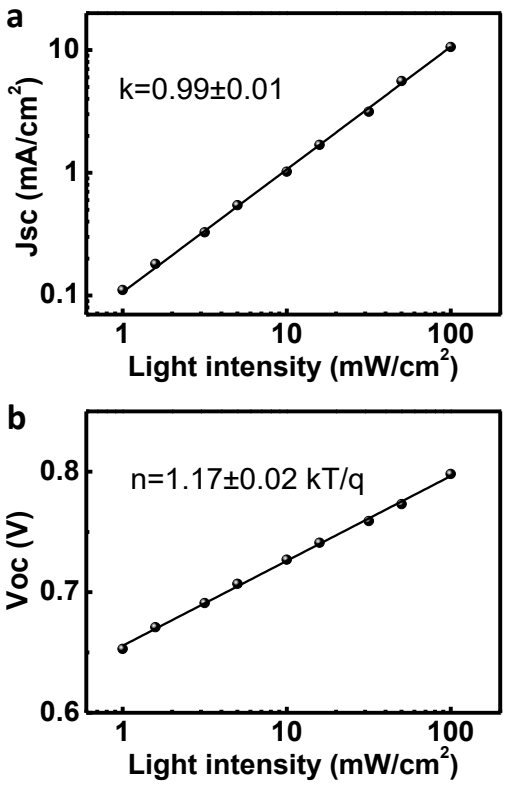

Figure 3.5. (a) J_{sc} as a function of light intensity in a double-logarithmic scale from an optimized PTB7:**1** device. (b) V_{oc} as a function of light intensity in a semi-logarithmic scale from an optimized PTB7:**1** device.

3.3 Conclusion

We discuss here a solution processed organic solar cell based on the combination of the helical electron-accepting PDI, **1**, and the commercially available, electron-donating PTB7 and PBDTT-TT. These solar cells show a photon conversion efficiency that is amongst the highest reported for non-fullerene based solar cells.[3-5] We demonstrate exciton generation in both donor and acceptor materials. Transient absorption spectroscopy reveals an ultra-fast electron transfer from PTB7 to **1** and a hole transfer from **1** to PTB7 with a time constant of ~0.2 ps. Incident light intensity dependent measurement suggests different recombination mechanisms at open-circuit and short-circuit conditions. By fine-tuning the molecular structure of the PDI-dimer, we will be able to further improve these materials

performance in solar cells.

3.4 Experimental Section

3.4.1. Device fabrication

Helical PDI **1** was synthesized according to a previously reported method.[7] PTB7 and PBDTT-TT was purchased from 1-material. The synthesis of ZnO precursor was described elsewhere.[23] Prepatterned ITO-coated glass with a sheet resistance of ~15Ω/sq was cleaned with detergent, ultrasonicated in DI water, acetone and isopropanol for 30 min, respectively. Subsequently, we treated the substrates by UV-Ozone for 10 min. The prepared ZnO precursor was spin-cast onto the ITO substrate at 3000 rpm for 1 min, followed by annealing at 200 ºC for 1 h in air, to form a thin film with approximate thickness of 20 nm. The BHJ active layer was prepared by spin-coating a mixed solution containing polymer and **1** in chlorobenzene at a total concentration of 25 mg/ml at 1000 rpm for 2 min. The thickness of the prepared active layers is about 90 nm for PTB7:**1** and 130 nm for PBDTT-TT:**1**, respectively. Active layers were heated at 80 ºC for 10 min in the nitrogen filled glove box to remove the residual solvent. Finally, a 5 nm MoO_x layer was deposited first and then a 100 nm Al electrode were subsequently deposited through a shadow mask by thermal evaporation under a vacuum about 1×10^{-6} torr. The active area of the device was 9 mm^2.

3.4.2. Characterization

Absorption spectra were obtained on Shimadzu UV 1800 UV-Vis. The current-density–voltage (J–V) curves were measured by a Keithley 2635A source measure unit. The photocurrent was measured under AM 1.5G illumination at 100 mW/cm^2 under a Newport solar Simulator (Model # 66485). A KG5-Si reference cell traceable to Newport

was used to calibrate light intensity. External quantum efficiency measurements were performed using a 300 W Xenon arc lamp (Newport Oriel) with filtered monochromatic light from a Conerstone 260 1/4 M double grating monochromator (Newport 74125). A silicon photodiode calibrated at Newport was utilized as the reference cell. Atomic force microscopy (AFM) was performed by a PSIA XE100.

3.5 Supplementary materials

3.5.1. Absorption spectrum

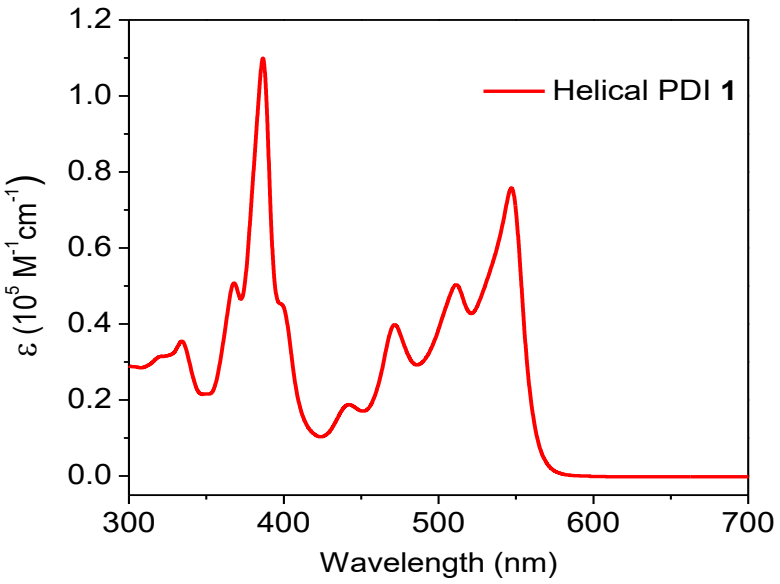

Figure 3.6. (a) UV-vis absorption spectrum of helical PDI **1**. (1 x 10^{-5} M concentration in dichloromethane with a path length l = 1 cm)

3.5.2. Device performance

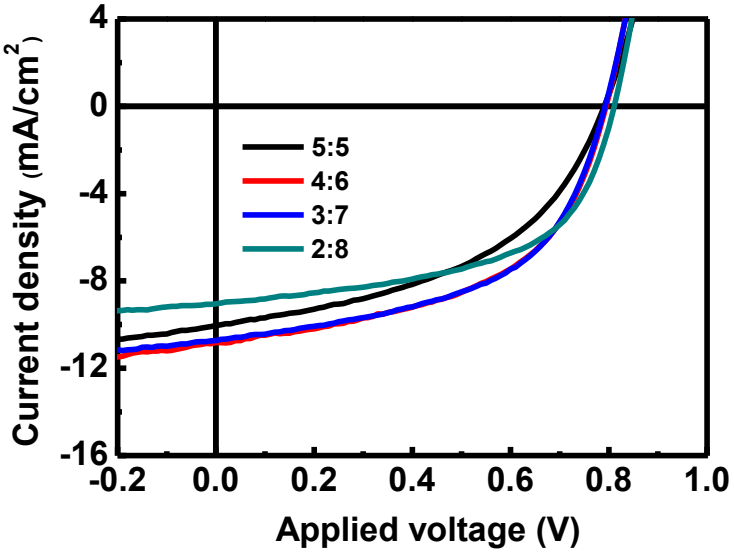

Figure 3.7. Current density versus voltage (J–V) characteristics of PTB7:**1** solar cells with different blend ratios (PTB7 to **1**). The active layers were spun cast from chlorobenzene solutions with a total concentration of 25 mg/ml.

Table 3.2. Summary of device parameters of PTB7:**1** solar cells with different blend ratios.

PTB7 : 1 mass ratio	J_{sc} (mA/cm^2)	V_{oc} (V)	FF (%)	PCE (%)[a]
5:5	10.0 ± 0.2	0.789 ± 0.003	46.7 ± 0.7	3.66 ± 0.05 (3.72)
4:6	10.8 ± 0.2	0.796 ± 0.006	51.5 ± 0.5	4.44 ± 0.04 (4.47)
3:7	10.5 ± 0.2	0.796 ± 0.006	53.6 ± 0.5	4.47 ± 0.03 (4.50)
2:8	9.1 ± 0.1	0.810 ± 0.005	55 ± 1	4.0 ± 0.1 (4.1)

[a]The average PCE value was calculated from six devices for each ratio; highest PCE values in parentheses.

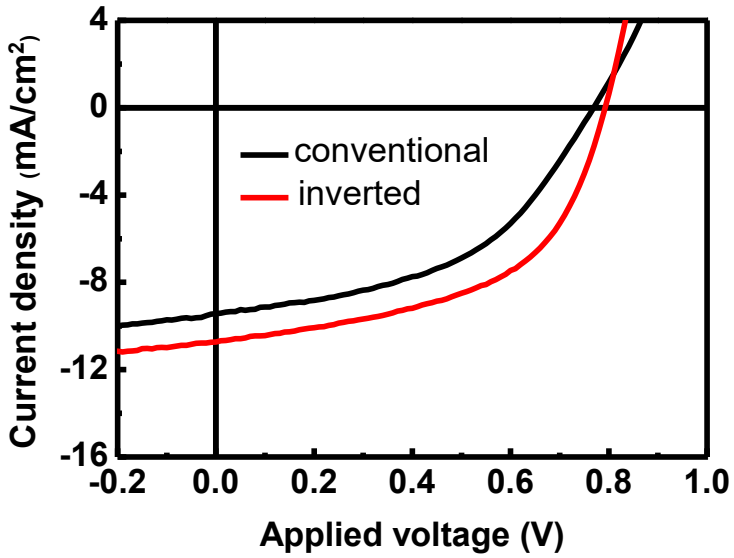

Figure 3.8. Current density versus voltage (J–V) characteristics of PTB7:**1** solar cells in a conventional structure (black) and an inverted structure (red) at a D/A mass ratio of 3:7.

Table 3.3. Device parameters of PTB7:**1** solar cells with conventional and inverted structure.

	J_{sc} (mA/cm^2)	V_{oc} (V)	FF (%)	PCE(%)[a]
conventional	9.5±0.2	0.759±0.007	46±1	3.3±0.2 (3.5)
Inverted	10.5±0.2	0.796±0.006	53.6±0.5	4.47±0.03 (4.50)

[a] The average PCE value was calculated from six devices for each ratio; highest PCE values in parentheses.

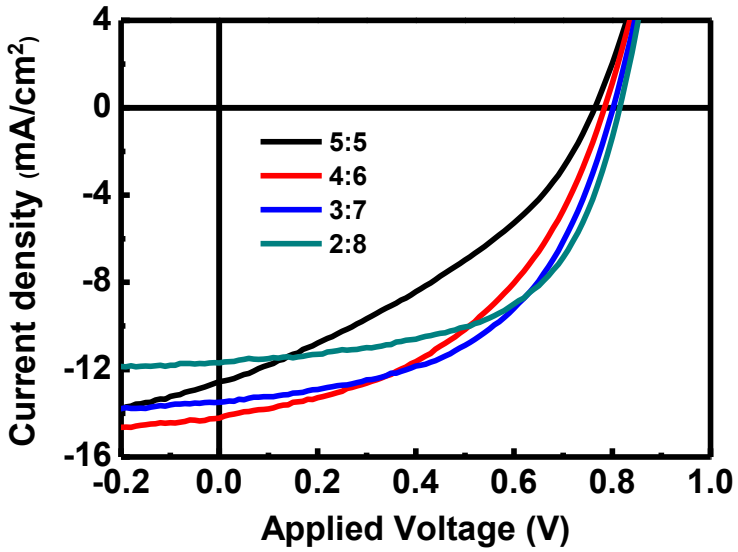

Figure 3.9. Current density versus voltage (J–V) characteristics of PBDTT-TT:**1** solar cells with different blend ratios (PBDTT-TT to **1**). The active layers were spun cast from chlorobenzene solutions with a total concentration of 25 mg/ml.

Table 3.4. Summary of device parameters of PBDTT-TT:**1** solar cells with different blend ratios.

PBDTT-TT : 1 mass ratio	Jsc(mA/cm²)	Voc(V)	FF(%)	PCE(%) [a]
5:5	12.4±0.3	0.770±0.007	36.2±0.4	3.45±0.06 (3.50)
4:6	14.0±0.2	0.782±0.005	44.6±0.8	4.89±0.11 (5.10)
3:7	13.6±0.1	0.795±0.004	51.1±0.6	5.52±0.05 (5.59)
2:8	11.8±0.1	0.808±0.004	56.0±0.7	5.36±0.04 (5.40)

[a] The average PCE value was calculated from six devices for each condition; highest PCE values in parentheses.

3.5.3. AFM height images of spin-cast films

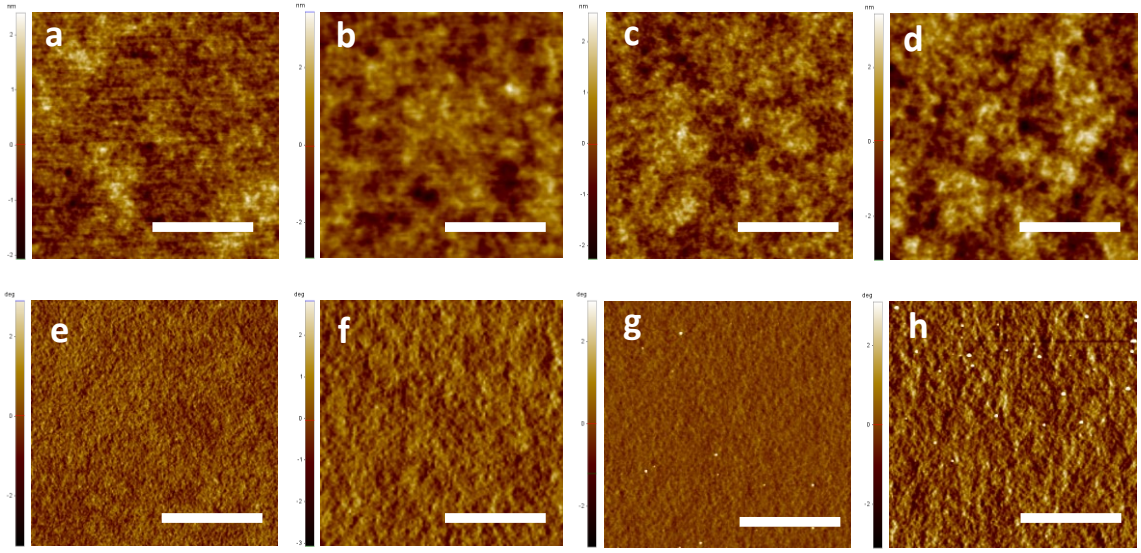

Figure 3.10. AFM height (a-d) and phase (e-h) images of PTB7: **1** blend films at a mass ratio of 3:7 processed from chlorobenzene solutions without DIO (a and e), and with 1 v/v% DIO (b and f), 1 v/v% CN (c and g) and 1 v/v% DIO + 1v/v% CN (d and h). All the films were annealed at 80 ºC for 10 min in the nitrogen-filled glove box. The scale bar is 1 μm.

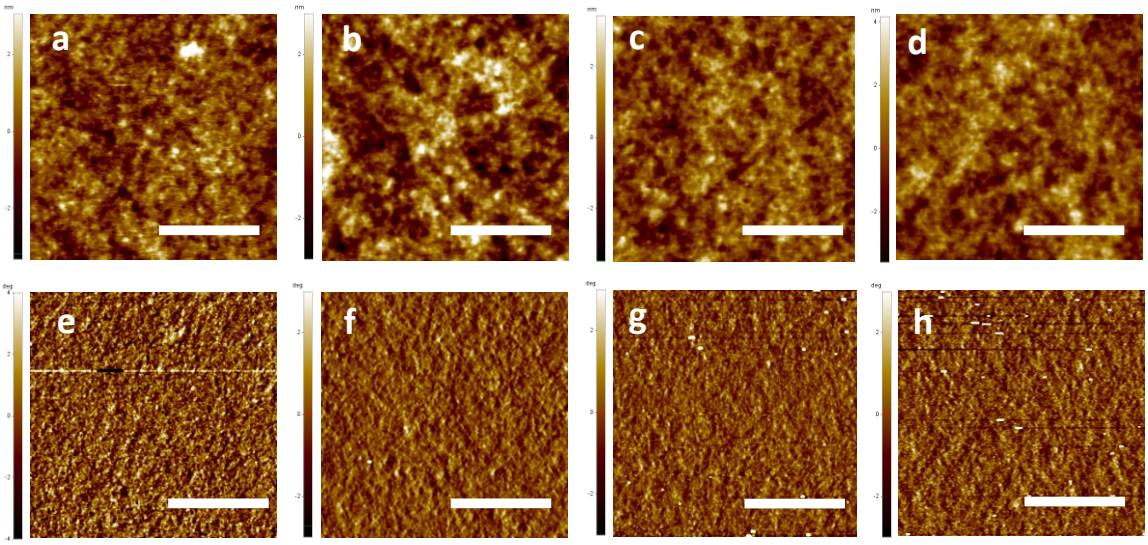

Figure 3.11. AFM height (a-d) and phase (e-h) images of PBDTT-TT: **1** blend films at a mass ratio of 3:7 processed from chlorobenzene solutions without DIO (a and e), and with 1 v/v% DIO (b and f), 1 v/v% CN (c and g) and 1 v/v% DIO + 1v/v% CN (d and h). All the films were annealed at 80 ^{o}C for 10 min in the nitrogen-filled glove box. The scale bar is 1 μm.

3.5.4. Carrier mobilities

Carrier mobility was measured by space charge limit current (SCLC) method. Hole-only devices were fabricated with a device configuration of ITO/PEDOT:PSS/PTB7(PBDTT-TT):**1**/MoO_x/Al. Electron-only devices were fabricated with a device configuration of ITO/ZnO/PTB7(PBDTT-TT):**1**/Al. The mobility was determined by fitting the dark current to the model of a single carrier SCLC, described by the equation:

$$J = \frac{9}{8}\varepsilon_0\varepsilon_r\mu\frac{V^2}{d^3}$$

where J is the current density, μ is the carrier mobility under zero field, ε_0 is the permittivity of free space, ε_r is the material relative permittivity (assumed to be 3 here), d is the active layer thickness (85 nm for PTB7:**1** and 130nm for PBDTT-TT:**1**), and V is the effective voltage. The effective voltage can be obtained by subtracting the built-in voltage (V_{bi}) from the applied voltage (V_{ap}),[3] $V=V_{ap} - V_{bi}$. V_{bi} is 0 V for hole-only devices and 0.23 V for electron-only devices. The carrier mobility can be calculated from the slope of the $J^{1/2} \sim V$ curves.

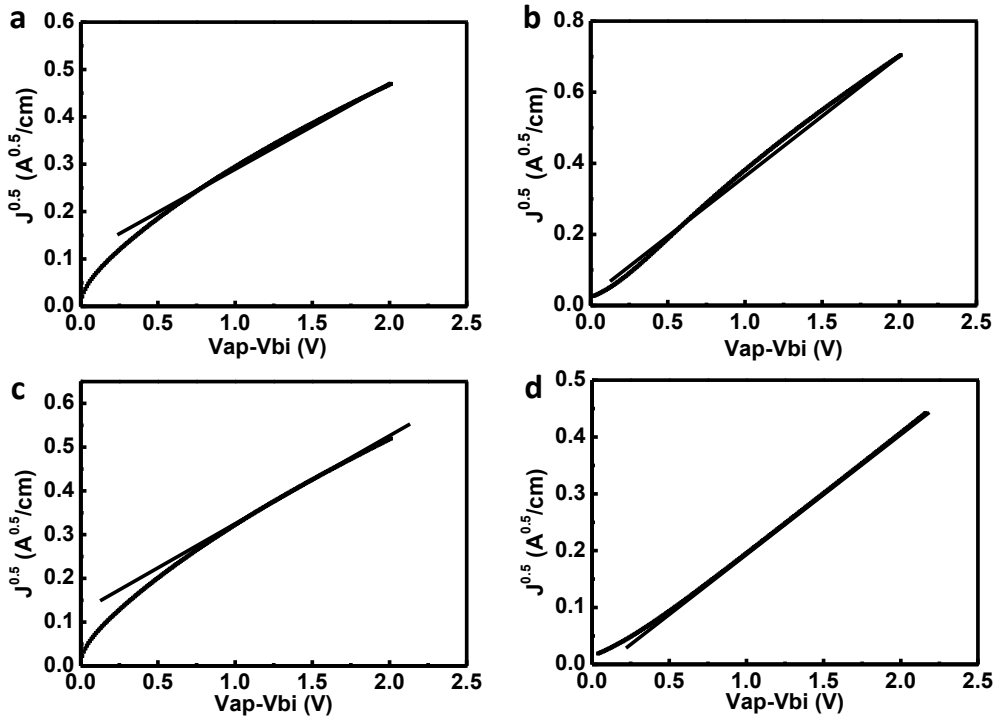

Figure 3.12. $J^{1/2}$ vs V plots for (a) a hole-only device, (b) an electron-only device from PTB7:**1** blend and (c) a hole-only device, (d) an electron-only device from PBDTT-TT:**1** blend.

3.5.5. Femtosecond transient absorption

To investigate charge transfer in the solar cells, we employed the transient absorption spectroscopy. The pump laser light (~100 fs pulse width) comes from an optical parametric amplifier pumped by a Ti:sapphire femtosecond regenerative amplifier (800 nm, 1 kHz rep-rate). The probe light is a white-light supercontinuum (450-900 nm, ~100 fs pulse width). The pump and probe beams overlapped under a small angle. The detection consists of a pair of high-resolution multichannel detector arrays coupled to a high-speed data acquisition system.

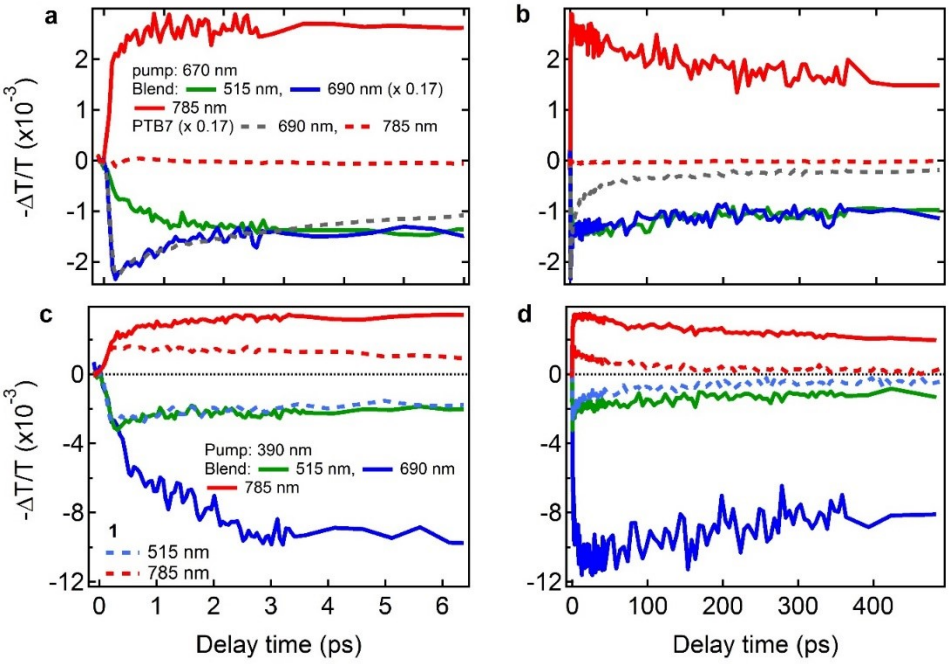

Figure 3.13. Dynamic traces at different probe wavelengths for neat PTB7, neat **1** and a blend of **1** and PTB7 (solid-curves) films pumping at 670 nm (a, b) and 390 nm (c, d). The short and the long time windows are shown in the left and the right panels, respectively.

Figure 3.13 presents the dynamic traces of three different samples pumping at 670 nm and 390 nm. At the pump wavelength of 670 nm (Figure 3.13 a & b) we preferentially excite PTB7 in the blended film. The bleaching dynamics of PTB7 in the blended film at 690 nm probe is similar to that of the neat PTB7 at first 2 ps (Figure 3.13a). After 2 ps the dynamics for the blended film decays much slower and is similar to that of **1** bleaching at 515 nm probe (Figure 3.13b) with a time constant is given in the Table 3.5. The similar decay dynamics for the bleaching features of PTB7 and **1** in the blended film indicates that after 2 ps the dominant decay channel in the blended film is charge recombination via interfaces between the donor and acceptor. We obtained the similar results when pumping at 390 nm in which most of the photo excitation takes place in **1**.

Table 3.5. The decay time constants at different pump and probe wavelengths for the blended film at a long time window. The results were obtained by single exponential fits in the range of 10 to 500 ps time window.

	Probe at 515 nm	Probe at 690 nm	Probe at 785 nm
Pump at 390 nm	0.7 ± 0.07 ns	1.1 ± 0.1 ns	0.95 ± 0.04 ns
Pump at 670 nm	0.98 ± 0.06 ns	1.2 ± 0.05 ns	0.9 ± 0.1 ns

3.5.6. Incident light intensity dependence of photocurrent

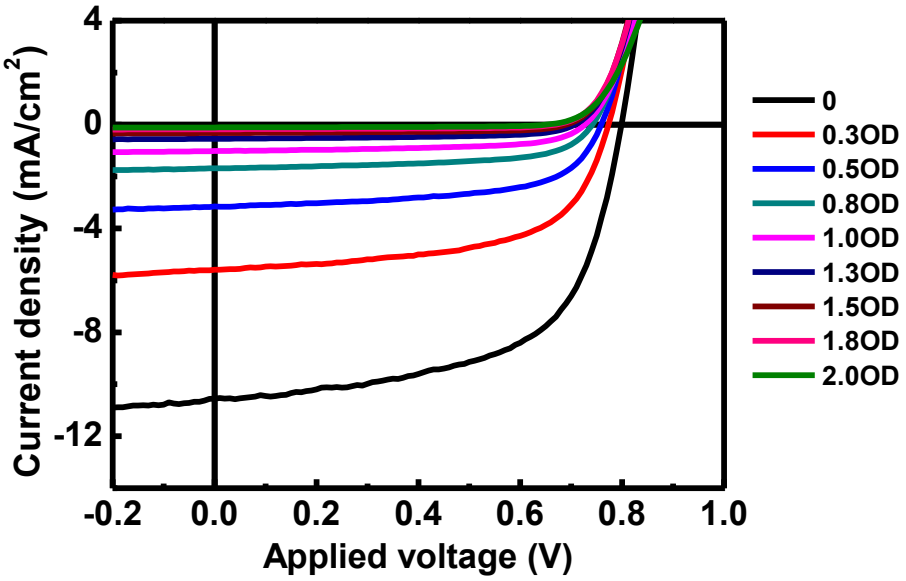

Figure 3.14. Current density versus voltage (J–V) characteristics for a PTB7:**1** solar cell under AM 1.5 G illumination with a set of neutral density filters.

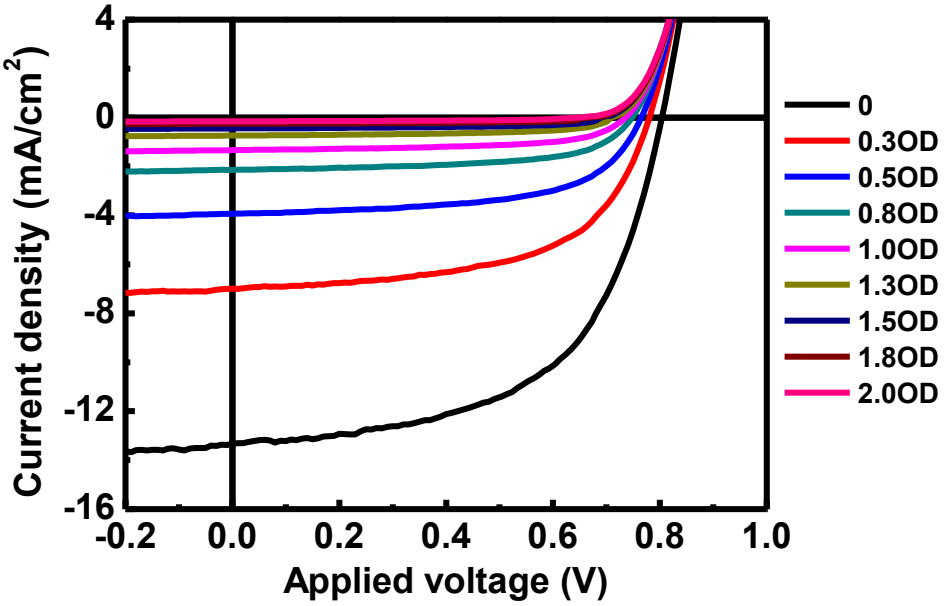

Figure 3.15. Current density versus voltage (J–V) characteristics for a PBDTT-TT:**1** solar cell under AM 1.5 G illumination with a set of neutral density filters.

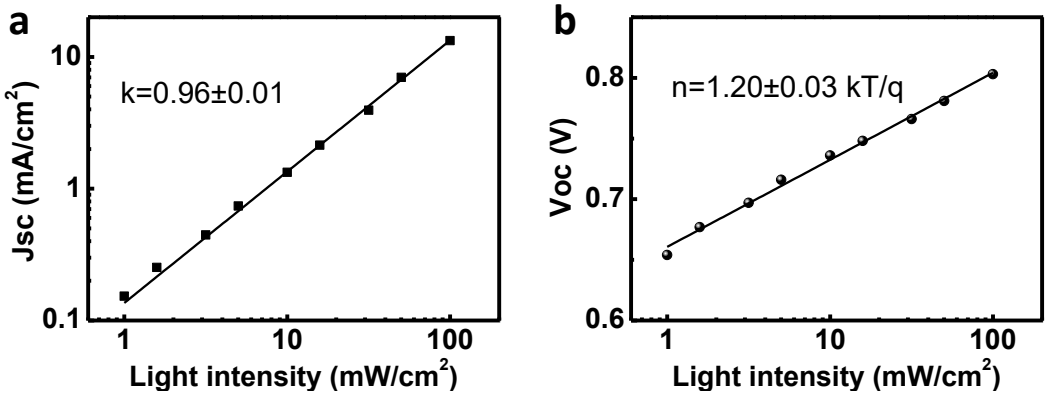

Figure 3.16. (a) J_{sc} as a function of light intensity in a double-logarithmic scale from an optimized PBDTT-TT:**1** device. (b) V_{oc} as a function of light intensity in a semi-logarithmic scale from an optimized PBDTT-TT:**1** device.

3.6 References and Notes

1. (a) Dou, L.; You, J.; Hong, Z.; Xu, Z.; Li, G.; Street, R. A.; Yang, Y. *Adv. Mater.* **2013**, *25* , 6642-6671; (b) Thompson, B. C.; Fréchet, J. M. J. *Angew. Chem. Int. Ed.* **2008**,

47, 58-77.

2. (a) Lenes, M.; Shelton, S. W.; Sieval, A. B.; Kronholm, D. F.; Hummelen, J. C.; Blom, P. W. M. *Adv. Funct. Mater.* **2009**, *19*, 3002-3007; (b) Ross, R. B.; Cardona, C. M.; Guldi, D. M.; Sankaranarayanan, S. G.; Reese, M. O.; Kopidakis, N.; Peet, J.; Walker, B.; Bazan, G. C.; Van Keuren, E.; Holloway, B. C.; Drees, M. *Nat. Mater.* **2009**, *8*, 208-212; (c) He, Y.; Chen, H.-Y.; Hou, J.; Li, Y. *J. Am. Chem. Soc.* **2010**, *132*, 1377-1382. (d)Anctil, A.; Babbitt, C. W.; Raffaelle, R. P.; Landi, B. J. *Environ. Sci. Technol.* **2011**, *45*, 2353–2359.

3. Examples of non-fullerene bulk-junction solar cells: (a) Woo, C. H.; Holcombe, T. W.; Unruh, D. A.; Sellinger, A.; Fréchet, J. M. J. *Chem. of Mater.* **2010,** *22*, 1673-1679; (b) Zhou, Y.; Dai, Y.-Z.; Zheng, Y.-Q.; Wang, X.-Y.; Wang, J.-Y.; Pei, J. *Chem. Commun.* **2013,** *49* , 5802-5804; (c) Winzenberg, K. N.; Kemppinen, P.; Scholes, F. H.; Collis, G. E.; Shu, Y.; Birendra Singh, T.; Bilic, A.; Forsyth, C. M.; Watkins, S. E. *Chem. Commun.* **2013,** *49*, 6307-6309; (d) Ren, G.; Ahmed, E.; Jenekhe, S. A. *J. Mater. Chem.* **2012,** *22*, 24373-24379; Li, H.; Kim, F. S.; Ren, G.; Hollenbeck, E. C.; Subramaniyan, S.; Jenekhe, S. A. *Angew. Chem. Int. Ed.* **2013,** *52*, 5513-5517; (e) Boudreault, P.-L. T.; Michaud, A.; Leclerc, M. *Macromol. Rapid Comm.* **2007,** *28*, 2176-2179; (f) Douglas, J. D.; Chen, M. S.; Niskala, J. R.; Lee, O. P.; Yiu, A. T.; Young, E. P.; Fréchet, J. M. J. *Adv. Mater.* **2014**, *26*, 4313-4319; (g) Eftaiha, A. F.; Sun, J.-P.; Hill, I. G.; Welch, G. C. *J. Mater. Chem. A* **2014**, *2*, 1201-1213.

4. Examples of non-fullerene solar cells based on PDIs: (a) Lin, Y.; Wang, Y.; Wang, J.; Hou, J.; Li, Y.; Zhu, D.; Zhan, X. *Adv. Mater.* **2014**, *26*, 5137-5142. (b) Sharenko, A.; Proctor, C. M.; van der Poll, T. S.; Henson, Z. B.; Nguyen, T.-Q.; Bazan, G. C. *Adv. Mater.* **2013**, *25*, 4403-4406; (c) Zhang, X.; Lu, Z.; Ye, L.; Zhan, C.; Hou, J.; Zhang, S.; Jiang, B.; Zhao, Y.; Huang, J.; Zhang, S.; Liu, Y.; Shi, Q.; Liu, Y.; Yao, J. *Adv. mater.* **2013**, *25*, 5791–5797; (d) Jiang, W.; Ye, L.; Li, X.; Xiao, C.; Tan, F.; Zhao, W.; Hou, J.; Wang, Z. *Chem. Commun.* **2014**, *50*, 1024-1026; (e) Lu, Z.; Jiang, B.; Zhang, X.; Tang, A.; Chen, L.; Zhan, C.; Yao, J. *Chem. Mater.* **2014**, *26*, 2907-2914; (f) Zhou, Y.; Kurosawa, T.; Ma, W.; Guo, Y.; Fang, L.; Vandewal, K.; Diao, Y.; Wang, C.; Yan, Q.; Reinspach, J.; Mei, J.; Appleton, A. L.; Koleilat, G. I.; Gao, Y.; Mannsfeld, S. C. B.; Salleo, A.; Ade, H.; Zhao, D.; Bao, Z. *Adv. Mater.* **2014,** *26*, 3767-3772. (g) Zang, Y.; Li, C.-Z.; Chueh, C.-C.; Williams, S. T.; Jiang, W.; Wang, Z.-H.; Yu, J.-S.; Jen, A. K. Y. *Adv. Mater.* **2014**, *26*, 5708-5714.

5. Higher PCE has been achieved in the fullenrene-free organic solar cell with a multilayer structure, see: Cnops, K.; Rand, B. P.; Cheyns, D.; Verreet, B.; Empl, M. A.; Heremans, P. *Nat. Commun.* **2014**, *5*, 3406.

6. Li, Y.; Wang, C.; Li, C.; Di Motta, S.; Negri, F.; Wang, Z. *Org. Lett.* **2012**, *14*, 5278-5281.

7. Zhong, Y.; Kumar, B.; Oh, S.; Trinh, M. T.; Wu, Y.; Elbert, K.; Li, P.; Zhu, X.; Xiao, S.; Ng, F.; Steigerwald, M. L.; Nuckolls, C. *J. Am. Chem. Soc.* **2014**, *136*, 8122–8130.

8. Strong aggregation is a problem for PDIs in organic BHJs, see: (a) Sharma, G. D.; Suresh, P.; Mikroyannidis, J. A.; Stylianakis, M. M. *J. Mater. Chem.* **2010**, *20*, 561-567; (b)

Kamm, V.; Battagliarin, G.; Howard, I. A.; Pisula, W.; Mavrinskiy, A.; Li, C.; Müllen, K.; Laquai, F. *Adv. Energy Mater.* **2011**, *1*, 297-302.

9. C7-helical PDI has very poor solubility in chroloform and chlorobenzene and cannot form smooth films by spin-coating process.

10. (a) Liang, Y.; Xu, Z.; Xia, J.; Tsai, S.-T.; Wu, Y.; Li, G.; Ray, C.; Yu, L. *Adv. Mater.* **2010**, *22*, E135-E138; (b) He, Z. C.; Zhong, C. M.; Su, S. J.; Xu, M.; Wu, H. B.; Cao, Y. *Nat. Photonics.* **2012**, *6*, 591-595.

11. (a) Cui, C.; Wong, W.-Y.; Li, Y. *Energy Environ. Sci.* **2014,** *7*, 2276-2284; (b) Liao, S.-H.; Jhuo, H.-J.; Cheng, Y.-S.; Chen, S.-A. *Adv. Mater.* **2013,** *25*, 4766-4771.

12. (a) Lee, J. K.; Ma, W. L.; Brabec, C. J.; Yuen, J.; Moon, J. S.; Kim, J. Y.; Lee, K.; Bazan, G. C.; Heeger, A. J. *J Am. Chem. Soc.* **2008,** *130*, 3619-3623; (b) Graham, K. R.; Wieruszewski, P. M.; Stalder, R.; Hartel, M. J.; Mei, J.; So, F.; Reynolds, J. R. *Adv. Funct. Mater.* **2012,** *22*, 4801-4813; (c) Guo, X.; Cui, C.; Zhang, M.; Huo, L.; Huang, Y.; Hou, J.; Li, Y. *Energy Environ. Sci.* **2012,** *5*, 7943-7949.

13. Malliaras, G. G.; Salem, J. R.; Brock, P. J.; Scott, C. *Phys. Rev. B* **1998**, *58*, R13411-R13414.

14. Lee, B. R.; Jung, E. D.; Nam, Y. S.; Jung, M.; Park, J. S.; Lee, S.; Choi, H.; Ko, S.-J.; Shin, N. R.; Kim, Y.-K.; Kim, S. O.; Kim, J. Y.; Shin, H.-J.; Cho, S.; Song, M. H. *Adv. Mater.* **2014,** *26*, 494-500.

15. (a) Giaimo, J. M.; Lockard, J. V.; Sinks, L. E.; Scott, A. M.; Wilson, T. M.; Wasielewski, M. R. *J Phys. Chem. A* **2008,** *112*, 2322-2330; (b) Ramanan, C.; Smeigh, A. L.; Anthony, J. E.; Marks, T. J.; Wasielewski, M. R. *J Am. Chem. Soc.* **2011,** *134*, 386-397; (c) Eaton, S. W.; Shoer, L. E.; Karlen, S. D.; Dyar, S. M.; Margulies, E. A.; Veldkamp, B. S.; Ramanan, C.; Hartzler, D. A.; Savikhin, S.; Marks, T. J.; Wasielewski, M. R. *J Am. Chem. Soc.* **2013**. *135*, 14701–14712.

16. (a) Piris, J.; Dykstra, T. E.; Bakulin, A. A.; Loosdrecht, P. H. M. v.; Knulst, W.; Trinh, M. T.; Schins, J. M.; Siebbeles, L. D. A. *J Phys. Chem. C* **2009,** *113*, 14500-14506; (b) Howard, I. A.; Laquai, F.; Keivanidis, P. E.; Friend, R. H.; Greenham, N. C. *J Phys. Chem. C* **2009,** *113*, 21225-21232; (c) Holman, M. W.; Yan, P.; Adams, D. M.; Westenhoff, S.; Silva, C. *J Phys. Chem. A* **2005,** *109*, 8548-8552.

17. Ford, W. E.; Kamat, P. V. *J Phys. Chem.* **1987,** *91*, 6373-6380.

18. (a) Hwang, I.; Beaupre, S.; Leclerc, M.; Scholes, G. D.*Chem. Sci.* **2012**, *3*, 2270-2277; (b) Hwang, I. W.; Soci, C.; Moses, D.; Zhu, Z.; Waller, D.; Gaudiana, R.; Brabec, C. J.; Heeger, A. J.. *Adv. Mater.* **2007**, *19*, 2307-2312; (c) Grancini, G.; Maiuri, M.; Fazzi, D.; Petrozza, A.; Egelhaaf, H-J.; Brida, D.; Gerullo, G.; Lanzani, G.; *Nat. Mater.* **2013**, *12*, 29-33; (d) Gélinas, S.; Rao, A.; Kumar, A.; Smith, S. L.; Chin, A. W.; Clark, J.; van der Poll, T. S.; Bazan, G. C.; Friend, R. H.; *Science*. **2014**, *343*, 512-516.

19. Kaake, L. G.; Jasieniak, J. J.; Bakus, R. C.; Welch, G. C.; Moses, D.; Bazan, G. C.; Heeger, A. J. *J. Am. Chem. Soc.* **2012**, *134*, 19828-19838.

20. (a) Koster, L. J. A.; Mihailetchi, V. D.; Ramaker, R.; Blom, P. W. M.*Appl. Phys. Lett.* **2005**, *86*, 123509; (b) Cowan, S. R.; Roy, A.; Heeger, A. J. *Phys. Rev. B* **2010**, *82*, 245207.

21. Koster, L. J. A.; Mihailetchi, V. D.; Xie, H.; Blom, P. W. M. *Appl. Phys. Lett.***2005**, *87*, 203502.

22. Foertig, A.; Kniepert, J.; Gluecker, M.; Brenner, T.; Dyakonov, V.; Neher, D.; Deibel, C. *Adv. Funct. Mater.* **2014**, *24*, 1306-1311.

23. Jo, J.; Pouliot, J.-R.; Wynands, D.; Collins, S. D.; Kim, J. Y.; Nguyen, T. L.; Woo, H. Y.; Sun, Y.; Leclerc, M.; Heeger, A. J. *Adv. Mater.* **2013,** *25*, 4783-4788.

Chapter 4 Molecular Helices as Electron Acceptors in High-Performance Organic Solar Cells

Chapter 4 is reproduced with permission from the authors: Zhong, Y.; Trinh, M. T.; Chen, R.; Purdum, G. E.; Khlyabich, P. P.; Sezen, M.; Oh, S.; Zhu, H.; Fowler, B.; Zhang, B.; Wang, W.; Nam, C.-Y.; Sfeir, M. Y.; Black, C. T.; Steigerwald, M. L.; Loo, Y.-L.; Ng, F.; Zhu, X.-Y.; Nuckolls, C. *Nat. Commun.* **2015**, *6*, 8242; Copyright 2015 Macmillan Publishers Limited. Device fabrication, characterization, AFM experiments and data analysis were performed by myself with assistance from Rongsheng Chen, Boyuan Zhang, Wei Wang and Chang-Yong Nam. Transient absorption measurements were conducted by M. Tuan Trinh. GIXD measurements were performed by Geoffrey E. Purdum, Petr P. Khlyabich and Melda Sezen. Synthesis was carried out by Fay Ng with assistance from Brandon Fowler and Seokjoon Oh. Ultrafast fluorescence upconversion experiments were performed by Haiming Zhu. DFT calculations were performed by Michael L. Steigerwald.

4.1 Introduction

In the past decade, the record power conversion efficiency (PCE) of organic bulk heterojunction (BHJ) solar cells has reached over 10 % for single junction cells[1,2] and more than 12 % for tandem cells,[3] mainly by synthesizing and incorporating new electron donors,[4,5] optimizing film morphology,[1,6] developing interfacial layers[7-9] and designing new device structures.[10-12] One lagging area is the development of new electron acceptors for organic solar cells. To date, highly efficient BHJ solar cells almost exclusively utilize fullerene derivatives, such as [6,6]-phenyl-$C_{61/71}$-butyric acid methyl ester ($PC_{61}BM$ and $PC_{71}BM$), as electron acceptors.[13] Theoretical analysis suggests that the superiority of

fullerene over non-fullerene electron acceptors is in the charge separation.[14] Recently, several studies, including our own, have reported solution-processed BHJ devices using non-fullerene acceptors that have achieved PCEs of 6 % - 7 %.[15-19] Continued progress will require the design, synthesis, and testing of new motifs for electron acceptors.

We herein use two helical n-type molecules that differ in their lengths as highly efficient electron acceptors. These fullerene-free BHJ solar cells achieve PCEs of 8.3 %, with high short circuit current density (15.2 $mAcm^{-2}$) and fill factors as large as 68 %. The film morphology of the mixed donor/acceptor active layer is a mesh-like network of acceptors with pores that are tens of nanometers in diameter. Transient absorption spectroscopy (TAS) reveals that excitons generated in both the donor and acceptor phases contribute to the photocurrent by effective hole and electron transfer at the interface between donor and acceptor.

4.2 Molecule design and characterization.

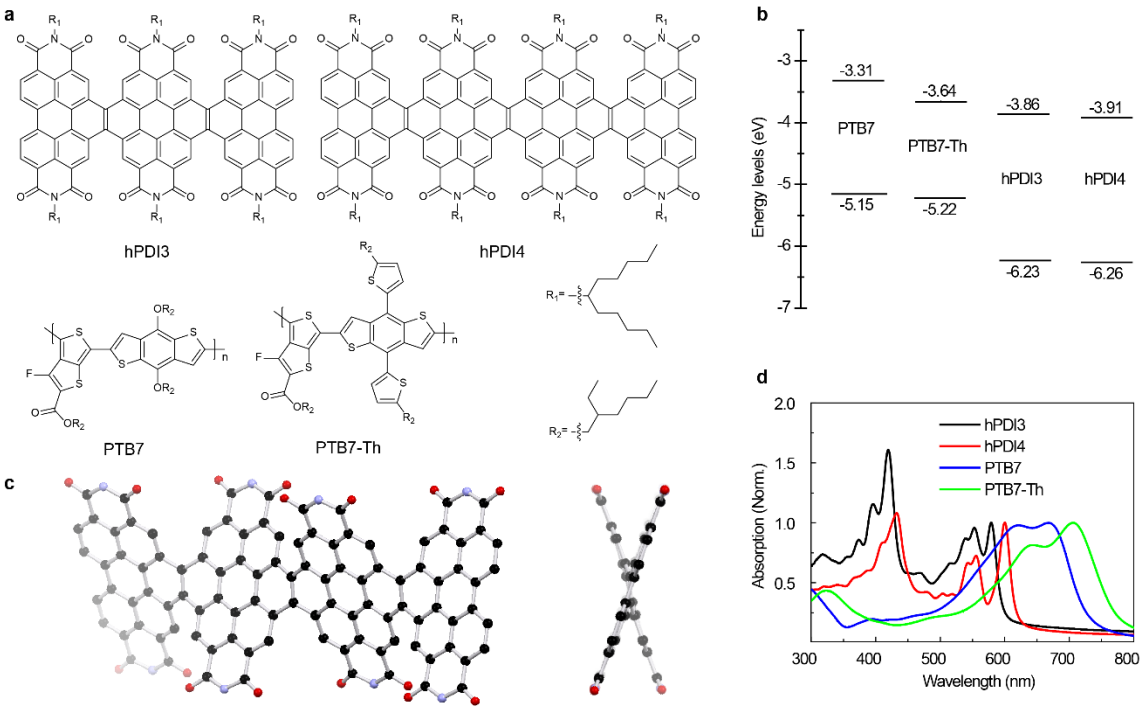

Figure 4.1. Molecular structures of helical perylene diimide oligomers and polymers. **a**, Chemical structures of hPDI3, hPDI4, PTB7 and PTB7-Th. **b.** Schematic of the energy levels of hPDI3, hPDI4, PTB7 and PTB7-Th. Energy levels of PTB7 and PTB7-Th were adopted from ref. 7 and ref. 5, respectively. Energy levels of hPDI3 and hPDI4 were adopted from ref. 21. **c**, Molecular model of hPDI4 in a waggling conformation from DFT calculations. Hydrogens and alkyl side chains have been removed for clarity. Black = carbon; red = oxygen; blue = nitrogen. **d**, Film absorption spectra of hPDI3, hPDI4, PTB7 and PTB7-Th normalized at their low-energy λ_{max}.

The two helices have different lengths and are constructed by fusing either three or four perylene diimide (PDI) units together with a two-carbon bridge (hPDI3 and hPDI4 in Figure 4.1a).[20] Recently, we found that a shorter version of helical molecules was useful in BHJ solar cells.[16] Like the shorter one, the longer acceptors explored here also have relatively high electron mobilities (0.04-0.05 $cm^2V^{-1}s^{-1}$ in thin film transistors), good electron-accepting ability, and LUMO levels (~-3.9 eV) that are appropriately matched to those of commercially available electron donating polymers (Figure 4.1b).[20] Like prior non-fullerene electron acceptors that have been moderately successful in solar cells,[15,21,22] these molecules possess nonplanar molecular structures due to the steric congestion in the cove areas defined by the junction point between the PDIs. There are several iso-energetic conformations within these oligomers because of the inversion of the helicity at each of these junctions (Figure 4.1c, Figure 4.5 and Supplementary Note 1 in Section 4.8). Because of the nonplanar structure and the associated conformational dynamics, these molecules do not aggregate strongly in thin films.[23] Both of the molecules absorb light strongly in the wavelength range from 350 to 600 nm (Figure 4.1d) with a maximum molar extinction

coefficient of 1.5×10^5 M^{-1} cm^{-1} for hPDI3 and 1.8×10^5 M^{-1} cm^{-1} for hPDI4 (see Figure 4.6a.). The strong light absorption, the lack of aggregation, and the propensity of the isolated linear structure to form networks,[24] indicate that these two molecules have the potential to outperform PDI monomers and dimers in BHJ solar cells.

4.3 Solar cell characterization.

Our device demonstrations using the compounds hPDI3 and hPDI4 as electron acceptors are based on the commercially available low bandgap semiconducting polymer donors polythieno[3,4-b]-thiophene-co-benzodithiophene (PTB7)[4] and poly[4,8-bis(5-(2-ethylhexyl)thiophen-2-yl)benzo[1,2-b;4,5-b′]dithiophene-2,6-diyl-alt-(4-(2-ethylhexyl)-3-fluorothieno[3,4-b]thiophene)-2-carboxylate-2,6-diyl] (PTB7-Th)[5] (shown in Figure 4.1a). The absorption bands of PTB7 and PTB7-Th are red-shifted relative to those of hPDI3 and hPDI4 (Figure 4.1d). Films of hPDI3 or hPDI4 blended with PTB7 or PTB7-Th show broad, intense absorptions spanning the wavelength range from 350 to 800 nm (Figure 4.6b).

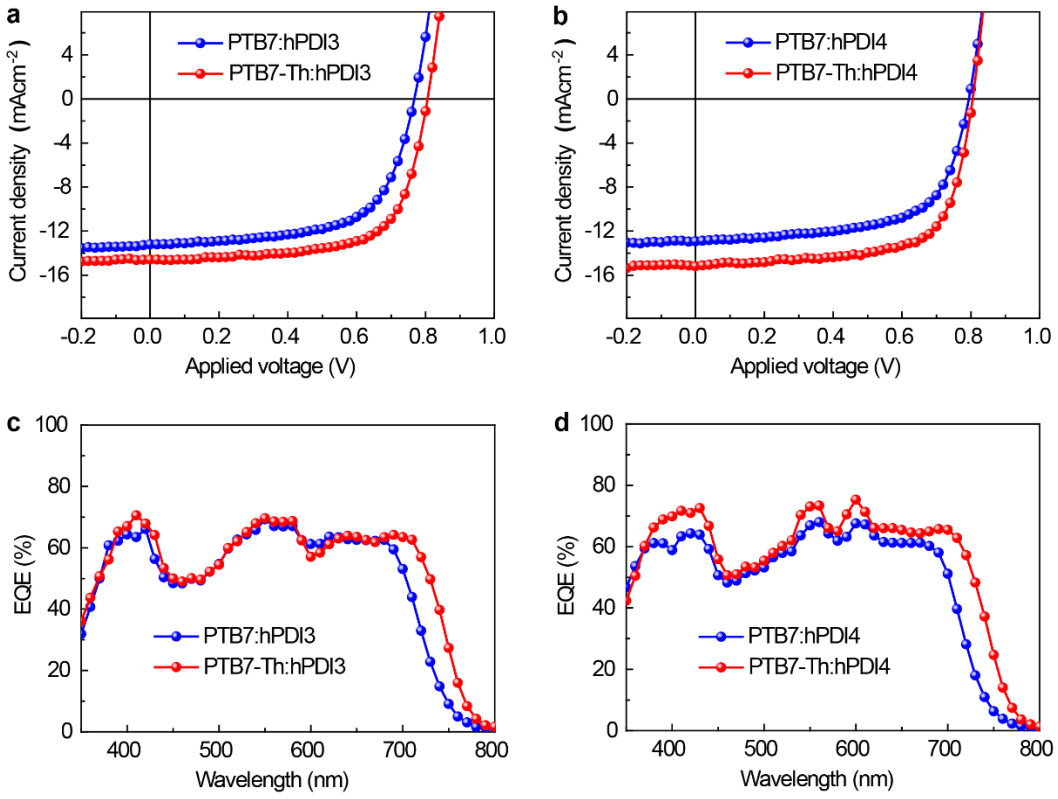

Figure 4.2. Device performance of best solar cells based on molecular helices. **a** and **b**, *J-V* curves for **a**, PTB7:hPDI3 and PTB7-Th:hPDI3 solar cells, **b**, PTB7:hPDI4 and PTB7-Th:hPDI4 solar cells under optimized conditions and simulated AM 1.5G irradiation (100 $mWcm^{-2}$). **c** and **d,** EQE spectra of **c**, PTB7:hPDI3, PTB7-Th:hPDI3 and **d**, PTB7:hPDI4 , PTB7-Th:hPDI4 solar cells under optimized conditions.

For each combination of blended polymer and helical molecule device active layer, we varied the ratio of donor and acceptor and optimized the film morphology with the solvent additive diiodooctane (DIO)[6] (See details about device optimization process in Figure 4.7-4.10 and Table 4.2-4.5 in Section 4.8). Our devices were fabricated in an inverted configuration, using ZnO as the electron transport layer and MoO_3 as the hole transport layer.[13] For devices based on acceptor hPDI3, we obtain optimal device performance with donor:acceptor mass ratio of 1:1.5, with 1 % DIO additive (v/v). Typical

current density−voltage ($J-V$) curves for PTB7:hPDI3 and PTB7-Th**:**hPDI3 solar cells are shown in Figure 4.2a. The solar cell parameters are listed in Table 4.1. PTB7-Th:hPDI3 exhibits a larger J_{sc} of 14.5 mAcm^{-2} as compared to 13.2 mAcm^{-2} for PTB7:hPDI3 due to the red-shifted absorption of PTB7-Th relative to PTB7. While the open-circuit voltage (V_{oc}) is comparable at 0.77 eV-0.81 eV, the fill factor (FF) increases from 63 % for PTB7:hPDI3 to 67 % for PTB7-Th:hPDI3. Overall, devices comprised of PTB7-Th:hPDI3 outperform those comprised of PTB7:hPDI3**,** exhibiting a maximal PCE of 7.9 % for PTB7-Th:hPDI3 as compared to 6.4 % for PTB7:hPDI3.

Table 4.1. Summary of device parameters of the best solar cells. [a]Values were measured and certified by Newport Corporation.

	J_{sc} (mAcm^{-2}) Highest/Avg.	**V_{oc} (V) Highest/Avg.**	**FF (%) Highest/Avg.**	**PCE (%) Highest/Avg.**
PTB7:hPDI3	13.2/13.0 ± 0.2	0.77/ 0.76 ± 0.01	63/62 ± 1	6.4/6.3 ± 0.1
PTB7-Th:hPDI3	14.5/14.3 ± 0.3	0.81/ 0.80 ± 0.01	67/67 ± 1	7.9/7.7 ± 0.2
PTB7:hPDI4	12.9/12.7 ± 0.3	0.79/0.78 ± 0.01	64/63 ± 1	6.5/6.4 ± 0.1
PTB7-Th:hPDI4	15.2/15.0 ± 0.2	0.80/0.80 ± 0.01	68/68 ± 1	8.3/8.1 ± 0.2
PTB7-Th: hPDI4[a]	15.1	0.802	68.2	8.27

For solar cells based on the electron acceptor hPDI4, we achieved optimal device performance with donor-to-acceptor mass ratio of 1:1 and 1 % DIO additive (v/v). Typical current density-voltage curves are shown in Figure 4.2b. Optimized devices show similar performance to those based on hPDI3, with PTB7:hPDI4 and PTB7-Th:hPDI4 solar cells reaching maximum PCE of 6.5 % and 8.3 %, respectively (device characteristics summarized in Table 4.1). Device performance of a PTB7-Th:hPDI4 solar cell has been independently certified by Newport Corporation, as shown in Table 4.1 and Figure 4.11.

These device characteristics are similar to those reported in fullerene-based cells (PTB7-Th:$PC_{71}BM$) with the same interfacial layers (ZnO and MoO_3)[2,5,25,26] and represent record highs for non-fullerene bulk heterojunctions with the highest non-fullerene BHJ having a PCE of 6.8 %.[15-18] These molecules are the first example of electron acceptors that are on par with fullerene derivatives in efficient BHJ solar cells with a PCE > 8 %, and provide a new route to exploring improvements to BHJ device performance.

Previously-reported solar cells with non-fullerene acceptors typically have J_{sc} less than 14 $mAcm^{-2}$ and FF values below 60 %,[15-18] which may be indicators of sub-optimal charge carrier collection. The improved J_{sc} and FF values in devices containing helical PDIs may be due to the efficient exciton generation, separation and carrier transport. Plots of the photocurrent density (J_{ph}) versus effective voltage (V_{eff}) yield information about exciton generation rates and the charge collection probabilities $P(E,T)$ at J_{sc} conditions (Figure 4.12). Here, V_{eff} is defined as $V_{eff} = V_0 - V_a$, where V_0 is the voltage where J_{ph} equals zero and V_a is the applied bias voltage. For both hPDI3-based and hPDI4-based devices, J_{ph} reaches the saturation current density at a relatively low V_{eff} (1.8 V). The PTB7-Th-based devices have slightly higher saturation current density than the PTB7-based device, consistent with the trend of J_{sc} values, and is attributed to its broader spectral response (Table 4.6). Under J_{sc} conditions, the $P(E,T)$'s is 94 % for PTB7:hPDI3 and as high as 97 % for PTB7:hPDI4, PTB7-Th:hPDI3 and PTB7-Th:hPDI4 devices. From the light-intensity-dependent current density measurement, we find a near-unity exponent α in the expression of J_{sc} versus I^{α}, where I is incident light intensity (See Figure 4.13-4.20). This data also suggests that bimolecular recombination and space-charge effect are suppressed at J_{sc} conditions.[27]

We measure the electron and hole mobilities in the optimal blend films by the space-charge-limited current (SCLC) method.[28] For PTB7-Th:hPDI3 blended film, the hole and electron mobilities are $(1.0 \pm 0.1) \times 10^{-4}$ and $(1.5 \pm 0.1) \times 10^{-4}$ $cm^2V^{-1}s^{-1}$, respectively. For PTB7-Th:hPDI4 blended film, the hole and electron mobilities are $(1.2 \pm 0.1) \times 10^{-4}$ and $(1.5 \pm 0.3) \times 10^{-5}$ cm^2 V^{-1} s^{-1}, respectively (Figure 4.21 and Supplementary Note 2 in Section 4.8). The lower electron mobility in PTB7-Th:hPDI4 compared to that of PTB7-Th:hPDI3 is probably due to reduced mass ratio of the electron acceptor in the blended film (50 % in PTB7-Th:hPDI4 versus 60 % in PTB7-Th:hPDI3). PTB7-Th:hPDI4 blended film exhibits similar electron mobility to fullerene-based blended film[29] while PTB7-Th:hPDI3 shows even more balanced electron and hole mobility.

Figure 4.2c and 4.2d display the external quantum efficiency (EQE) spectra for each of the devices. These devices show broad and strong photoresponse from 350 nm to 800 nm. Compared with the PTB7-based solar cells, the PTB7-Th solar cells show a significant increase in the photoresponse between 700 to 800 nm due to the red-shifted absorption of PTB7-Th. The integrated J_{sc} values for PTB7:hPDI3, PTB7:hPDI4, PTB7-Th:hPDI3 and PTB7-Th:hPDI4 are 13.2 $mAcm^{-2}$, 13.1 $mAcm^{-2}$, 14.4 $mAcm^{-2}$ and 15.1 $mAcm^{-2}$, respectively. These values agree well with measured values with a mismatch that is within 2 % for all the devices. Spectra for the solar cells based on hPDI4 show an increase at 600 nm due to the intense absorption band for hPDI4 in this region. It is notable that all the EQE data consist of maximal transition bands around 550 nm that is mainly from the absorption of the acceptors. For those PTB7-Th-based solar cells, the highest EQE values are even beyond 70 %. The important conclusion is that the photogenerated excitons from electron acceptors contribute greatly to the photocurrent in these solar cells.

4.4 Exciton generation and charge transfer.

Two advantages of these molecules over C_{60} and its derivatives are its significantly higher optical absorption cross section for the molecules in the visible part of the solar spectrum, and its easily tunable bandgap. The helical electron acceptors can thus complement low bandgap electron donors for an efficient harvesting of solar radiation in a broad wavelength region. To establish this dual light-harvesting mechanism, we use transient absorption (TA) spectroscopy to investigate exciton generation in the donor and acceptor and charge transfer between the two materials.

Figure 4.3a compares TA spectra for neat films of hPDI3, PTB7 and the blend at 0 and 5 ps, respectively upon photo excitation at 670 nm. At this wavelength, only PTB7 is excited, as confirmed by the absence of TA signal for hPDI3 (red). The spectrum from neat PTB7 (black) features ground-state bleaching (GB) peaks at 620 and 680 nm and a broad excited state absorption (ESA) peaks at ~1400 nm; these features decay bi-exponentially with time constants of 3.2 ± 0.3 ps and 50 ± 4 ps (see Figure 4.22 and Supplementary Note 3 in Section 4.8). In the blend, this ESA feature decays rapidly, with two time constants of 0.12 ± 0.03 ps and 1.4 ± 0.2 ps (Figure 4.3b), suggesting ultrafast electron transfer from photo-excited PTB7 to the electron acceptor, hPDI3. The ultrafast decay of the ESA at ~1410 nm is accompanied by a new ESA at ~1120 nm that is assigned to hole polaron absorption in PTB7. This assignment is consistent with previous spectroscopic measurement on chemical doped PTB7 that showed a polaron band at the same wavelength.[30] More evidences of this assignment are contained in the Figure 4.23-4.24 and Supplementary Note 4 in Section 4.8.

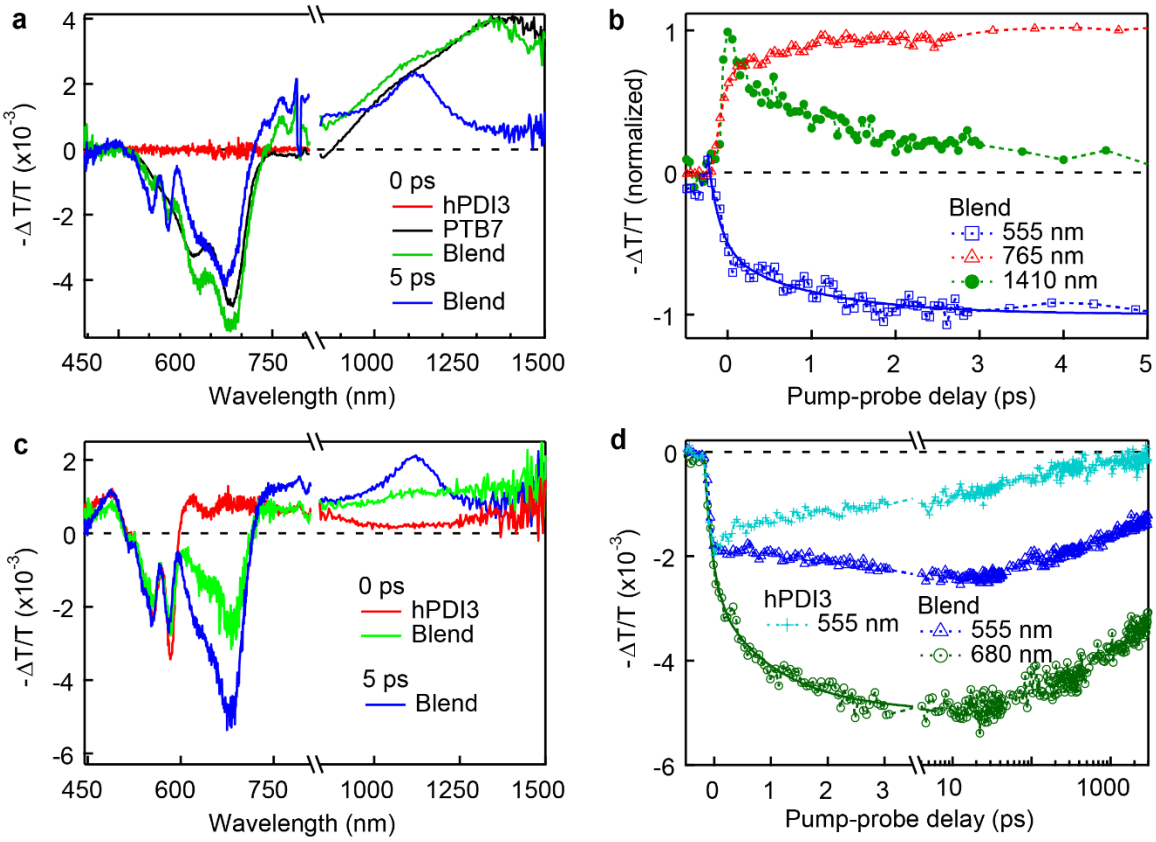

Figure 4.3. Spectral and temporal resolved ultrafast exciton dissociation. Transient absorption spectra for the films of neat hPDI3, neat PTB7 and their blended films, excited by 670 nm (**a**) and 415 nm (**c**). **b**, Normalized dynamics in the blend at 555 nm (hPDI3 bleaching peak), polaron absorption at 765 nm and exciton ESA peak in PTB7 at 1410 nm. **d**, Dynamics at 555 nm for the neat hPDI3 and at 555 and 680 nm for the blended film upon 415 nm excitation. The curve for neat hPDI3 (light blue) was scaled by a factor of 0.8. The pump density was ~20 μJcm^{-2} per pulse.

The dynamics of exciton dissociation into charge carriers is characterized by two time scales, as shown by the biexponential fit (τ_1 = 0.12 ± 0.03 ps; and τ_2 = 1.4 ± 0.2 ps) to the ESA signal probed at 1410 nm (green dots and fit in Figure 4.3b). This is more obvious in the ESA signal at ~765 nm (red dots in Figure 4.3b) that is negligible for the

neat PTB7 but appears in the blend. The new ESA in this region is assigned to the polaron absorption both in hPDI3 and PTB7. Bi-exponential fit (red curve, in Figure 4.3b) to the dynamics at 765 nm yields time constants of $\tau_1 = 0.12 \pm 0.03$ ps (70% relative weight) and $\tau_2 = 1.3 \pm 0.2$ ps (30 % relative weight). These time constants are identical to those obtained from fit to signal at 1410 nm and both wavelengths probe the same dynamics: the decay of exciton in PTB7 (1410 nm) and rise of polaron absorption (765 nm). We assign τ_1 (= 0.12 ± 0.03 ps) to the ultrafast exciton dissociation of PTB7 at the interface with electron acceptor hPDI3[16,31-35] and τ_2 (= 1.3 ± 0.2 ps) to the diffusion of excitons in PTB7 toward interfaces prior to dissociation.[36] Further confirming the assignment of charge transfer dynamics, we show that the appearance of ground-state bleaching (GB) from hPDI3 at 555 nm tracks the charge transfer dynamics (blue dots/fit in Figure 4.3b).

We now turn to complementary light harvesting by hPDI3 at its peak absorption wavelength of 415 nm (see Figure 4.1d). For neat hPDI3, excitation at this wavelength leads to GB at 555 and 580 nm, as well as a broad ESA feature in the range of ~600-1000 nm (Figure 4.3c). In the blend, excitation of hPDI3 leads to a rise of the bleaching of PTB7 at 680 nm. This bleaching signal grows with two time constants: $\tau_1' = 0.14 \pm 0.02$ ps and $\tau_2' = 1.2 \pm 0.3$ ps (green dots and fit in Figure 4.3d). The former is assigned to ultrafast hole transfer from photoexcited hPDI3 to PTB7 and the latter to exciton diffusion time in hPDI3 toward interfaces prior to hole transfer. Exciton dissociation is also evident by the quenching of fluorescence from PTB7 upon excitation of hPDI3 (Figure 4.25 and Supplementary Note 5 in Section 4.8). This interpretation is supported by the growth of ESA of hole polaron absorption in PTB7 at 1120 nm (see Figure 4.3c, blue spectrum at 5 ps). The charge separation process in the blend leads to a ~2-orders of magnitude increase

in the time constant for the recovery of hPDI3 (probed at 555 nm, blue dot/fit in Figure 4.3d) as compared to the same process in neat hPDI3 (light blue dots/fit in Figure 4.3d). The similar longer carrier lifetime was also found in the blended film at different excitation wavelengths (Figure 4.22). The much longer carrier recombination times in the blend than those in neat films are attributed to slower bimolecular recombination of the spatially separated charges in the blend.

The TA results presented above establish that photoexcitation of either the donor or the acceptor contribute to charge carrier generation. Like $PC_{71}BM$ based BHJs,[31-34] ultrafast exciton generation from these acceptors in the blended film compensates photoexcitation of the donor, resulting in broad photoresponse over the visible light region. The prevalent use of fullerene has led to the proposal that the spherical shape of fullerene plays an unique role in providing connectivity and electronic delocalization essential for ultrafast charge separation.[14,37] However, our findings show that fullerene is not particularly special and the helical conjugated molecules can also lead to efficient charge separation in BHJs.

4.5 Morphology characterization.

It is well known that proper phase separation and interpenetrating networks of donor and acceptor domains are critical to charge separation and carrier transport. Many studies on the film morphology in polymer/fullerene solar cells suggest optimal morphology for device operation is to have aggregated domains with sizes on approximately tens of nanometers for both the donor and acceptor.[13,38] However, film morphology of non-fullerene solar cells has received less attention.[15-18] To study the morphology of our blend films, we first performed grazing-incident X-ray diffraction

(GIXD) to understand molecular packing in our blend films. Neat films of both PTB7 and PTB7-Th are semicrystalline, as evident by the presence of their (100) reflections located at q = 0.35 and q = 0.30 Å^{-1}, respectively, in the corresponding x-ray diffraction patterns in Figure 4.26a and b.[39,40] The x-ray diffraction patterns also reveal (010) reflections in the out-of-plane direction between q = 1.55 and q = 1.85 Å^{-1}. Since the (010) reflections correspond to the direction of pi-stacking, the intensity anisotropy corresponding to the (010) reflections indicate that both PTB7 and PTB7-Th preferentially adopt a face-on orientation. This assertion is consistent with the observation that the intensities of the (100) reflections of the polymer donors are each concentrated at the equator. That the intensity distributions associated with the (100) and (010) reflections of PTB7-Th are sharper than those associated with the corresponding reflections of PTB7 indicates that the crystallites of PTB7-Th exhibit a higher degree of face-on orientation compared to PTB7. The GIXD pattern of hPDI3 in Figure 4.26c also exhibits a first-order reflection at q = 0.35 Å^{-1}. Given that the intensity distribution of this reflection does not vary substantially with azimuthal angle, crystallites of hPDI3 do not adopt any preferential orientation. Figure 4.26d and e exhibit the GIXD patterns of thin films comprising each of the polymer donor with hPDI3. The primary reflections of the polymer donors and hPDI3 overlap substantially. We are thus not able to make meaningful comparison based on the intensities in this q-range. Comparing the GIXD patterns of the blends at higher q-range with those of the constituent polymer donors does, however, reveal differences. We observe that the (010) reflections in the GIXD patterns of the blends to be substantially weaker than those in the patterns of the polymer donor constituents. Further, the weak intensities associated with the (010) reflections in the GIXD patterns of the blends appear to be more isotropic with azimuthal

angle. Collectively, these observations suggest the addition of hPDI3 to disrupt the crystallization of the polymer donor constituents, and crystallites that form are less oriented compared to those in thin films comprising the polymer donor constituents alone.

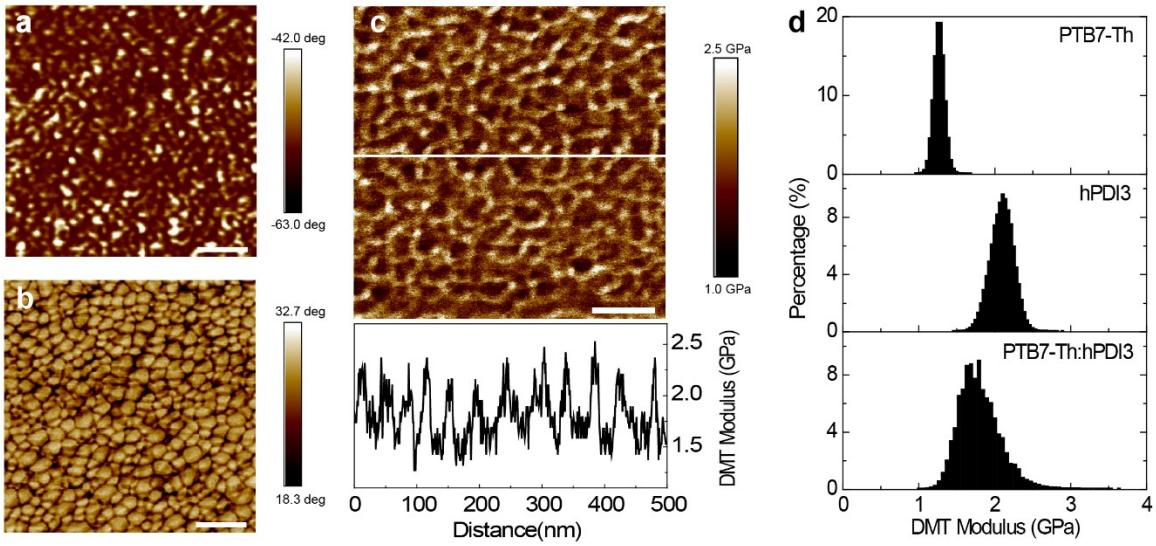

Figure 4.4. Film morphology of PTB7-Th: hPDI3 blend film. **a,** Top surface phase image of BHJ thin film measured in tapping mode. **b**, Internal phase image of blended thin film measured in tapping mode. **c**, Internal DMT (Derjaguin, Muller, Toropov) modulus image of blended thin film measured in peak force QNM mode. Bottom graph is line-cut analysis of image **c**. **d**, DMT modulus of PTB7-Th and hPDI3 pure thin films and PTB7-Th:hPDI3 blend film. The scale bar is 100 nm in a-c.

We investigated the PTB7-Th:hPDI3 blended film morphology using both tapping-mode and quantitative nanomechanical (QNM) mode[41] atomic force microscopy (AFM) (Figure 4.4). While the height image of the top film surface is very smooth (RMS roughness of 0.58 nm), the phase image shows evidence of a distinct phase separation, with domain size of ~10-20 nm. (Figure 4.4a and Figure 4.27). We used an oxygen plasma to remove ~30 nm of material from the top surface to investigate the blend's internal morphology[41-

[43]. Here, the phase image clearly shows a continuous interpenetrating network with a feature size in the range of 20-40 nm (Figure 4.4b) – a morphology clearly favorable for exciton dissociation and charge transport. Nanomechanical measurements show that the continuous network (dark regions in Figure 4.4b) has a DMT (Derjaguin, Muller, Toropov) modulus of ~2.2 GPa, which is similar to that of the pure film of hPDI3 (Details about DMT model in Supplementary Note 6 in Section 4.8). However, the isolated embedded in the continuous network domains (bright regions in Figure 4.4b) have a smaller DMT modulus (~1.5 GPa), closer to that of a pure PTB7-Th film (Figures 4.4c and 4.4d). These results suggest an active layer composed of an interpenetrating network of hPDI3-rich domains, embedded in PTB7-Th-rich matrix. Our blend films shares very similar morphology to that of PTB7:$PC_{71}BM$, which is considered an optimal morphology to enable efficient charge generation and transport in BHJ solar cells.[41]

4.6 Conclusion

This study introduces a new class of highly efficient electron acceptors for organic BHJ solar cells, consisting of helical conjugated perylene diimide oligomers. We have demonstrated solar cells with power conversion efficiencies comparable to previous reports from devices using fullerene derivatives. We believe the values reported here represent a lower limit for what is achievable, and that creating electron donor materials that are matched both structurally and electronically with these molecules is a clear path to further improvement.

4.7 Experimental Section

4.7.1. Materials.

hPDI3 and hPDI4 were synthesized according to a previously reported method.[20]

PTB7 and PTB7-Th were purchased from 1-materal Inc. Synthesis of ZnO sol-gel precursor was described elsewhere.[44] Zinc acetate dihydrate, ethanolamine, 2-methoxyethanol, DIO and all of the solvents were purchased from Sigma Aldrich.

4.7.2. Device fabrication.

Prepatterned ITO-coated glass with a sheet resistance of ~15Ωsq^{-1} was cleaned with detergent, ultrasonicated in DI water, acetone and isopropanol for 30 min, respectively. Subsequently, we treated the substrates by UV-Ozone for 10 min. The prepared ZnO precursor was spin-cast onto the ITO substrate at 3000 rpm for 1 min, followed by annealing at 200 ºC for 1 h in air, to form a thin film with approximate thickness of 20 nm. Active layers were prepared by spin-coating a mixed solution containing polymer and acceptor in chlorobenzene at a total concentration of 25 mgmL^{-1}. The thickness of the prepared active layers is about 100 nm. Active layers were heated at 80 ºC for 10 min in the nitrogen filled glove box to remove the residual solvent. Finally, a 7 nm MoO_3 layer was deposited first and then a 100 nm Al electrode were subsequently deposited through a shadow mask by thermal evaporation under a vacuum about 1×10^{-6} torr.

4.7.3. Characterization.

The current density–voltage (*J–V*) curves were measured by a Keithley 2635A source measure unit. The photocurrent was measured under AM 1.5G illumination at 100 mW/cm^2 under a Newport solar Simulator. A KG5-Si reference cell traceable to Newport was used to calibrate light intensity. Mismatch of Integrated J_{sc} values from EQE with the AM 1.5G solar spectrum agreed and the measured values are within 2 %. Spectral mismatch factors (*M*) calculated according to a standard procedure reported elsewhere[45] were applied to all the devices. The effective device area was defined as 6.25 mm^2 by an

aperture mask except that a 4 mm^2 aperture mask was used for the certified device at Newport Corporation. Average device parameters were obtained from at least 6 devices at each condition and at least 12 devices at the optimal condition for each donor-acceptor combination. External quantum efficiency measurements were performed using a QE system from PV Measurements Inc. Absorption spectra were obtained on Shimadzu UV 1800 UV-Vis.

4.7.4. Transient absorption spectroscopy.

To investigate charge transfer in the solar cells, we employed the transient absorption spectroscopy. The pump laser light (~100 fs pulse width) comes from an optical parametric amplifier pumped by a Ti:sapphire femtosecond regenerative amplifier (800 nm, 1 kHz rep-rate). The probe light is a white-light supercontinuum (450-900 nm and 850-1600 nm for the visible and near IR range, respectively). The pump and probe beams overlapped under a small angle. The detection consists of a pair of high-resolution multichannel detector arrays coupled to a high-speed data acquisition system.

4.7.5. Grazing-incident X-ray diffraction.

GIXD experiments were conducted at the G1 station (11.8 ± 0.1 keV) of the Cornell High Energy Synchrotron Source. The beam was chosen to be 0.05 mm tall and 1 mm wide. The width of each sample was 5 mm. The x-ray beam was aligned above the film's critical angle but below that of the substrate, at a 0.18° incident angle with the substrate. X-ray scattering was collected with a two-dimensional Pilatus 200 K detector, positioned 84.5 mm from the sample. All GIXD images have been background subtracted.

4.7.6. Atomic force microscopy.

AFM measurements were carried out in tapping mode and PeakForce QNM

(Quantitative NanoMechanics) mode on a Bruker Multi-Mode AFM at ambient conditions. A commercial silicon cantilever (RTESPA, MPP-11120-10, Bruker) was used in this study with a typical radius of curvature of ~8 nm and a nominal spring constant of ~40 Nm^{-1}. Nanomechanical mapping was operated at constant peak force. The etching treatment was performed on the sample surface using oxygen plasma (Plasma Etch Inc. Model: PE-50) to etch out ~30 nm from the top surface.

4.8 Supplementary materials

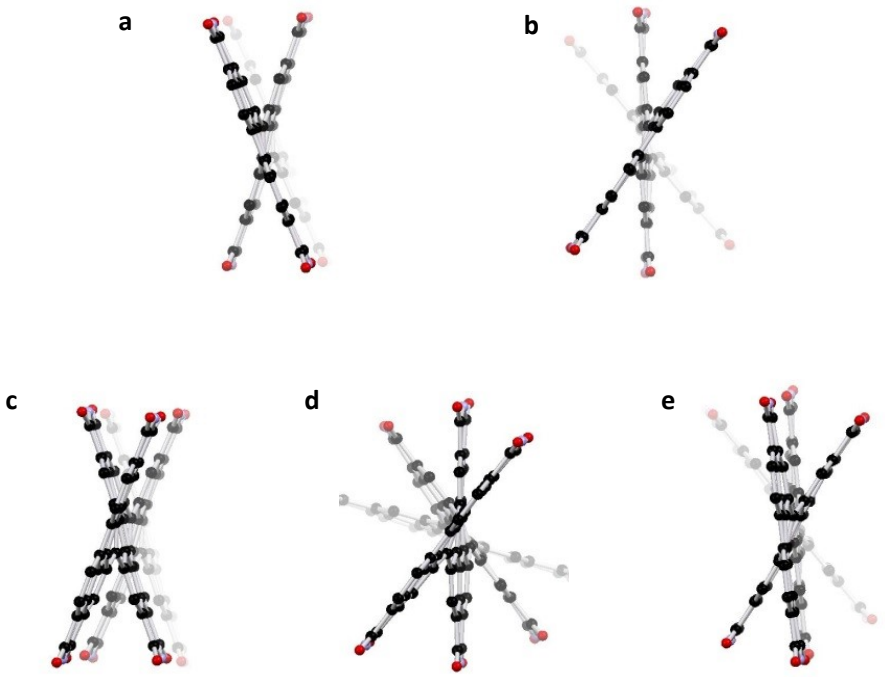

Figure 4.5. Molecular conformation from DFT calculation. DFT models of (a-b) hPDI3 and (c-e) hPDI4. hPDI3 consists of two iso-energetic conformations, (a) "waggling" and (b) "helical". hPDI4 consists of three iso-energetic conformations, (c) "waggling", (d) "helical" and (e) "mixed". Hydrogens and alkyl side chains have been removed for clarity. Black = carbon; red = oxygen; blue = nitrogen.

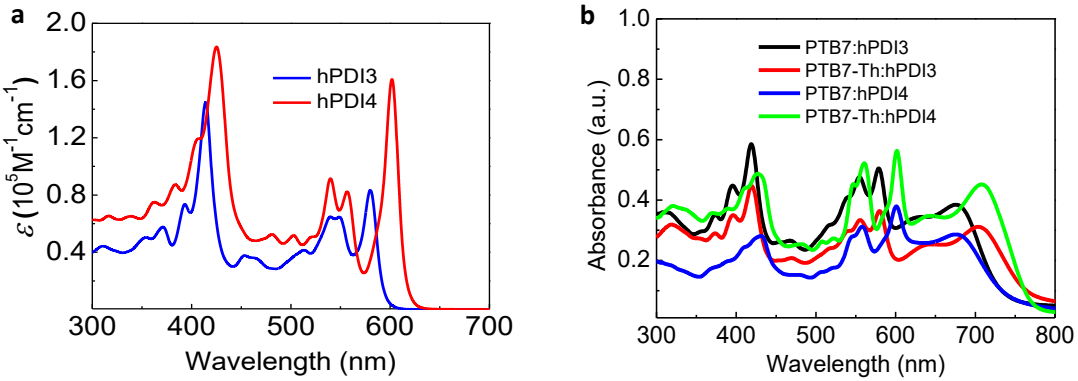

Figure 4.6. (a) Solution absorption spectra of hPDI3 and hPDI4. (1×10^{-5} M concentration in dichloromethane with a path length $l = 1$ cm) (b) Film absorption spectra of PTB7:hPDI3 (1:1.5), PTB7:hPDI4 (1:1), PTB7-Th:hPDI3 (1:1.5) and PTB7-Th:hPDI4 (1:1).

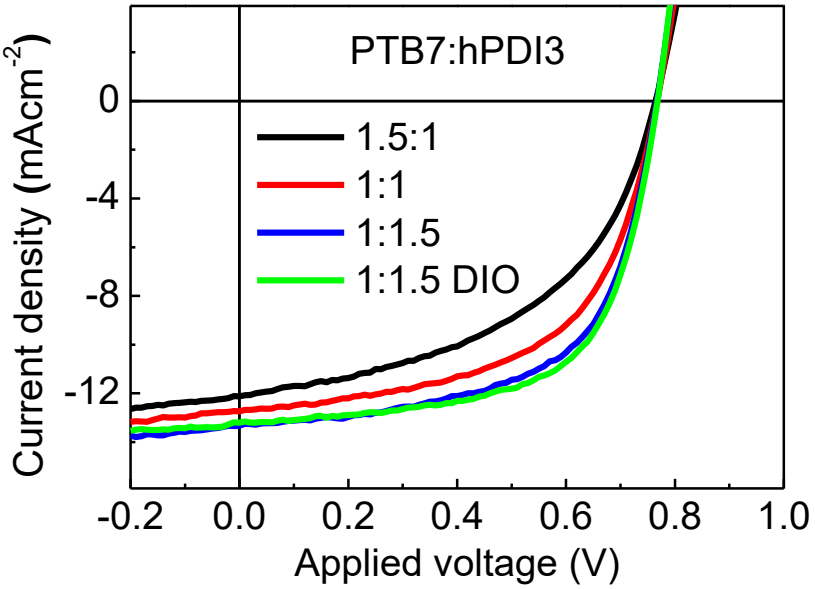

Figure 4.7. Device performance of PTB7:hPDI3 solar cells. Current density versus voltage (*J*–*V*) characteristics of PTB7:hPDI3 solar cells with different blend ratios (PTB7 to hPDI3) and 1% v/v DIO.

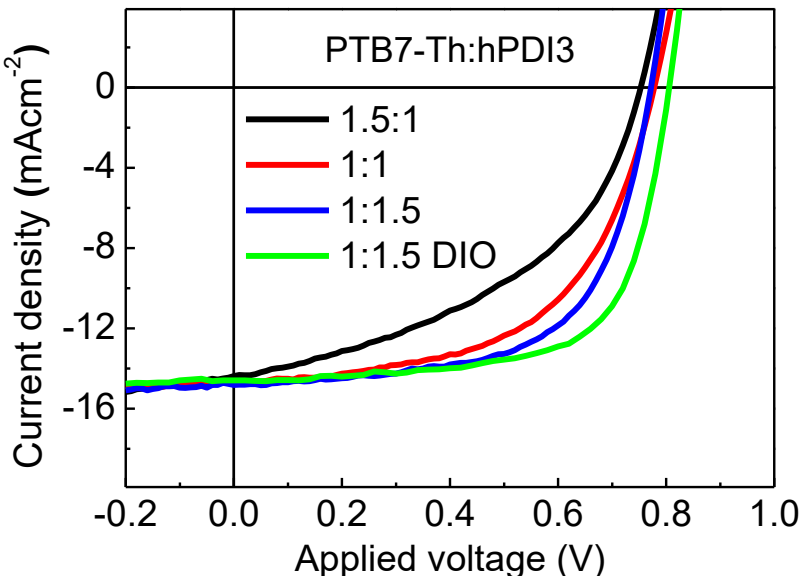

Figure 4.8. Device performance of PTB7-Th:hPDI3 solar cells. Current density versus voltage (*J–V*) characteristics of PTB7-Th:hPDI3 solar cells with different blend ratios (PTB7-Th to hPDI3) and 1% v/v DIO.

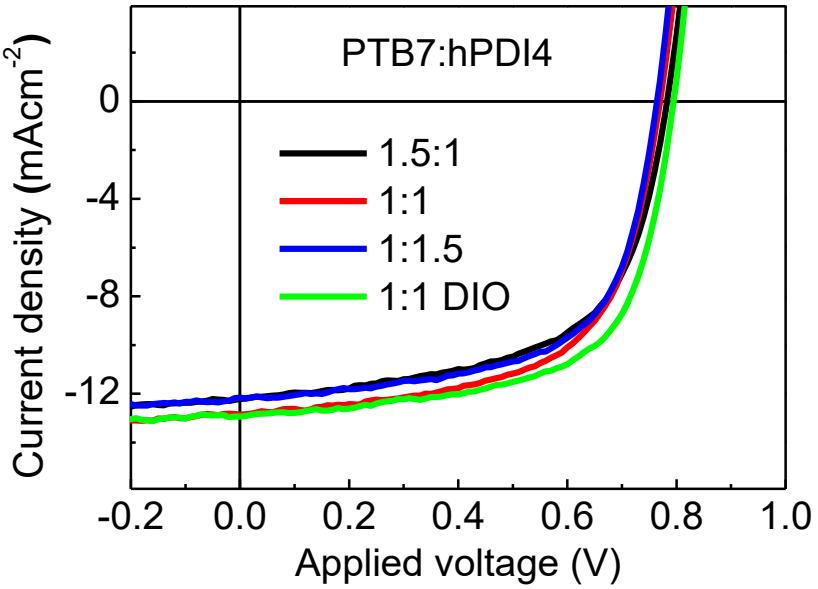

Figure 4.9. Device performance of PTB7:hPDI4 solar cells. Current density versus voltage (*J–V*) characteristics of PTB7:hPDI4 solar cells with different blend ratios (PTB7 to hPDI4)

and 1% v/v DIO.

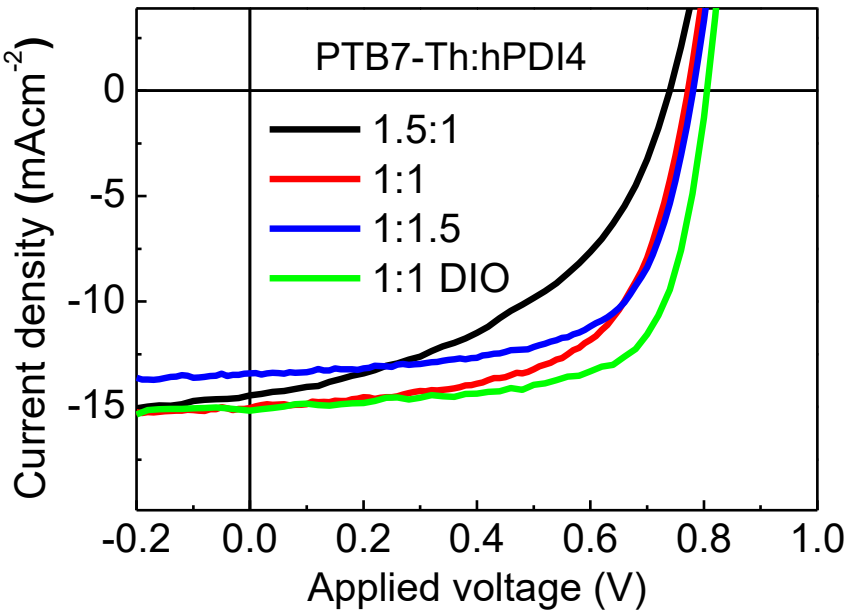

Figure 4.10. Device performance of PTB7-Th:hPDI4 solar cells. Current density versus voltage (*J*–*V*) characteristics of PTB7-Th:hPDI4 solar cells with different blend ratios (PTB7-Th to hPDI4) and 1% v/v DIO.

Newport	ACCREDITED Calibration Cert. # 2893.01	Technology and Application Center **PV Lab** Newport Calibration Cert. # 1250

DUT S/N: 78P2
Newport Calibration #: 1250
Manufacturer: Professor Nuckolls Group
Material: OPV
Temperature Sensor: None
Environmental conditions at the time of calibration: Temperature: 24 ± 3 °C; Humidity: 33 ± 4 %

The above DUT has been tested using the following methods to meet the ISO 17025 Standard by the PV Lab at Newport Corporation. Quoted uncertainties are expanded using a coverage factor of $k = 2$ and expressed with an approximately 95% level of confidence. Measurement of total irradiance is traceable to the World Radiometric Reference (WRR) and all other measurements and uncertainties are traceable to either NIST or CNRC and the International System of Units (SI). The performance parameters reported in this certificate apply only at the time of the test, and do not imply future performance.

Efficency [%]	8.27	± 0.18	V_oc [V]	0.8023	± 0.0112	I_sc [A]	0.000596	± 0.000011
P_max [mW]	0.326	± 0.007	V_max [V]	0.6546	± 0.0071	I_max [A]	0.000498	± 0.000006
FF [%]	68.2	± 1.0	Area [cm^2]	0.0394	± 0.0001	M	0.989	± 0.004

Methods:

I-V: ASTM E948-15 *Standard Test Method for Electrical Performance of Photovoltaic Cells Using Reference Cells Under Simulated Sunlight*
QE: ASTM E1021-15 *Standard Test Method for Spectral Responsivity Measurements of Photovoltaic Devices*

Standard Reporting Conditions:

Spectrum: AM1.5-G (ASTM G173-03/IEC 60904-3 ed. 2)
1000.0 W/m^2 at 25.0°C

Secondary Reference Cell:

Device S/N: PVM 284 KG5
Device Material: mono-Si
Window Material: KG5
Certification: National Renewable Energy Laboratory
A2LA accreditation certificate # 2236.01
ISO Tracking #: 1811
Certified short circuit current (I_{sc}) under standard reporting conditions (SRC): 33.803mA
Calibration due date: 11-Aug-15

Solar Simulator:

Spectrum: Newport Corporation filename *Sol3A_Spectroradiometer_Scan_0168.xls*
Total irradiance: 1000 W/m^2 based on I_{sc} of the above Secondary Reference Cell

Quantum Efficiency for DUT:

Newport Corporation filename *QE 1250 P2.log*
Spectral mismatch correction factor: M = 0.989 ± 0.004

DUT Calibration Procedures:

Newport Corporation document WI1 (EQE).docx
Newport Corporation document Area Measurement WI2 (Area).docx
Newport Corporation document WI3 (IV.Sweep).docx

Newport		Technology and Application Center PV Lab Calibration Number 1250

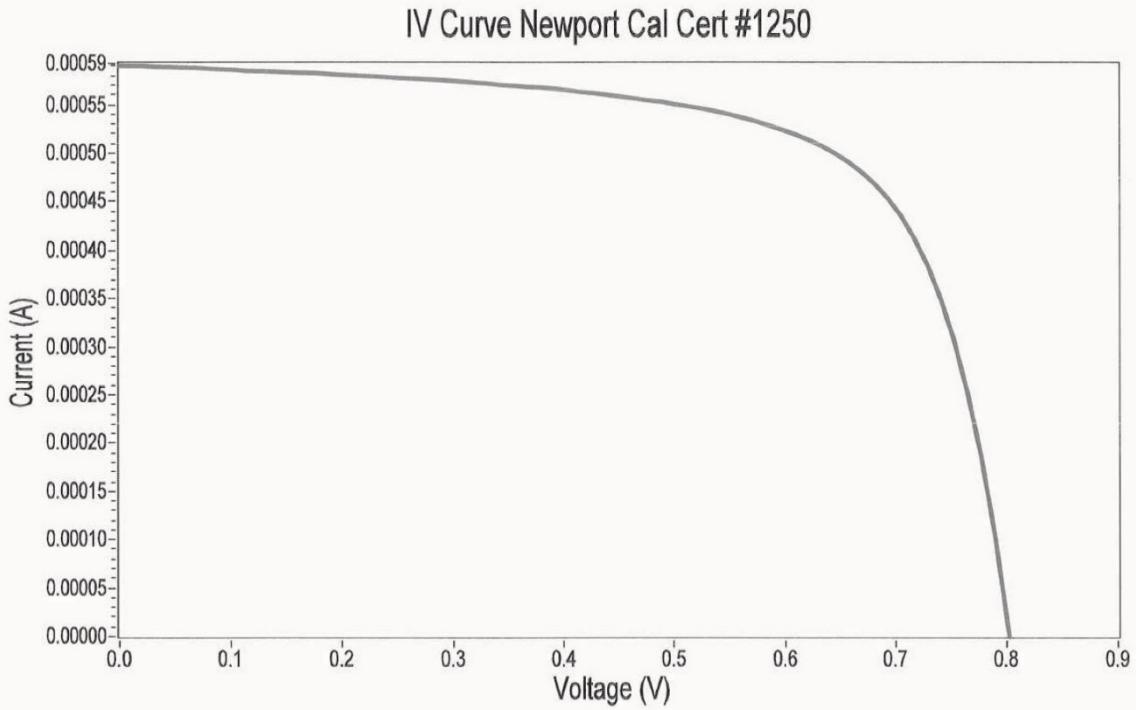

Cal Cert Data V1_2	Issue Date: Jun 05, 2015	Page 1of 4
	Reviewed and Approved by: Geoffrey Wicks	

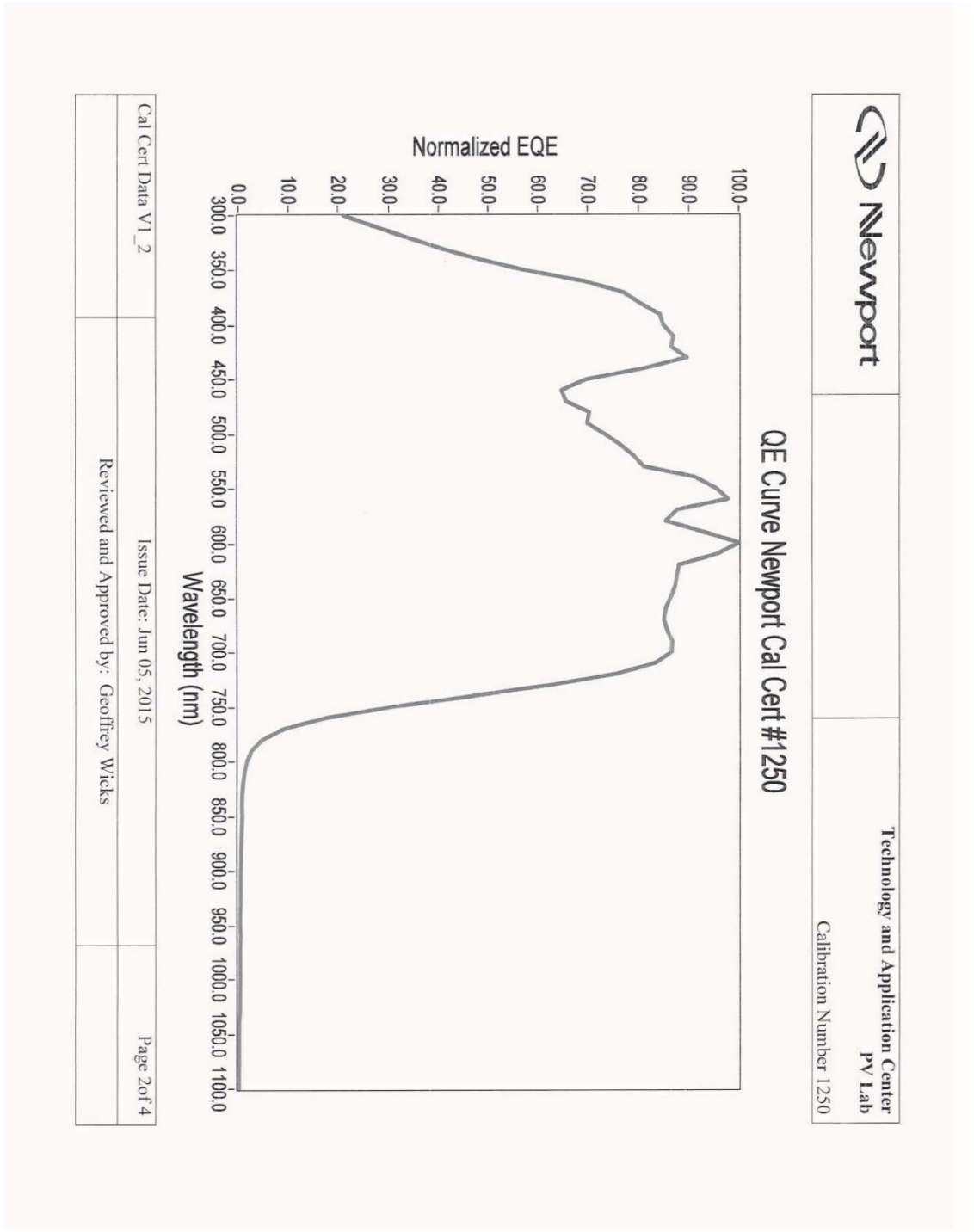

Figure 4.11. Device characteristics of the PTB7-Th:hPDI4 solar cell tested by Newport Corporation.

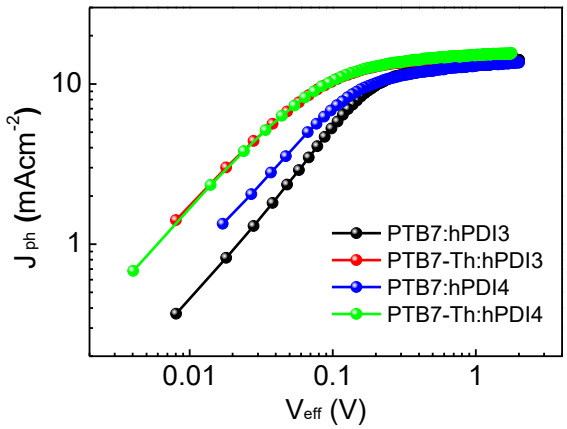

Figure 4.12. Photocurrent density (J_{ph}) versus effective voltage (V_{eff}) characteristics of PTB7:hPDI3, PTB7-Th:hPDI3, PTB7:hPDI4 and PTB7-Th:hPDI4 solar cells .

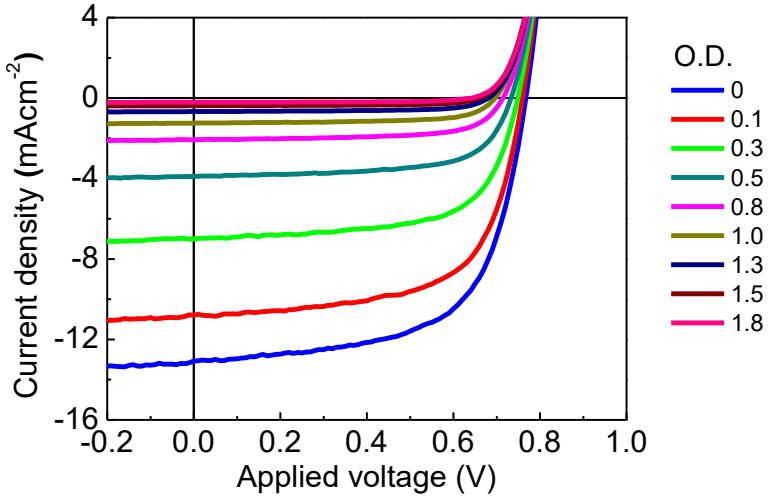

Figure 4.13. Incident light intensity dependence of photocurrent on PTB7:hPDI3 solar cells. Current density versus voltage (*J–V*) characteristics for a PTB7:hPDI3 solar cell under AM 1.5 G illumination with a set of neutral density filters.

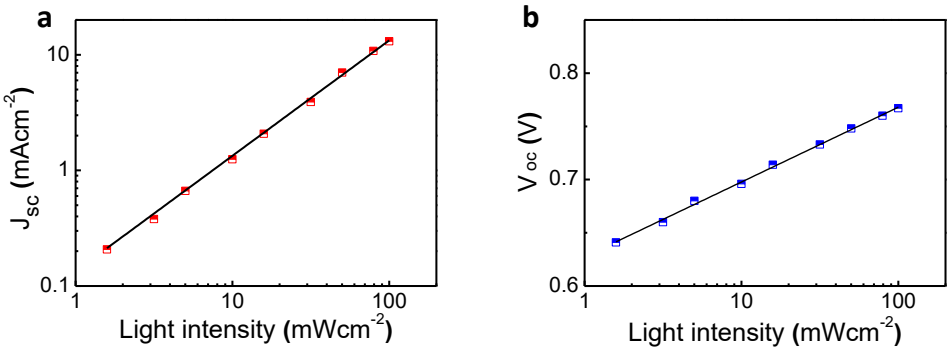

Figure 4.14. Carrier recombination of PTB7:hPDI3 solar cells. (a) J_{sc} as a function of light intensity in a double-logarithmic scale from an optimized PTB7:hPDI3 device. The slope was calculated to be $k = 1.00 \pm 0.03$. (b) V_{oc} as a function of light intensity in a semi-logarithmic scale from an optimized PTB7:hPDI3 device. The slope was calculated to be $n = 1.17 \pm 0.02$ kT/e.

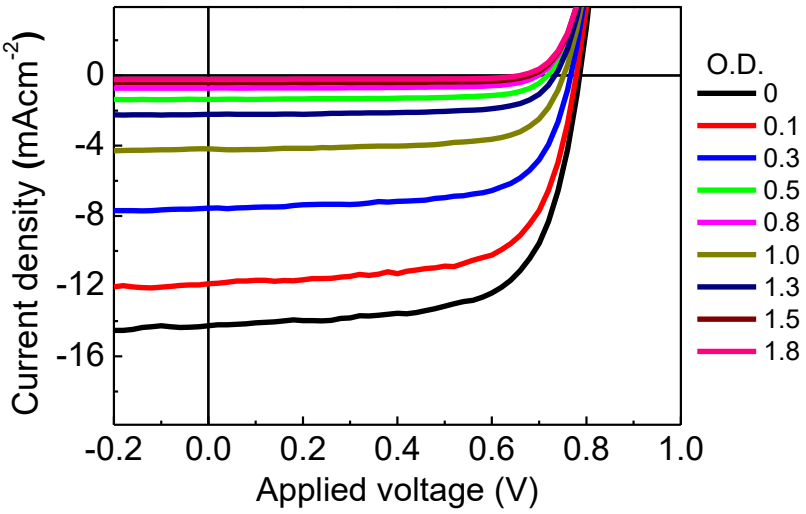

Figure 4.15. Incident light intensity dependence of photocurrent on PTB7-Th:hPDI3 solar cells. Current density versus voltage (J–V) characteristics for a PTB7-Th:hPDI3 solar cell under AM 1.5 G illumination with a set of neutral density filters.

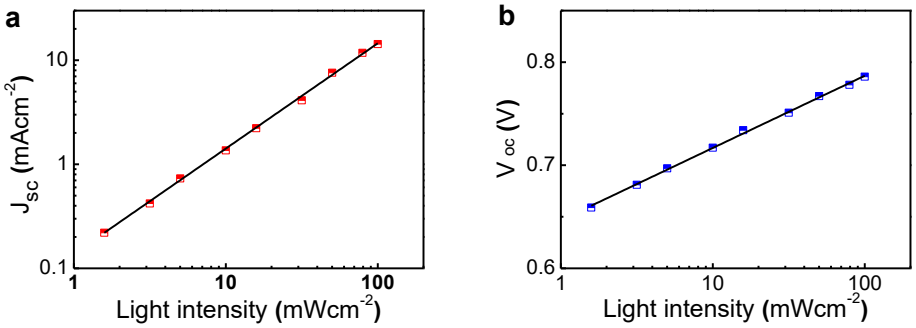

Figure 4.16. Carrier recombination of PTB7-Th:hPDI3 solar cells. (a) J_{sc} as a function of light intensity in a double-logarithmic scale from an optimized PTB7-Th:hPDI3 device. The slope was calculated to be $k = 1.01 \pm 0.03$. (b) V_{oc} as a function of light intensity in a semi-logarithmic scale from an optimized PTB7-Th:hPDI3 device. The slope was calculated to be $n = 1.17 \pm 0.02$ kT/e.

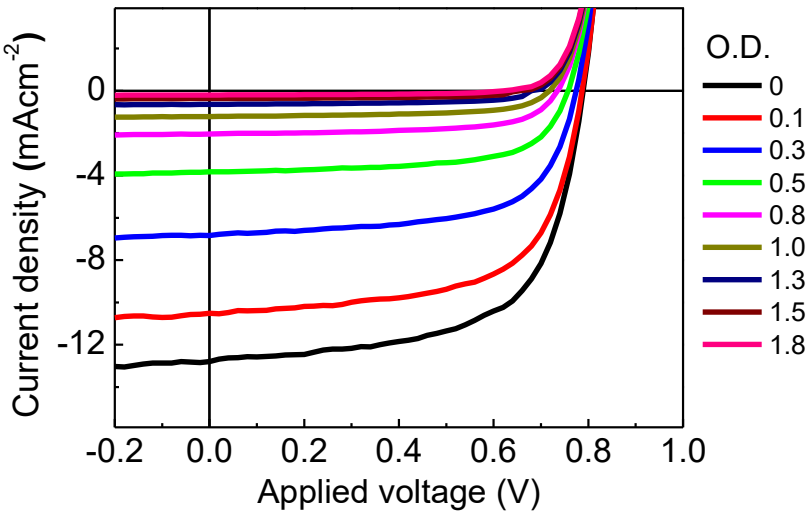

Figure 4.17. Incident light intensity dependence of photocurrent on PTB7:hPDI4 solar cells. Current density versus voltage (J–V) characteristics for a PTB7:hPDI4 solar cell under AM 1.5 G illumination with a set of neutral density filters.

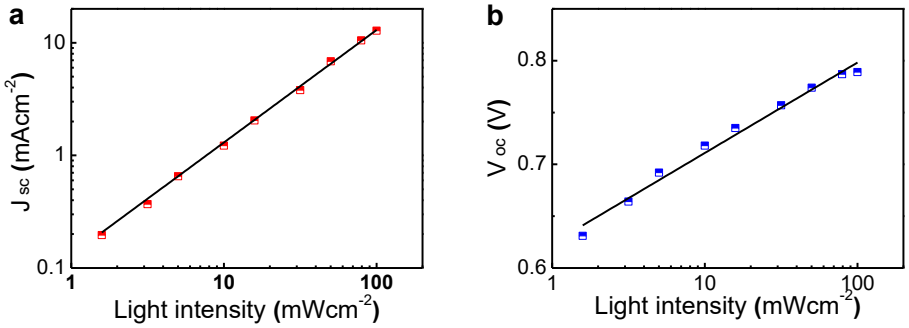

Figure 4.18. Carrier recombination of PTB7:hPDI4 solar cells. (a) J_{sc} as a function of light intensity in a double-logarithmic scale from an optimized PTB7:hPDI4 device. The slope was calculated to be $k = 1.00 \pm 0.03$. (b) V_{oc} as a function of light intensity in a semi-logarithmic scale from an optimized PTB7:hPDI4 device. The slope was calculated to be $n = 1.46 \pm 0.06$ kT/e.

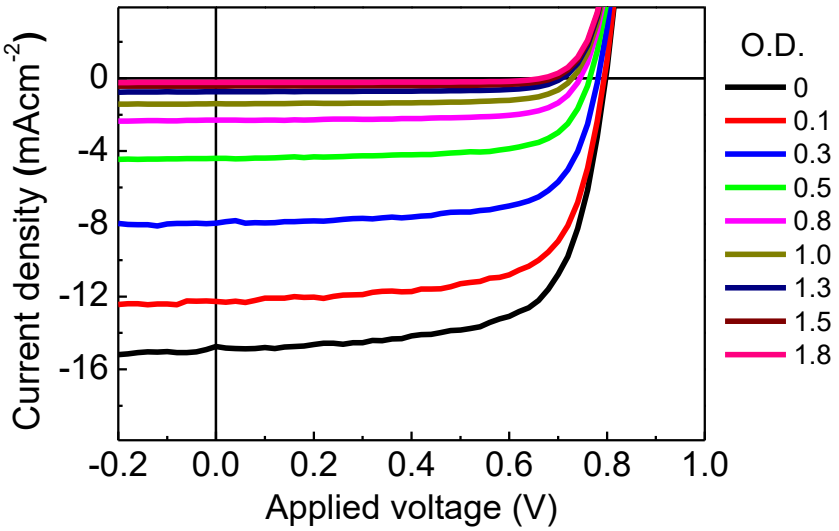

Figure 4.19. Incident light intensity dependence of photocurrent on PTB7-Th:hPDI4 solar cells. Current density versus voltage (J–V) characteristics for a PTB7-Th:hPDI4 solar cell under AM 1.5 G illumination with a set of neutral density filters.

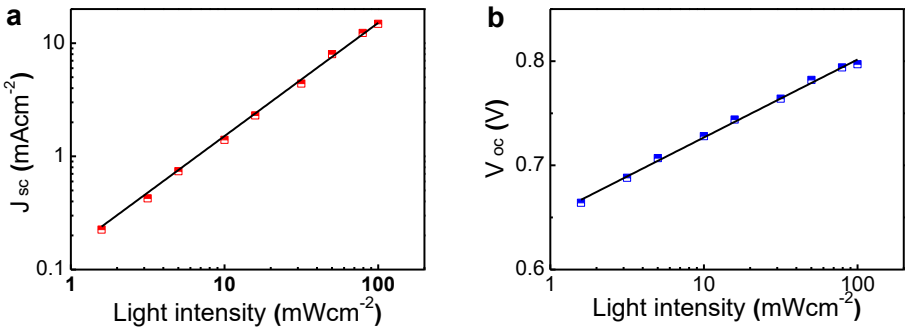

Figure 4.20. Carrier recombination of PTB7-Th:hPDI4 solar cells. (a) J_{sc} as a function of light intensity in a double-logarithmic scale from an optimized PTB7-Th:hPDI4 device. The slope was calculated to be $k = 1.00 \pm 0.03$. (b) V_{oc} as a function of light intensity in a semi-logarithmic scale from an optimized PTB7-Th:hPDI4 device. The slope was calculated to be $n = 1.25 \pm 0.03$ kT/e.

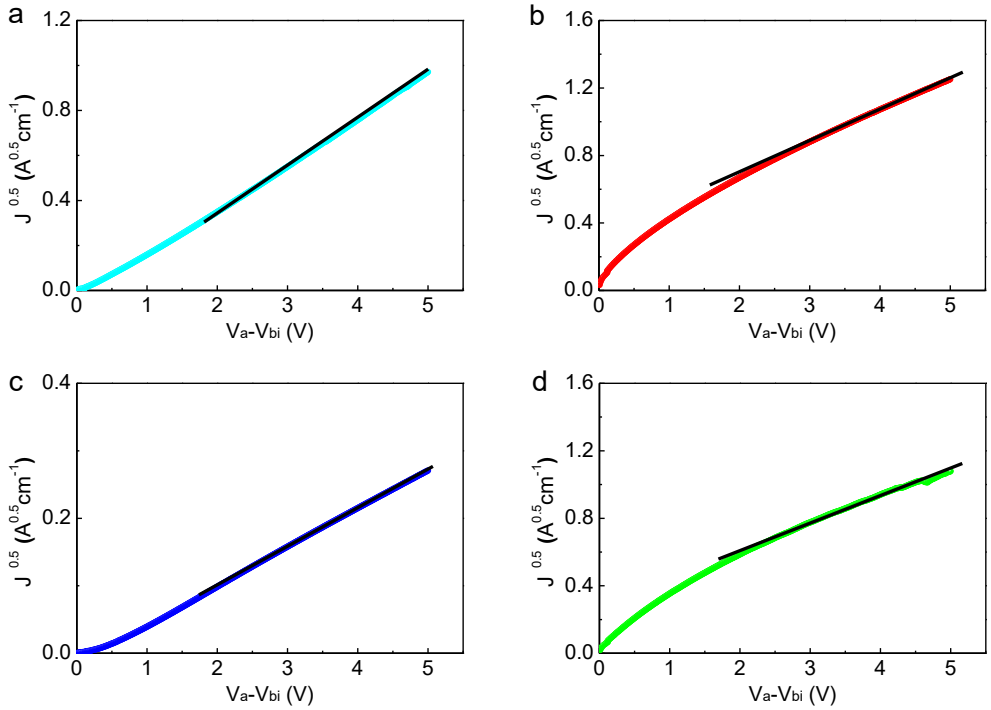

Figure 4.21. $J^{0.5}$ vs. V plots for (a) an electron-only device, (b) a hole-only device from PTB7-Th:hPDI3 blend and (c) an electron-only device, (d) a hole-only device from PTB7-Th:hPDI4 blend.

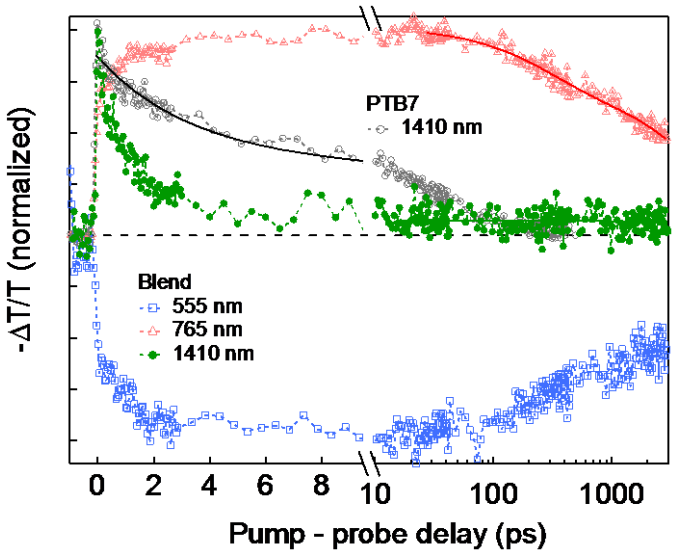

Figure 4.22. Exciton/carrier dynamics upon 670 nm excitation. Exciton dynamics at 1410 nm in the neat PTB7 film (grey) and the PTB7:hPDI3 blended film (green). Charge (polaron) dynamics at 555 (blue) and 765 (red) nm for the blended film.

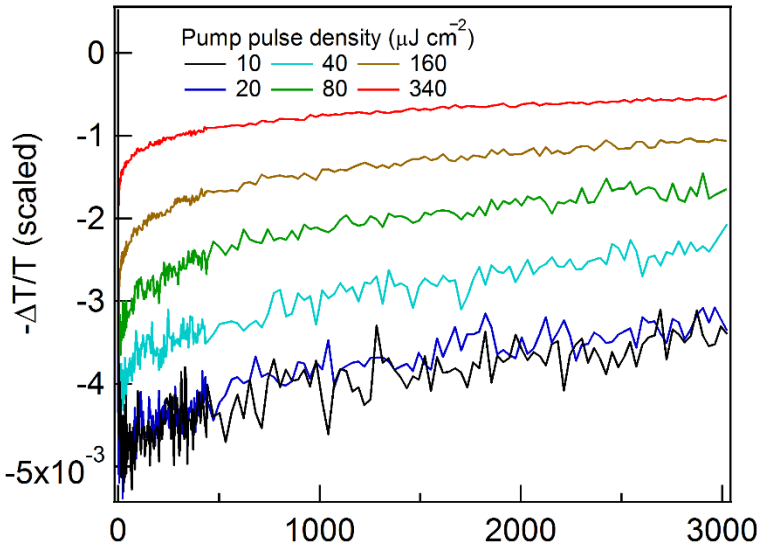

Figure 4.23. Dynamics at 680 nm (PTB7 bleaching) upon 415 nm excitation at various pump intensities for the blended film. The curves were normalized for the pump intensities. The dynamics are similar for the pump intensities of 10 and 20 μJcm^{-2} indicating of

negligible non-linear effect at these pump intensities. At pump intensities larger than 40 μJcm^{-2} the fast component appears due to carrier-carrier annihilation. The initial bleaching values is lower for a higher pump intensities (from 40 μJcm^{-2}) due to the annihilation that takes place earlier than exciton diffusion time.

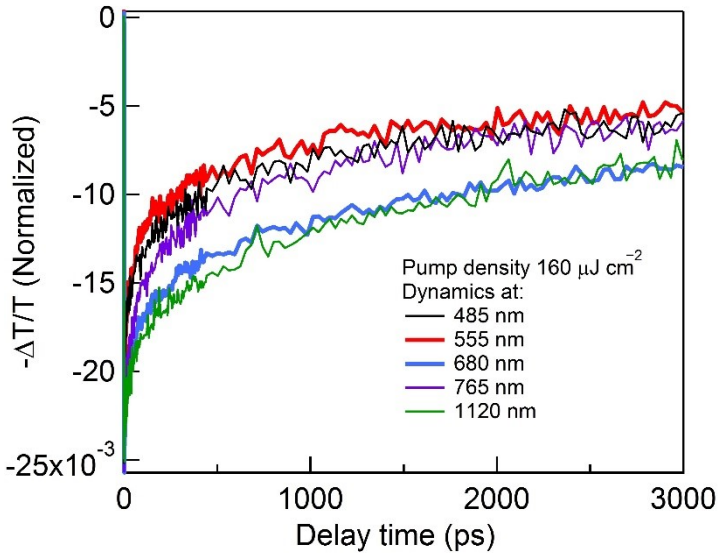

Figure 4.24. Normalized dynamics at various probe wavelengths for the blend at a high pump density (160 μJcm^{-2}). Excitation wavelength was 415 nm. Dynamics at 555 (red) and 680 (blue) nm represent the bleaching dynamics for hPDI3 and PTB7 in the blend, respectively. Dynamics at 485 nm, 555 nm, 765 nm and 1120 nm was scaled by a factor of -3.2, 1.5, -3.15 and -1.9, respectively, for normalization.

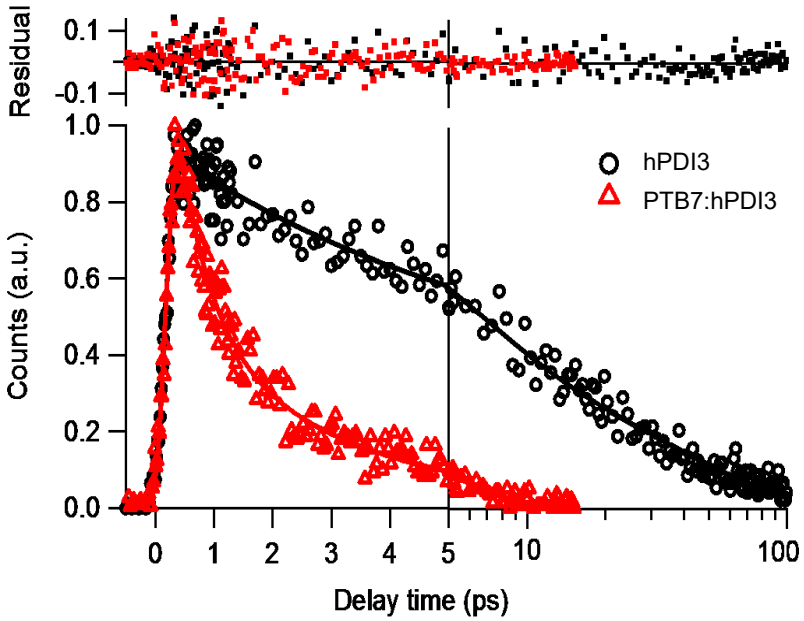

Figure 4.25. Upconverted fluorescence decay kinetics for hPDI3 (black circles) and blended film (red triangles). The decay kinetics are fitted by bi-exponential decay function. The excitation wavelength is 508 nm and the upconverted PL is centered at 580 nm.

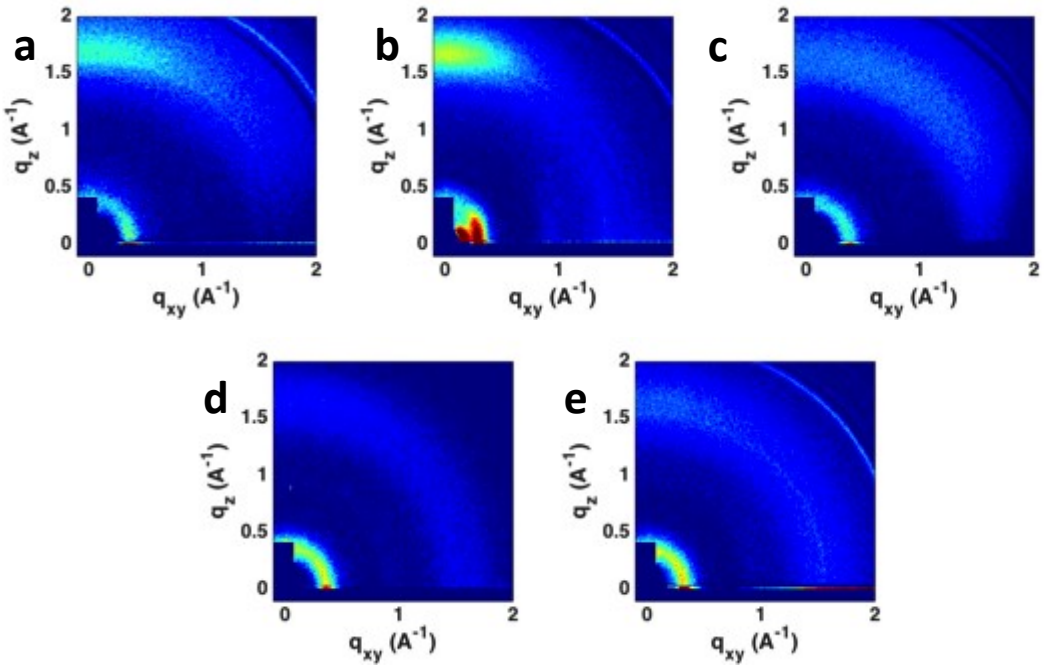

Figure 4.26. Grazing incident X-ray diffraction. GIXD images of (a) PTB7, (b) PTB7-Th,

(c) hPDI3, (d) PTB7:hPDI3 with 1% DIO and (e) PTB7-Th:hPDI3 with 1% DIO on ZnO coated ITO substrates. Blend films of PTB7:hPDI3 and PTB7-Th:hPDI3 were prepared at same conditions as used in optimal solar cells.

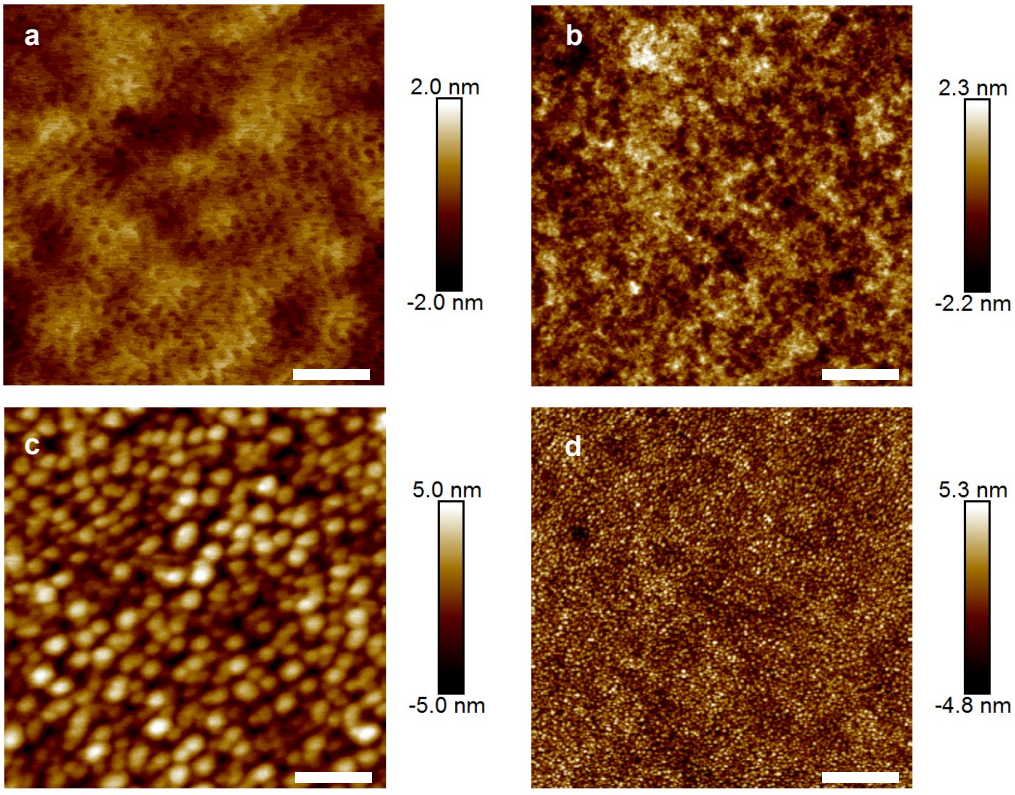

Figure 4.27. Top surface (a and b) and internal (c and d) morphology of PTB7-Th:hPDI3 blend films at a mass ratio of 1:1.5 processed from chlorobenzene solutions with 1v/v% DIO. All the films were annealed at 80 ^{o}C for 10 min in the nitrogen-filled glove box. Height images of (a and c) 500 nm × 500nm scan, and of (b and d) 3um × 3um scan. The scale bar is 100 nm in (a) and (c), and 600 nm in (b) and (d), respectively.

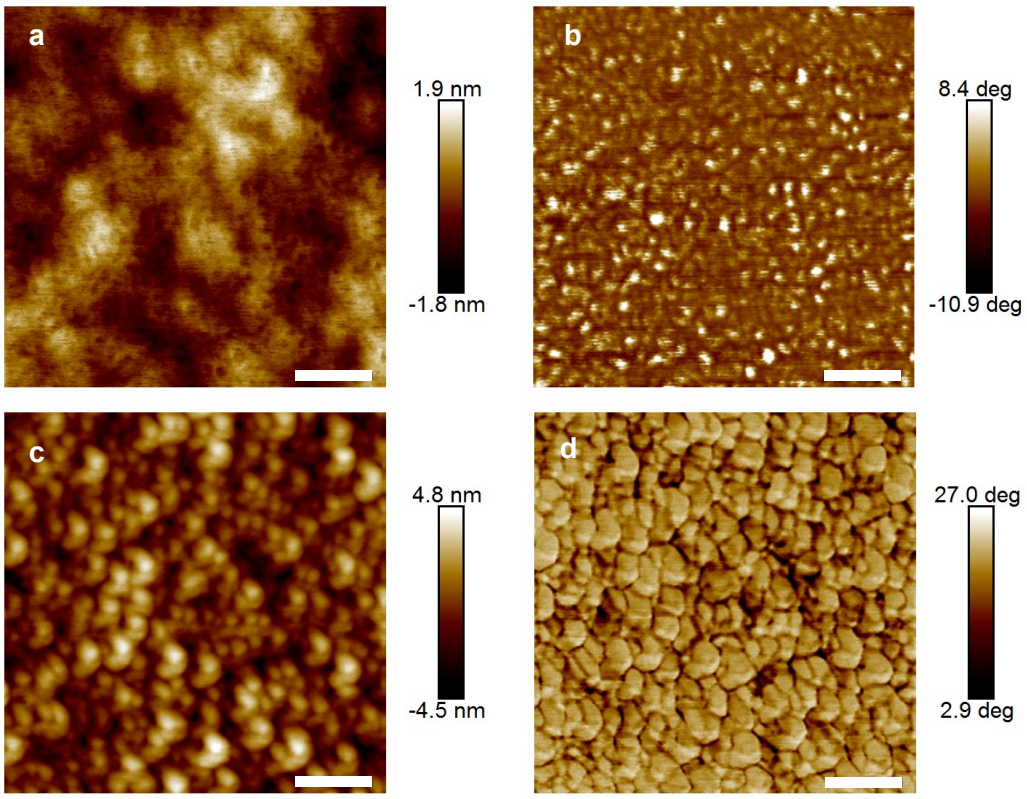

Figure 4.28. Top surface (a and b) and internal (c and d) morphology of PTB7:hPDI3 blend films at a mass ratio of 1:1.5 processed from chlorobenzene solutions with 1v/v% DIO. All the films were annealed at 80 ºC for 10 min in the nitrogen-filled glove box. (a) Height image of top surface, (b) phase image of top surface, (c) height image of internal morphology and (d) phase image of internal morphology. The scale bar is 100 nm.

Table 4.2. Summary of device parameters of best PTB7:hPDI3 solar cells with different conditions.

PTB7:hPDI3	J_{sc} (mAcm^{-2}) Highest/Avg.	V_{oc} (V) Highest/Avg.	FF (%) Highest/Avg.	PCE (%) Highest/Avg.
1.5:1	12.1/12.0 ± 0.2	0.76/0.75 ± 0.01	49/48 ± 1	4.5/4.4 ± 0.1
1:1	12.7/ 12.5 ± 0.2	0.77/0.76 ± 0.01	56/55 ± 1	5.5/5.4 ± 0.1

1:1.5	13.3/ 13.1 ± 0.2	0.77/0.76 ± 0.01	61/60 ± 1	6.2/6.1 ± 0.1
1:1.5 w/ 1% DIO	13.2/13.0 ± 0.2	0.77/ 0.76 ± 0.01	63/62 ± 1	6.4/6.3 ± 0.1

Table 4.3. Summary of device parameters of best PTB7-Th:hPDI3 solar cells with different conditions.

PTB7-Th:hPDI3	J_{sc} (mAcm^{-2}) Highest/Avg.	V_{oc} (V) Highest/Avg.	FF (%) Highest/Avg.	PCE (%) Highest/Avg.
1.5:1	14.4/14.1 ± 0.3	0.75/0.75 ± 0.01	47/ 47 ± 1	5.1/4.9 ± 0.2
1:1	14.7/14.5 ± 0.2	0.78/0.77 ± 0.01	56/55 ± 1	6.4/6.3 ± 0.1
1:1.5	14.8/14.5 ± 0.3	0.77/0.77 ± 0.01	62 /62 ± 1	7.1/6.9 ± 0.2
1:1.5 w/ 1% DIO	14.5/14.3 ± 0.3	0.81/0.80 ± 0.01	67/67 ± 1	7.9/7.7 ± 0.2

Table 4.4. Summary of device parameters of best PTB7:hPDI4 solar cells with different conditions.

PTB7:hPDI4	J_{sc} (mAcm^{-2}) Highest/Avg.	V_{oc} (V) Highest/Avg.	FF (%) Highest/Avg.	PCE (%) Highest/Avg.
1.5:1	12.2/12.0 ± 0.3	0.78/0.77 ± 0.01	60/59 ± 1	5.7/5.4 ± 0.3
1:1	13.1/12.9 ± 0.2	0.77/0.76 ± 0.01	62/61 ± 1	6.2/6.1 ± 0.1
1:1.5	12.2/12.1 ± 0.2	0.76/0.76 ± 0.01	62/62 ± 1	5.8/5.6 ± 0.2
1:1 w/ 1% DIO	12.9/12.7 ± 0.3	0.79/0.78 ± 0.01	64/63 ± 1	6.5/6.4 ± 0.1

Table 4.5. Summary of device parameters of best PTB7-Th:hPDI4 solar cells with different conditions.

PTB7-Th:hPDI4	J_{sc} (mAcm^{-2})	V_{oc} (V)	FF (%)	PCE (%)
1.5:1	14.5/14.5 ± 0.2	0.74/0.74 ± 0.01	46/45 ± 1	4.9/4.7 ± 0.2
1:1	15.0/14.9 ± 0.3	0.77/0.77 ± 0.01	61/61 ± 1	7.1/7.0 ± 0.1
1:1.5	13.4/13.2 ± 0.2	0.78/0.78 ± 0.01	65/65 ± 1	6.8/6.6 ± 0.2
1:1 w/ 1% DIO	15.2/15.0 ± 0.2	0.80/0.80 ± 0.01	68/68 ± 1	8.3/8.1 ± 0.2

Table 4.6. Summary of saturated photocurrent, exciton generation rate and charge collection probability at J_{sc} condition of best solar cells.

	PTB7:hPDI3	PTB7:hPDI4	PTB7-Th:hPDI3	PTB7-Th:hPDI4
$\boldsymbol{J_{ph,sat}}$ **(mAcm^{-2})**	14.1	13.6	15.0	15.6
$\boldsymbol{G_{max}}$ **(cm^{-3}s^{-1})**	8.8 x 10^{21}	8.5 x 10^{21}	9.4 x 10^{21}	9.7 x 10^{21}
$\boldsymbol{P_c}$ **($\boldsymbol{J_{sc}}$)**	0.94	0.97	0.97	0.97

Supplementary Note 1. DFT calculation methods. All quantum chemical calculations were performed using Jaguar, version 8.2, Schrodinger, Inc., New York, NY, 2013. (See A. D. Bochevarov, E. Harder, T. F. Hughes, J. R. Greenwood, D. A. Braden, D. M. Philipp, D. Rinaldo, M. D. Halls, J. Zhang, R. A. Friesner, "Jaguar: A HighPerformance Quantum Chemistry Software Program with Strengths in Life and Materials Sciences", Int. J. Quantum Chem., 2013, 113(18), 2110-2142). All geometries were optimized using the B3LYP functional and the 6-31G** basis set. In the case of each molecule, the energies of the different conformations were compared by performing additional calculations at the several optimized geometries using the larger cc-pvtz basis set. We observe no significant energy differences between the different local minima in either case.

To simplify the calculations, we replaced the $C_{11}H_{23}$ side chain attached to each nitrogen atom with a single H. The influence of alkyl N-substituents on the electronic structures is negligible due to the nodes of frontier orbitals at the imide nitrogens. The twisted conformation of the molecules is a consequence of repulsion between the two C −H bonds on the inner bay position of adjacent perylene diimide (PDI) units. DFT calculations show that hPDI3 has two isoenergetic conformers while hPDI4 has three. Multiple conformations originate from the relative helicity at each of the fusing points of adjacent PDI units.

Supplementary Note 2. Carrier mobility measurement. Carrier mobility was measured by space charge limit current (SCLC) method. Hole-only devices were fabricated with a device configuration of ITO/PEDOT:PSS/PTB7-Th:hPDI3 or hPDI4/MoO_3/Al. Electron-only devices were fabricated with a device configuration of ITO/ZnO/ PTB7-Th:hPDI3 or hPDI4/Al. The mobility was determined by fitting the dark current to the model of a single carrier SCLC, described by the equation:

$$J = \frac{9}{8}\varepsilon_0\varepsilon_r\mu\frac{V^2}{d^3} \quad (1)$$

where J is the current density, μ is the carrier mobility under zero field, ε_0 is the permittivity of free space, ε_r is the material relative permittivity (assumed to be 3 here), d is the active layer thickness (100 nm for PTB7-Th:hPDI3 and 110nm for PTB7-Th:hPDI4), and V is the effective voltage. The effective voltage can be obtained by subtracting the built-in voltage (V_{bi}) from the applied voltage (V_a), $V=V_a - V_{bi}$. V_{bi} is 0 V for hole-only devices and 0.23 V for electron-only devices. The carrier mobility can be calculated from the slope of the $J^{0.5}$~V curves. The mobility values were averaged from 4 devices for each one.

Supplementary Note 3. Exciton/carrier dynamics. Supplementary Figure 18

shows exciton/carrier dynamics upon 670 nm excitation. The excited state absorption (ESA) exciton dynamics at 1410 nm (grey curve) for the neat PTB7 film decays bi-exponentially with two time constants of 3.25 ± 0.2 ps and 56 ± 2 ps. In the blend, the dynamics at this wavelength (green) decays with one order of magnitude shorter lifetimes in comparison to that of the neat film indicating of ultrafast electron transfer from PTB7 to hPDI3. While the exciton feature for PTB7 in the blends rapidly decay, the dynamics at 555 and 765 nm decay much slower with time constants of 275 ± 40 ps and 6.5 ± 0.6 ns. The slower decay is attributed to bimolecular recombination between electron in hPDI3 and hole in PTB7.

Supplementary Note 4. Assignment of excited state absorption. Supplementary Figure 20 shows normalized dynamics at different probe wavelengths upon 415 nm excitation at 160 μJcm^{-2} excitation intensity for the blended film. At this high pump intensity, the carrier-carrier annihilation takes place in PTB7 and hPDI3 domains. The annihilation rate depends on the charge density and mobility in each domain. The dynamics at 555 (red) and 680 (blue) nm represent to the bleaching dynamics of hPDI3 and PTB7 in the blend, respectively. These bleaching dynamics decay differently because carrier-carrier annihilation rates are different in these two domains. While the ESA dynamics at 485 nm (black) is similar to that at 555 nm, the ESA dynamics at 1120 nm (green) is similar to 1120 nm dynamics. These results suggest that the ESA at 485 nm comes from polaron (electron) absorption in hPDI3 while the ESA at 1120 nm comes from polaron (hole) absorption in PTB7. The ESA dynamics at 765 nm (purple) decays as a mixing of bleaching dynamics in hPDI3 and PTB7 indicates that at this probe wavelength region there is an overlap of ESAs for polarons in both donor and acceptor.

Supplementary Note 5. Ultrafast fluorescence upconversion. The fluorescence

upconversion experiment was based on a Ti: Sapphire regenerative amplifier laser system with average power of 1.1 W, lasing wavelength of 805 nm, repetition rate of 250 kHz and pulse duration of about 100 fs (Coherent Mira seeded RegA). 85% of fundamental pulse was sent to pump Coherent optical parametric amplifier, from which 508 nm excitation beam was generated. The fluorescence emitted from the sample was collected and focused into a 0.5 mm thick type I BBO crystal by a pair of off-axis parabolic silver mirror and spatially overlapped with the rest (15%) of fundamental beam as gate pulse. The upconverted emission was sent through a monochromator (corresponding to emission wavelength at 580 nm, the peak of hPDI3 emission) and detected by photomultiplier tube.

Supplementary Note 6. Atomic force microscopy. AFM measurements were carried out in tapping mode and PeakForce QNM (Quantitative NanoMechanics) mode on a Bruker Multi-Mode AFM at ambient conditions. A commercial silicon cantilever (RTESPA, MPP-11120-10, Bruker) was used in this study with a typical radius of curvature of ~8 nm and a nominal spring constant of ~40 Nm^{-1}. Nanomechanical mapping was operated at constant peak force. The etching treatment was performed on the sample surface using O_2 plasma (Plasma Etch Inc. Model: PE-50) to etch out ~30 nm from the top surface. The reduced Young's Modulus, E^*, is obtained by fitting the retract curve using the Derjaguin, Muller, Toropov (DMT) model given by

$$F_{\text{tip}} = \frac{4}{3}E^*\sqrt{Rd^3} + F_{\text{adh}} \quad (2)$$

where F_{tip} is the force on the tip, F_{adh} is the adhesion force, R is the tip end radius and d is the tip sample separation. The reduced modulus is related to the sample modulus by the following equation:

$$E^* = \left[\frac{1-\nu_t^2}{E_t} + \frac{1-\nu_s^2}{E_s}\right]^{-1} \quad (3)$$

where ν_t and E_t are the Poisson's ratio and Young's modulus of the tip and ν_s and E_s are the Poisson's ratio and Young's modulus of the sample. We assume that the tip modulus, E_t, is much larger than the sample modulus, E_s, and can be approximated as infinite and calculate the sample modulus using the sample Poisson's Ratio. Poisson's ratio generally ranges between about 0.2 and 0.5 (perfectly incompressible) giving a difference between the reduced modulus and the sample modulus between 4% and 25%. Because the sample's Poisson's ratio is not generally known, here we report reduced Young's modulus as many publications do.[46]

4.9 References and notes

(1) Liu, Y.; Zhao, J.; Li, Z.; Mu, C.; Ma, W.; Hu, H.; Jiang, K.; Lin, H.; Ade, H.; Yan, H. *Nat. Commun.* **2014**, *5*, 5293.

(2) Liao, S. H.; Jhuo, H. J.; Yeh, P. N.; Cheng, Y. S.; Li, Y. L.; Lee, Y. H.; Sharma, S.; Chen, S. A. *Sci. Rep.* **2014**, *4*, 6813.

(3) Heliatek consolidates its technology leadership by establishing a new world record for organic solar technology with a cell efficiency of 12%. Available at http://www.heliatek.com/en/press/press-releases/details/heliatek-consolidates-its-technology-leadership-by-establishing-a-new-world-record-for-organic-solar-technology-with-a-cell-effi. (January, 2013).

(4) Liang, Y.; Xu, Z.; Xia, J.; Tsai, S.-T.; Wu, Y.; Li, G.; Ray, C.; Yu, L. *Adv. Mater.* **2010**, *22*, E135.

(5) Liao, S.-H.; Jhuo, H.-J.; Cheng, Y.-S.; Chen, S.-A. *Adv. Mater.* **2013**, *25*, 4766.

(6) Lee, J. K.; Ma, W. L.; Brabec, C. J.; Yuen, J.; Moon, J. S.; Kim, J. Y.; Lee, K.; Bazan, G. C.; Heeger, A. J. *J. Am. Chem. Soc.* **2008**, *130*, 3619.

(7) He, Z. C.; Zhong, C. M.; Su, S. J.; Xu, M.; Wu, H. B.; Cao, Y. *Nature Photon.* **2012**, *6*, 591.

(8) Page, Z. A.; Liu, Y.; Duzhko, V. V.; Russell, T. P.; Emrick, T. *Science* **2014**, *346*, 441.

(9) Zhang, Z.-G.; Qi, B.; Jin, Z.; Chi, D.; Qi, Z.; Li, Y.; Wang, J. *Energy Environ. Sci.* **2014**, *7*, 1966.

(10) You, J.; Dou, L.; Yoshimura, K.; Kato, T.; Ohya, K.; Moriarty, T.; Emery, K.; Chen, C.-C.; Gao, J.; Li, G.; Yang, Y. *Nat. Commun.* **2013**, *4*, 1446.

(11) Lu, L. Y.; Xu, T.; Chen, W.; Landry, E. S.; Yui, L. P. *Nature Photon.* **2014**, *8*, 716.

(12) Cnops, K.; Rand, B. P.; Cheyns, D.; Verreet, B.; Empl, M. A.; Heremans, P. *Nat. Commun.* **2014**, *5*, 3406.

(13) Dou, L.; You, J.; Hong, Z.; Xu, Z.; Li, G.; Street, R. A.; Yang, Y. *Adv. Mater.* **2013**, *25*, 6642.

(14) Savoie, B. M.; Rao, A.; Bakulin, A. A.; Gelinas, S.; Movaghar, B.; Friend, R. H.; Marks, T. J.; Ratner, M. A. *J. Am. Chem. Soc.* **2014**, *136*, 2876.

(15) Zang, Y.; Li, C. Z.; Chueh, C. C.; Williams, S. T.; Jiang, W.; Wang, Z. H.; Yu, J. S.; Jen, A. K. *Adv. Mater.* **2014**, *26*, 5708.

(16) Zhong, Y.; Trinh, M. T.; Chen, R.; Wang, W.; Khlyabich, P. P.; Kumar, B.; Xu, Q.; Nam, C.-Y.; Sfeir, M. Y.; Black, C.; Steigerwald, M. L.; Loo, Y.-L.; Xiao, S.; Ng, F.; Zhu, X. Y.; Nuckolls, C. *J. Am. Chem. Soc.* **2014**, *136*, 15215.

(17) Lin, Y.; Wang, J.; Zhang, Z. G.; Bai, H.; Li, Y.; Zhu, D.; Zhan, X. *Adv. Mater.* **2015**, *27*, 1170.

(18) Lin, Y. Z.; Zhang, Z. G.; Bai, H. T.; Wang, J. Y.; Yao, Y. H.; Li, Y. F.; Zhu, D. B.; Zhan, X. W. *Energy Environ. Sci.* **2015**, *8*, 610.

(19) Jung, J. W.; Jo, J. W.; Chueh, C. C.; Liu, F.; Jo, W. H.; Russell, T. P.; Jen, A. K. *Adv. Mater.* **2015**, *27*, 3310.

(20) Zhong, Y.; Kumar, B.; Oh, S.; Trinh, M. T.; Wu, Y.; Elbert, K.; Li, P.; Zhu, X.; Xiao, S.; Ng, F.; Steigerwald, M. L.; Nuckolls, C. *J. Am. Chem. Soc.* **2014**, *136*, 8122.

(21) Hiszpanski, A. M.; Saathoff, J. D.; Shaw, L.; Wang, H.; Kraya, L.; Lüttich, F.; Brady, M. A.; Chabinyc, M. L.; Kahn, A.; Clancy, P.; Loo, Y.-L. *Chem. Mater.* **2015**, *27*, 1892.

(22) Li, H.; Earmme, T.; Ren, G.; Saeki, A.; Yoshikawa, S.; Murari, N. M.; Subramaniyan, S.; Crane, M. J.; Seki, S.; Jenekhe, S. A. *J. Am. Chem. Soc*.**2014**, *136*, 14589.

(23) Ball, M.; Zhong, Y.; Wu, Y.; Schenck, C.; Ng, F.; Steigerwald, M.; Xiao, S.; Nuckolls, C. *Acc. Chem. Res.* **2015**, *48*, 267.

(24) Savoie, B. M.; Kohlstedt, K. L.; Jackson, N. E.; Chen, L. X.; Olvera de la Cruz, M.; Schatz, G. C.; Marks, T. J.; Ratner, M. A. *Proc. Natl. Acad. Sci. U. S. A.* **2014**, *111*, 10055.

(25) Chen, J. D.; Cui, C.; Li, Y. Q.; Zhou, L.; Ou, Q. D.; Li, C.; Li, Y.; Tang, J. X. *Adv. Mater.* **2015**, *27*, 1035.

(26) Cui, C.; Wong, W.-Y.; Li, Y. *Energy Environ. Sci.* **2014**, *7*, 2276.

(27) Cowan, S. R.; Roy, A.; Heeger, A. J. *Physical Review B* **2010**, *82*, 245207.

(28) Malliaras, G. G.; Salem, J. R.; Brock, P. J.; Scott, C. *Phys. Rev. B* **1998**, *58*, R13411.

(29) Lee, B. R.; Jung, E. D.; Nam, Y. S.; Jung, M.; Park, J. S.; Lee, S.; Choi, H.; Ko, S.-J.; Shin, N. R.; Kim, Y.-K.; Kim, S. O.; Kim, J. Y.; Shin, H.-J.; Cho, S.; Song, M. H. *Adv. Mater.* **2014**, *26*, 494.

(30) Basel, T.; Huynh, U.; Zheng, T. Y.; Xu, T.; Yu, L. P.; Vardeny, Z. V. *Adv. Funct. Mater.* **2015**, *25*, 1895.

(31) Provencher, F.; Berube, N.; Parker, A. W.; Greetham, G. M.; Towrie, M.; Hellmann, C.; Cote, M.; Stingelin, N.; Silva, C.; Hayes, S. C. *Nat. Commun.* **2014**, *5*, 4288.

(32) Gélinas, S.; Rao, A.; Kumar, A.; Smith, S. L.; Chin, A. W.; Clark, J.; van der Poll, T. S.; Bazan, G. C.; Friend, R. H. *Science* **2014**, *343*, 512.

(33) Bernardo, B.; Cheyns, D.; Verreet, B.; Schaller, R. D.; Rand, B. P.; Giebink, N. C. *Nat. Commun.* **2014**, *5*, 3245.

(34) Tamura, H.; Burghardt, I. *J. Am. Chem. Soc.* **2013**, *135*, 16364.

(35) Jailaubekov, A. E.; Willard, A. P.; Tritsch, J. R.; Chan, W.-L.; Sai, N.; Gearba, R.; Kaake, L. G.; Williams, K. J.; Leung, K.; Rossky, P. J.; Zhu, X. Y. *Nature Mater.* **2013**, *12*, 66.

(36) Kaake, L. G.; Jasieniak, J. J.; Bakus, R. C.; Welch, G. C.; Moses, D.; Bazan, G. C.; Heeger, A. J. *J. Am. Chem. Soc.* **2012**, *134*, 19828.

(37) Savoie, B. M.; Jackson, N. E.; Chen, L. X.; Marks, T. J.; Ratner, M. A. *Acc. Chem. Res.* **2014**, *47*, 3385.

(38) Chen, W.; Xu, T.; He, F.; Wang, W.; Wang, C.; Strzalka, J.; Liu, Y.; Wen, J.; Miller, D. J.; Chen, J.; Hong, K.; Yu, L.; Darling, S. B. *Nano Lett.* **2011**, *11*, 3707.

(39) Hammond, M. R.; Kline, R. J.; Herzing, A. A.; Richter, L. J.; Germack, D. S.; Ro, H.-W.; Soles, C. L.; Fischer, D. A.; Xu, T.; Yu, L.; Toney, M. F.; DeLongchamp,

D. M. *ACS Nano* **2011**, *5*, 8248.

(40) Huang, W. C.; Gann, E.; Thomsen, L.; Dong, C. K.; Cheng, Y. B.; McNeill, C. R. *Adv. Energy Mater.* **2015**, *5*, 1401259.

(41) Wang, D.; Liu, F.; Yagihashi, N.; Nakaya, M.; Ferdous, S.; Liang, X.; Muramatsu, A.; Nakajima, K.; Russell, T. P. *Nano Lett.* **2014**, *14*, 5727.

(42) Hedley, G. J.; Ward, A. J.; Alekseev, A.; Howells, C. T.; Martins, E. R.; Serrano, L. A.; Cooke, G.; Ruseckas, A.; Samuel, I. D. W. *Nat. Commun.* **2013**, *4*, 2867.

(43) Kong, J.; Hwang, I.-W.; Lee, K. *Adv. Mater.* **2014**, *26*, 6275.

(44) Jo, J.; Pouliot, J.-R.; Wynands, D.; Collins, S. D.; Kim, J. Y.; Nguyen, T. L.; Woo, H. Y.; Sun, Y.; Leclerc, M.; Heeger, A. J. *Adv. Mater.* **2013**, *25*, 4783.

(45) Shrotriya, V.; Li, G.; Yao, Y.; Moriarty, T.; Emery, K.; Yang, Y. *Adv. Funct. Mater.* **2006**, *16*, 2016.

(46) examples can be found in Bruker PeakPorce QNM user guide, www.bruker.com/products/surface-analysis/atomic-force-microscopy/modes/modes/imaging-modes/peakforce-qnm.html. (2015)

Chapter 5 Macrocyclization in the Design of Organic n-Type Electronic Materials

Chapter 5 is reproduced with permission from the authors: Ball, M.; Zhong, Y.; Fowler, B.; Zhang, B.; Li, P.; Etkin, G.; Paley, D. W.; Decatur, J.; Dalsania, A. K.; Li, H.; Xiao, S.; Ng, F.; Steigerwald, M. L.; Nuckolls, C. *J. Am. Chem. Soc.* **2016**, *138*, DOI: 10.1021/jacs.6b05474.; Copyright 2016 American Chemical Society. Deivce fabrication and characterization were performed by myself with assistance from Boyuan Zhang and Ankur K. Dalsania. Synthesis was carried out by Melissa Ball with assistance from Brandon Fowler and Panpan Li. Compound characterization was performed by Melissa Ball and myself with assistance from Grisha Etkin, Daniel W. Paley and John Decatur. DFT calculations were performed by Melissa Ball and Michael L. Steigerwald.

5.1. Introduction

We compare cyclic and acyclic π-conjugated molecules as n-type electronic materials and find that the cyclic molecules have numerous benefits in organic photovoltaics (OPVs**)**. Conjugated macrocycles[1–27] have several potential advantages as organic electronic materials: (1) their contorted structure[28] should facilitate intermolecular contacts and charge transport; (2) they lack endgroups that are known to create defects in linear polymers and act as trap-sites for charges as they move through materials;[29–33] (3) often they have an altered electronic structure;[1,7] and (4) they have a defined cavity that can be a host for electronically useful guest molecules.[6,22,34–36] Figure 1 displays the cyclic and acyclic molecules designed and synthesized for this study. The two conjugated cycles incorporate multiple repeat units of the redox-active, diphenyl-perylenediimide (**P**) subunit.

One macrocycle alternates a bithiophene (**B**) unit with a **P** unit to form the -**P**-**B**-**P**-**B**- cyclic pattern, denoted here **cPBPB**, where "**c**" denotes cyclic. A second macrocycle (**cP$_4$**) directly links the diphenyl-perylenediimide subunits into a tetrameric structure. We compare these macrocycles to a series of acyclic molecules (denoted with an "**a**" in Figure 5.1) that link varying numbers of **P** subunits and find that the conjugated cycles have bathochromically shifted UV-vis absorbances, are more easily reduced, have higher electron mobility and better morphology in blended films. All of these factors contribute to the more than doubling of the power conversion efficiency (PCE) observed in solar cells using these macrocycles as n-type, electron-transporting material. This is the first report directly comparing analogous cyclic and acyclic π-conjugated molecules as n-type materials in OPVs.

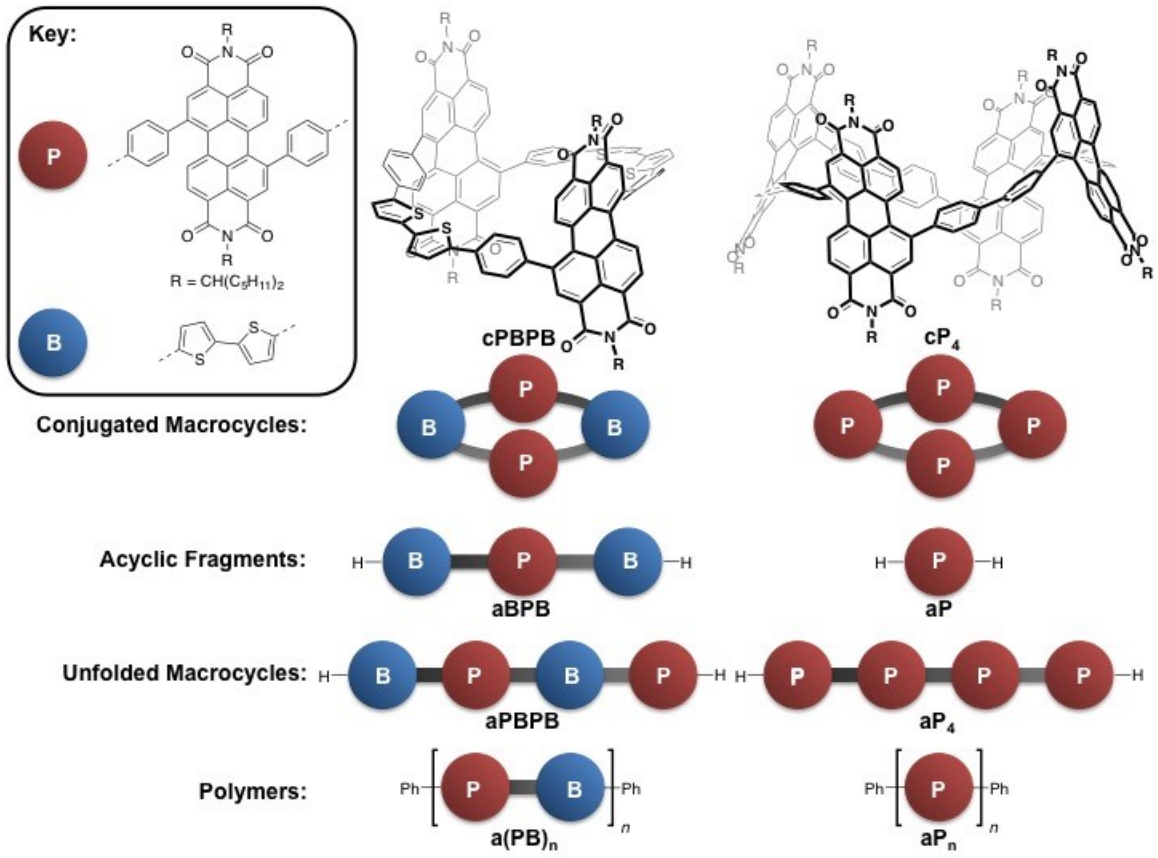

Figure 5.1. Structures of compounds designed and synthesized to compare as acyclic and cyclic, π-conjugated molecules for n-type electronic materials. We use the letter "**P**" to denote a diphenyl PDI and "**B**" for a bithiophene. Likewise, we use "**c**" and "**a**" for cyclic and acyclic, respectively.

5.2. Results and discussion

5.2.1. Design.

We designed a series of cyclic and acyclic π-conjugated molecules (Figure 5.1) that contain the redox active diphenyl-PDI subunit. PDIs possess many desirable properties such as efficient electron transport,[37–41] high molar absorptivities,[28,42,43] and ease of functionalization.[44–46] Derivatives of PDI are efficacious in solar cells when combined with electron rich conjugated polymers.[43,47–49] We have developed a method to regioselectively create diaryl substituted versions of the PDI. From these diaryl substituted PDI subunits, we build the two macrocycles, **cPBPB** and **cP$_4$**, using a tetranucleur platinum macrocyclization followed by reductive eliminations.[4,7,14] The DFT minimized structures for **cPBPB**[20] and **cP$_4$** are shown in Figure 5.2.

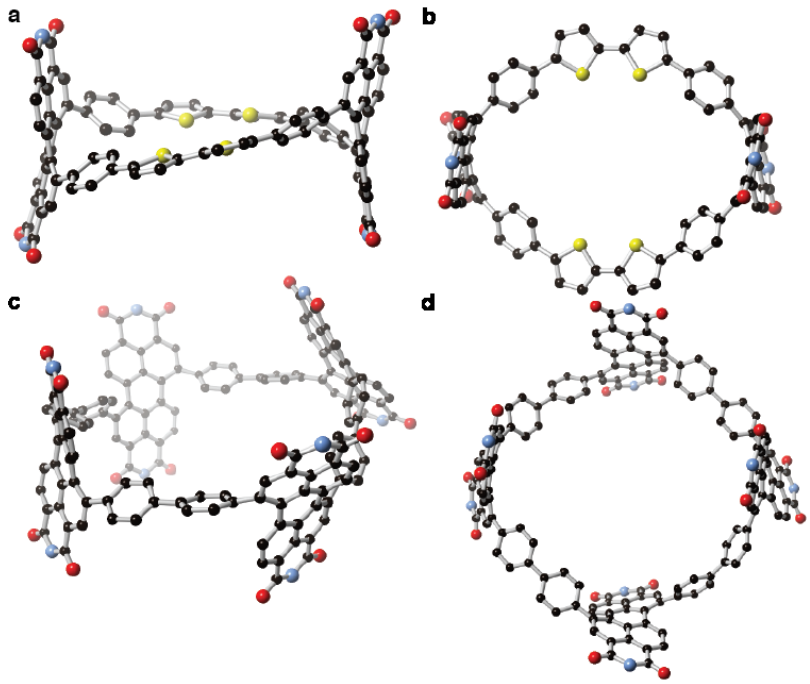

Figure 5.2. (a) Energy minimized structures from DFT for **cPBPB**. The (*S,S*)-stereoisomer is shown.[20] (b) Cavity view of **cPBPB**. (c) Energy minimized structures from DFT for **cP$_4$**. The (*S,S,S,S*)-stereoisomer is shown. (d) Cavity view for **cP$_4$**. Carbon = gray, nitrogen = blue, oxygen = red, sulfur = yellow. Hydrogen atoms have been removed to clarify the view. A methyl group substitutes the sidechains in the calculations. The methyl group, too, has been removed to clarify the view in the structures presented here.

For comparison to **cPBPB** and **cP$_4$**, we synthesized a series of acyclic molecules (also shown in Figure 5.1). The simplest structures are **aBPB** and **aP**, each possesses one **P** subunit. We also synthesized the precise analogs, "unfolded" macrocycles, that have one of their bonds cleaved and terminated with hydrogen atoms (**aPBPB** and **aP$_4$**). As a final point of comparison, we created the polymeric version of the macrocycles [**a(PB)$_n$** and **aP$_n$**]. The Supporting Information contains details of the synthesis and characterization of the cyclic and acyclic molecules used in this study.

5.2.2. OPVs.

We fabricated devices from each of these macrocyclic and acyclic molecules. We chose the low-bandgap semiconducting polymer poly[4,8-bis(5-(2-ethylhexyl)thiophen-2-yl)benzo[1,2-b;4,5-b′]dithiophene-2,6-diyl-alt-(4-(2-ethylhexyl)-3-fluorothieno[3,4-b]thiophene)-2-carboxylate-2,6-diyl] (PTB7-Th)[50,51] as the electron donating component in our devices. PTB7-Th is widely used as a high-performance donor material in both fullerene and non-fullerene based solar cells.[52,53] PTB7-Th is complementary to all molecules synthesized, as it absorbs more low energy light (~550 nm to 800 nm). Figure 5.7 contains the film absorption spectra for all the compounds. We spin cast the mixture of PTB7-Th and the cyclic or acyclic molecules to form a bulk heterojunction (BHJ) solar cell.[54] We used an inverted configuration of ITO/ZnO(20 nm)/PTB7-Th:acceptor/MoO_3(7 nm)/Ag(100 nm) for all of our solar cell devices.[55] A schematic of the device is shown in Figure 5.3a.

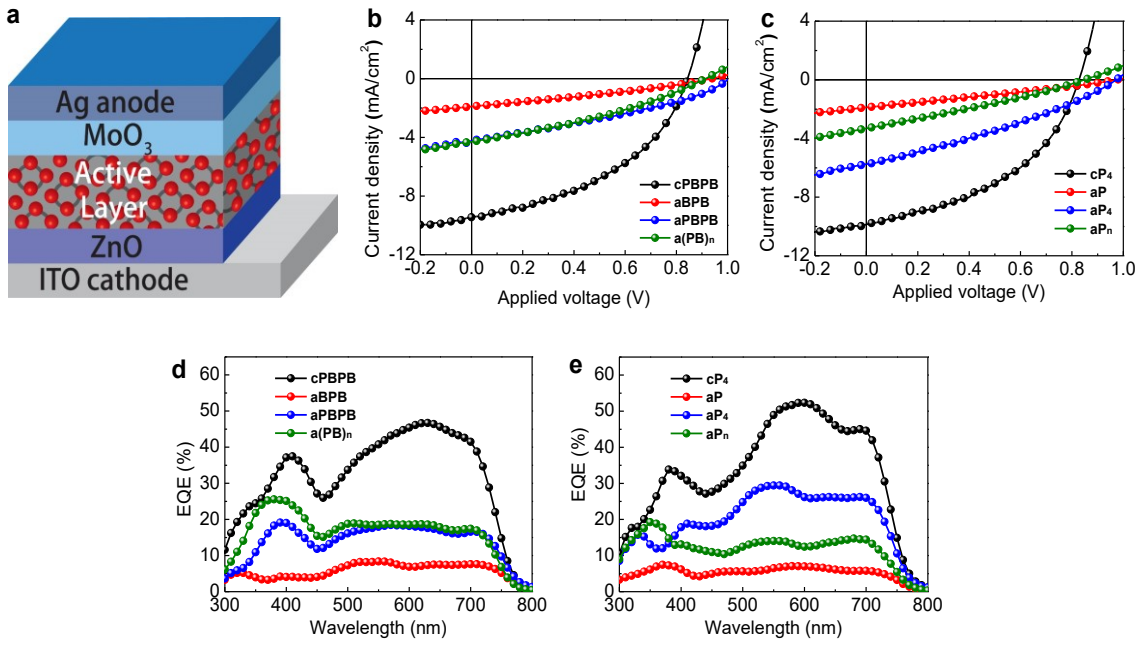

Figure 5.3. (a) Schematic of the solar cell device fabricated in this study. (b-e) *J-V* curves

for (b) **cPBPB**-series and (c) **cP4**-series solar cells under simulated AM 1.5G irradiation (100 mWcm^{-2}). EQE spectra for (d) **cPBPB** -series and (e) **cP4**-series solar cells.

Figure 5.3b-e displays the OPV properties and the EQE measurements for each of the cyclic and acyclic molecules. Details for the optimization including varying the ratio of donor and acceptor, the additives and the film thickness are included in the Section 5.5. The optimal active layers were ~100 nm in thickness. For the cyclic molecules, the optimal mass ratio was 1:2 for donor:acceptor. Furthermore, we optimized the films by using 1-chloronaphthalene (CN) as a solvent additive to control film morphology (Figure 5.10).[41] **cPBPB**'s PCE increases to 3.3% on average with a maximal value of 3.5%. Using an analogous procedure, we were able to achieve a PCE of 3.6% for **cP4** (see Figure 5.9, Table 5.4 and Table 5.1). This is the first example of a macrocycle being used as the electron acceptor in an OPV.

Figure 5.3d and Figure 5.3e show the external quantum efficiency (EQE) curves for PTB7-Th:**cPBPB** and the PTB7-Th:**cP4** solar cells. All the devices show broad photo-response from 350 nm to 800 nm, consistent with the absorption spectra (Figure 5.7). Each EQE spectrum shows two transitions; a narrow band centered at ~400 nm and a broad band centered at 620 nm for **cPBPB** and at 600 nm for **cP4**. The EQE spectrum for **cP4** shows an increase relative to **cPBPB** at ~700 nm. We note that both macrocycles show strong absorption from 400 nm to 650 nm (see Figure 5.4), indicating that photoexcitation in acceptor domains contributes to photocurrent in this type of solar cell. The integrated J_{sc} values are 9.2 and 9.8 mAcm^{-2} for PTB7-Th:**cPBPB** and the PTB7-Th:**cP4** solar cells , respectively. These values agree well with the measured J_{sc}, with a < 3% mismatch. Upon addition of the CN additive, the EQE enhances over a broad range of wavelengths,

particularly from 550 nm to 750 nm (Figure 5.8 and Figure 5.9). Atomic force microscopy (AFM) of the films confirms that CN changes the film morphology, resulting in more efficient charge dissociation and transport (Figure 5.10). Like $PC_{71}BM$ and some non-fullerene acceptors,[47,52] complementary absorption between the macrocycles and the donor material is beneficial for harvesting light in the visible light region to maximize photocurrent.

Table 5.1. Summary of device parameters of the solar cells based on the cyclic and acyclic molecules. Highest PCE values are shown in parentheses.

	J_{sc} (mA cm^{-2})	V_{oc} (V)	FF	PCE (%)
cPBPB	9.2 ± 0.3	0.84 ± 0.01	0.44 ± 0.01	3.3 ± 0.2 (3.5)
aBPB	1.6 ± 0.2	0.94 ± 0.01	0.30 ± 0.01	0.46 ± 0.04 (0.53)
aPBPB	4.2 ± 0.1	1.00 ± 0.01	0.33 ± 0.01	1.3 ± 0.1 (1.4)
a(PB)$_n$	4.2 ± 0.2	0.90 ± 0.01	0.33 ± 0.01	1.1 ± 0.2 (1.3)
cP$_4$	9.7 ± 0.2	0.83 ± 0.01	0.44 ± 0.01	3.5 ± 0.1 (3.6)
aP	1.7 ± 0.1	0.97 ± 0.02	0.28 ± 0.01	0.46 ± 0.03 (0.51)
aP$_4$	5.8 ± 0.1	0.97 ± 0.01	0.32 ± 0.01	1.6 ± 0.2 (1.8)
aP$_n$	3.2 ± 0.1	0.85 ± 0.01	0.28 ± 0.01	0.73 ± 0.04 (0.78)

We next compare the OPV results from the cyclic molecules to the acyclic molecules. Table 5.1 summarizes the device data. The key finding is that all of the acyclic molecules showed poor device performance on both an absolute and relative bases. Figure 5.3b and 5.3c display the *J-V* curves for all the devices. We observe a couple of trends from this study: (1) smaller oligomer acyclic molecules (**aBPB, aPBPB**, **aP** and **aP$_4$**) and the

polymers [**a(PB)$_n$** and **aP$_n$**] show decreased J_{sc} relative to the cyclic compounds; (2) the acyclic molecules also show higher V_{oc} values as compared to the cyclic acceptors; and (3) the poor PCEs in the devices from acyclic molecules are mainly attributed to the reduced J_{sc} and FFs relative to the cyclic ones. Figure 5.3d and 5.3e display comparison of external quantum spectra of the cyclics versus the acyclics. Overall, the photocurrent generation in cyclic-based devices is much larger than the acyclic-based devices. These results indicate that the cyclic acceptors have enhanced photocarrier generation and better charge transport.

To better understand the performance difference between the cyclic and acyclic molecules, we examined the electrochemistry, UV-vis absorption, electron mobility and morphology of the films. These studies are described below.

5.2.3. Electrochemistry.

We probe the variations in the frontier orbital energies for the macrocycles and their acyclic analogues using cyclic voltammetry (CV) (see Figure 5.11 in the Section 5.5). The onset of the first oxidation and reduction peaks provide an estimate of the highest occupied molecular orbital (HOMO) and lowest unoccupied molecular orbital (LUMO) levels, respectively.[56] We find the acyclic molecules possess a more negative first reduction potential than the cyclic molecules. As a result, we observe higher energies for the LUMO for each of the acyclic molecules. The electrochemical data are summarized in Table 5.2.

The energy offset between the donor's HOMO and acceptor's LUMO is one of the factors that determines the V_{oc}s in BHJ solar cells.[57] The values obtained from CV results are in good agreement with the V_{oc} trend from the devices. Previous studies show a direct correlation between relatively large V_{oc} values coupled with low J_{sc} when the band offset does not provide sufficient driving force for exciton dissociation at the donor/acceptor

interfaces.[58,59] Here, the observed trend suggests that the high LUMO levels, particularly in the short acyclic compounds, result in a higher occurrence of recombination and lower $J_{sc.}$[59,60]

Table 5.2. Comparison of the band-gaps estimated from CV and UV-vis absorption spectroscopy, and OFET performance.

	Electrochemical[a]			Optical[b]	FET
	E_{LUMO}/eV	E_{HOMO}/eV	E_{gap} /eV	E_{gap} /eV	μ /$cm^2V^{-1}s^{-1}$
cPBPB	-3.87	-5.39	1.52	2.02	$(1.5 \pm 0.2)\times10^{-3}$
aBPB	-3.80	-5.42	1.62	2.18	$(4.3 \pm 0.2)\times10^{-4}$
aPBPB	-3.80	-5.40	1.60	1.79	-
a(PB)$_n$	-3.86	-5.45	1.59	2.21	$(2.3 \pm 0.3)\times10^{-4}$
cP$_4$	-3.90	-5.69	1.79	2.12	$(1.5 \pm 0.2)\times10^{-3}$
aP	-3.75	-	-	2.25	$(2.0 \pm 0.3)\times10^{-5}$
aP$_4$	-3.82	-5.77	1.95	2.23	-
aP$_n$	-3.86	-5.75	1.89	2.21	$(1.9 \pm 0.3)\times10^{-5}$

[a]HOMO and LUMO levels were estimated from onset of the first oxidation and reduction peaks. [b]Optical band gaps were estimated from the wavelength at the absorption maximum.

5.2.4. Absorption Spectroscopy.

Figure 5.4 compares the UV-vis absorption spectra of **cPBPB** and **cP$_4$** to their acyclic counterparts. It is well documented that contorting linear molecules into cyclic structures significantly alters the electronic properties.[7,1] Absorptions in the cyclic compounds are bathochromically shifted relative to the linear, unstrained acyclic molecules. The CV data is also consistent with the UV-vis data. **cPBPB** and **cP$_4$** have smaller HOMO-LUMO gaps relative to each of the corresponding acyclic molecules studied (Figure 5.4). Greater visible light absorption contributes to the more efficient solar cells for the cyclic molecules, providing the higher J_{sc} parameter for the cyclic molecules relative to the

acyclic molecules.

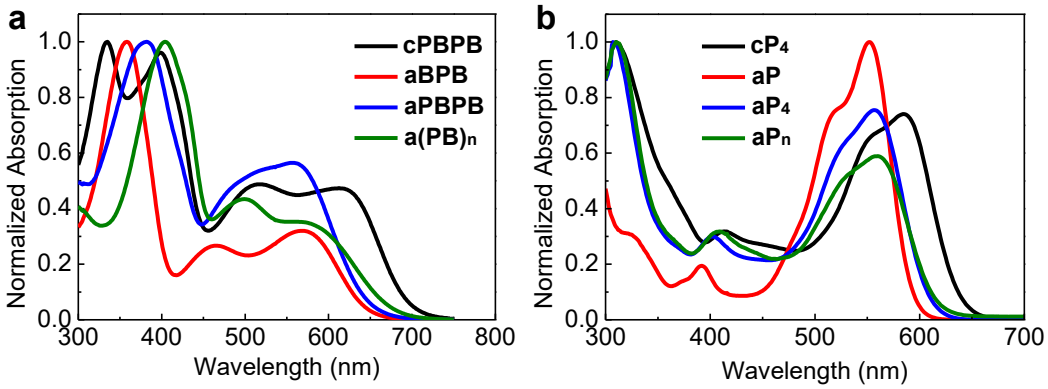

Figure 5.4. UV-vis absorption spectra measured in solution: (a) for **cPBPB, aBPB, aPBPB** and **a(PB)$_n$** (b) for **cP$_4$**, **aP**, **aP$_4$**, and **aP$_n$** normalized to each absorption maxima, where absorption max = 1.

5.2.5. Electron mobility.

Another factor that is critical for OPV device performance is electron transport through the acceptor phase. Poor carrier mobility impedes the carrier extraction and results in increased carrier recombination inside OPV devices. This negatively impacts the J_{sc}, FF and overall solar cell performance. To investigate the electron mobility of these compounds, we fabricated organic field-effect transistors (OFETs). All molecules measured form n-type, electron-transporting thin-film semiconductors.[37,61] Figure 5.5 displays typical transfer curves in the saturation regime. The mobility was calculated in the saturation regime using $I_{DS} = (W/2L)C_i\mu(V_G - V_T)^2$, where W and L are the width and length of the channel, C_i (11.5 nFcm^{-2}), μ, and V_T correspond to the capacitance per unit area of the gate insulator, the field effect mobility, and the threshold voltage, respectively.[62] Both **cPBPB** and **cP$_4$** show electron mobility of $(1.5 \pm 0.2) \times 10^{-3}$ cm^{2}V^{-1}s^{-1}. One of the key findings is the cyclic molecules have a far greater ability to transport electrons in thin-film devices

relative to the acyclic molecules. Table 5.2 shows electron mobility for six of the compounds studied. **cPBPB**'s average mobility is five-fold higher than its acyclic counterparts; **cP$_4$**'s mobility is nearly two orders of magnitude higher than its counterparts. The cyclic structures' far greater ability to transport electrons contributes to the overall better solar cell performance.

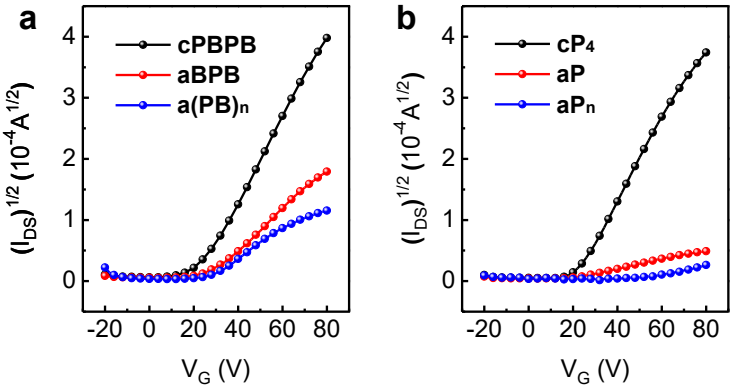

Figure 5.5. OFET transfer characteristics plotted in $(I_{DS})^{1/2}$-V_G axes for (a) **cPBPB, aBPB** and **a(PB)$_n$** (b) for **cP$_4$**, **aP**, and **aP$_n$**. The V_{DS} is 80V.

5.2.6. Morphology.

At the nanoscale level, phase separation between the donor and the acceptor plays an important role in providing an efficient donor/acceptor interface and a continuous pathway for carrier transport. Appropriate aggregation and phase separation is critical to device performance of BHJs in terms of charge dissociation and carrier transport. We performed AFM to study the surface morphology of the active layers. Figure 5.6 displays phase images of the six active layers studied. The corresponding height images are displayed in Figure 5.12. For both **cPBPB** and **cP$_4$**, the active layers possess clear phase separation as shown in Figure 5.6a and 5.6d. The average domain size is estimated to be 20-40 nm. For the polymeric **a(PB)$_n$** and **aP$_n$**, the domain sizes are relatively small (10-30nm). It is difficult to detect efficient phase segregation in these films. The active layers

containing **aBPB** and **aP** have large domain sizes; they are in the range of 50-70nm, as shown in Figure 5.6b and 5.6e. These features exceed twice the typical exciton diffusion length (ca. 10-20nm) in organic semiconductors. Thus, photogenerated excitons within the domain recombine before they reach the donor/acceptor interface.[54,63] The over-aggregation in the **aBPB** and **aP** solar cells likely results in carrier recombination and poor device performance. In the **cPBPB**- and **cP$_4$**-based BHJ systems, phase aggregation is essential to the device performance as it enables an efficient donor/acceptor interface and a 3D continuous pathway for efficient carrier transport.

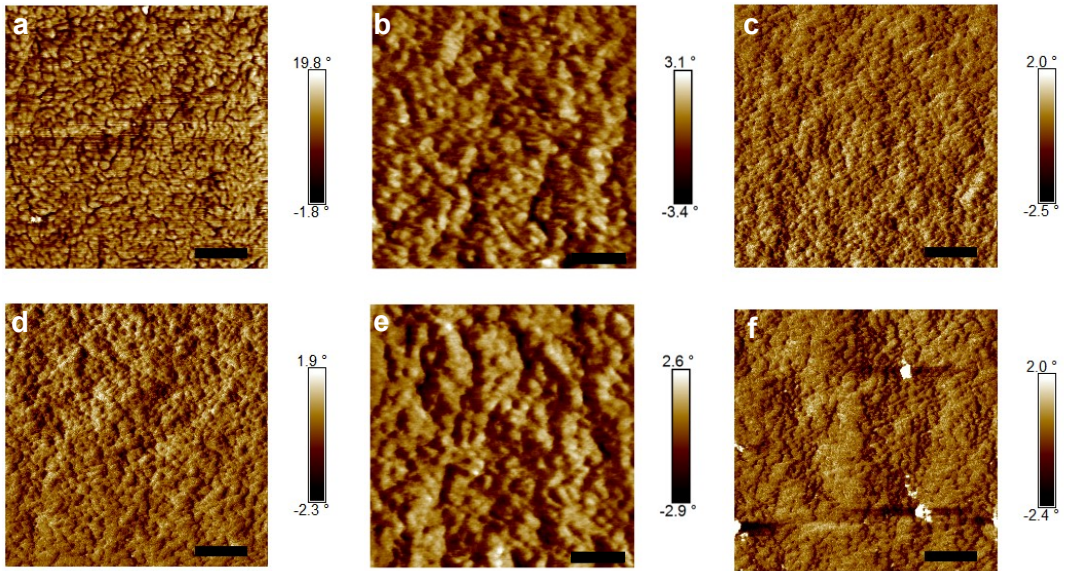

Figure 5.6. AFM phase images of bulkjunction films for (a) **cPBPB**, (b) **aBPB**, (c) **a(PB)$_n$**, (d) **cP$_4$**, (e) **aP**, and (f) **aP$_n$**. The mass ratio of donor-to-acceptor is fixed at 1:2. 1 % CN additive was used. The scale bar is 200 nm.

5.3. Conclusion

This is the first study comparing cyclic structures to their acyclic counterparts in OPVs. We found that the cyclic structures far outperform the acyclic controls in organic photovoltaics. We find it interesting that **cPBPB** and **cP$_4$** perform similarly as the electron

transporting material in OPVs even though **cPBPB** has a bathochromically shifted UV-vis compared to that of **cP4**. The origin of the increase in the efficiency of the devices when cyclic molecules are used in place of acyclic ones is multifaceted. When compared to the acyclic molecules, the macrocycles: (1) have better energy alignment with the donor material; (2) absorb more visible light; (3) are more efficient at transporting electrons; and (4) shows optimal phase separation for BHJ solar cells. The ease with which we can tune the energetics and therefore the properties of these macrocycles – through a different linker subunit or incorporating oligomeric PDI subunits – will magnify these initial findings.[53] This study also offers the intriguing possibility of tuning the geometry of the donor so that it is shape matched to these cyclic electron accepting structures as a means to creating highly efficient devices.

5.4. Experimental section

5.4.1. Synthesis.

All reactions were performed in oven-dried or flame-dried round bottom flasks unless otherwise noted. The flasks were fitted with rubber septa and reactions were conducted under a positive pressure of nitrogen unless otherwise noted. Anhydrous and anaerobic solvents were obtained from a Glass Contour solvent system consisting of a Schlenk manifold with purification columns packed with activated alumina and supported copper catalyst. Reaction monitoring by thin layer chromatography (TLC) was performed on J.T. Baker Baker-flex Silica Gel IB2-F (25 mm x 75 mm) TLC plates. TLC visualization was accomplished by visible observation and irradiation with a UV lamp.

5.4.2. Reagents.

Commercial reagents were used without further purification. $Pt(COD)Cl_2$ was

purchased from Strem Chemicals, and all other reagents were purchased from Sigma-Aldrich.

5.4.3. Purificaton.

Automated flash chromatography was performed using a Teledyne Isco Combiflash Rf200 and Redisep Rf Silica columns. Preparative high performance liquid chromatography (HPLC) was performed on a Waters Prep150 instrument equipped with a UV-vis detector, an automated fraction collector, and a Nacalai Tesque COSMOSIL Buckyprep column (20 mm I.D. x 250 mm, 5 μm).

5.4.4. Spectrometers.

^{1}H NMR spectra were recorded on a Bruker 500 MHz or 400 MHz spectrometer. ^{13}C NMR spectra were recorded on a Bruker 125 MHz or 100 MHz spectrometer with complete proton decoupling. NMR spectra were recorded at 300 K unless otherwise noted. Chemical shifts for protons are reported in parts per million (ppm) downfield from tetramethylsilane (TMS) and are referenced to residual protium in the said NMR solvent. Chemical shifts for carbon are reported in ppm downfield from TMS and are referenced to the carbon resonances of the indicated solvent. Data are represented as follows: chemical shift, multiplicity (s = singlet, d = doublet, dd= doublet of doublets, t = triplet, m = multiplet), coupling constants in Hz, and integration.

High-resolution mass spectrometry (HRMS) was performed on (1) a Waters XEVO G2-XS QTOF instrument equipped with a UPC^{2} SFC inlet, and electrospray (ESI) and atmospheric pressure chemical (APCI) ionization sources; or (2) a Bruker UltrafleXtreme MALDI TOF/TOF instrument using a dithranol matrix.

UV-vis absorption spectra were recorded on a Shimadzu UV-1800

spectrophotometer using a 1.0 cm quartz cell. Infrared (IR) spectra were recorded on a Perkin Elmer Spectrum400 FTIR spectrometer using a PIKE ATR attachment.

GPC analysis was done on an Agilent Technologies 1200 Infinity Series GPC fitted with a refractive index detector and a UV-visible detector. All samples were eluted at 1.0 mL/min through two Agilent Technologies PLgel 5 μm MIXED-D 300x7.5mm columns and monitored by their UV-vis signal. M_n and M_w were assigned based off of polystyrene standards.

5.4.5. Atomic force microscopy.

AFM measurements were carried out in tapping mode on a Bruker Multi-Mode AFM at ambient conditions. A commercial silicon cantilever (RTESPA, MPP-11120-10, Bruker) was used in this study with a typical radius of curvature of ~8nm and a nominal spring constant of ~40 Nm^{-1}.

5.4.6. Cyclic Voltammetry.

Cyclic voltammograms (CVs) were recorded on a CH166 electrochemical workstation using an Ag/AgCl electrode as the reference electrode at room temperature. Experiments were performed in CH_2Cl_2 with NBu_4PF_6 as the supporting electrolyte at a scan rate of 0.1 V/s.[56]

5.4.7. Thin film transistors.

To create the devices, we first silanize the substrate (300 nm of SiO_2 on a Si wafer) with octadecyltrichlorosilane (OTS). Au is deposited onto the substrate as bottom-contact source and drain electrodes (40 nm) with a width of 105 μm and length of 20 μm. Next, we spin-cast organic films onto the surface at 1,000 r.p.m. for 1 min, to form transistors using the silicon wafer as the global back gate for the device. Finally, the samples were annealed

under inert atmosphere at 160℃ for 10 minutes to optimize device performance except that the a-P4 film was annealed at 120℃. The thin film transistors were tested on the Agilent 4155C semiconductor parameter analyzer.

5.4.8. Solar cell fabrication.

PTB7-Th was purchased from 1-Material Inc. Synthesis of ZnO sol-gel precursor was described elsewhere.[55] Zinc acetate dihydrate, ethanolamine, 2-methoxyethanol, DIO and all of the solvents were purchased from Sigma Aldrich. Pre-patterned ITO-coated glass with a sheet resistance of ~15 Ωsq^{-1} was cleaned with detergent and ultrasonicated in deionized water, acetone and isopropanol for 30 min, respectively. Subsequently, we treated the substrates by ultraviolet-ozone for 10min. The prepared ZnO precursor was spin-cast onto the ITO substrate at 3,000 r.p.m. for 1 min, followed by annealing at 200 ºC for 1h in air, to form a thin film with approximate thickness of 20 nm. Active layers were prepared by spin-coating a mixed solution containing polymer and acceptor in chlorobenzene at a total concentration of 25 $mgml^{-1}$. The thickness of the prepared active layers is about 100 nm. Finally, a 7 nm MoO_3 layer was deposited first and then a 100-nm Ag electrode was subsequently deposited through a shadow mask by thermal evaporation under a vacuum about 1×10^{-6} torr. The current density–voltage (*J–V*) curves were measured by a Keithley 2635A source measure unit. The photocurrent was measured under AM 1.5G illumination at 100 $mWcm^{-2}$ under a Newport solar Simulator. A KG5-Si reference cell traceable to Newport was used to calibrate light intensity. The effective device area was defined as 6.25 mm^2 by an aperture mask. EQE measurements were performed using a QEXL system from PV Measurements Inc.

5.5. Supplementary materials

5.5.1. Figures and Tables Referenced in the Manuscript

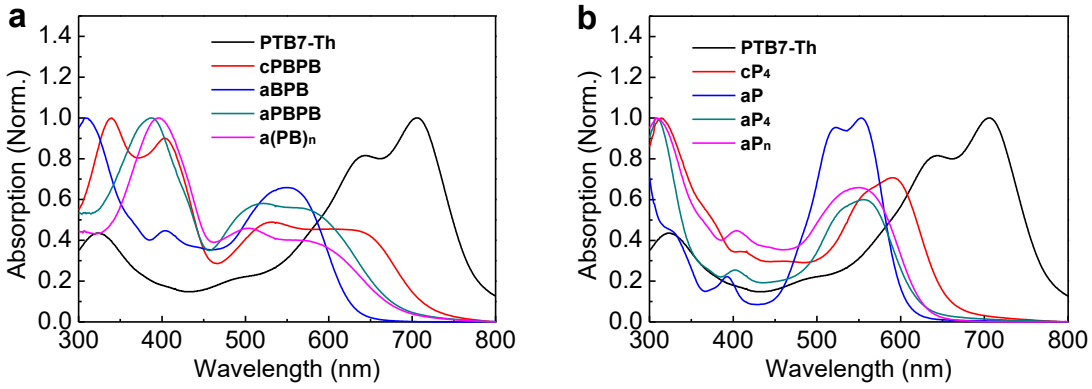

Figure 5.7. UV-vis absorption spectra measured in films: (a) for **cPBPB, aBPB, aPBPB** and **a(PB)$_n$** (b) for **cP$_4$**, **aP**, **aP$_4$**, and **aP$_n$** normalized to each absorption maxima, where absorption max = 1.

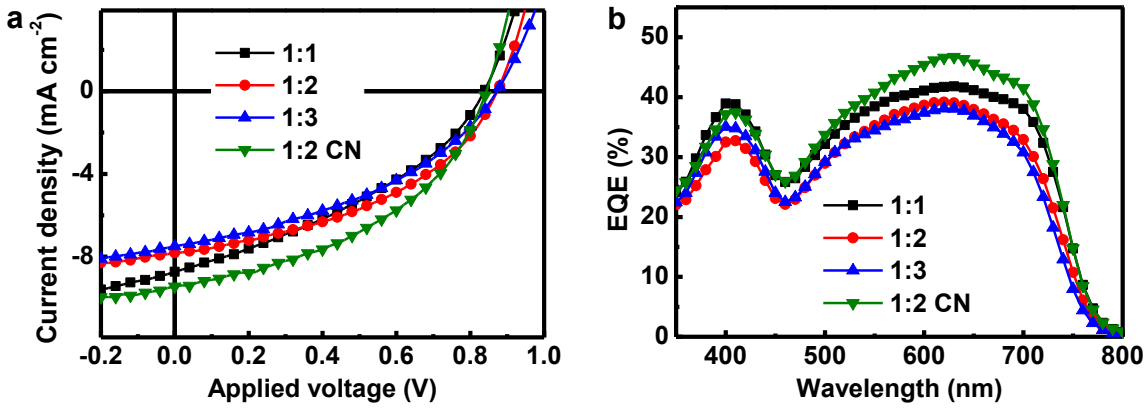

Figure 5.8. Device performance of PTB7-Th:**cPBPB** solar cells. (a) Current density versus voltage (*J*–*V*) characteristics of PTB7-Th:**cPBPB** solar cells with different blend ratios (PTB7-Th to **cPBPB**) and 1% v/v CN. (b) EQE spectra of corresponding PTB7-Th:**cPBPB** solar cells.

Table 5.3. Summary of device parameters of best PTB7-Th:**cPBPB** solar cells with different conditions. Average PCE values were calculated from six devices for each

condition; the highest PCE values are shown in parentheses.

Mass ratio	J_{sc} (mAcm^{-2})	V_{oc} (V)	FF	PCE (%)
1:1	8.5 ± 0.3	0.83 ± 0.01	0.36 ± 0.01	2.5 ± 0.1 (2.6)
1:2	7.6 ± 0.2	0.87 ± 0.01	0.43 ± 0.01	2.8 ± 0.1 (2.9)
1:3	7.4 ± 0.1	0.87 ± 0.01	0.40 ± 0.01	2.5 ± 0.1 (2.6)
1:2 with CN	9.2 ± 0.3	0.84 ± 0.01	0.44 ± 0.01	3.3 ± 0.2 (3.5)

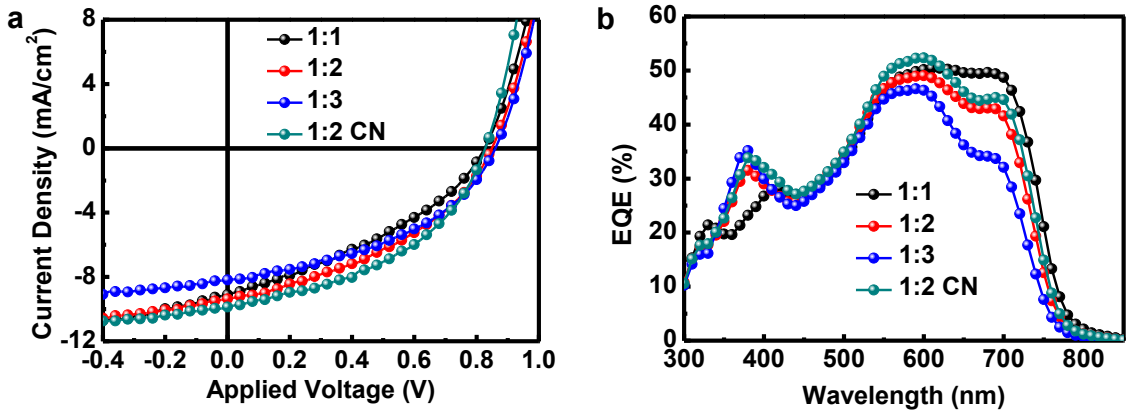

Figure 5.9. Device performance of PTB7-Th:**cP$_4$** solar cells. (a) Current density versus voltage (*J*–*V*) characteristics of PTB7-Th:**cP$_4$** solar cells with different blend ratios (PTB7-Th to **cP$_4$**) and 1% v/v CN. (b) EQE spectra of corresponding PTB7-Th:**cP$_4$** solar cells.

Table 5.4. Summary of device parameters of best PTB7-Th:**cP$_4$** solar cells with different conditions. Average PCE values were calculated from six devices for each condition; the highest PCE values are shown in parentheses.

Mass ratio	J_{sc} (mAcm^{-2})	V_{oc} (V)	FF	PCE (%)
1:1	8.6 ± 0.3	0.82 ± 0.01	0.37 ± 0.01	2.6 ± 0.2 (2.8)
1:2	8.8 ± 0.2	0.85 ± 0.01	0.41 ± 0.01	3.0 ± 0.1 (3.2)

1:3	7.6 ± 0.2	0.86 ± 0.01	0.43 ± 0.01	2.8 ± 0.2 (3.0)
1:2 with CN	9.7 ± 0.2	0.83 ± 0.01	0.44 ± 0.01	3.5 ± 0.1 (3.6)

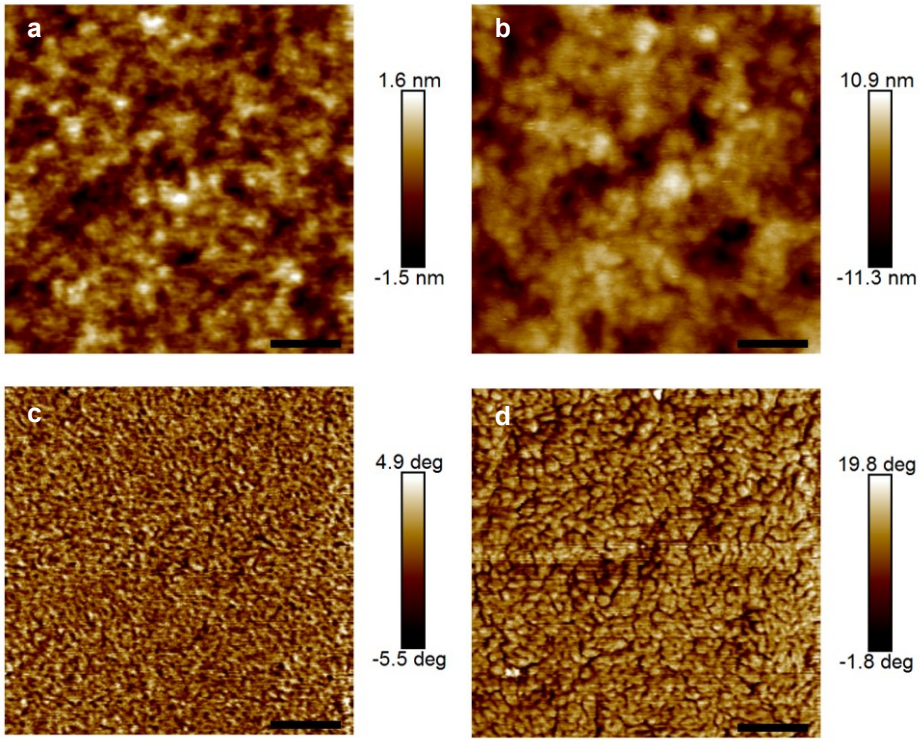

Figure 5.10. AFM height images of PTB7-Th:**cPBPB** films at a donor:acceptor ratio of 1:2 (a) without CN and (b) with 1 % CN. AFM phase images of PTB7-Th:**cPBPB** films at a donor:acceptor ratio of 1:2 (c) without CN and (d) with 1 % CN. The scale bar is 200 nm. Both of the active layers have very smooth surface, with root-mean-square roughness (RMS) of 0.5 nm and 2.6 nm for films both with/without 1% CN, respectively. When turning to the phase images, we observed fibrous domains in the active layer without CN. However, this feature is too fine to be quantified under the instrument limit (~8 nm). In contrast, the active layer with the 1% CN additive possesses clear phase separation as shown in d. The average domain size is estimated to be 20-40 nm. Here CN plays a critical role in phase aggregation, which is essential to the device performance.

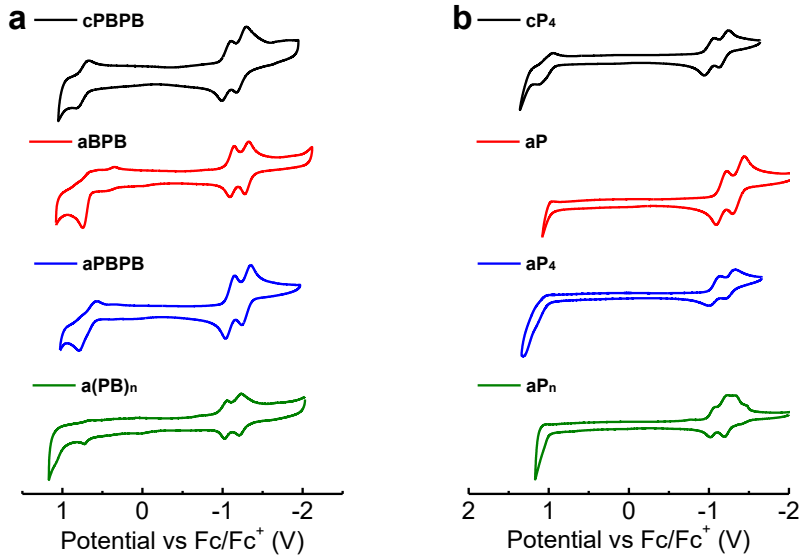

Figure 5.11. Cyclic voltammograms (a) for **cPBPB, aBPB, aPBPB** and **a(PB)$_n$** (b) for **cP$_4$**, **aP**, **aP$_4$**, and **aP$_n$.**

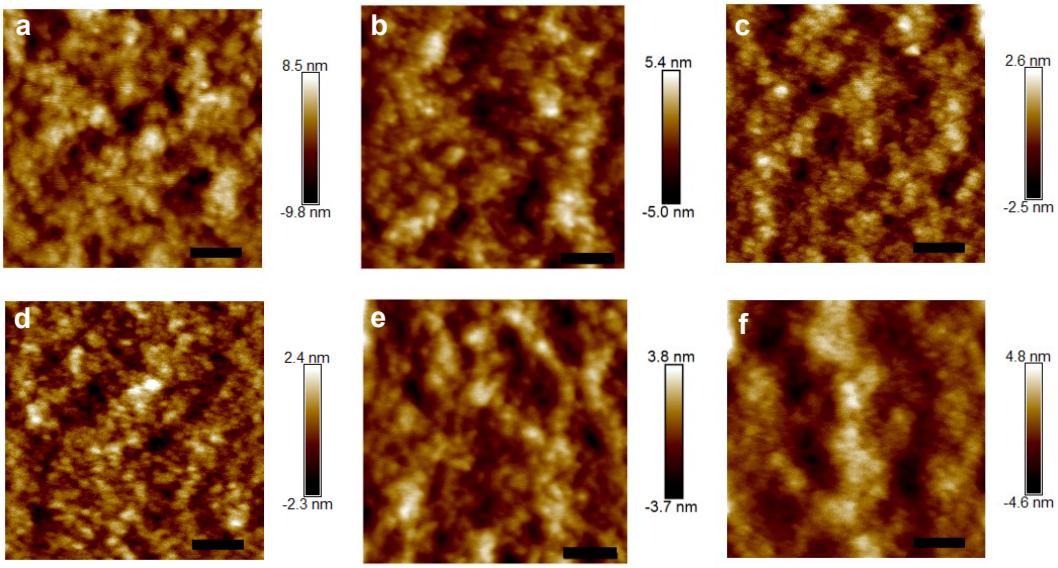

Figure 5.12. AFM height images of bulkjunction films for (a) **cPBPB**, (b) **aBPB**, (c) **a(PB)$_n$**, (d) **cP$_4$**, (e) **aP**, and (f) **aP$_n$**. The mass ratio of donor-to-acceptor is fixed at 1:2. 1 % CN additive was used. The scale bar is 200 nm.

5.5.2. Synthetic Procedures and Characterization Data

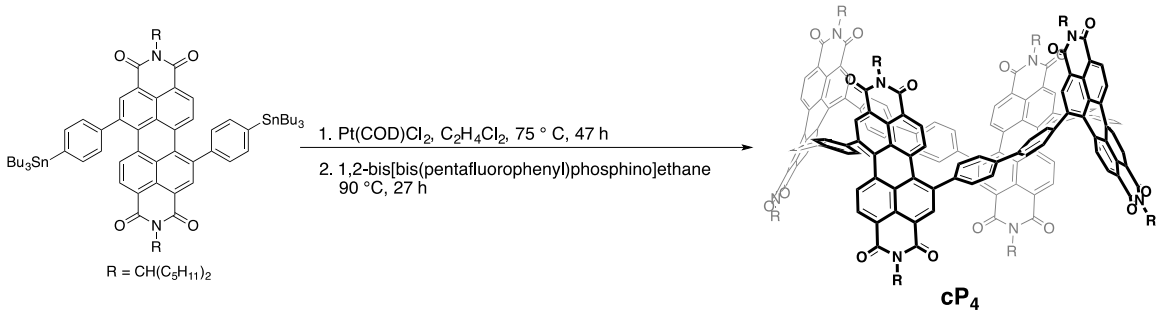

. ***Synthesis of cP4.*** Regio-pure 1,7-Bis[4-(tributylstannyl)-phenyl]-PDI ,was synthesized by the published procedure,[20] from regio-pure *N,N*-′di(6-undecyl)-1,7-dibromoperylene-3,4:9,10-tetracarboxylic diimide. The 1,6- and 1,7-regioisomers of *N,N*′-di(6-undecyl)-dibromoperylene-3,4:9,10-tetracarboxylic diimide were separated using prep HPLC on a COSMOSIL Buckyprep 20 x 250 mm, 18.9 mL/min and 12:88 CH_2Cl_2:hexanes prior to the Suzuki coupling. Bis-stannane (1.04 g, 0.727 mmol, 1.00 equiv) and Pt(COD)Cl_2 (0.272 g, 0.727 mmol, 1.00 equiv) were added to an oven-dried, 2-neck, 500-mL roundbottom flask with a stir bar. 1,2-Dichloroethane (300 mL) was added, and the mixture was sparged with N_2 for 30 min at ambient temperature. Under positive pressure of N_2, the flask was placed in an oil bath at 75 °C with stirring for 47 h. The mixture was allowed to cool to ambient temperature before adding 1,2-bis[bis(pentafluorophenyl)phosphino]ethane (2.76 g, 3.63 mmol, 5.00 equiv). The mixture was stirred at room temperature for 30 min, fitted with a reflux condenser, and placed in an oil bath at 90 °C for 27 h. The mixture was allowed to cool to room temperature then concentrated under reduced pressure. The crude mixture was loaded onto a silica column (120 g Redisep Rf Silica) and made more pure by a gradient elution from 9:1 CH_2Cl_2/hexanes to CH_2Cl_2 to 9:1 CH_2Cl_2/MeOH at 85 mL/min. Fractions containing **cP4**

were identified by MALDI-TOF MS and were collected and concentrated. These fractions were further purified by preparative HPLC on a COSMOSIL Buckyprep column (20 x 250 mm) with an eluent of 12% CH_2Cl_2/hexanes (v/v) at a flow rate of 18.9 mL/min. The pure fractions were concentrated to give **cP4** as a dark purple solid (0.0530 g, 0.0150 mmol, 8% yield). **^{1}H NMR** (500 MHz, $C_2D_2Cl_4$, 413 K) δ 8.62 (s, 8H), 8.39 (d, J = 8.0 Hz, 8H), 8.32 (d, J = 8.0 Hz, 8H), 7.75 (d, J = 8.4 Hz, 16H), 7.64 (br d, J = 7.7 Hz, 16H), 5.21 – 5.13 (m, 8H), 2.30 – 2.18 (m, 16H), 2.00 – 1.89 (m, 16H), 1.44 – 1.29 (m, 96H), 0.89 (t, J = 7.0 Hz, 48H). **^{13}C NMR** (125 MHz, $C_2D_2Cl_4$, 383 K) δ 163.82, 163.57, 141.33, 140.40, 134.93, 134.52, 132.57, 130.13, 129.89, 129.52, 129.35, 128.46 (br), 127.45, 122.64, 122.30, 54.74, 32.34, 31.44, 26.38, 22.13, 13.53. **IR** (cm^{-1}) 2955, 2927, 2860, 1695, 1657, 1595, 1585, 1456, 1407, 1324, 1238, 1180, 1127, 1096, 1003, 812. **HRMS** (MALDI–) calculated *m/z* for $[C_{232}H_{240}N_8O_{16}]^-$ 3393.821, found 3393.715.

Broadening of peaks (br) at this temperature likely results from slow rotation of the benzene rings.

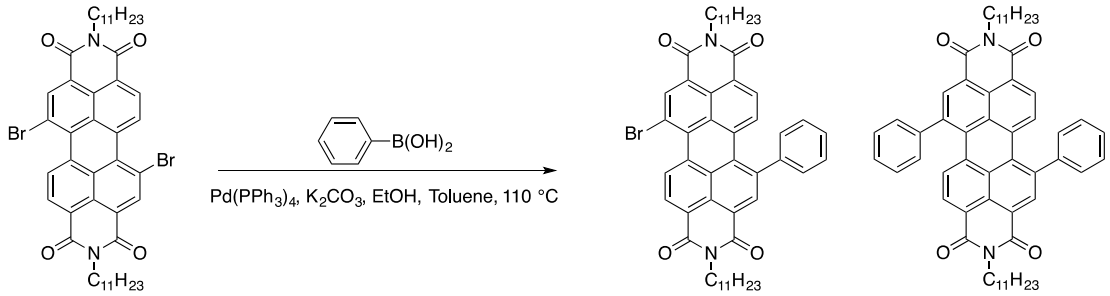

SI-1 **aP**

Synthesis of SI-1 and aP. The 1,6- and 1,7-regioisomers of *N,N′*-di(6-undecyl)-dibromoperylene-3,4:9,10-tetracarboxylic diimide were separated using prep HPLC on a COSMOSIL Buckyprep 20 x 250 mm, 18.9 mL/min and 12:88 CH_2Cl_2:hexanes. *N,N′*-Di(6-undecyl)-1,7-dibromoperylene-3,4:9,10-tetracarboxylic diimide (0.600 g, 0.703 mmol, 1.00 equiv), phenyl boronic acid (0.0430 g, 0.352 mmol, 0.500 equiv), aqueous

K_2CO_3 (2 M, 6.00 mL), EtOH (1.20 mL) and toluene (18.0 mL) were added to a two-neck 100-mL round bottom flask equipped with a stir bar. The mixture was sparged with N_2 for thirty minutes. While under N_2, tetrakis(triphenylphosphine)palladium(0) (0.0810 g, 0.0703 mmol, 0.100 equiv) was added. The mixture was further sparged for ten minutes before being fitted with a condenser and placed in a 100 °C oil bath under N_2, stirring for twenty-four hours. The crude mixture was extracted with ethyl acetate and brine, concentrated and purified by column chromatography (40 g Redisep Rf Silica) using a gradient from 0% to 100% CH_2Cl_2/hexanes at 40 mL/min. Further purification by prep HPLC (COSMOSIL Buckyprep 20 x 250 mm, 18.9 mL/min and 3:93 CH_2Cl_2:hexanes) yielded **SI-1** (0.0930 g, 0.109 mmol, 16%) and **aP** (0.0290 g, 0.0341, 5.0%) **SI-1**: **^{1}H NMR** (400 MHz, $CDCl_3$) δ 9.54 (d, J = 8.2 Hz, 1H), 8.90 (br, 1H), 8.66 (br, 2H), 8.11 (br, 1H), 7.80 (d, J = 8.2 Hz, 1H), 7.49 (br, 5H), 5.24 – 5.16 (m, 1H), 5.12 (br, 1H), 2.30 – 2.17 (m, 4H), 1.88 – 1.79 (m, 4H), 1.26 (br, 24H), 0.85 (br, 12H). **^{13}C NMR** (100 MHz, $CDCl_3$) δ 164.61, 164.26, 163.53, 162.54, 141.96, 141.43, 138.48, 137.83, 135.74, 135.07, 133.91, 133.70, 133.63, 131.62, 130.37, 130.30, 130.18, 129.99, 129.77, 129.58, 129.28, 128.99, 128.80, 128.67, 128.24, 127.70, 127.41, 123.87, 123.16, 122.45, 121.76, 120.29, 54.87, 54.76, 32.34, 32.26, 31.75, 31.72, 26.58, 22.57, 22.54, 14.04. **IR** (cm^{-1}) 2955, 2925, 2857, 1698, 1657, 1596, 1587, 1456, 1447, 1403, 1326, 1239, 1184, 914, 812, 734. **HRMS** (APCI+) calculated *m/z* for $[C_{52}H_{57}N_2O_4Br+H]^+$ 853.3580, found 853.3572. **aP**: **^{1}H NMR** (400 MHz, $CDCl_3$) δ 8.62 (br, 2H), 8.12 (br, 2H), 7.82 (d, J = 8.2 Hz, 2H), 7.59 – 7.55 (m, 4H), 7.54 – 7.45 (m, 6H), 5.15 (br, 2H), 2.29 – 2.16 (m, 4H), 1.88 – 1.76 (m, 4H), 1.37 – 1.18 (m, 24H), 0.83 (t, J = 6.6 Hz, 12H). **^{13}C NMR** (100 MHz,$CDCl_3$) δ 164.70, 163.63, 142.23, 141.08, 135.78, 135.10, 134.81, 132.49, 130.22, 130.16, 129.91, 129.23, 129.17,

129.03, 128.59, 127.90, 122.87, 122.53, 122.13, 121.77, 54.65, 32.32, 31.75, 26.59, 22.55, 14.04. **IR** (cm^{-1}) 2956, 2925, 2860, 1695, 1657, 1598, 1585, 1409, 1325, 1242, 910, 814. **HRMS** (APCI-) calculated m/z for $[C_{58}H_{62}N_2O_4]^-$ 850.4710, found 850.4704.

Broadening (br) of peaks in the ^1H NMR spectrum is due to rotational isomers about the imide side chains.[20,64]

Multiple peaks for the same carbon in the ^{13}C NMR spectrum reflect rotational isomers about the imide side chains that have been seen previously.[20,64]

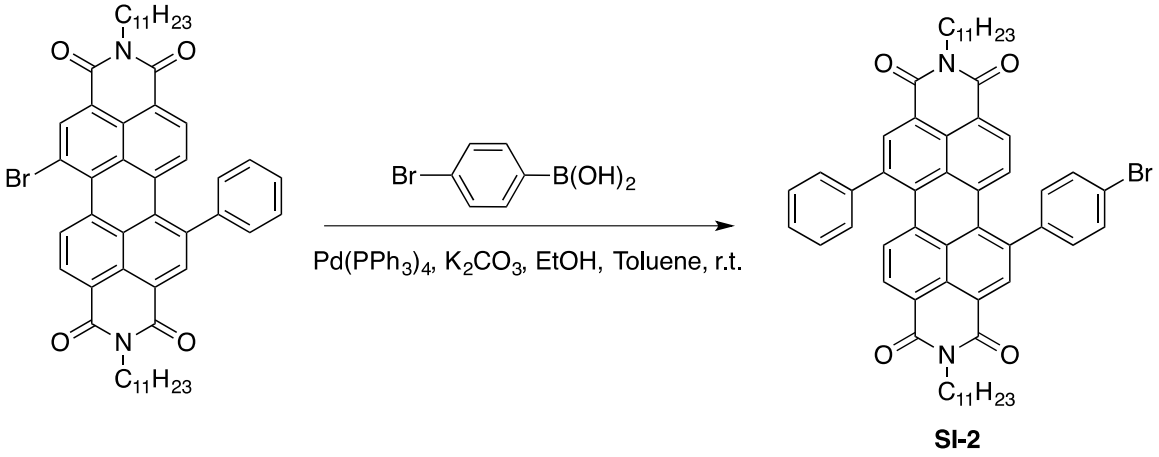

SI-2

Synthesis of SI-2. **SI-1** (0.120 g, 0.141 mmol, 1.00 equiv), 4-bromophenylboronic acid (0.0850 g, 0.422 mmol, 3.00 equiv), aqueous K_2CO_3 (2 M, 1.20 mL), EtOH (0.240 mL) and toluene (3.60 mL) were added to 20 mL scintillation vial equipped with a stir bar. The mixture was sparged with N_2 for thirty minutes. While under N_2, tetrakis(triphenylphosphine)palladium(0) (0.0160 g, 0.0104 mmol, 0.100 equiv) was added. The mixture was further sparged for ten minutes and stirred overnight at room temperature. The crude mixture was extracted with ethyl acetate and brine, concentrated and purified by column chromatography (40 g Redisep Rf Silica) using a gradient from 0% to 100%

CH_2Cl_2/hexanes at 40 mL/min. Impure fractions were further purified by prep HPLC (COSMOSIL Buckyprep 20 x 250 mm, 18.9 mL/min and 7:93 CH_2Cl_2:hexanes) to yield a total 0.0700 g (0.0750 mmol, 54%) of **SI-2**. **^{1}H NMR** (400 MHz, $C_2D_2Cl_4$, 390K) δ (s, 1H), 8.60 (s, 1H), 8.24 (d, J = 8.2 Hz, 1H), 8.18 (d, J = 8.2 Hz, 1H), 7.92 (d, J = 8.1 Hz, 2H), 7.74 (d, J = 8.4 Hz, 2H), 7.65 – 7.51 (m, 7H), 5.23 – 5.14 (m, 2H), 2.32 – 2.24 (m, 4H), 1.98 – 1.93 (m, 4H), 1.38 (br, 24H), 0.93 (br, 12H).**^{13}C NMR** (100 MHz, $C_2D_2Cl_4$, 390K) δ 163.98, 163.92, 163.88, 142.54, 141.56, 141.36, 139.62, 135.32, 134.90, 134.83, 134.54, 133.46, 132.51, 132.34, 130.79, 130.22, 130.19, 130.10, 129.63, 129.44, 129.34, 129.04, 128.70, 128.19, 128.15, 123.17, 123.14, 123.08, 123.01, 122.75, 55.43, 32.67, 31.74, 26.68, 22.42, 13.80. **IR** (cm^{-1}) 2955, 2926, 2860, 1697, 1658, 1597, 1587, 1459, 1408, 1325, 1241, 1185, 813. **HRMS** (APCI+) calculated *m/z* for $[C_{58}H_{61}N_2O_4Br+H]^+$ 929.3893, found 929.3885.

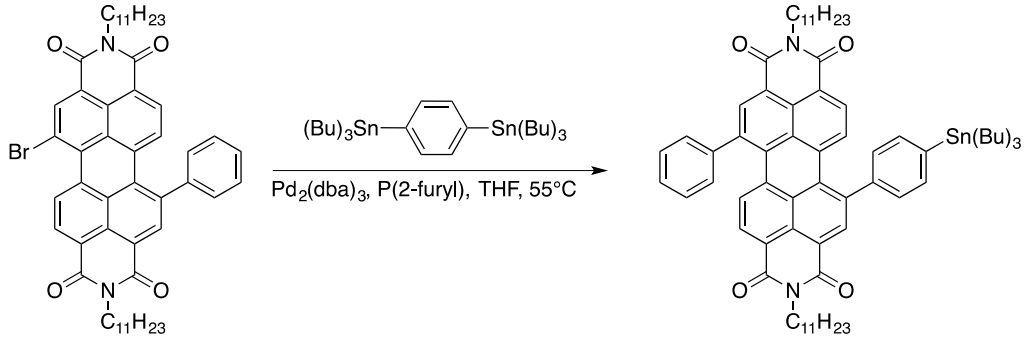

SI-1 **SI-3**

Synthesis of SI-3. **SI-1** (0.0930 g, 0.109 mmol, 1.00 equiv), 1,4-bis(tributylstannyl)benzene (0.0600 mL, 0.0720 mmol, 2.50 equiv) and THF (90.0 mL) were added to a 20 mL scintillation vial equipped with a stir bar. The mixture was sparged with N_2 for thirty minutes. While under N_2, tris(dibenzylideneacetone)dipalladium (0.0100 g, 0.0109 mmol, 0.100 equiv) and tri(2-furyl)phosphine (0.0110 g, 0.0436 mmol, 0.400

equiv) were added. The mixture was further sparged for ten minutes before being placed in a 55 °C oil bath and stirred overnight. The crude mixture was condensed and purified by column chromatography (40 g Redisep Rf Silica) using a gradient from 0% to 100% CH_2Cl_2/hexanes at 40 mL/min to yield **SI-3** (0.0770 g, 0.0680 mmol, 62% yield). **^{1}H NMR** (500 MHz, $CDCl_3$) δ 8.62 (br, 2H), 8.11 (br, 2H), 7.88 (d, J = 8.5 Hz, 1H), 7.81 (d, J = 6.3 Hz, 1H), 7.63 – 7.54* (m, J = 7.1 Hz, 4H), 7.52 – 7.48 (m, 5H), 5.15 (br, 2H), 2.25 – 2.21 (m, 4H), 1.82 (br, 4H), 1.66 – 1.54* (m, 6H), 1.43 – 1.35 (m, 6H), 1.26 (br, 24H), 1.18 – 1.09* (m, 6H), 0.94 (t, J = 7.3 Hz, 9H), 0.83 (br t, J = 6.6 Hz, 12H). **^{13}C NMR** (125 MHz, $CDCl_3$) δ 164.77, 163.66, 143.14, 142.28, 141.68, 141.33, 141.00, 138.19, 138.08, 135.87, 135.41, 135.16, 134.91, 134.76, 132.57, 132.40, 130.20, 130.17, 130.15, 129.97, 129.84, 129.26, 129.06, 128.58, 128.28, 127.92, 127.87, 122.83, 122.50, 122.14, 121.77, 54.63, 32.34, 31.77, 29.14*, 27.37*, 26.60, 26.59, 22.56, 14.05, 13.73, 9.75*. **IR** (cm^{-1}) 2956, 2925, 2855, 1697, 1657, 1598, 1586, 1459, 1447, 1408, 1325, 1264, 1239, 863, 814, 739. **HRMS** (APCI+) calculated *m/z* for $[C_{70}H_{88}N_2O_4Sn+H]^+$ 1141.5844, found 1141.5859. Broadening (br) of peaks in the ^{1}H NMR spectrum is due to rotational isomers about the imide side chains. [20,64]

*Tin satellite peaks visible. Multiple peaks for the same carbon in the ^{13}C NMR spectrum reflect rotational isomers about the imide side chains that have been seen previously. [20,64]

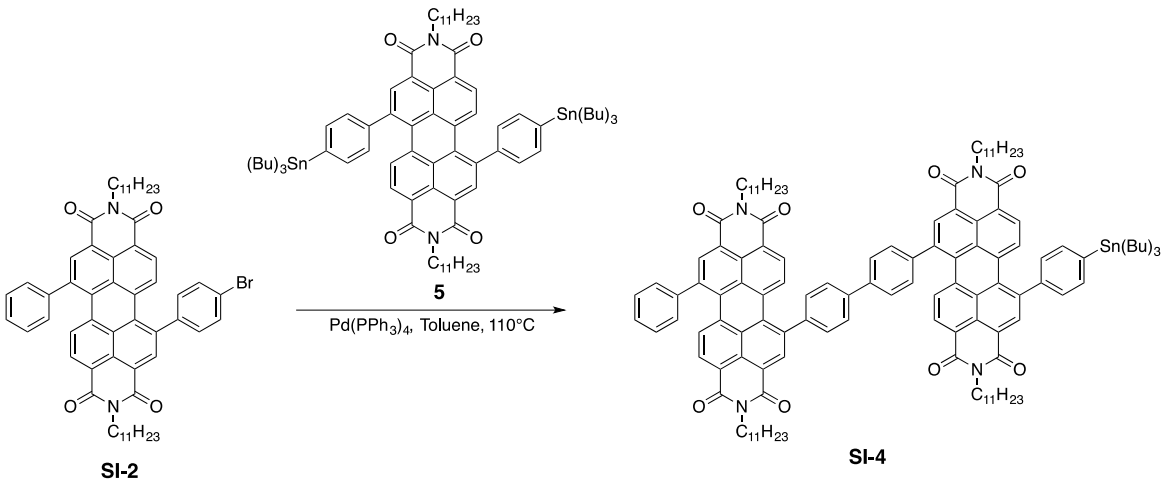

Synthesis of SI-4. **SI-2** (0.0750 g, 0.0810 mmol, 1.00 equiv) and 1,7-bis[4-(tributylstannyl)-phenyl]-PDI (0.463 g, 0.324 mmol, 4.00 equiv) were dissolved in toluene (8.00 mL) in a 20 mL scintillation vial equipped with a stir bar. The mixture was sparged with N_2 for thirty minutes. While under N_2, tetrakis(triphenylphosphine)palladium(0) (0.00900 g, 0.00810 mmol, 0.100 equiv) was added. The mixture was further sparged for ten minutes before being placed in a 110 °C oil bath and stirred overnight. The crude mixture was condensed and purified by column chromatography (40 g Redisep Rf Silica) using a gradient from 0% to 100% CH_2Cl_2/hexanes at 40 mL/min. Further purification by preparative HPLC (COSMOSIL Buckyprep 20 x 250 mm, 18.9 mL/min, 7:93 CH_2Cl_2:hexanes) yielded **SI-4** (0.0270 g, 0.0140 mmol, 17% yield). **^{1}H NMR** (500 MHz, $CDCl_3$) δ 8.67 (br, 4H), 8.17 (br, 4H), 8.03 (d, *J* = 3.2 Hz, 1H), 8.01 (d, *J* = 3.2 Hz, 1H), 7.91 (d, J = 8.5 Hz, 1H), 7.87 (d, J = 7.6, 4H), 7.85 (d, J = 9.1 Hz, 1H), 7.74 (d, J = 2.0 Hz, 2H), 7.73 (d, J = 2.3 Hz, 2H), 7.61 – 7.59* (m, 4H), 7.54 – 7.50* (m, 5H), 5.17 (br, 4H), 2.27 – 2.19 (br m, 8H), 1.83 (br, 8H), 1.67 – 1.60* (m, 6H), 1.44 – 1.35 (m, 6H), 1.35 – 1.21 (br m, 48H), 1.19 – 1.11* (m, 6H), 0.95 (t, J = 7.3 Hz, 9H), 0.86 – 0.81 (m, 24H). **^{13}C NMR** (100 MHz, $CDCl_3$) δ 164.70, 163.64, 143.19, 142.22, 141.78, 141.72, 141.66, 141.40,

141.15, 140.48, 140.39, 140.20, 140.15, 138.10, 135.82, 135.01, 134.82, 132.57, 130.28, 130.21, 130.03, 129.79, 129.35, 129.34, 129.28, 129.16, 129.07, 128.75, 128.64, 128.30, 127.97, 127.93, 122.90, 122.62, 122.21, 121.90, 54.68, 32.34, 31.78, 29.15*, 27.38*, 26.61, 22.58, 14.07, 13.75, 9.76*. **IR** (cm^{-1}) 2955, 2927, 2859, 1698, 1659, 1599, 1587, 1457, 1409, 1326, 1240, 1183, 814. **HRMS** (APCI+) calculated *m/z* for $[C_{128}H_{148}N_4O_8Sn+Na]^+$ 2012.0217, found 2012.0212.

Broadening (br) of peaks in the ^1H NMR spectrum is due to rotational isomers about the imide side chains. [20,64]

*Tin satellite peaks visible. Multiple peaks for the same carbon in the ^{13}C NMR spectrum reflect rotational isomers about the imide side chains that have been seen previously. [20,64]

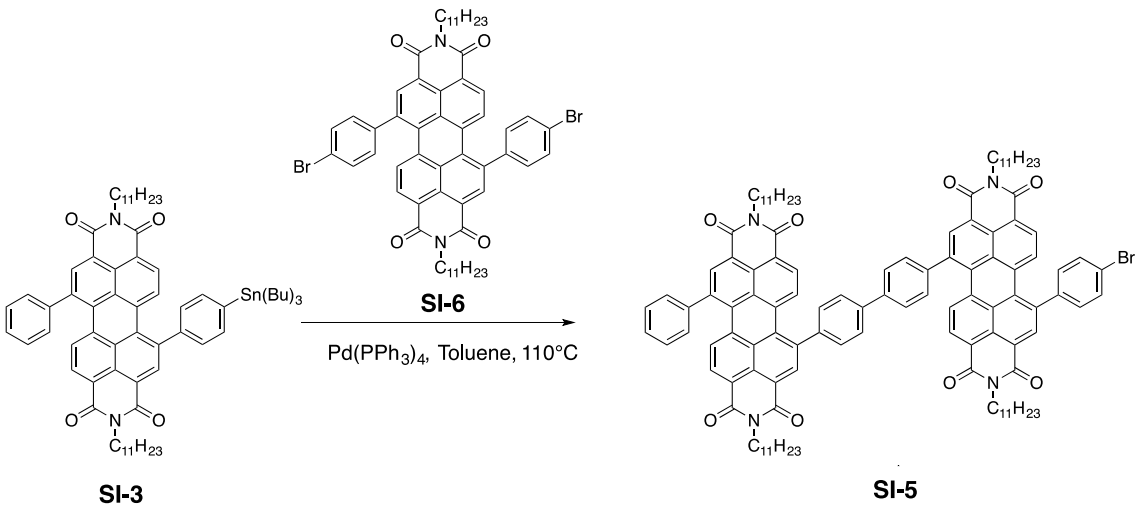

***Synthesis of SI-5*. SI-3** (0.0550 g, 0.0480 mmol, 1.00 equiv) and *N,N′*-di(6-undecyl)-1,7-di(4-bromophenyl)- perylene-3,4:9,10-tetracarboxylic diimide (**SI-6**) (0.194 g, 0.193 mmol, 4.00 equiv) were dissolved in toluene (6 mL) in a 20 mL scintillation vial equipped with a stir bar. The mixture was sparged with N_2 for thirty minutes. While under N_2, tetrakis(triphenylphosphine)palladium(0) (0.00600 g, 0.00480 mmol, 0.100 equiv) was

added. The mixture was further sparged for ten minutes before being placed in a 110 °C oil bath and stirred overnight. The crude mixture was condensed and purified by column chromatography (24 g Redisep Rf Silica) using a gradient from 0% to 100% CH_2Cl_2/hexanes at 40 mL/min. Further purification using preparative HPLC (Buckyprep, isocratic 15:85 CH_2Cl_2:hexane) yielded **SI-5** (0.0150 g, 0.00800 mmol, 18% yield). **^{1}H NMR** (500 MHz, $CDCl_3$) δ 8.71 – 8.58 (br m, 4H), 8.24 – 8.12 (br m, 4H), 8.02 (d, *J* = 8.4 Hz, 2H), 7.87 (d, *J* = 7.9 Hz, 4H), 7.85 (d, *J* = 8.2 Hz, 2H), 7.74 – 7.72 (m, 4H), 7.67 (d, *J* = 8.0 Hz, 2H), 7.60 (d, *J* = 7.1 Hz, 2H), 7.54 – 7.48 (m, 5H), 5.17 (br, 4H), 2.23 (br, 8H), 1.83 (br, 8H), 1.26 (br, 48H), 0.86 – 0.81 (br m, 24H). **^{13}C NMR** (100 MHz, $CDCl_3$) δ 164.70, 163.59, 142.20, 141.75, 141.60, 141.16, 141.07, 140.65, 140.45, 140.24, 140.12, 139.64, 135.89, 135.47, 135.17, 134.81, 134.49, 133.43, 132.53, 130.81, 130.36, 130.29, 130.20, 130.06, 130.01, 129.80, 129.76, 129.50, 129.33, 129.30, 129.26, 129.07, 128.79, 128.75, 128.65, 128.04, 127.99, 127.97, 123.08, 122.99, 122.65, 122.32, 121.88, 54.70, 32.33, 31.78, 26.62, 22.59, 14.09. **IR** (cm^{-1}) 2954, 2924, 2858, 1697, 1657, 1598, 1587, 1457, 1408, 1324, 1239, 1183, 814. **HRMS** (APCI+) calculated *m/z* for $[C_{116}H_{121}N_4O_8Br+Na]^+$ 1799.8265, found 1799.8259.

Broadening (br) of peaks in the ^{1}H NMR spectrum is due to rotational isomers about the imide side chains. [20,64]

Multiple peaks for the same carbon in the ^{13}C NMR spectrum reflect rotational isomers about the imide side chains that have been seen previously. [20,64]

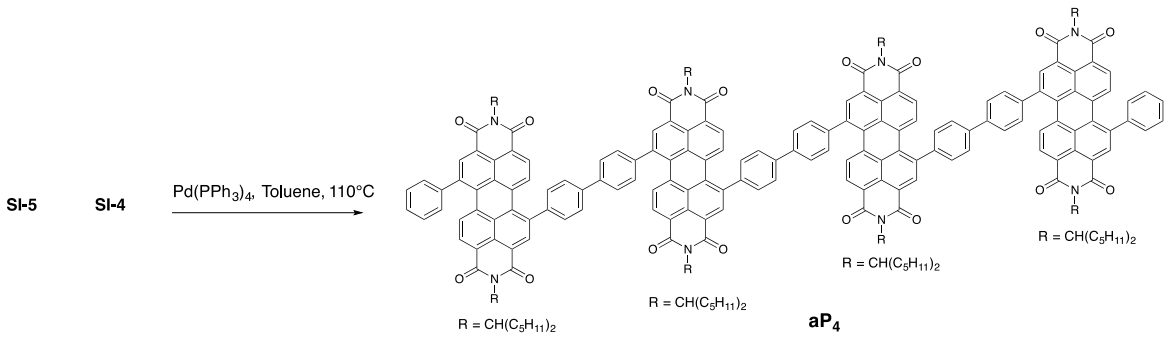

Synthesis of aP₄. **SI-4** (0.0170 g, 0.00800 mmol, 1.00 equiv) and **SI-5** (0.0150 g, 0.00800 mmol, 1.00 equiv) were dissolved in toluene (2.0 mL) in a 20 mL scintillation vial equipped with a stir bar. The mixture was sparged with N_2 for thirty minutes. While under N_2, tetrakis(triphenylphosphine)palladium(0) (0.00600 g, 0.00480 mmol, 0.100 equiv) was added. The mixture was further sparged for ten minutes before being placed in a 110 °C oil bath and stirred for eight hours. The crude mixture was filtered through Celite, concentrated and purified by preparative TLC using a mobile phase of 70:30 CH_2Cl_2:hexanes. The product was washed with hexanes and precipitated from methanol to yield **aP₄** (0.00900 g, 0.00300 mmol, 62% yield). **^{1}H NMR** (500 MHz, $C_2D_2Cl_4$, 370 K) δ 8.75 (s, 4H), 8.72 (s, 2H), 8.67 (s, 2H), 8.32 – 8.26 (m, 6H), 8.19 (d, *J* = 8.2 Hz, 2H), 8.14 (d, J = 8.0 Hz, 2H), 8.14 (d, J = 8.2 Hz, 2H), 8.12 (d, *J* = 8.3 Hz, 2H), 7.99 – 7.91 (m, 14H), 7.84 – 7.78 (m, 12H), 7.66 (d, *J* = 7.0 Hz, 4H), 7.62 – 7.56 (m, 6H), 5.25 – 5.15 (br m, 8H), 2.33 – 2.21 (br m, 16H), 2.00 – 1.90 (br m, 16H), 1.45 – 1.27 (br m, 96H), 0.98 – 0.88 (br m, 48H). **^{13}C NMR** (125 MHz, $C_2D_2Cl_4$, 370 K) δ 163.81, 142.26, 141.79, 140.98, 140.40, 140.30, 140.27, 135.11, 134.68, 134.64, 132.34, 132.31, 132.26, 130.04, 129.97, 129.52, 129.23, 129.13, 128.83, 128.63, 128.46, 127.96, 127.88, 122.77, 122.50, 54.70, 32.36, 31.53, 26.47, 26.45, 22.24, 22.23, 13.69. **IR** (cm^{-1}) 2956, 2924, 2856, 1696, 1657, 1598, 1587, 1457, 1408, 1324, 1262, 1239, 1182, 1097, 1029, 861, 813, 740. **HRMS** (MALDI–) calculated

m/z for $[C_{232}H_{242}N_8O_{16}]^-$ 3395.8369, found 3395.8363.

Broadening (br) of peaks in the ^{1}H NMR spectrum is due to rotational isomers about the imide side chains. [20,64]

Multiple peaks for the same carbon in the ^{13}C NMR spectrum reflect rotational isomers about the imide side chains that have been seen previously.[20,64]

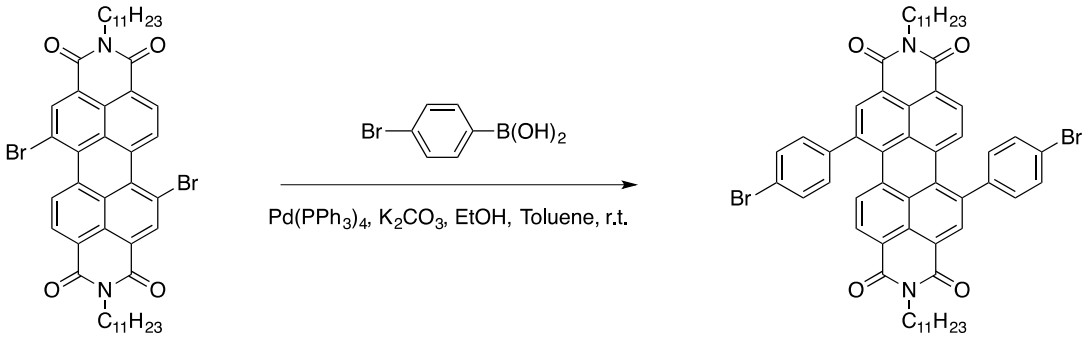

SI-6

Synthesis of 1,7-N,N'-di(6-undecyl)-1,7-di(4-bromophenyl)- perylene-3,4:9,10-tetracarboxylic diimide (SI-6). The 1,6- and 1,7-regioisomers of *N,N'*-di(6-undecyl)-dibromoperylene-3,4:9,10-tetracarboxylic diimide were separated using prep HPLC on a COSMOSIL Buckyprep 20 x 250 mm, 18.9 mL/min and 12:88 CH2Cl2:hexanes. *N,N'*-Di(6-undecyl)-1,7-dibromoperylene-3,4:9,10-tetracarboxylic diimide (0.200 g, 0.234 mmol, 1.00 equiv), 4-bromophenylboronic acid (0.141 g, 7.01 mmol, 3.00 equiv), aqueous K_2CO_3 (2 M, 2.00 mL), EtOH (0.400 mL) and toluene (6.00 mL) were added to 20 mL scintillation vial equipped with a stir bar. The mixture was sparged with N_2 for thirty minutes. While under N_2, tetrakis(triphenylphosphine)palladium(0) (0.0270 g, 0.0234 mmol, 0.100 equiv) was added. The mixture was further sparged for ten minutes and stirred overnight at room temperature. A small aliquot was taken 24 hours later and showed ~10% conversion to product by ^{1}H NMR. Additional tetrakis(triphenylphosphine)palladium(0)

(0.108 g, 0.0936 mmol, 0.400 equiv) was added. The reaction was monitored for forty-eight hours and another 0.400 equiv of catalyst was added. In total, the reaction completed in 72 hours. The crude mixture was extracted with ethyl acetate and brine, concentrated and purified by column chromatography (40 g Redisep Rf Silica) using a gradient from 0% to 100% CH_2Cl_2/hexanes at 40 mL/min. Impure fractions were further purified by preparative TLC to yield a total 0.091 g (0.0905 mmol, 39%) of **SI-6**. **^{1}H NMR** (500 MHz, $CDCl_3$) δ 8.58 (br, 2H), 8.18 (br, 2H), 7.82 (d, J = 8.1 Hz, 2H), 7.65 (d, J = 8.3 Hz, 4H), 7.45 (d, J = 8.4 Hz, 4H). 5.16 (br, 2H), 2.28 – 2.16 (m, 4H), 1.88 – 1.77 (m, 4H), 1.38 – 1.18 (br m, 24H) 0.81 (br t, J = 6.9 Hz, 12H). **^{13}C NMR** (125 MHz, $CDCl_3$) δ 164.52, 163.43, 140.98, 139.73, 135.45, 134.73, 134.42, 133.43, 132.36, 130.74, 130.28, 130.10, 129.34, 129.20, 128.00, 123.11, 122.76, 122.38, 122.01, 54.76, 32.30, 31.74, 26.58, 22.56, 14.04. **IR** (cm^{-1}) 2955, 2928, 2858, 1697, 1657, 1598, 1587, 1487, 1456, 1409, 1324, 1239, 1183, 1072, 1012, 814. **HRMS** (APCI+) calculated *m/z* for $[C_{58}H_{60}N_2O_4Br_2+H]^+$ 1007.2998, found 1007.2994.

Broadening (br) of peaks in the ^{1}H NMR spectrum is due to rotational isomers about the imide side chains. [20,64]

Multiple peaks for the same carbon in the ^{13}C NMR spectrum reflect rotational isomers about the imide side chains that have been seen previously. [20,64]

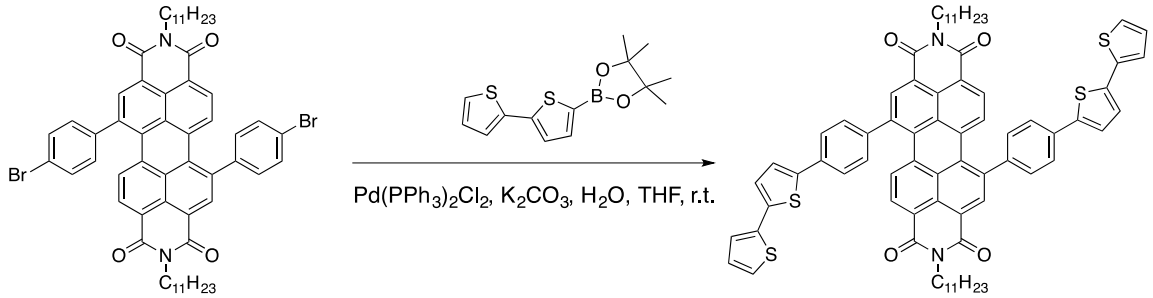

aBPB

Synthesis of aBPB. *N,N′*-Di(6-undecyl)-1,7-di(4-bromophenyl)-perylene-3,4:9,10-tetracarboxylic diimide (0.100 g, 0.0990 mmol, 1.00 equiv), 2,2′-bithiophene-5-boronic acid pinacol ester (1.74 g, 0.596 mmol, 6.00 equiv), K_2CO_3 (0.218 g, 1.58 mmol, 16.0 equiv), H_2O (1.00 mL) and THF (3.00 mL) were added to 20 mL scintillation vial equipped with a stir bar. The mixture was sparged with N_2 for thirty minutes. While under N_2, bis(triphenylphosphine)palladium chloride (0.0110 g, 0.0150 mmol, 0.150 equiv) was added. The mixture was further sparged for ten minutes and stirred overnight at room temperature. The crude mixture was extracted with ethyl acetate and brine, concentrated and purified by column chromatography using a gradient from 0% to 100% CH_2Cl_2/hexanes to yield **aBPB** (0.112 g, 0.0950 mmol, 94%). **^{1}H NMR** (500 MHz, $C_2D_2Cl_4$) δ 8.64 (br, 2H), 8.17 (br, 2H), 7.99 (br, 2H), 7.76 (d, J = 7.9 Hz, 4H), 7.65 (d, J = 8.3 Hz, 4H), 7.40 (d, J = 3.8 Hz, 2H), 7.30 (dd, J = 5.1, 1.1 Hz, 2H), 7.28 (dd, J = 3.6, 1.1 Hz, 2H), 7.24 (d, J = 3.7 Hz, 2H), 7.09 (dd, J = 5.1, 3.6 Hz, 2H), 5.12 (br, 2H), 2.26 – 2.11 (br m, 4H), 1.86 (br, 4H), 1.37 – 1.22 (br m, 24H), 0.88 – 0.82 (br m, 12H). **^{13}C NMR** (125 MHz, $C_2D_2Cl_4$) δ 164.47, 164.37, 163.41, 163.30, 141.70, 140.97, 140.11, 137.25, 136.99, 135.48, 134.77, 134.55, 134.08, 132.26, 130.00, 129.67, 129.24, 129.09, 128.00, 127.78, 126.91, 124.80, 124.77, 124.63, 123.91, 122.83, 122.42, 122.10, 121.74, 54.52, 32.16, 31.66, 26.53, 22.49, 14.09. **IR** (cm^{-1}) 2927, 2857, 1694, 1654, 1586, 1497, 1409, 1326, 1240, 1006, 950, 887, 838. **HRMS** (APCI+) calculated *m/z* for $[C_{74}H_{70}N_2O_4S_4+H]^+$ 1179.4297, found 1179.4301.

Broadening (br) of peaks in the ^{1}H NMR spectrum is due to rotational isomers about the imide side chains. [20,64]

Multiple peaks for the same carbon in the ^{13}C NMR spectrum reflect rotational isomers about the imide side chains that have been seen previously. [20,64]

aBPB **SI-7**

Synthesis of SI-7. **aBPB** (0.0740 g, 0.0640 mmol, 1.00 equiv) was dissolved in toluene (6.00 mL) and sparged with N_2 for fifteen minutes while at -20 ºC. *N*-Bromosuccinimide (0.0110 g, 0.0640 mmol, 1.00 equiv) was added and aluminum was placed over the reaction flask to protect from light. The reaction was stirred for twenty-four hours and allowed to warm to room temperature. The reaction mixture was concentrated and purified by column chromatography using a gradient from 0% to 100% CH_2Cl_2/hexanes to yield **SI-7** (0.00800 g, 0.00600 mmol, 10%). **^{1}H NMR** (500 MHz, CD_2Cl_2) δ 8.62 (br, 2H), 8.15 (br, 2H), 8.00 (d, J = 6.9 Hz, 1H), 7.98 (d, J = 6.9 Hz, 1H), 7.80 – 7.77 (m, 4H), 7.65 (d, J = 8.1 Hz, 4H), 7.41 (d, J = 3.8 Hz, 1H), 7.39 (d, J = 3.8 Hz, 1H), 7.31 (d, J = 4.7 Hz, 1H), 7.29 (d, J = 3.5 Hz, 1H), 7.25 (d, J = 3.7 Hz, 1H), 7.19 (d, J = 3.8 Hz, 1H), 7.09 (dd, J = 5.1, 3.6 Hz, 1H), 7.06 (d, J = 3.8 Hz, 1H), 7.03 (d, J = 3.8 Hz, 1H), 5.12 (br, 2H), 2.24 – 2.12 (br m, 4H), 1.86 (br, 4H), 1.33 – 1.24 (br m, 24H), 0.89 – 0.83 (br m, 12H). **^{13}C NMR*** (100 MHz, $C_2D_2Cl_4$) δ 142.25, 141.70, 141.17, 140.13, 138.53, 137.27, 136.99, 136.10, 134.92, 134.58, 134.10, 133.88, 132.30, 130.84, 130.02, 129.69, 129.09, 128.00, 127.79, 126.96, 125.05, 124.79, 124.66, 123.96, 123.91, 111.12, 54.55, 32.16, 31.65, 26.53, 22.48, 14.08. **IR** (cm^{-1}) 2954, 2926, 2857, 1697, 1656, 1597, 1586, 1457, 1409, 1326, 1241, 1185, 838, 813, 796.

HRMS (ESI+) calculated *m/z* for $[C_{74}H_{69}N_2O_4S_4Br+H]^+$ 1257.3402, found 1257.3392.

*Partial spectrum reported due to limited solubility.

Broadening (br) of peaks in the ^1H NMR spectrum is due to rotational isomers about the imide side chains. [20,64]

Multiple peaks for the same carbon in the ^{13}C NMR spectrum reflect rotational isomers about the imide side chains that have been seen previously. [20,64]

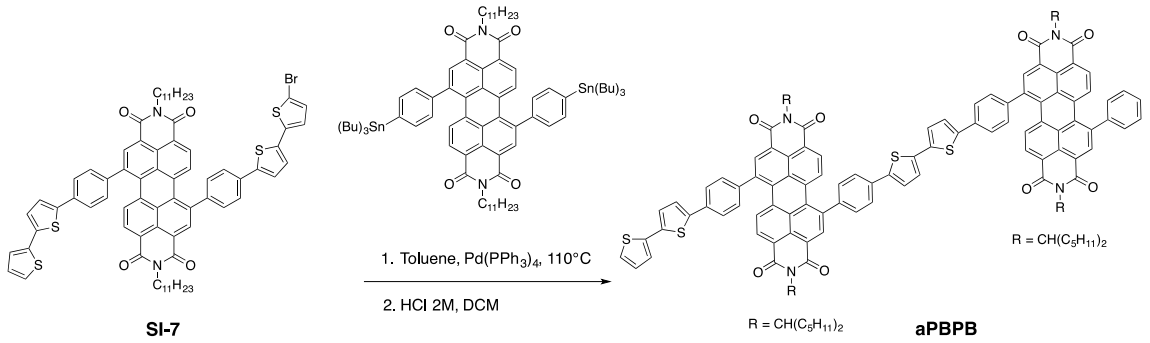

SI-7 aPBPB

***Synthesis of aPBPB*. SI-7** (0.0230 g, 0.0180 mmol, 1.00 equiv) and 1,7-bis[4-(tributylstannyl)-phenyl]-PDI (0.105 g, 0.0780 mmol, 4.00 equiv) were dissolved in toluene (6.00 mL) in a 20 mL scintillation vial equipped with a stir bar. The mixture was sparged with N_2 for thirty minutes. While under N_2, tetrakis(triphenylphosphine)palladium(0) (0.00200 g, 0.00200 mmol, 0.100 equiv) was added. The mixture was further sparged for ten minutes before being placed in a 107 °C oil bath and stirred overnight. The crude mixture was concentrated and purified by preparative TLC using a mobile phase of 50:50 CH_2Cl_2:hexanes. The product was passed through a small silica plug to remove residual impurities. The product was then dissolved in CH_2Cl_2 (2.0 mL) and HCl (2.0 mL) and stirred at room temperature for two days. The crude mixture was extracted with water and CH_2Cl_2, concentrated and purified by column chromatography (4 g Redisep Rf Silica) using a gradient from 0% to 100% CH_2Cl_2/hexanes.

The product was precipitated from CH_2Cl_2 and methanol to yield **aPBPB** as a purple solid (0.0050 g, 0.0020 mmol, 14%). **^{1}H NMR** (400 MHz, $C_2D_2Cl_4$) δ 8.62 (br, 4H), 8.17 (br, 4H), 8.03 – 7.98 (m, 3H), 7.84 (d, J = 8.4 Hz, 1H), 7.83 – 7.77 (m, 6H), 7.70 – 7.63 (m, 6H), 7.61 (br d, J = 6.3 Hz, 2H), 7.58 – 7.51 (m, 3H), 7.45 (br d, J = 3.1 Hz, 2H), 7.41 (d, J = 3.8 Hz, 1H), 7.32 (d, J = 3.9 Hz, 2H), 7.30 – 7.27 (m, 2H), 7.25 (d, J = 3.7 Hz, 1H), 7.11 – 7.06 (m, 1H), 5.16 (br, 4H), 2.31 – 2.13 (br m, 8H), 1.89 – 1.76 (br m, 8H) , 1.27 (br, 48H), 0.84 (br t, J = 6.6 Hz, 24H). **^{13}C NMR** (100 MHz, $C_2D_2Cl_4$) δ 165.13, 164.00, 142.97, 142.87, 142.53, 142.18, 142.14, 142.03, 141.56, 140.82, 140.79, 140.76, 137.89, 137.71, 137.67, 137.66, 135.90, 135.31, 134.72, 134.65, 134.62, 133.09, 130.79, 130.63, 130.47, 130.43, 129.89, 129.81, 129.66, 129.07, 128.56, 128.53, 128.49, 127.51, 127.47, 125.52, 125.34, 125.30, 125.23, 125.08, 124.45, 123.60, 123.26, 122.88, 122.52, 54.99, 54.48, 54.40, 32.84, 32.34, 27.14, 23.16, 14.38. **IR** (cm^{-1}) 2954, 2925, 2854, 1697, 1659, 1597, 1587, 1459, 1409, 1326, 1265, 1248, 1240, 814, 740. **HRMS** (ESI+) calculated *m/z* for $[C_{132}H_{130}N_4O_8S_4+H]^+$ 2027.8850, found 2027.8820.

Broadening (br) of peaks in the ^{1}H NMR spectrum is due to rotational isomers about the imide side chains. [20,64]

Multiple peaks for the same carbon in the ^{13}C NMR spectrum reflect rotational isomers about the imide side chains that have been seen previously. [20,64]

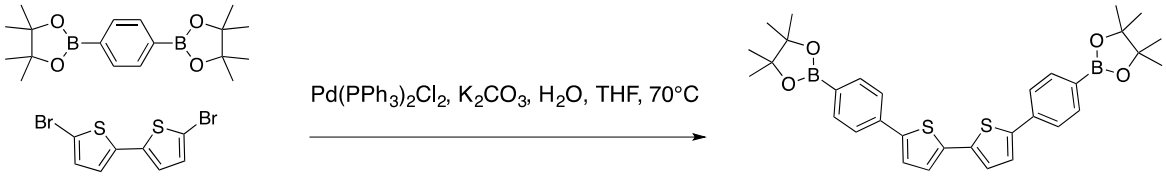

SI-8

***Synthesis of SI-8*:** 1,4-Benzenediboronic acid bis(pinacol) ester (0.815 g, 2.47 mmol, 4.00

equiv), 5,5′-dibromo-2,2′-bithiophene (0.200 g, 0.617 mmol, 1.00 equiv) and K_2CO_3 (2.12 g, 15.0 mmol, 25.00 equiv) were dissolved in THF (21.0 mL) and H_2O (6.00 ml) in a 100 mL round bottom flask equipped with a stir bar. The mixture was sparged with N_2 for thirty minutes. While under N_2, bis(triphenylphosphine)palladium chloride (0.0430 g, 0.0620 mmol, 0.100 equiv) was added. The mixture was further sparged for thirty minutes before being placed in a 70 °C oil bath and stirred overnight. The crude mixture was extracted with brine and ethyl acetate. The organic layer was collected, concentrated and purified by column chromatography using a gradient of 0 - 100% of hexanes/DCM. The final product was a pale yellow solid (0.030 g, 0.0526, 9%). **^{1}H NMR** (400 MHz, CD_2Cl_2) δ 7.80 (d, J = 8.2 Hz, 2H), 7.64 (d, J = 8.2 Hz, 2H), 7.36 (d, J = 3.8 Hz, 1H), 7.24 (d, J = 3.8 Hz, 1H), 1.36 (s, 24H). **IR** (cm^{-1}) 2973, 2934, 2857, 1605, 1399, 1362, 1145, 1093, 963, 859, 806. **HRMS** (ESI+) calculated *m/z* for $[C_{32}H_{36}B_2O_4S_2]^+$ 570.2241, found 570.2252.

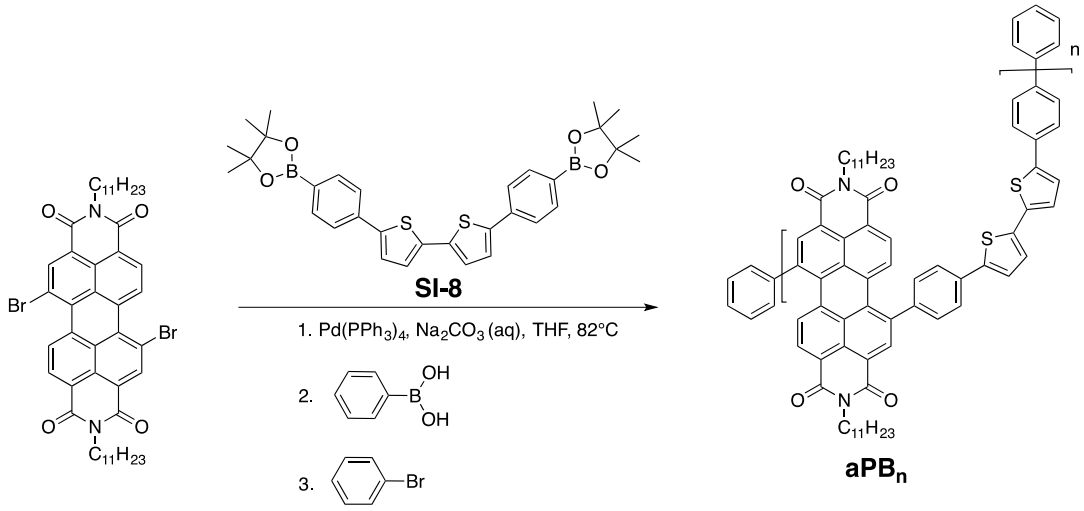

Synthesis of a(PB)$_n$. *N,N′*-Di(6-undecyl)-1,7-dibromoperylene-3,4:9,10-tetracarboxylic diimide (0.0420 g, 0.0490 mmol, 1.03 equiv), **SI-8** (0.027 g, 0.0474 mmol, 1.00 equiv), aqueous Na_2CO_3 (2 M, 2.20 mL) and THF (4.00 mL) were added to a 20 mL scintillation vial equipped with a stir bar. The mixture was sparged with N_2 for thirty minutes. While

under N_2, tetrakis(triphenylphosphine)palladium(0) (0.002 g, 0.002 mmol, 0.0400 equiv) was added. The mixture was further sparged for ten minutes and stirred for 48 hours at 82 °C. Then phenylboronic acid (0.0170 g, 0.142 mmol, 3.30 equiv) was added to the reaction and allowed to stir for three hours at 82 °C, followed by bromobenzene (0.200 mL, 1.90 mmol, 40 equiv). The reaction was left stirring overnight. The crude mixture was extracted with ethyl acetate and brine and concentrated. Solids were crashed out with methanol and further purified using soxhlet extraction using methanol, followed by hexanes. The final product was recovered using chloroform. The reaction yielded 0.040 g, 82% yield*. **^{1}H NMR*** (500 MHz, $C_2D_2Cl_4$) δ 8.71 (s, 2H), 8.27 (d, J = 8.0 Hz, 2H), 8.10 (d, J = 8.0 Hz, 2H), 7.86 (d, J = 7.5 Hz, 4H), 7.71 (d, J = 8.0 Hz, 4H), 7.47 (d, J = 3.0 Hz, 2H), 7.37 (d, J = 3.4 Hz, 2H), 5.26 – 5.16 (m, 2H), 2.28 (br, 4H), 1.99 (br, 4H), 1.43 (br, 24H)**, 0.95 (br, 12H). **GPC**: Mn = 6,388; Mw = 30,238 and PDI = 4.73; solvent = chloroform; λ = 440 nm. **HRMS** (MALDI) shows oligomers with repeating units of 1012 m/z up to the eight-mer.

* Polymer yields do not incorporate phenyl caps.

**The broad peak at 1.43 ppm indicates water in the sample and prevents integration of the overlapping alkyl protons.

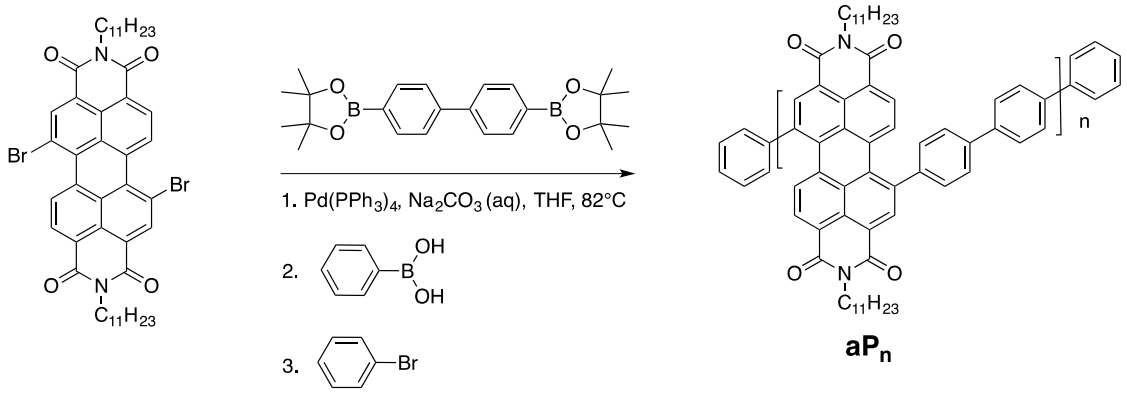

Synthesis of aP_n. *N,N′*-Di(6-undecyl)-1,7-dibromoperylene-3,4:9,10-tetracarboxylic diimide (0.200 g, 0.234 mmol, 1.00 equiv), 4,4′-biphenyldiboronic acid bis(pinacol) ester (0.0950 g, 0.234 mmol, 1.00 equiv), aqueous Na_2CO_3 (2 M, 11.0 mL) and THF (19.0 mL) were added to 100 mL two-neck, round bottom flask equipped with a stir bar. The mixture was sparged with N_2 for thirty minutes. While under N_2, tetrakis(triphenylphosphine)palladium(0) (0.0110 g, 0.009 mmol, 0.0400 equiv) was added. The mixture was further sparged for ten minutes and stirred for 48 hours at 78 °C. Then, commercially available phenylboronic acid (0.0940 g, 0.767 mmol, 3.30 equiv) was added to the reaction and allowed to stir for two hours at 78 °C, followed by bromobenzene (1.0 ml, 9.55 mmol, 41.0 equiv). The reaction was left stirring overnight. The crude mixture was extracted with ethyl acetate and brine and concentrated. Solids were crashed out with methanol and further purified using soxhlet extraction using methanol, followed by hexanes. The final product was recovered using chloroform. The reaction yielded 0.181 g for a 91% yield*. **^{1}H NMR*** (500 MHz, $C_2D_2Cl_4$) δ 8.77 (s, 2H), 8.33 (d, J = 8.5 Hz, 2H), 8.18 (d, J = 8.3 Hz, 2H), 7.99 (d, J = 8.1 Hz, 4H), 7.84 (d, J = 7.8 Hz, 4H), 5.27 – 5.20 (m, 2H), 2.31 (br, 4H), 1.99 (br, 4H), 1.42 (br, 24H)**, 0.95 (br, 12H). **GPC:** M_n = 16,950; M_w = 61,169 and PDI = 3.61; solvent = THF; λ = 500 nm. **HRMS** (MALDI) shows oligomers with repeating units of 849 m/z up to the nine-mer.

* Polymer yields do not incorporate phenyl caps.

**The broad peak at 1.43 ppm indicates water in the sample and prevents integration of the overlapping alkyl protons.

5.6. References and notes

(1) Krömer, J.; Rios-Carreras, I.; Fuhrmann, G.; Musch, C.; Wunderlin, M.;

Debaerdemaeker, T.; Mena-Osteritz, E.; Bäuerle, P. *Angew. Chem. Int. Ed.* **2000**, *39*, 3481.

(2) Nakao, K.; Nishimura, M.; Tamachi, T.; Kuwatani, Y.; Miyasaka, H.; Nishinaga, T.; Iyoda, M. *J. Am. Chem. Soc.* **2006**, *128*, 16740.

(3) Jasti, R.; Bhattacharjee, J.; Neaton, J. B.; Bertozzi, C. R. *J. Am. Chem. Soc.* **2008**, *130*, 17646.

(4) Zhang, F.; Gotz, G.; Winkler, H. D. F.; Schalley, C. A.; Bauerle, P. *Angew. Chem. Int. Ed.* **2009**, *48*, 6632.

(5) Omachi, H.; Matsuura, S.; Segawa, Y.; Itami, K. *Angew. Chem. Int. Ed.* **2010**, *49*, 10202.

(6) Iwamoto, T.; Watanabe, Y.; Sadahiro, T.; Haino, T.; Yamago, S. *Angew. Chem. Int. Ed.* **2011**, *50*, 8342.

(7) Iwamoto, T.; Watanabe, Y.; Sakamoto, Y.; Suzuki, T.; Yamago, S. *J. Am. Chem. Soc.* **2011**, *133*, 8354.

(8) Segawa, Y.; Miyamoto, S.; Omachi, H.; Matsuura, S.; Senel, P.; Sasamori, T.; Tokitoh, N.; Itami, K. *Angew. Chem. Int. Ed.* **2011**, *50*, 3244.

(9) Segawa, Y.; Senel, P.; Matsuura, S.; Omachi, H.; Itami, K. *Chem. Lett.* **2011**, *40*, 423.

(10) Sprafke, J. K.; Kondratuk, D. V; Wykes, M.; Thompson, A. L.; Hoffmann, M.; Drevinskas, R.; Chen, W.-H.; Yong, C. K.; Kärnbratt, J.; Bullock, J. E.; Malfois, M.; Wasielewski, M. R.; Albinsson, B.; Herz, L. M.; Zigmantas, D.; Beljonne, D.; Anderson, H. L. *J. Am. Chem. Soc.* **2011**, *133*, 17262.

(11) Hitosugi, S.; Nakanishi, W.; Isobe, H. *Chem. - Asian J.* **2012**, *7*, 1550.

(12) Hitosugi, S.; Yamasaki, T.; Isobe, H. *J. Am. Chem. Soc.* **2012**, *134*, 12442.

(13) Ishii, Y.; Nakanishi, Y.; Omachi, H.; Matsuura, S.; Matsui, K.; Shinohara, H.; Segawa, Y.; Itami, K. *Chem. Sci.* **2012**, *3*, 2340.

(14) Kayahara, E.; Sakamoto, Y.; Suzuki, T.; Yamago, S. *Org. Lett.* **2012**, *14*, 3284.

(15) Omachi, H.; Segawa, Y.; Itami, K. *Acc. Chem. Res.* **2012**, *45*, 1378.

(16) Evans, P. J.; Darzi, E. R.; Jasti, R. *Nat. Chem.* **2014**, *6*, 404.

(17) Kayahara, E.; Patel, V. K.; Yamago, S. *J. Am. Chem. Soc.* **2014**, *136*, 2284.

(18) Yamago, S.; Kayahara, E.; Iwamoto, T. *Chem. Rec.* **2014**, *14*, 84.

(19) Asai, K.; Fukazawa, A.; Yamaguchi, S. *Chem. Commun.* **2015**, *51*, 6096.

(20) Ball, M.; Fowler, B.; Li, P.; Joyce, L. A.; Li, F.; Liu, T.; Paley, D.; Zhong, Y.; Li, H.; Xiao, S.; Ng, F.; Steigerwald, M. L.; Nuckolls, C. *J. Am. Chem. Soc.* **2015**, *137*, 9982.

(21) Chang, S.-W.; Horie, M. *Chem. Commun.* **2015**, *51*, 9113.

(22) Chen, Q.; Trinh, M. T.; Paley, D. W.; Preefer, M. B.; Zhu, H.; Fowler, B. S.; Zhu, X.-Y.; Steigerwald, M. L.; Nuckolls, C. *J. Am. Chem. Soc.* **2015**, *137*, 12282.

(23) Darzi, E. R.; Hirst, E. S.; Weber, C. D.; Zakharov, L. N.; Lonergan, M. C.; Jasti, R. *ACS Cent. Sci.* **2015**, *1*, 335.

(24) Ito, H.; Mitamura, Y.; Segawa, Y.; Itami, K. *Angew. Chem. Int. Ed.* **2015**, *54*, 159.

(25) Jiang, H.-W.; Tanaka, T.; Mori, H.; Park, K. H.; Kim, D.; Osuka, A. *J. Am. Chem. Soc.* **2015**, *137*, 2219.

(26) Kuwabara, T.; Orii, J.; Segawa, Y.; Itami, K. *Angew. Chem. Int. Ed.* **2015**, *54*, 9646.

(27) Van Raden, J. M.; Darzi, E. R.; Zakharov, L. N.; Jasti, R. *Org. Biomol. Chem.* **2016**, *14*, 5721.

(28) Ball, M.; Zhong, Y.; Wu, Y.; Schenck, C.; Ng, F.; Steigerwald, M.; Xiao, S. X.; Nuckolls, C. *Acc. Chem. Res.* **2015**, *48*, 267.

(29) Nicolai, H. T.; Kuik, M.; Wetzelaer, G. A. H.; de Boer, B.; Campbell, C.; Risko, C.; Brédas, J. L.; Blom, P. W. M. *Nat. Mater.* **2012**, *11*, 882.

(30) Mandoc, M. M.; de Boer, B.; Paasch, G.; Blom, P. W. M. *Phys. Rev. B* **2007**, *75*, 193202.

(31) Arias, A. C.; MacKenzie, J. D.; McCulloch, I.; Rivnay, J.; Salleo, A. *Chem. Rev.* **2010**, *110*, 3.

(32) Kaake, L. G.; Barbara, P. F.; Zhu, X.-Y. *J. Phys. Chem. Lett.* **2010**, *1*, 628.

(33) Sirringhaus, H. *Adv. Mater.* **2005**, *17*, 2411.

(34) Iyoda, M.; Yamakawa, J.; Rahman, M. J. *Angew. Chem. Int. Ed.* **2011**, *50*, 10522.

(35) Iwamoto, T.; Watanabe, Y.; Takaya, H.; Haino, T.; Yasuda, N.; Yamago, S. *Chem. – Eur. J.* **2013**, *19*, 14061.

(36) Nakanishi, Y.; Omachi, H.; Matsuura, S.; Miyata, Y.; Kitaura, R.; Segawa, Y.; Itami, K.; Shinohara, H. *Angew. Chem. Int. Ed.* **2014**, *53*, 3102.

(37) Anthony, J. E.; Facchetti, A.; Heeney, M.; Marder, S. R.; Zhan, X. W. *Adv. Mater.* **2010**, *22*, 3876.

(38) Zhou, E. J.; Cong, J. Z.; Wei, Q. S.; Tajima, K.; Yang, C. H.; Hashimoto, K. *Angew. Chem. Int. Ed.* **2011**, *50*, 2799.

(39) Li, C.; Wonneberger, H. *Adv. Mater.* **2012**, *24*, 613.

(40) Sharenko, A.; Proctor, C. M.; van der Poll, T. S.; Henson, Z. B.; Nguyen, T. Q.; Bazan, G. C. *Adv. Mater.* **2013**, *25*, 4403.

(41) Cai, Y.; Huo, L.; Sun, X.; Wei, D.; Tang, M.; Sun, Y. *Adv. Energy Mater.* **2015**, *5*, 1500032.

(42) Nolde, F.; Pisula, W.; Muller, S.; Kohl, C.; Mullen, K. *Chem. Mater.* **2006**, *18*, 3715.

(43) Zhong, Y.; Kumar, B.; Oh, S.; Trinh, M. T.; Wu, Y.; Elbert, K.; Li, P. P.; Zhu, X. Y.; Xiao, S. X.; Ng, F.; Steigerwald, M. L.; Nuckolls, C. *J. Am. Chem. Soc.* **2014**, *136*, 8122.

(44) Yan, Q. F.; Zhao, D. H. *Org. Lett.* **2009**, *11*, 3426.

(45) Huo, L. J.; Zhou, Y.; Li, Y. F. *Macromol. Rapid Commun.* **2008**, *29*, 1444.

(46) Würthner, F.; Saha-Möller, C. R.; Fimmel, B.; Ogi, S.; Leowanawat, P.; Schmidt, D. *Chem. Rev.* **2016**, *116*, 962.

(47) Zhong, Y.; Trinh, M. T.; Chen, R. S.; Wang, W.; Khlyabich, P. P.; Kumar, B.; Xu, Q. Z.; Nam, C. Y.; Sfeir, M. Y.; Black, C.; Steigerwald, M. L.; Loo, Y. L.; Xiao, S. X.; Ng, F.; Zhu, X. Y.; Nuckolls, C. *J. Am. Chem. Soc.* **2014**, *136*, 15215.

(48) Meng, D.; Sun, D.; Zhong, C.; Liu, T.; Fan, B.; Huo, L.; Li, Y.; Jiang, W.; Choi, H.; Kim, T.; Kim, J. Y.; Sun, Y.; Wang, Z.; Heeger, A. J. *J. Am. Chem. Soc.* **2016**, *138*, 375.

(49) Wu, Q.; Zhao, D.; Schneider, A. M.; Chen, W.; Yu, L. *J. Am. Chem. Soc.* **2016**, *138*, 7248.

(50) Liang, Y.; Xu, Z.; Xia, J.; Tsai, S.-T.; Wu, Y.; Li, G.; Ray, C.; Yu, L. *Adv. Mater.* **2010**, *22*, E135.

(51) Liao, S.-H.; Jhuo, H.-J.; Cheng, Y.-S.; Chen, S.-A. *Adv. Mater.* **2013**, *25*, 4766.

(52) He, Z.; Xiao, B.; Liu, F.; Wu, H.; Yang, Y.; Xiao, S.; Wang, C.; Russell, T. P.; Cao, Y. *Nat. Photonics* **2015**, *9*, 174.

(53) Zhong, Y.; Trinh, M. T.; Chen, R.; Purdum, G. E.; Khlyabich, P. P.; Sezen, M.; Oh, S.; Zhu, H.; Fowler, B.; Zhang, B.; Wang, W.; Nam, C.-Y.; Sfeir, M. Y.; Black, C. T.; Steigerwald, M. L.; Loo, Y.-L.; Ng, F.; Zhu, X.-Y.; Nuckolls, C. *Nat. Commun.* **2015**, *6*, 8242.

(54) Heeger, A. J. *Adv. Mater.* **2014**, *26*, 10.

(55) Sun, Y.; Seo, J. H.; Takacs, C. J.; Seifter, J.; Heeger, A. J. *Adv. Mater.* **2011**, *23*, 1679.

(56) You, J. B.; Dou, L. T.; Yoshimura, K.; Kato, T.; Ohya, K.; Moriarty, T.; Emery, K.; Chen, C. C.; Gao, J.; Li, G.; Yang, Y. *Nat. Commun.* **2013**, *4*, 10.

(57) Elumalai, N. K.; Uddin, A. *Energy Environ. Sci.* **2015**, *9*, 291.

(58) Wang, M.; Wang, H.; Yokoyama, T.; Liu, X.; Huang, Y.; Zhang, Y.; Nguyen, T.-Q.; Aramaki, S.; Bazan, G. C. *J. Am. Chem. Soc.* **2014**, *136*, 12576.

(59) Li, W.; Hendriks, K. H.; Furlan, A.; Wienk, M. M.; Janssen, R. A. J. *J. Am. Chem. Soc.* **2015**, *137*, 2231.

(60) Hendriks, K. H.; Wijpkema, A. S. G.; van Franeker, J. J.; Wienk, M. M.; Janssen, R. A. J. *J. Am. Chem. Soc.* **2016**, DOI: 10.1021/jacs.6b05868.

(61) Zhao, Y.; Guo, Y.; Liu, Y. *Adv. Mater.* **2013**, *25*, 5372.

(62) Newman, C. R.; Frisbie, C. D.; Filho, da S.; Brédas, J.-L.; Ewbank, P. C.; Mann, K. R. *Chem. Mater.* **2004**, *16*, 4436.

(63) Dou, L.; You, J.; Hong, Z.; Xu, Z.; Li, G.; Street, R. A.; Yang, Y. *Adv. Mater.* **2013**, *25*, 6642.

(64) Rajasingh, P.; Cohen, R.; Shirman, E.; Shimon, L. J. W.; Rybtchinski, B. J. Org.

Chem. 2007, 72, 5973.

Chapter 6 Rigid, Conjugated Macrocycles for High Performance Organic Photodetectors

This chapter is based on the following manuscript: Boyuan Zhang, M. Tuan Trinh, Brandon Fowler, Melissa Ball, Qizhi Xu, Fay Ng, Michael L. Steigerwald, X.-Y. Zhu*, Colin Nuckolls*, and Yu Zhong*, "Rigid, Conjugated Macrocycles for High Performance Organic Photodetectors", *J. Am. Chem. Soc., submitted*. Boyuan Zhang and I fabricated and characterized all the devices with assistance from Qizhi Xu. Brandon Fowler and Melissa Ball synthesized all the compounds with assistance from Fay Ng. M. Tuan Trinh conducted TA measurements and data analysis. Melissa Ball and Michael L. Steigerwald performed DFT calculations.

6.1. Introduction

In this chapter, we describe a new molecular design for creating organic photodetectors (OPDs) with unparalleled ability to detect photons. The use of organic materials as the active component in photodetectors is attractive because of the potential ease of their fabrication as light-weight and mechanically flexible devices.[1-4] One critical parameter that limits OPDs performance is high dark current, because it determines the noise current level and sensitivity of an OPD. The current state-of-the-art for OPDs employs a number of modifications such as, carrier blocking layers,[5] vertical phase separation[6] and thick active layers,[7] to lower the dark current. An alternative approach is to use reaction chemistry to build the desired properties into the structure of the active molecule to minimize the charge carriers in the active layers.

The dark current in organic, electronic materials is multi-faceted, and its origins are

not completely understood. Covalent defects formed upon photo/thermo-activation[8-10] and mechanically deformed sp^2 carbon-carbon bonds in π-conjugated molecules are known to produce charged defects that introduce carriers.[11-14] Fullerenes, which are one of the most ubiquitous organic electronic materials, undergo a facile dimerization when irradiated.[8,9] This also contributes to the dark current.[11]

To address these issues, we designed a macrocycle that consists of redox-active diphenyl perylenediimide (**P**) wrapped into a tetrameric structure (Figure 6.1A). We call this **cP4**. We find that when we incorporate **cP4** into OPDs the devices have high sensitivity for visible light detection in a very simple device structure. The macrocycle contains several key design elements to yield the highly sensitive OPD result: (1) the rigid structure, constrained in a ring, minimizes the number of charged defects originated from deformed sp^2 carbons; (2) no covalent defects are formed upon photo/thermo-activation; (3) it is efficacious at transporting electrons; (4) and it has high visible light absorption that yields significant photocurrent in a bulk heterojunction photodiode.[15] Using this design we are able to suppress the dark current density while retaining high responsivity in an ultra-sensitive non-fullerene OPD. Without the need for extra carrier blocking layers, the highest detectivity in our device approaches 10^{14} Jones at near zero bias voltage. This detectivity is comparable to the best fullerene-based photodetectors, and the sensitivity at low working voltages (< 0.1 V) is a record for non-fullerene OPDs. A direct comparison between **cP4** and an acyclic control molecule reveals that **cP4**'s superior performance originates from its rigid, conjugated, and macrocyclic structure.

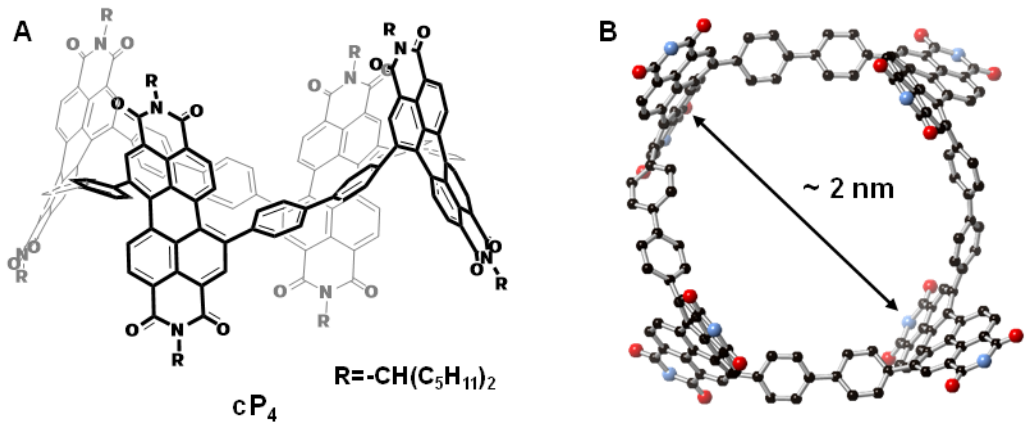

Figure 6.1. (A) Molecular structure of **cP4**. (B) Energy minimized structures from DFT for **cP4**. Carbon = gray, nitrogen = blue, oxygen = red. Hydrogen atoms have been removed to clarify the view. A methyl group substitutes the sidechains in the calculations. The methyl group, too, has been removed to clarify the view in the structures presented here.

6.2. Results and discussion

In a previous study, we found that **cP4** is an n-type semiconductor that transports electrons in both field effect transistors and solar cells.[15] Figure 6.1B shows **cP4**'s energy minimized structure, according to density functional theory (DFT). **cP4**'s ~ 2 nm diameter cavity in its interior is large enough to thread donor polymers (Figure 6.1B); its branched sidechains impart high solubility in common organic solvents. In solution, the lowest-energy absorption peak at 585 nm has an extinction coefficient of 7.9×10^4 $M^{-1}cm^{-1}$ (Figure 6.5). The active layer of the photodetector is a blended film of **cP4** and the commercially available polymer donor PTB7-Th.[16,17] The absorption of PTB7-Th is bathochromically shifted relative to **cP4** (Figure 6.2A). Figure 6.2B shows a model of a simple device structure that was used in this study. Figure 6.2C contains the energy diagram of the materials used in this device. We note the energy offset between the donor's lowest unoccupied molecular orbital (LUMO) and the acceptor's LUMO is well-matched (Figure

6.2C); energy levels were estimated from cyclic voltammetry (CV).[15,18] The thickness of the active film is ~150 nm.

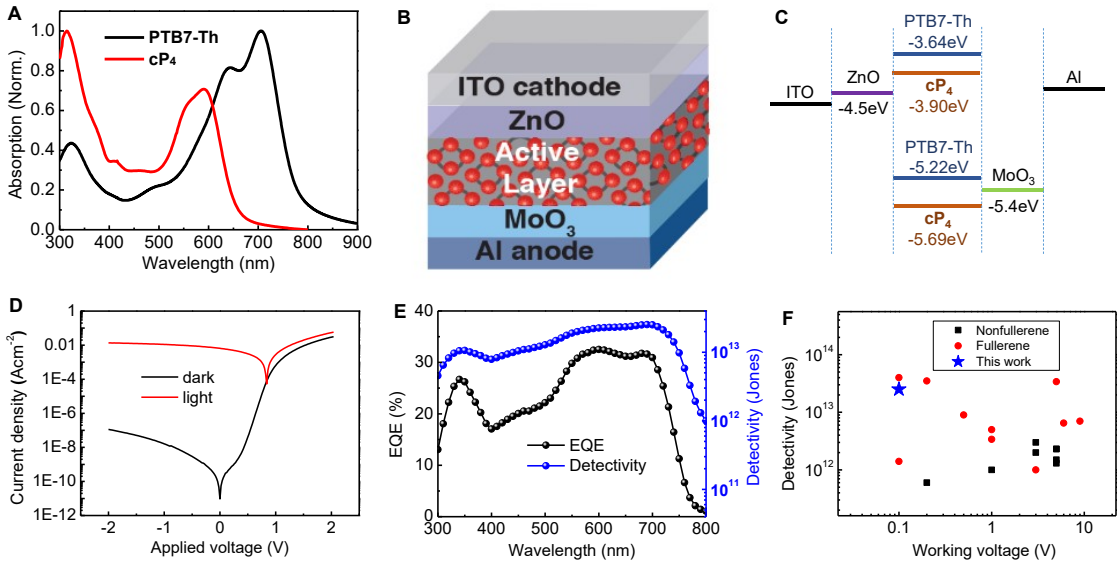

Figure 6.2. (A) Normalized film absorption spectra of PTB7-Th and **cP4**. (B) Device structure for the inverted organic photodetector. (C) Schematic of the energy levels of ITO, ZnO, PTB7-Th, **cP4**, MoO_3 and Al. Energy levels of PTB7-Th and **cP4** were estimated from cyclic voltammetry measurements in solution and adopted from ref. 18 and ref. 15, respectively. (D) Current density-voltage curves under dark condition and simulated AM 1.5 G irradiation (100mWcm^{-2}). (E) External quantum efficiency and specific detectivity spectra calculated at -0.1 V bias voltage. (F) Comparison of detectivity and working voltage in reported organic photodetectors and this work.[5,7,19-32]

Figure 6.2D displays the current-voltage curves for a typical OPD under dark conditions and simulated AM 1.5G irradiation (100 mWcm^{-2}). One of the exciting findings is that the OPD possesses extremely small dark current at reverse bias voltage. The dark *J-V* curve shows a high rectification ratio of >10^5 at ±2 V and a dark current density as small as 1.4×10^{-10} Acm^{-2} at -0.1 V. This dark current density is one order of magnitude lower

than the best fullerene-free OPDs[7] and comparable with fullerene-based OPDs and perovskite photodetectors.[5,33] Notably, both fullerene-based OPDs and perovskite photodetectors need extra electron or hole blocking layers in order to achieve a low level of the dark current.[5,33] Equally important is the large photocurrent that is generated upon photoexcitation at small reverse bias voltages. The on/off ratio is $>10^7$ calculated at -0.1 V under simulated AM 1.5G irradiation (100 $mWcm^{-2}$). The OPD device described here can operate at small bias voltages and even at zero bias. This compares favorably with previously reported non-fullerene OPDs; they require much larger reverse bias voltages (typically -1V ~ -3 V) to operate due to the poor carrier extraction.[22-25,30]

Ultralow dark current could result from poor carrier transport ability. This is not the case for **cP4**. As discussed above, **cP4** effectively transports electrons generated upon photoexcitation. This allows the OPD to operate at a small bias voltage. We inherently achieve high photocurrent and low dark current simultaneously in the **cP4** OPD with a thin active layer and a simple device structure. **cP4** is an ideal design for an electron acceptor to create a highly sensitive non-fullerene OPD.

Table 6.1. Summary of OPD device parameters measured at -0.1 V bias voltage.

	J_d (Acm^{-2})	EQE (%)	R (AW^{-1})	D^* (Jones)
cP4	1.5×10^{-10}	33 @600nm	0.18 @690nm	2.5×10^{13} @690nm
$PC_{71}BM$	5.6×10^{-7}	70 @640nm	0.39 @710nm	9.2×10^{11} @710nm
aPn	1.0×10^{-9}	22 @350nm	0.09 @680nm	4.8×10^{12} @680nm

Table 6.1 summarizes the responsivity (R), specific detectivity (D^*), external quantum efficiency (EQE) and dark current (J_d) for the OPD device data for the PTB7-Th:**cP4** blended films. The devices have a linear dynamic range (LDR) > 140 dB (Figure

6.6) and cutoff frequency of 467 kHz (Figure 6.7). Overall the device characteristics are excellent; in particular, **cP4** greatly excel in detectivity. We find that the specific detectivity is more than 10^{13} Jones over the whole visible light region at -0.1V. The highest D^* was calculated to be 2.5×10^{13} Jones at 700nm (Figure 6.2E). At zero bias, the calculated specific detectivity is as high as 1×10^{14} Jones. These values are among the highest detectivities for the state-of-the-art fullerene photodetector[5,19-22,26-29,32] and much higher than the best non-fullerene OPDs[7,23-25,30,31,34] (Figure 6.2F). Moreover, the **cP4**-based OPD requires much smaller working voltage compared with other non-fullerene OPDs because of their relatively high responsivity (R) near zero bias voltage (Figure 6.2F).

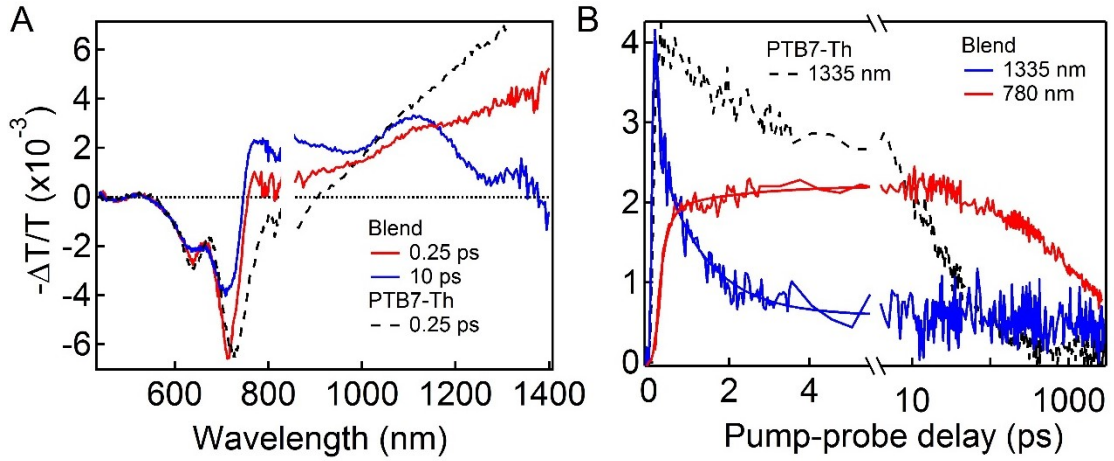

Figure 6.3. Transient absorption spectra (A) and dynamics (B) for the neat film of PTB7-Th and blended film of **cP4** and PTB7-Th pumped at 710 nm. The dashed-black curves are from PTB7-Th which were scaled for comparison.

One of the two key parameters responsible for high responsivity (R) is efficient charge generation from photo-excitation in the active layer. Extensive research on molecular donor/acceptor interfaces has pointed to the critical role of electronic delocalization in facilitating efficient charge separation at the donor/acceptor

interfaces.[35,36] In particular, the spherical fullerene based electron acceptors are believed to be transport charge efficiently due to their three dimensional connectivity in ensuring electronic delocalization on the acceptor side.[37,38] Can **cP4** provide similar connectivity and electronic delocalization that is necessary for charge separation? While the high responsivity near zero bias suggests the answer above is affirmative, we further support this by studying the efficient charge separation at the PTB7-Th/**cP4** interface using transient absorption (TA) spectroscopy (see Section 6.5 for the details of the experiment).

The linear absorption spectra in Figure 6.2A show that the donor material, PTB7-Th can be selectively excited at 710 nm in the blended film; subsequently, we can monitor electron transfer from PTB7-Th to **cP4**. At a short pump-probe delay (0.25 ps), we observe features arising from PTB7-Th (red curve in Figure 6.3A) with the bleaching at 630 and 715 nm and excited state absorption (ESA) in the near IR range. This is similar to the TA spectrum from the neat PTB7-Th film (black dashed curve in Figure 6.3A). The bleaching in PTB7-Th is reduced and new ESA transitions from 770 to 1300 nm evolve as the delay time increases. These new ESA features centered at 840 and 1120 nm are attributed to the charge (polaron) absorptions in the perylenediimide (PDI) and PTB7-Th moieties, respectively.[39-41] While the ESA of the PTB7-Th singlet dominates in the long probe wavelength range (> 1300 nm), the ESA of charges in either donor or acceptor materials is negligible. Thus, dynamics at 1335 nm are a good measure of exciton dissociation at the donor/acceptor interface. Figure 6.3B shows that the biexponential fit (blue curve) to the dynamics at 1335 nm (blue dots) yields time constants of 0.11 ± 0.04 ps (42% weight) and 1.2 ± 0.1 ps (58% weight). The charge buildup monitored by polaron ESA at 780 nm (red dots) gives nearly identical time constants (red curve). These time constants indicate

ultrafast electron transfer from PTB7-Th to **cP4**. The short time constant can be attributed to the instantaneous charge transfer near the interface upon photoexcitation, while the longer time constant is attributed to exciton diffusion in PTB7-th prior to the dissociation event.[40,41] For comparison, the singlet exciton lifetime in neat PTB7-Th is of the order of nanoseconds (black dashed curve in Figure 6.3B). This is much longer than that in the blend. We also observe similarly ultrafast hole transfer from **cP4** to PTB7-Th when both donor and acceptor are excited at 560 nm (see Section 6.5). These measurements confirm that **cP4** photodetector performance is comparable, if not better than that of a fullerene, for exciton dissociation in blend films.[42-45]

The second important parameter that determines the high detectivity in these devices is the dark current density. To gain insight into the origin of the device characteristics, we analyze the *J-V* curve under dark conditions to calculate the reverse saturation dark current J_0. The fitting method is detailed in the Supporting Information. The saturation dark current density is as low as 7.7×10^{-13} Acm^{-2} (Figure 6.9). The intrinsic conductivity is determined by the intrinsic free carrier density and the mobility. Photocurrent and thin film field effect transistor measurements reveal efficacious electron transporting ability.[15] Therefore, such a low level of J_0 indicates a small amount of intrinsic free carrier density. To verify that the intrinsic conductivity of the thin films is dominated by the charged defects, we measured the dependence of the dark current density on temperature. The activation energies are calculated to be (0.15 ± 0.01) eV and (0.20 ± 0.01) eV at -2 V and -0.5 V, respectively (Figure 6.10). These values are much smaller than the band gaps of the active organic components (Figure 6.2C) and are consistent with thermal activation energy of locally bound charged defects.[11,46]

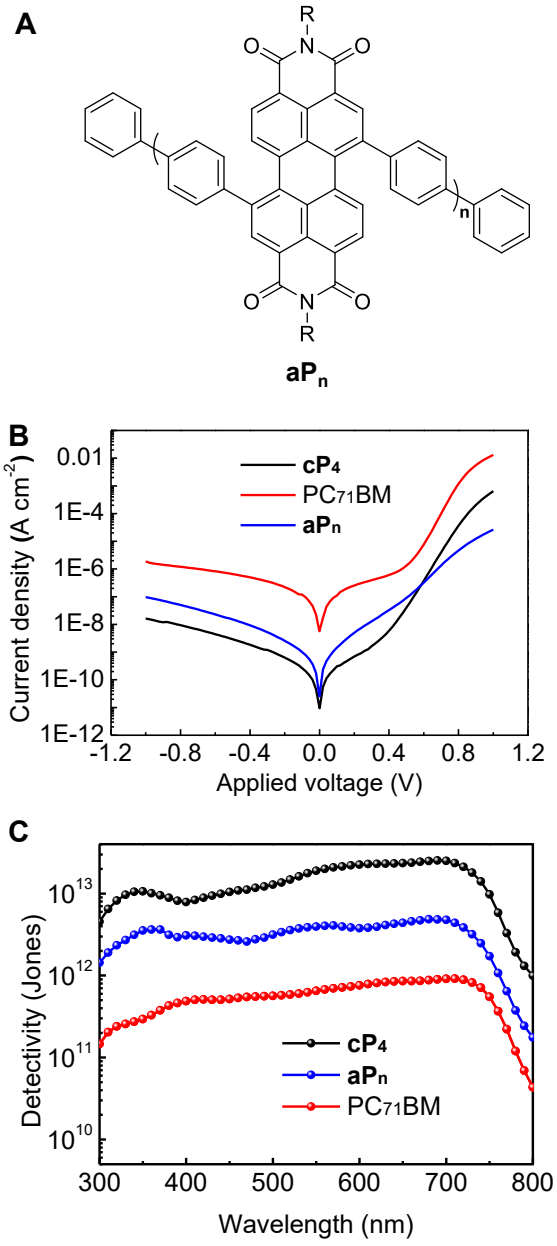

Figure 6.4. (A) Molecular structure of **aP$_n$** used to test the origin of the low dark current. (B) Dark current density-voltage curves for PC$_{71}$BM, **aP$_n$**, and **cP$_4$** based photodetectors with the same device structure as shown in Figure 6.2B. (C) Specific detectivity spectra for **cP$_4$**, **aP$_n$** and PC$_{71}$BM based OPDs calculated at -0.1V bias voltage.

To better understand the origin of the low density of charged defects in **cP$_4$**, we made a direct comparison between a PC$_{71}$BM and **cP$_4$** based OPD with the same device

structure as shown in Figure 6.2B. Although the responsivity (R) of the $PC_{71}BM$-based OPD is approximately two fold higher than that of the **cP4**-based device (Table 6.1 and Figure 6.12), the dark current of the $PC_{71}BM$-based device is 2-3 orders of magnitude higher than that of the **cP4**-based one (Figure 6.4B). It is obvious that the dark current level dominates the detectivity in this type of OPD. Thus, the detectivity of the **cP4**-based OPD is more than one order of magnitude higher than that of the $PC_{71}BM$-based one (Figure 6.4C). One of the origins of the high dark current is from the chemistry of fullerenes. $PC_{71}BM$ is known to undergo dimerization that is initiated by electron donors, metals, and photons.[8-10,47,48] In each of these cases, in a solid state film, the partners need to be unencumbered and in the correct orientation for the reaction to occur. In the absence of these conditions, the films will contain carriers that contribute to the relatively high dark current.[8-10] Fullerene-based OPDs made with fullerenes require extra blocking layers to minimize this relatively high dark current. Compared with fullerenes, PDIs are known to exhibit exceptional chemical, thermal and photochemical stability.[49-53] The PDI units in **cP4** have no easily accessible pathway to introduce these same type of covalent defects. This accounts for the low intrinsic conductivity in **cP4** OPDs.[11]

In order to assess the importance of the cyclic, rigid structure of **cP4**, we synthesized an acyclic, polymeric version, named **aP4** (Figure 6.4A). Overall, the **aPn** photodetector performs very well and shows high sensitivity. Although the responsivity of the **aPn** OPD is about one fourth of that in the $PC_{71}BM$ OPD, the dark current density in the **aPn** OPD is one order of magnitude lower than that in the $PC_{71}BM$ OPD (Figure 6.4B). As a result, the **aPn** OPD shows a doubling of the detectivity compared to the $PC_{71}BM$ OPD (Figure 6.4C). These results, once again, suggest that dark current dominates the

sensitivity and confirm the importance of incorporating chemically stable PDIs into electron acceptors in OPDs. Even so, the **aP$_n$** OPD is still not as effective as the **cP$_4$** OPD in terms of detectivity. As a comparison, the **aP$_n$**-based OPD has a dark current 1.0×10^{-9} Acm^{-2} at -0.1 V, which is about ten-fold higher than that of the **cP$_4$**-based device (see Table 6.1 and Figure 6.4B). In addition, the **aP$_n$**-based OPD also shows lower responsivity compared to **cP$_4$** devices (Table 6.1 and Figure 6.12). The resulting peak D^* for the **aP$_n$**-based OPD is 4.8×10^{12} Jones at 680 nm, only about one third of the peak value in the **cP$_4$**-based OPD. This is because intrinsic, charged defects in linear polymer semiconductors originate from endgroups[13,54,55] and deformed sp^2 carbons near the rotatable C-C single bonds.[11-14] The torsional effect is inevitable in linear molecules with flexible backbones. These problems are eliminated by winding linear molecules into rigid, conjugated macrocycles with no endgroups.[15,56] The macrocyclic **cP$_4$** possesses a locked conformation with higher rigidity (Figure 6.1B) and is expected to create fewer locally charged defects relative to the linear polymeric counterpart.

6.3. Conclusion

The results described above show that the rigid, cyclic molecular structure of is an important design criterion to achieve ultralow intrinsic conductivity in the OPDs. We found that the rigid, conjugated macrocycle is able to act as the electron acceptor in high performance OPDs. Using this molecular design we are able to suppress dark current density while retaining high responsivity in an ultra-sensitive non-fullerene OPD. Without the need for extra carrier blocking layers, this detectivity is comparable to the best fullerene-based photodetectors, and the sensitivity at low working voltages is a record for non-fullerene OPDs. It is clear from this study that the devices can be further improved by

designing the electron donating material to form a shape and electronic match for these macrocyclic electron acceptors.

6.4. Experimental section

6.4.1. Device fabrication

cP4 and **aPn** were synthesized according to a previously reported method.[15] PTB7-Th was purchased from 1-material. The synthesis of ZnO precursor was described elsewhere.[2] Prepatterned ITO-coated glass with a sheet resistance of ~15Ω/sq was cleaned with detergent, ultrasonicated in DI water, acetone and isopropanol for 30 min, respectively. Subsequently, we treated the substrates by UV-Ozone for 10 min. The prepared ZnO precursor was spin-cast onto the ITO substrate at 3000 rpm for 1 min, followed by annealing at 200 ºC for 1 h in air, to form a thin film with approximate thickness of 20 nm. The BHJ active layer was prepared by spin-coating a mixed solution containing polymer and acceptor in chlorobenzene. The thickness of the prepared active layers is about 150 nm. Finally, a 10 nm MoO_3 layer was deposited first and then a 100 nm Al electrode were subsequently deposited through a shadow mask by thermal evaporation under a vacuum about 1×10^{-6} torr. The active area of the device was 9 mm^2.

6.4.2. Characterization

Absorption spectra were obtained on Shimadzu UV 1800 UV-Vis. The current-density–voltage (J–V) curves were measured by a Keithley 2635A source measure unit. EQE measurements were performed using a QEXL system from PV Measurements Inc. For linear dynamic range measurement, a light-emitting diode (625 nm) was used as light source. For cutoff frequency measurement, the LED was modulated by a function generator (Tektronix CFG253). The photodetectors were connected to an oscilloscope (Tektronix

TDS 224) with an input impedance of 50 Ω.

Temperature-dependent current-voltage measurements were realized in a vacuum cryogenic probe station (Lakeshore TTP4). Computer-controlled source units were used to apply DC potentials (Yokogawa 7651). Current measurements were obtained using a current preamplifier (Stanford Research System SR570) and a digital multimeter (Keysight 34401A). All device measurements were performed in vacuum ($P < 1\times10^{-4}$ Torr) at different temperatures.

In the transient absorption experiments, the pump pulse comes from an optical parametric amplifier (tunable from UV to the near IR, 100 fs pulse width, 1 KHz rep-rate). The probe pulse is a white-light supercontinuum (from 450 to 900 nm and from 850 to 1600 nm for the visible and near IR range, respectively). The detection consists of a pair of high resolution multichannel detector arrays coupled to a high-speed data acquisition system (HELIOS, Ultrafast System Inc.). In order to avoid photo degradation, we kept samples in the inert gas both in storing and during measurements.

6.5. Supplementary materials

6.5.1. Absorption spectrum

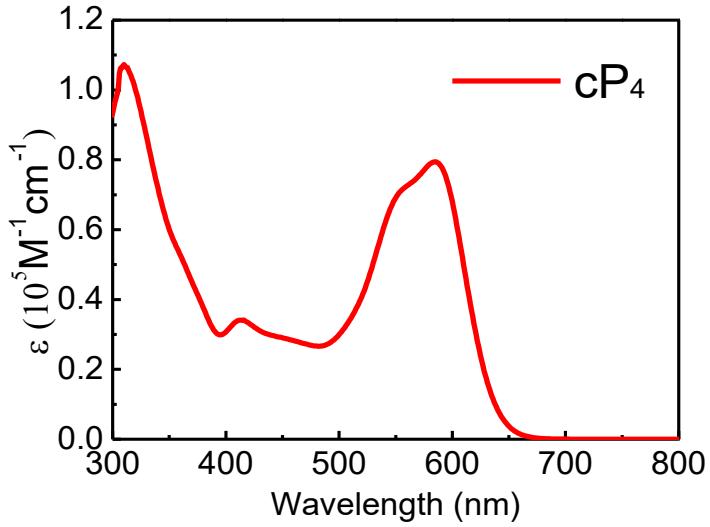

Figure 6.5. UV-vis absorption spectra of **cP4** (1×10^{-5} M concentration in dichloromethane with a path length l = 1 cm).

6.5.2. The linear dynamic range (LDR) measurement

The linear dynamic range (LDR) is expressed as LDR=20log(J_{high}/J_d), where J_{high} is the highest measurable current density in the linear response range and J_d is the dark current density.

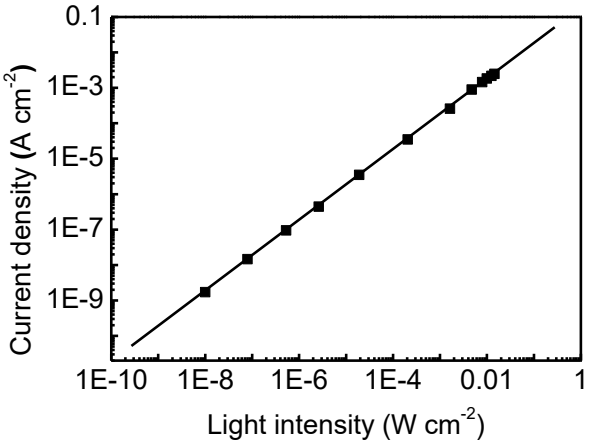

Figure 6.6. Linear dynamic range of the **cP4**-based OPD. A red light emitting diode (λ=625nm) was used as the light source.

6.5.3. Frequency-dependent measurement of the cP4-based OPD

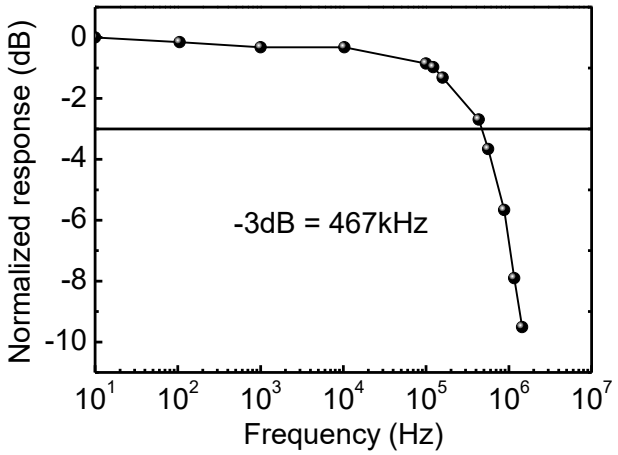

Figure 6.7. Frequency response of the **cP4**-based OPD. The device area is 0.09 cm^2.

6.5.4. Transient absorption spectra

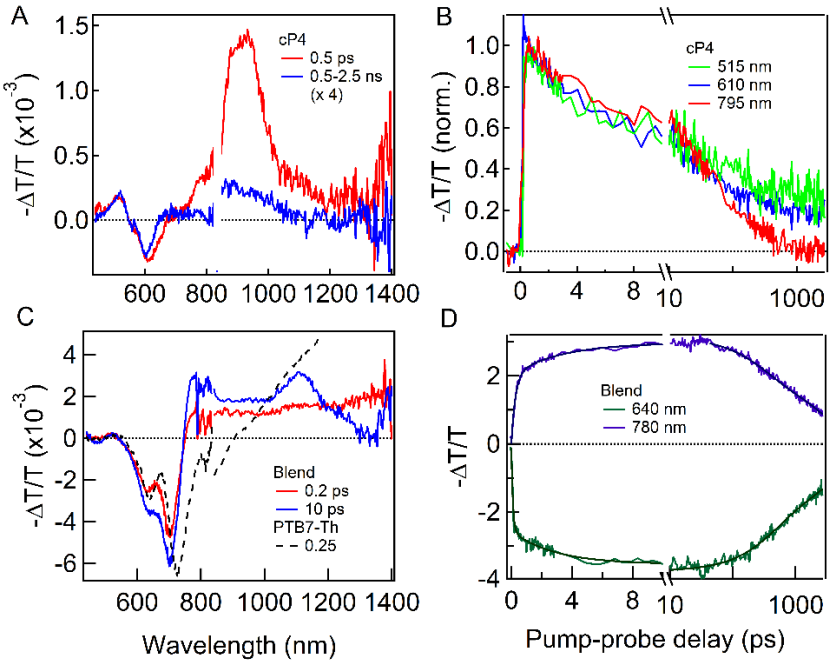

Figure 6.8. Transient absorption spectra and dynamics for the neat **cP4** (A, B) and the

blended film of **cP4** and PTB7-th (C,D) upon 560 nm excitation. The dashed-black curve in C is the spectrum from PTB7-Th upon the excitation of 710 nm. The signal from PTB7-th was scaled for comparison.

Figure 6.8A and B show the differential transmission spectra and dynamics for the neat film **cP4** upon 560 nm excitation. The negative feature centered at 600 nm is attributed to a bleaching of the ground state absorption under the presence of photo-excited excitons/charges. The positive features centered at 500 nm and from 700 nm to near IR are the excited state absorption (ESA) of the photo-excited excitons or charges. The ESA feature at 785 nm decays biexponentially with the time constants of 8 ± 0.7 ps (52%) and 122 ± 8 ps (48%) (red curve, Figure 6.8B). This feature is assigned to the singlet ESA, $S_1 \rightarrow S_N$ transition, similar to that of other PDI derivative compounds. The ESA dynamics at 500 nm and ground state bleaching, however, behave differently. More than 50 % of the ESA signal at 500 nm decays with a time constant that is similarly to the dynamics at 785 nm. The remaining signal (20%) lasts for a long time, ns time scale (green and blue curves). The long living signal can either come from photo excited charges or from triplet excitons.

At the same excitation wavelength, 560 nm, for the blend of **cP4** and PTB7-Th, we observed the dominance of ground state bleaching from PTB7-Th at the range of 575-750 nm (Figure 6.8C, the dashed-black curve is from the neat PTB7-Th pumping at 710 nm). Note that at this excitation wavelength, we excite both donor and acceptor materials. The ESA cross section and the ground state bleaching from the polymer are much stronger than that of **cP4** resulting in the dominance feature from the polymer even we excited both materials at 560 nm. At the longer time (10 ps, Figure 6.8C), the bleaching from PTB7-Th increases and the hole ESA feature in PTB7-Th at 1100 nm appears. The increase of

bleaching feature from PTB7-Th indicates the hole transfers from **cP4** to PTB7-Th. Since the ESA cross session at 780 nm for singlet in **cP4** is very small compared to that of charge ESA (compare Figure 6.8A and C), the ESA signal at this wavelength reflects the dynamics of charge generation from exciton dissociation. The fit to the dynamics at 780 nm gives two time constants, 0.2 ± 0.02 ps and 3.3 ± 0.4 ps (Figure 6.8D). These time constants reflect the electron and hole transfer upon 560 nm excitation. In addition, we observed a much longer charge lifetime in the blends (on the nanosecond time scale) when compared to that of the exciton dynamics in the neat films (Figure 6.8B and D). The longer charge lifetime is due to exciton dissociated into separating charges rather than charge transfer excitons.

6.5.5. Dark current-voltage characteristics

The dark current-voltage characteristics are described by $J_d=J_0\{\exp[e(V-JR_s)/nk_BT]-1\}$, where J_d is the dark current density, J_0 is the dark saturate current density, V is the applied voltage, n is the ideality factor, k_B is the Boltzmann constant, T is the temperature and e is the electron charge. The fitting method is described in ref. 33.

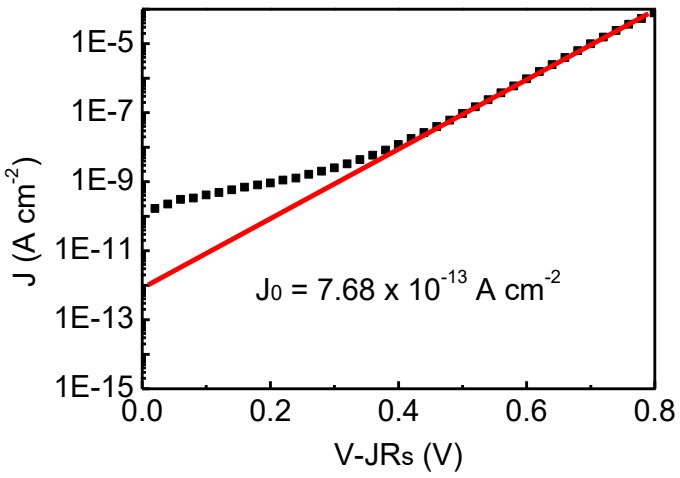

Figure 6.9. The device structure is ITO/ZnO/PBDTT-TT:**cP4**/MoO_3/Al. The original *J-V* curve is shown in Fig. 2d. Plot of d*V*/d*J* vs J^{-1} and linear fitting. (b) ln(*J*) vs (V-JR_s) and linear fitting. The J_0 is calculated to be 7.68×10^{-13} Acm^{-2}.

6.5.6. Dark current as a function of temperature

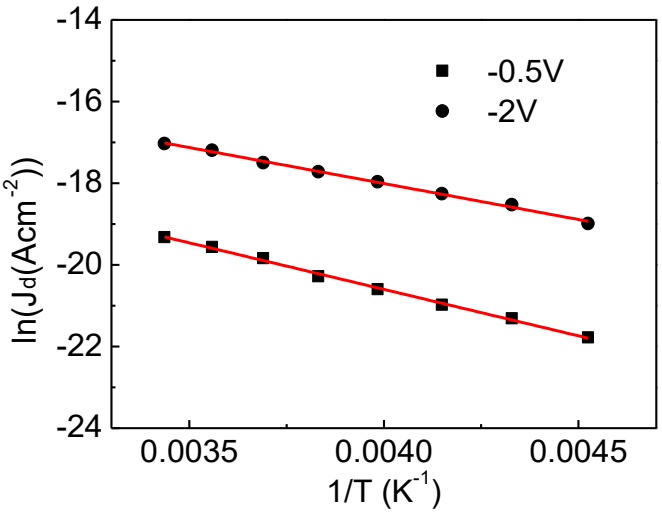

Figure 6.10. The dependence of the dark current density of the **cP4**-based OPD on temperature measured at −0.5 V and −2.0 V.

6.5.7. Device performance

The responsivity *R* was calculated from the following equation: $R=\lambda q/hc \times EQE$, where *EQE* is external quantum efficiency, λ the wavelength, *q* the electron charge, *h* the Planck constant, *c* the speed of light. When the noise current is dominated by the shot noise from the dark current, the specific detectivity (D^*) is given by $D^*=R/(2qJ_d)^{1/2}$, where *R* is the responsivity, *q* the electron charge and J_d the dark current density.

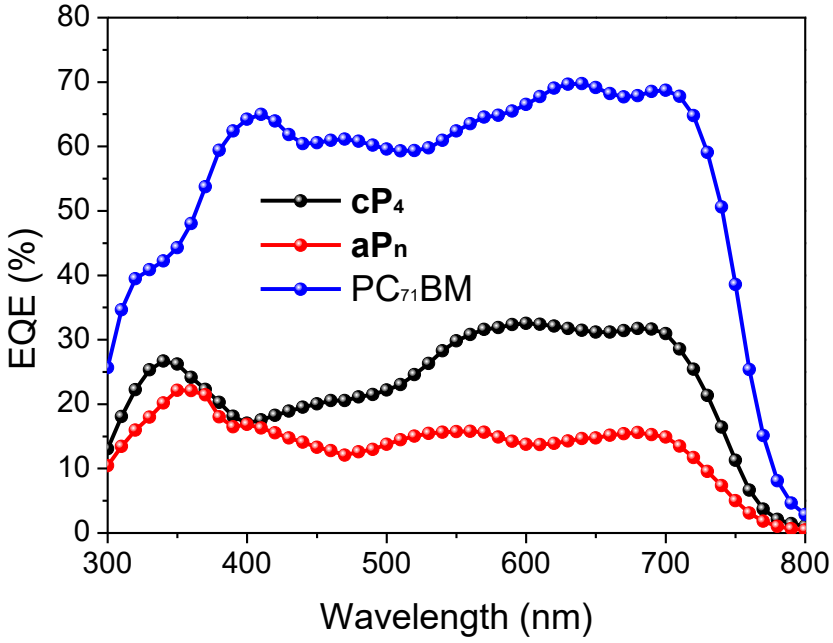

Figure 6.11. External quantum efficiency at different wavelength with inverted OPD structure at −0.1V.

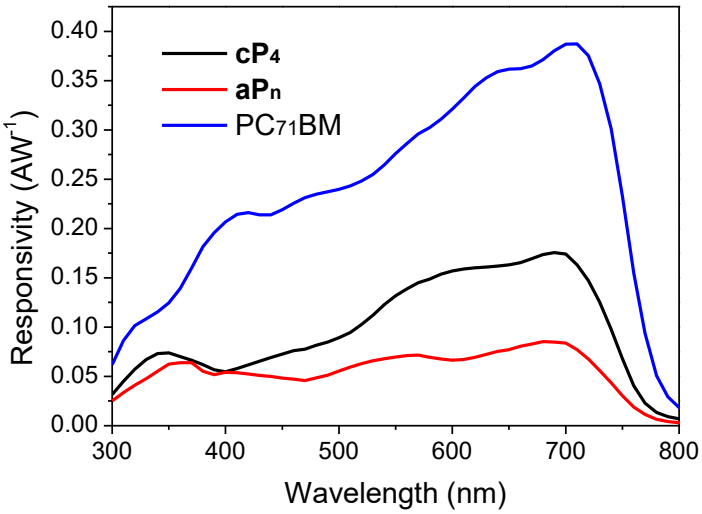

Figure 6.12. Calculated responsivity (R in AW^{-1}) spectra for different OPDs.

6.6. References and Notes

(1) Baeg, K.-J.; Binda, M.; Natali, D.; Caironi, M.; Noh, Y.-Y. *Adv. Mater.* **2013**, *25*, 4267.

(2) Sekitani, T.; Noguchi, Y.; Hata, K.; Fukushima, T.; Aida, T.; Someya, T. *Science* **2008**, *321*, 1468.

(3) Rogers, J. A.; Someya, T.; Huang, Y. G. *Science* **2010**, *327*, 1603.

(4) Ball, M.; Zhong, Y.; Wu, Y.; Schenck, C.; Ng, F.; Steigerwald, M.; Xiao, S.; Nuckolls, C. *Acc. Chem. Res.* **2015**, *48*, 267.

(5) Gong, X.; Tong, M.; Xia, Y.; Cai, W.; Moon, J. S.; Cao, Y.; Yu, G.; Shieh, C.-L.; Nilsson, B.; Heeger, A. J. *Science* **2009**, *325*, 1665.

(6) Zhang, L.; Yang, T.; Shen, L.; Fang, Y.; Dang, L.; Zhou, N.; Guo, X.; Hong, Z.; Yang, Y.; Wu, H.; Huang, J.; Liang, Y. *Adv. Mater.* **2015**, *27*, 6496.

(7) Kim, I. K.; Li, X.; Ullah, M.; Shaw, P. E.; Wawrzinek, R.; Namdas, E. B.; Lo, S. C. *Adv. Mater.* **2015**, *27*, 6390.

(8) Segura, J. L.; Martin, N. *Chem. Soc. Rev.* **2000**, *29*, 13.

(9) Tsetseris, L.; Pantelides, S. T. *Phys. Rev. B* **2011**, *84*, 195202.

(10) Sheka, E. F. *Chem. Phys. Lett.* **2007**, *438*, 119.

(11) Gregg, B. A. *Soft Matter* **2009**, *5*, 2985.

(12) Darling, S. B. *J. Phys. Chem. B* **2008**, *112*, 8891.

(13) Kaake, L. G.; Barbara, P. F.; Zhu, X. Y. *J. Phys. Chem. Lett.* **2010**, *1*, 628.

(14) Gregg, B. A.; Chen, S.-G.; Cormier, R. A. *Chem. Mater.* **2004**, *16*, 4586.

(15) Ball, M.; Zhong, Y.; Fowler, B.; Zhang, B.; Li, P.; Etkin, G.; Paley, D. W.; Decatur, J.; Dalsania, A. K.; Li, H.; Xiao, S.; Ng, F.; Steigerwald, M. L.; Nuckolls, C. *J. Am. Chem. Soc.* **2016**, *138*, DOI: 10.1021/jacs.6b05474.

(16) Liang, Y.; Xu, Z.; Xia, J.; Tsai, S.-T.; Wu, Y.; Li, G.; Ray, C.; Yu, L. *Adv. Mater.* **2010**, *22*, E135.

(17) Li, C.-Z.; Chang, C.-Y.; Zang, Y.; Ju, H.-X.; Chueh, C.-C.; Liang, P.-W.; Cho, N.; Ginger, D. S.; Jen, A. K. Y. *Adv. Mater.* **2014**, *26*, 6262.

(18) Liao, S.-H.; Jhuo, H.-J.; Cheng, Y.-S.; Chen, S.-A. *Adv. Mater.* **2013**, *25*, 4766.

(19) Armin, A.; Hambsch, M.; Kim, I. K.; Burn, P. L.; Meredith, P.; Namdas, E. B. *Laser & Photonics Rev.* **2014**, *8*, 924.

(20) Binda, M.; Iacchetti, A.; Natali, D.; Beverina, L.; Sassi, M.; Sampietro, M.

Appl. Phys. Lett. **2011**, *98*, 073303.

(21) Fang, Y.; Guo, F.; Xiao, Z.; Huang, J. *Adv. Opt. Mater.* **2014**, *2*, 348.

(22) Kim, I. K.; Pal, B. N.; Ullah, M.; Burn, P. L.; Lo, S.-C.; Meredith, P.; Namdas, E. B. *Adv. Opt. Mater.* **2015**, *3*, 50.

(23) Lee, K.-H.; Leem, D.-S.; Castrucci, J. S.; Park, K.-B.; Bulliard, X.; Kim, K.-S.; Jin, Y. W.; Lee, S.; Bender, T. P.; Park, S. Y. *ACS Appl. Mater. Interfaces* **2013**, *5*, 13089.

(24) Leem, D.-S.; Lee, K.-H.; Park, K.-B.; Lim, S.-J.; Kim, K.-S.; Wan Jin, Y.; Lee, S. *Appl. Phys. Lett.* **2013**, *103*, 043305.

(25) Lim, S.-J.; Leem, D.-S.; Park, K.-B.; Kim, K.-S.; Sul, S.; Na, K.; Lee, G. H.; Heo, C.-J.; Lee, K.-H.; Bulliard, X.; Satoh, R.-I.; Yagi, T.; Ro, T.; Im, D.; Jung, J.; Lee, M.; Lee, T.-Y.; Han, M. G.; Jin, Y. W.; Lee, S. *Sci. Rep.* **2015**, *5*, 7708.

(26) Pierre, A.; Deckman, I.; Lechêne, P. B.; Arias, A. C. *Adv. Mater.* **2015**, *27*, 6411.

(27) Qi, J.; Zhou, X.; Yang, D.; Qiao, W.; Ma, D.; Wang, Z. Y. *Adv. Funct. Mater.* **2014**, *24*, 7605.

(28) Ramuz, M.; Bürgi, L.; Winnewisser, C.; Seitz, P. *Org. Electron.* **2008**, *9*, 369.

(29) Saracco, E.; Bouthinon, B.; Verilhac, J.-M.; Celle, C.; Chevalier, N.; Mariolle, D.; Dhez, O.; Simonato, J.-P. *Adv. Mater.* **2013**, *25*, 6534.

(30) Wang, J. B.; Li, W. L.; Chu, B.; Lee, C. S.; Su, Z. S.; Zhang, G.; Wu, S. H.; Yan, F. *Org. Electron.* **2011**, *12*, 34.

(31) Wang, X.; Lv, L.; Li, L.; Chen, Y.; Zhang, K.; Chen, H.; Dong, H.; Huang, J.; Shen, G.; Yang, Z.; Huang, H. *Adv. Funct. Mater.* **2016**, *26*, 6306.

(32) Zhang, L.; Yang, T.; Shen, L.; Fang, Y.; Dang, L.; Zhou, N.; Guo, X.; Hong, Z.; Yang, Y.; Wu, H.; Huang, J.; Liang, Y. *Adv. Mater.* **2015**, *27*, 6496.

(33) Dou, L.; Yang, Y.; You, J.; Hong, Z.; Chang, W.-H.; Li, G.; Yang, Y. *Nat. Commun.* **2014**, *5*, 5404.

(34) We do not discuss photomultiplication photodetectors here as they have different working mechanism and require high work voltages. Examples of photomultiplication photodetectors can be found in: Wang, W.; Zhang, F.; Bai, H.; Li, L.; Gao, M.; Zhang, M.; Zhan, X. *Nanoscale* **2016**, *8*, 5578.

(35) Zhu, X.; Monahan, N. R.; Gong, Z.; Zhu, H.; Williams, K. W.; Nelson, C.

A. *J. Am. Chem. Soc.* **2015**, *137*, 8313.

(36) Banerji, N. *J. Mater. Chem. C* **2013**, *1*, 3052.

(37) Savoie, B. M.; Jackson, N. E.; Chen, L. X.; Marks, T. J.; Ratner, M. A. *Acc. Chem. Res.* **2014**, *47*, 3385.

(38) Savoie, B. M.; Rao, A.; Bakulin, A. A.; Gelinas, S.; Movaghar, B.; Friend, R. H.; Marks, T. J.; Ratner, M. A. *J. Am. Chem. Soc.* **2014**, *136*, 2876.

(39) Zhong, Y.; Trinh, M. T.; Chen, R.; Wang, W.; Khlyabich, P. P.; Kumar, B.; Xu, Q.; Nam, C. Y.; Sfeir, M. Y.; Black, C.; Steigerwald, M. L.; Loo, Y. L.; Xiao, S.; Ng, F.; Zhu, X. Y.; Nuckolls, C. *J. Am. Chem. Soc.* **2014**, *136*, 15215.

(40) Zhong, Y.; Trinh, M. T.; Chen, R.; Purdum, G. E.; Khlyabich, P. P.; Sezen, M.; Oh, S.; Zhu, H.; Fowler, B.; Zhang, B.; Wang, W.; Nam, C. Y.; Sfeir, M. Y.; Black, C. T.; Steigerwald, M. L.; Loo, Y. L.; Ng, F.; Zhu, X. Y.; Nuckolls, C. *Nat. Commun.* **2015**, *6*, 8242.

(41) Kaake, L. G.; Moses, D.; Heeger, A. J. *J. Phys. Chem. Lett.* **2013**, *4*, 2264.

(42) Hwang, I. W.; Soci, C.; Moses, D.; Zhu, Z.; Waller, D.; Gaudiana, R.; Brabec, C. J.; Heeger, A. J. *Adv. Mater.* **2007**, *19*, 2307.

(43) Hwang, I.; Beaupre, S.; Leclerc, M.; Scholes, G. D. *Chem. Sci.* **2012**, *3*, 2270.

(44) Grancini, G.; Maiuri, M.; Fazzi, D.; Petrozza, A.; Egelhaaf, H. J.; Brida, D.; Cerullo, G.; Lanzani, G. *Nat. Mater.* **2013**, *12*, 29.

(45) Gélinas, S.; Rao, A.; Kumar, A.; Smith, S. L.; Chin, A. W.; Clark, J.; van der Poll, T. S.; Bazan, G. C.; Friend, R. H. *Science* **2014**, *343*, 512.

(46) Gregg, B. A. *J. Phys. Chem. C* **2009**, *113*, 5899.

(47) Wang, G.-W.; Komatsu, K.; Murata, Y.; Shiro, M. *Nature* **1997**, *387*, 583.

(48) Komatsu, K.; Wang, G.-W.; Murata, Y.; Tanaka, T.; Fujiwara, K.; Yamamoto, K.; Saunders, M. *J. Org. Chem.* **1998**, *63*, 9358.

(49) Huang, C.; Barlow, S.; Marder, S. R. *J. Org. Chem.* **2011**, *76*, 2386.

(50) Wurthner, F. *Chem. Commun.* **2004**, 1564.

(51) Kozma, E.; Catellani, M. *Dyes Pigm.* **2013**, *98*, 160.

(52) Würthner, F.; Saha-Möller, C. R.; Fimmel, B.; Ogi, S.; Leowanawat, P.; Schmidt, D. *Chem. Rev.* **2016**, *116*,962.

(53) Zhong, Y.; Kumar, B.; Oh, S.; Trinh, M. T.; Wu, Y.; Elbert, K.; Li, P.; Zhu, X.; Xiao, S.; Ng, F.; Steigerwald, M. L.; Nuckolls, C. *J. Am. Chem. Soc.* **2014**, *136*, 8122.

(54) Mandoc, M. M.; de Boer, B.; Paasch, G.; Blom, P. W. M. *Phys. Rev. B* **2007**, *75*, 193202.

(55) Nicolai, H. T.; Kuik, M.; Wetzelaer, G. A. H.; de Boer, B.; Campbell, C.; Risko, C.; Brédas, J. L.; Blom, P. W. M. *Nat. Mater.* **2012**, *11*, 882.

(56) Ball, M.; Fowler, B.; Li, P.; Joyce, L. A.; Li, F.; Liu, T.; Paley, D.; Zhong, Y.; Li, H.; Xiao, S.; Ng, F.; Steigerwald, M. L.; Nuckolls, C. *J. Am. Chem. Soc.* **2015**, *137*, 9982.

(57) Jo, J.; Pouliot, J. R.; Wynands, D.; Collins, S. D.; Kim, J. Y.; Nguyen, T. L.; Woo, H. Y.; Sun, Y.; Leclerc, M.; Heeger, A. J. *Adv. Mater.* **2013**, *25*, 4783.

Appendix A. ^{1}H and ^{13}C NMR spectra

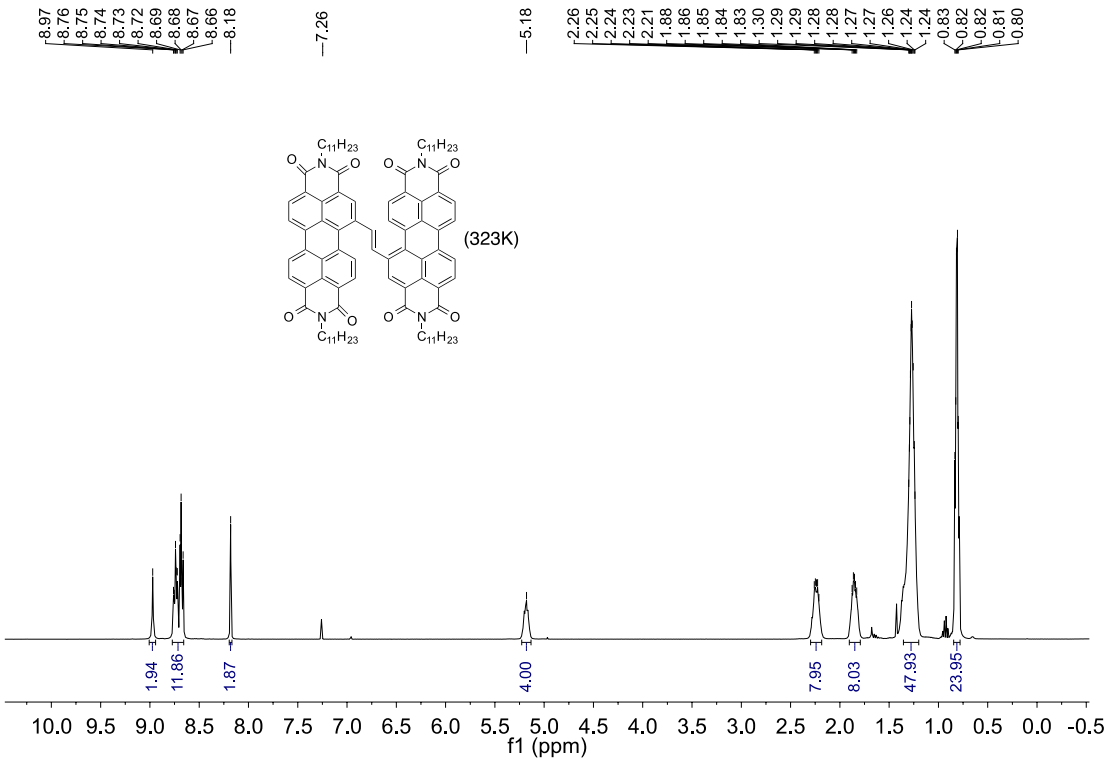

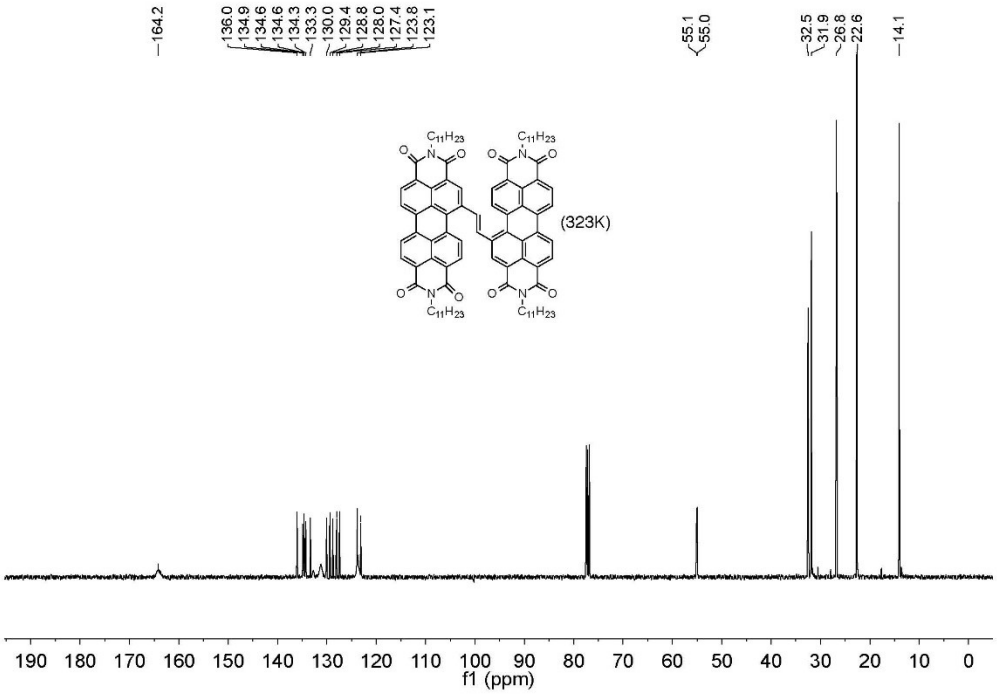
164.2
136.0
134.9
134.6
134.6
134.3
133.3
130.0
129.4
128.8
128.0
127.4
123.8
123.1
55.1
55.0
32.5
31.9
26.8
22.6
14.1
(323K)
f1 (ppm)

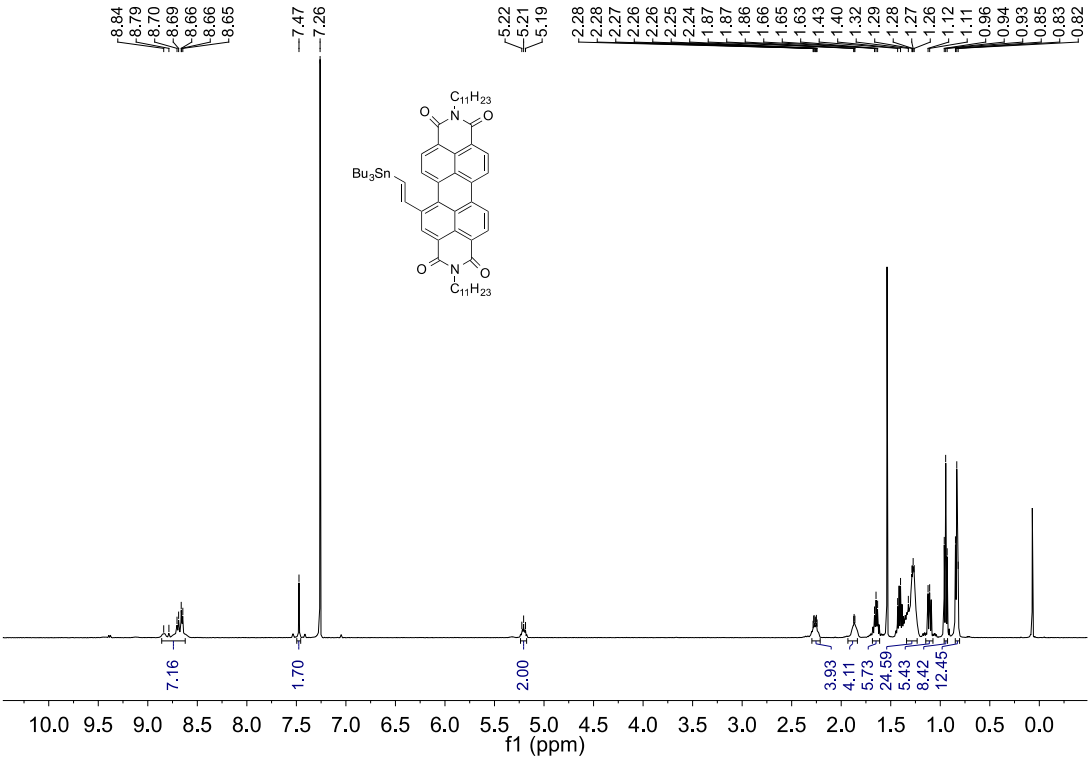
8.84
8.79
8.70
8.69
8.66
8.66
8.65
7.47
7.26
5.22
5.21
5.19
2.28
2.28
2.27
2.26
2.26
2.25
2.24
1.87
1.87
1.86
1.66
1.65
1.63
1.43
1.40
1.32
1.29
1.28
1.27
1.26
1.12
1.11
0.96
0.94
0.93
0.85
0.83
0.82
Bu3Sn
7.16
1.70
2.00
3.93
4.11
5.73
24.59
5.43
8.42
12.45
f1 (ppm)

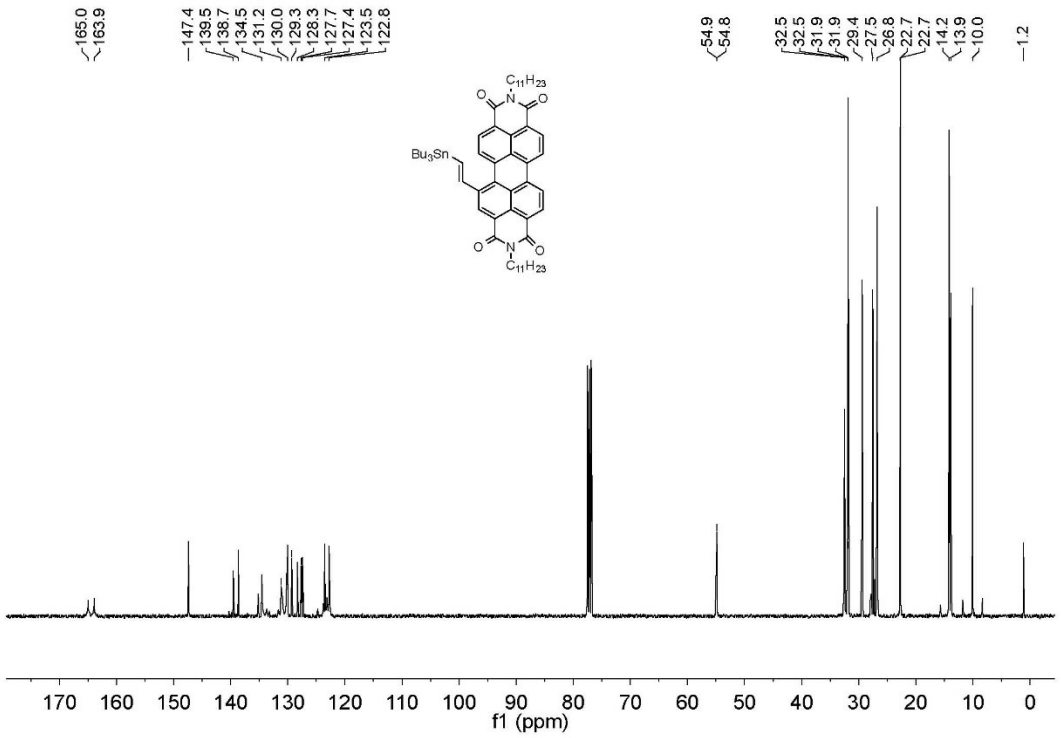
165.0
163.9
147.4
139.5
138.7
134.5
131.2
130.0
129.3
128.3
127.7
127.4
123.5
122.8
54.9
54.8
32.5
32.5
31.9
31.9
29.4
27.5
26.8
22.7
22.7
14.2
13.9
10.0
1.2
$C_{11}H_{23}$
Bu_3Sn
170 160 150 140 130 120 110 100 90 80 70 60 50 40 30 20 10 0
f1 (ppm)

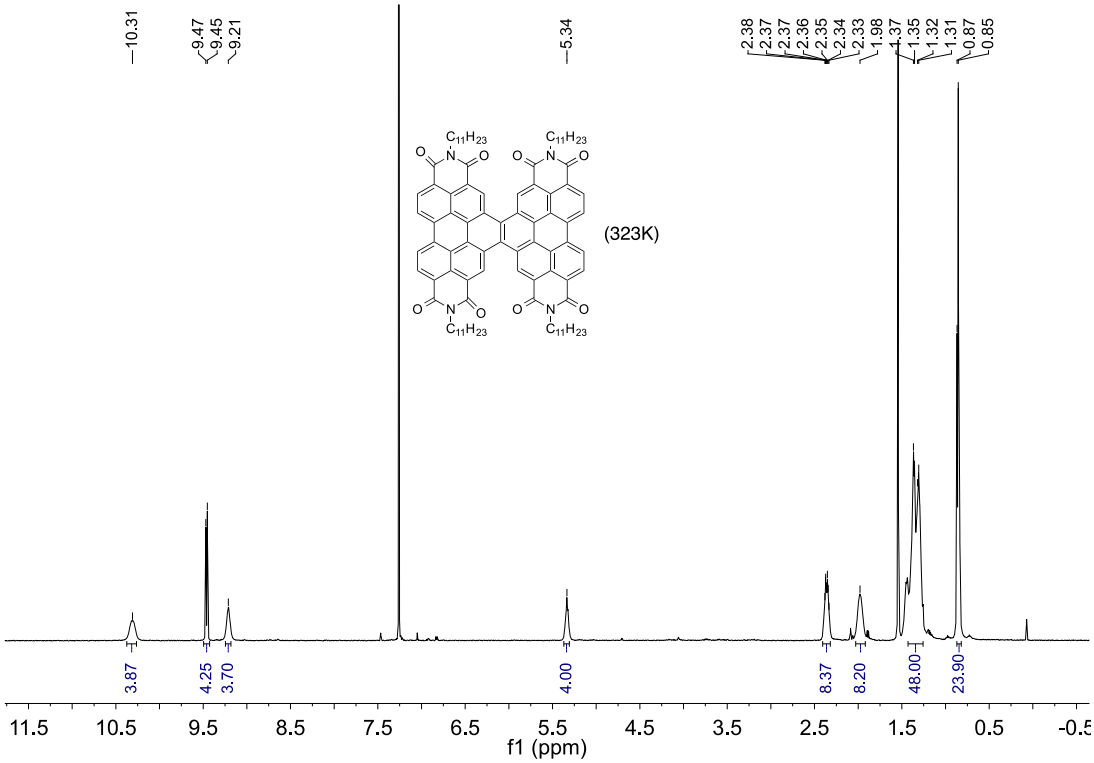
10.31
9.47
9.45
9.21
5.34
2.38
2.37
2.37
2.36
2.35
2.34
2.33
1.98
1.37
1.35
1.32
1.31
0.87
0.85
$C_{11}H_{23}$
(323K)
3.87
4.25
3.70
4.00
8.37
8.20
48.00
23.90
11.5 10.5 9.5 8.5 7.5 6.5 5.5 4.5 3.5 2.5 1.5 0.5 -0.5
f1 (ppm)

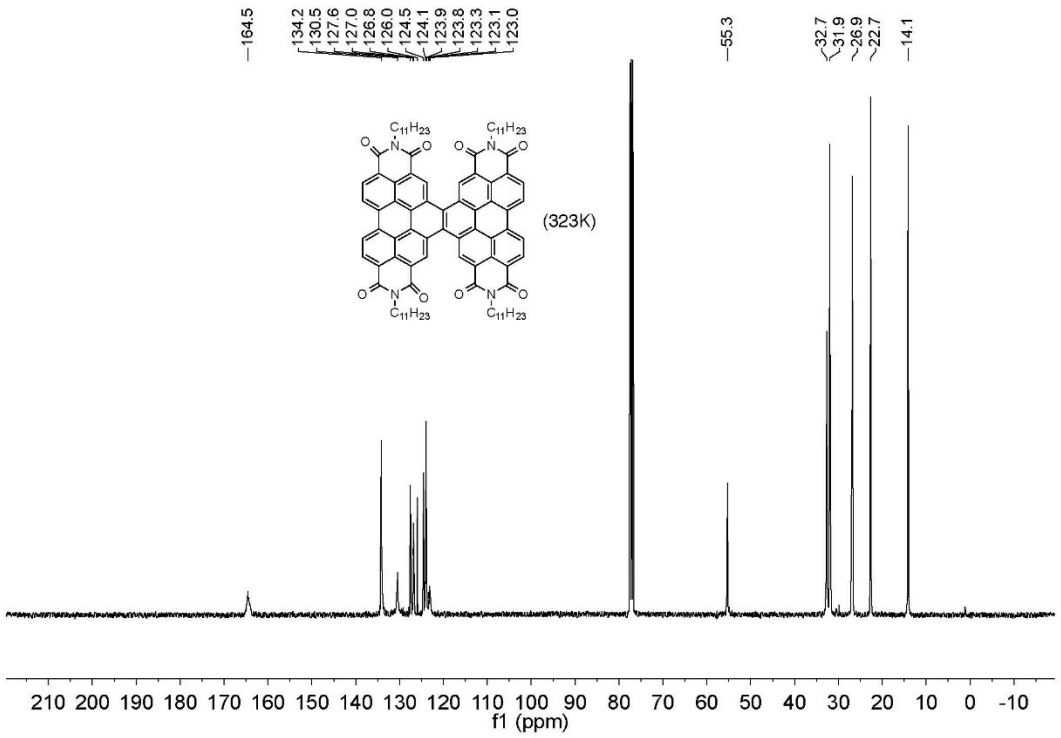
164.5
134.2
130.5
127.6
127.0
126.8
126.0
124.5
124.1
123.9
123.8
123.3
123.1
123.0
55.3
32.7
31.9
26.9
22.7
14.1
(323K)
210 200 190 180 170 160 150 140 130 120 110 100 90 80 70 60 50 40 30 20 10 0 -10
f1 (ppm)

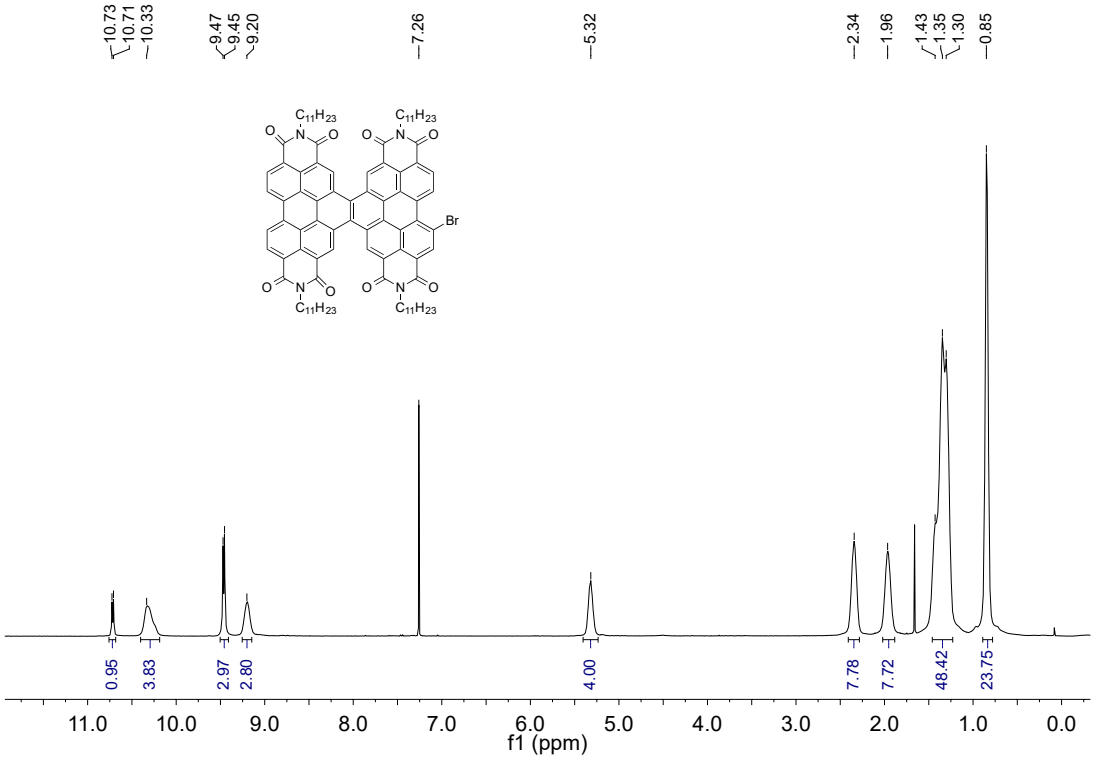
10.73
10.71
10.33
9.47
9.45
9.20
7.26
5.32
2.34
1.96
1.43
1.35
1.30
0.85
Br
0.95
3.83
2.97
2.80
4.00
7.78
7.72
48.42
23.75
11.0 10.0 9.0 8.0 7.0 6.0 5.0 4.0 3.0 2.0 1.0 0.0
f1 (ppm)

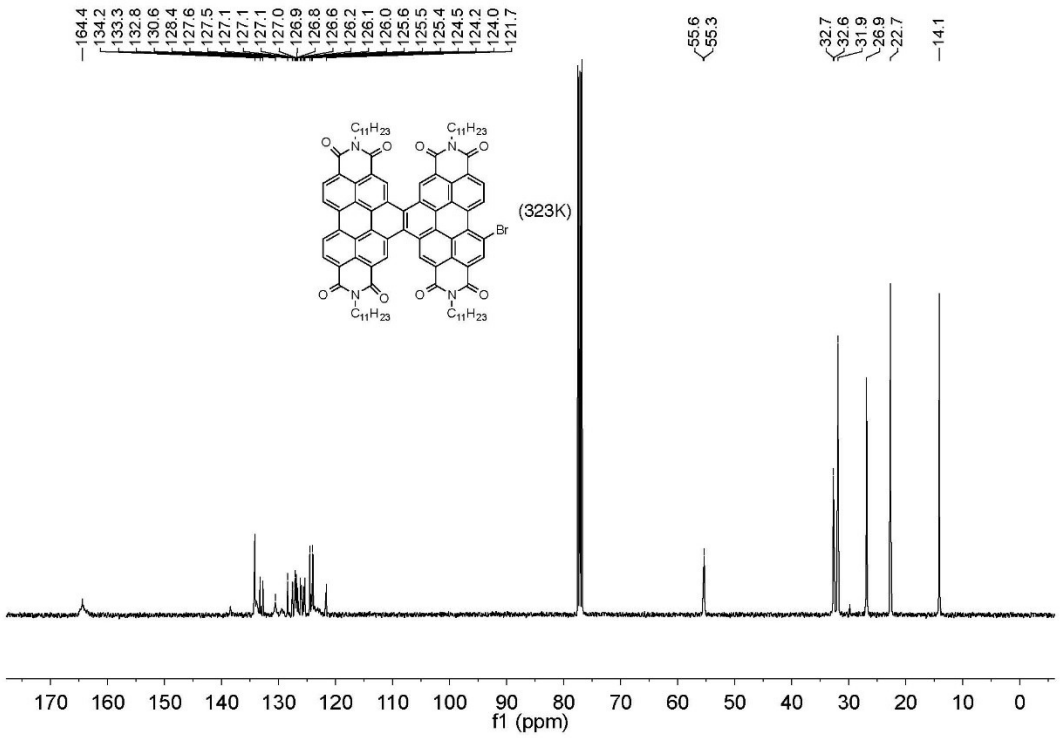
164.4
134.2
133.3
132.8
130.6
128.4
127.6
127.5
127.1
127.1
127.1
127.0
126.9
126.8
126.6
126.2
126.1
126.0
125.6
125.5
125.4
124.5
124.2
124.0
121.7
55.6
55.3
32.7
32.6
31.9
26.9
22.7
14.1
(323K)
Br
170 160 150 140 130 120 110 100 90 80 70 60 50 40 30 20 10 0
f1 (ppm)

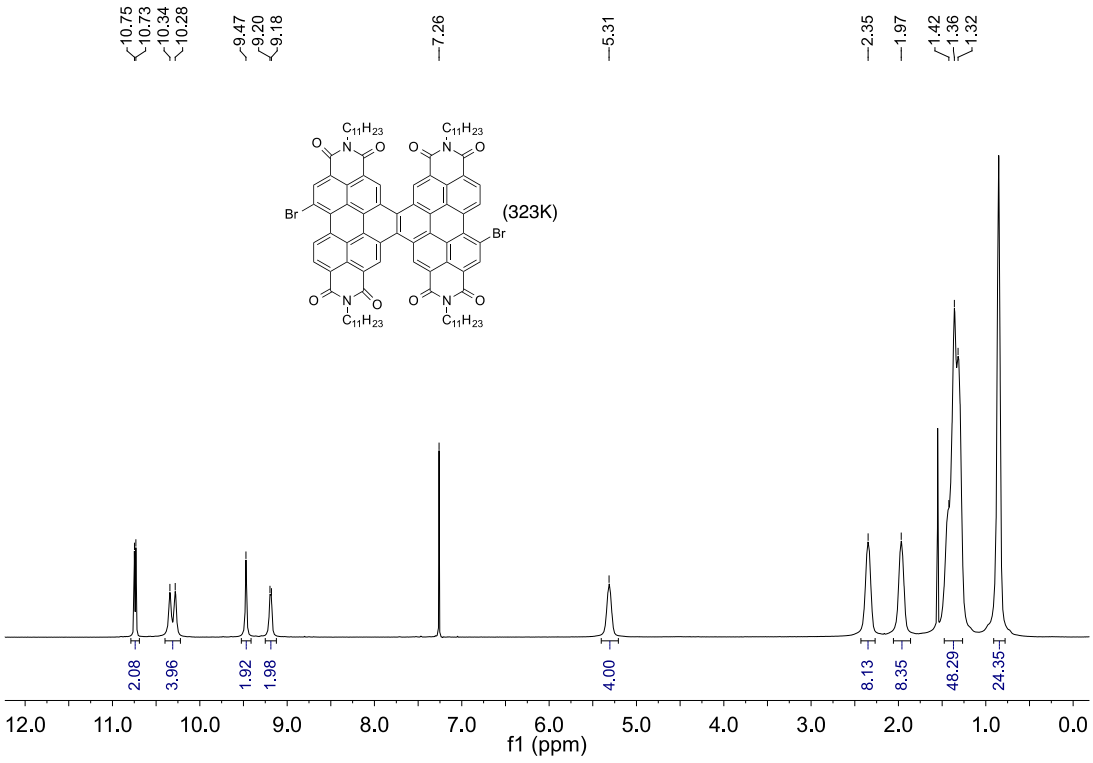
10.75
10.73
10.34
10.28
9.47
9.20
9.18
7.26
5.31
2.35
1.97
1.42
1.36
1.32
(323K)
Br
Br
2.08
3.96
1.92
1.98
4.00
8.13
8.35
48.29
24.35
12.0 11.0 10.0 9.0 8.0 7.0 6.0 5.0 4.0 3.0 2.0 1.0 0.0
f1 (ppm)

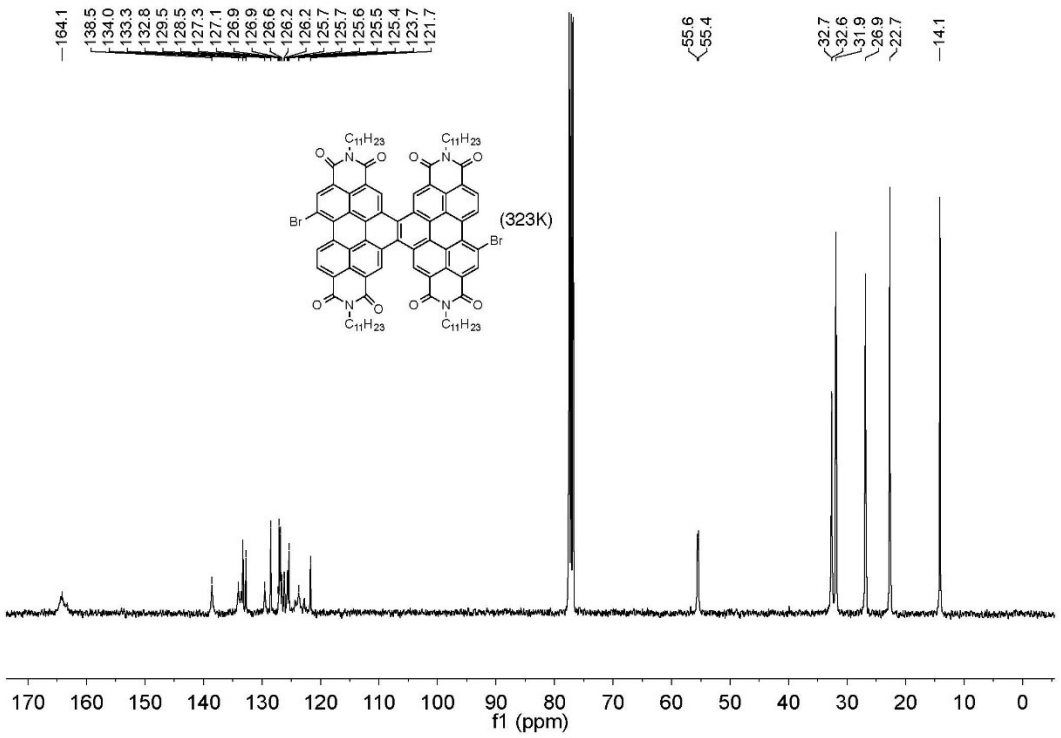
164.1
138.5
134.0
133.3
132.8
129.5
128.5
127.3
127.1
126.9
126.9
126.6
126.2
126.2
125.7
125.7
125.6
125.5
125.4
123.7
121.7
55.6
55.4
32.7
32.6
31.9
26.9
22.7
14.1
(323K)
f1 (ppm)

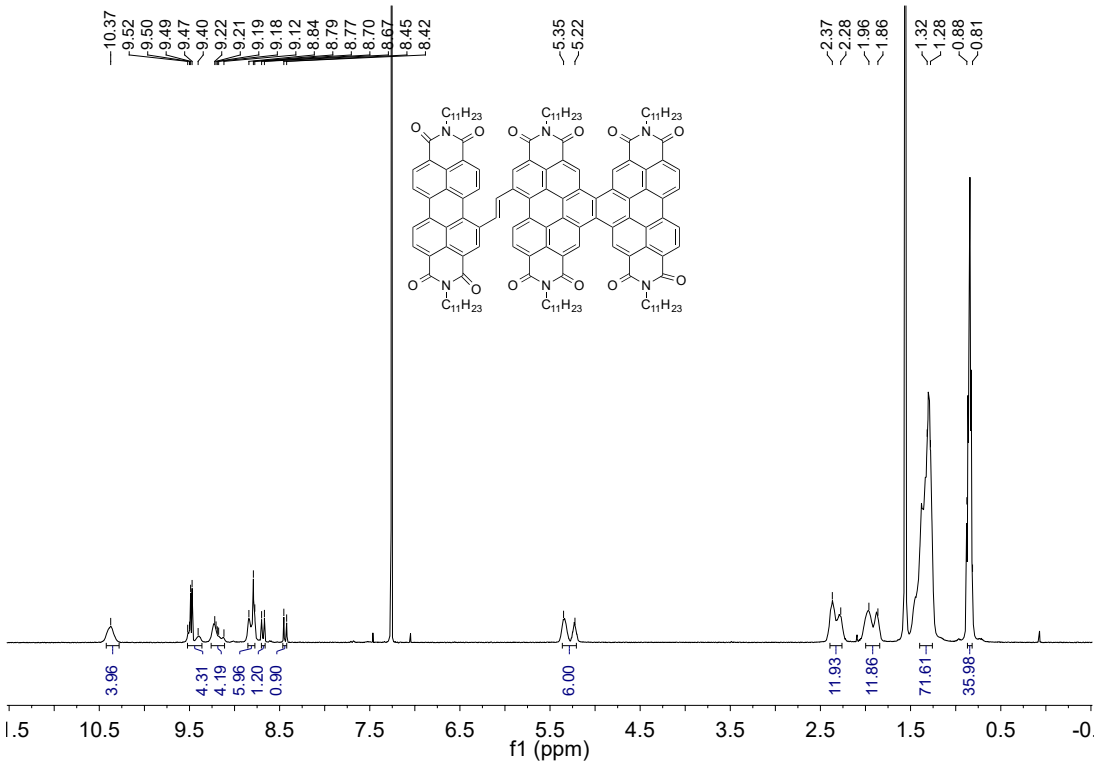
10.37
9.52
9.50
9.49
9.47
9.40
9.22
9.21
9.19
9.18
9.12
8.84
8.79
8.77
8.70
8.67
8.45
8.42
5.35
5.22
2.37
2.28
1.96
1.86
1.32
1.28
0.88
0.81
3.96
4.31
4.19
5.96
1.20
0.90
6.00
11.93
11.86
71.61
35.98
f1 (ppm)

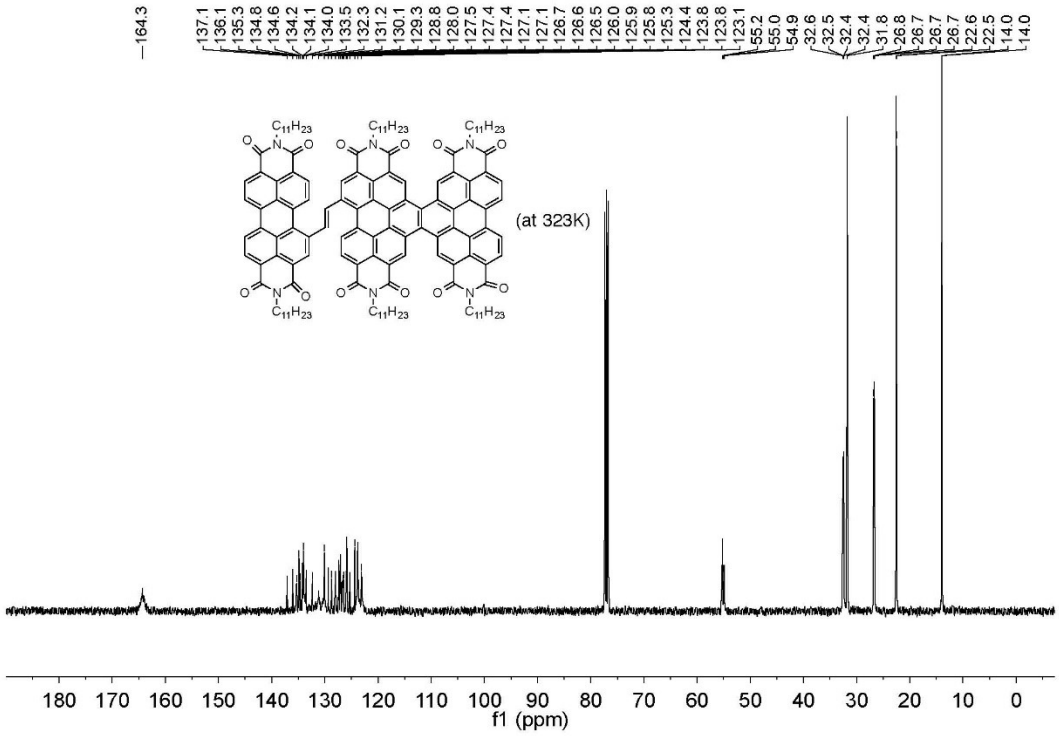
164.3
137.1
136.1
135.3
134.8
134.6
134.2
134.1
134.0
133.5
132.3
131.2
130.1
129.3
128.8
128.0
127.5
127.4
127.4
127.1
127.1
126.7
126.6
126.5
126.0
125.9
125.8
125.3
124.4
123.8
123.8
123.1
55.2
55.0
54.9
32.6
32.5
32.4
32.4
31.8
26.8
26.7
26.7
26.7
22.6
22.5
14.0
14.0
(at 323K)
180 170 160 150 140 130 120 110 100 90 80 70 60 50 40 30 20 10 0
f1 (ppm)

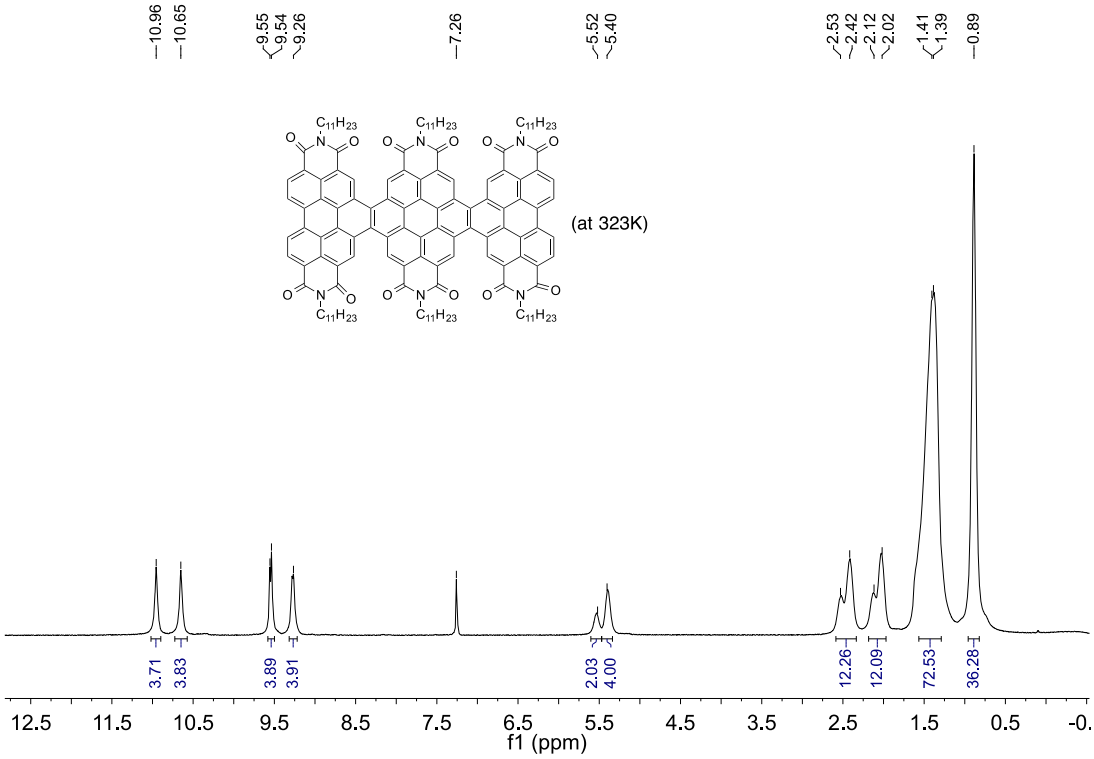
10.96
10.65
9.55
9.54
9.26
7.26
5.52
5.40
2.53
2.42
2.12
2.02
1.41
1.39
0.89
(at 323K)
3.71
3.83
3.89
3.91
2.03
4.00
12.26
12.09
72.53
36.28
12.5 11.5 10.5 9.5 8.5 7.5 6.5 5.5 4.5 3.5 2.5 1.5 0.5 -0.
f1 (ppm)

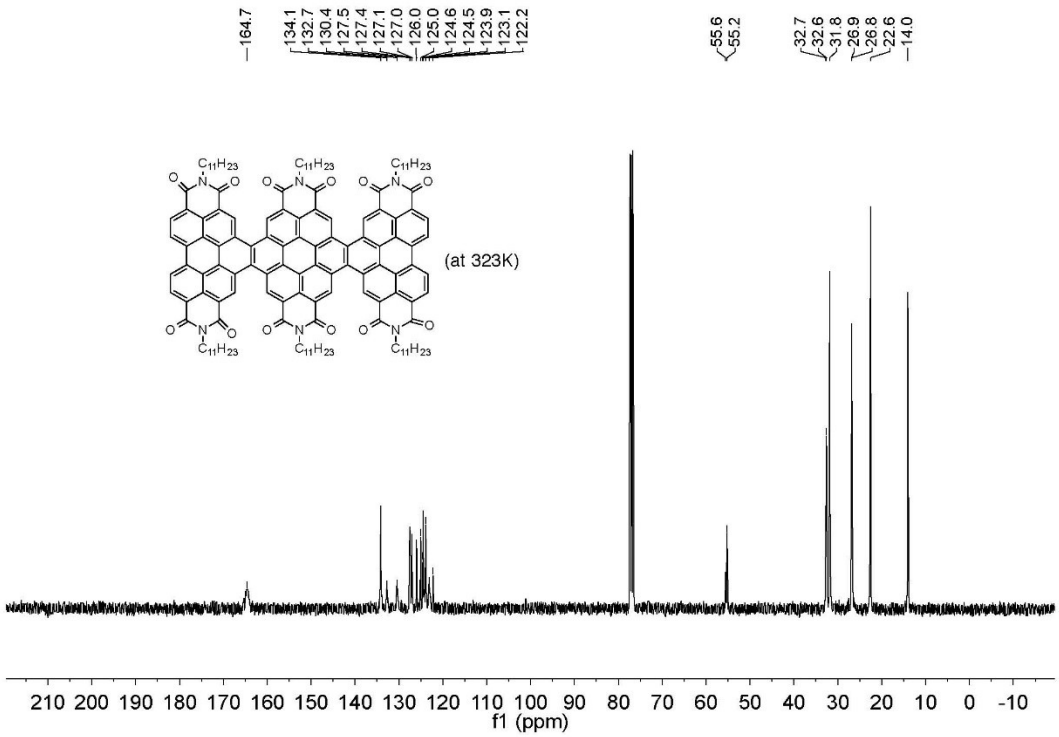
164.7
134.1
132.7
130.4
127.5
127.4
127.1
127.0
126.0
125.0
124.6
124.5
123.9
123.1
122.2
55.6
55.2
32.7
32.6
31.8
26.9
26.8
22.6
14.0
(at 323K)
210 200 190 180 170 160 150 140 130 120 110 100 90 80 70 60 50 40 30 20 10 0 -10
f1 (ppm)

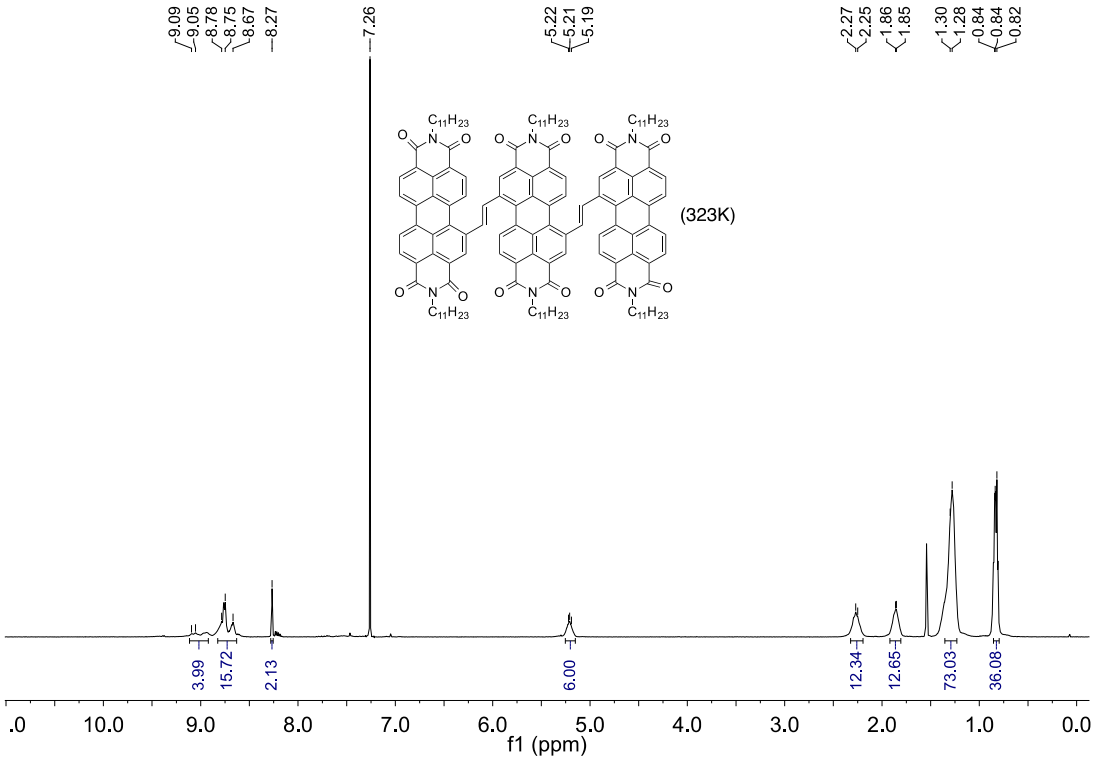
9.09
9.05
8.78
8.75
8.67
8.27
7.26
5.22
5.21
5.19
2.27
2.25
1.86
1.85
1.30
1.28
0.84
0.84
0.82
(323K)
3.99
15.72
2.13
6.00
12.34
12.65
73.03
36.08
.0 10.0 9.0 8.0 7.0 6.0 5.0 4.0 3.0 2.0 1.0 0.0
f1 (ppm)

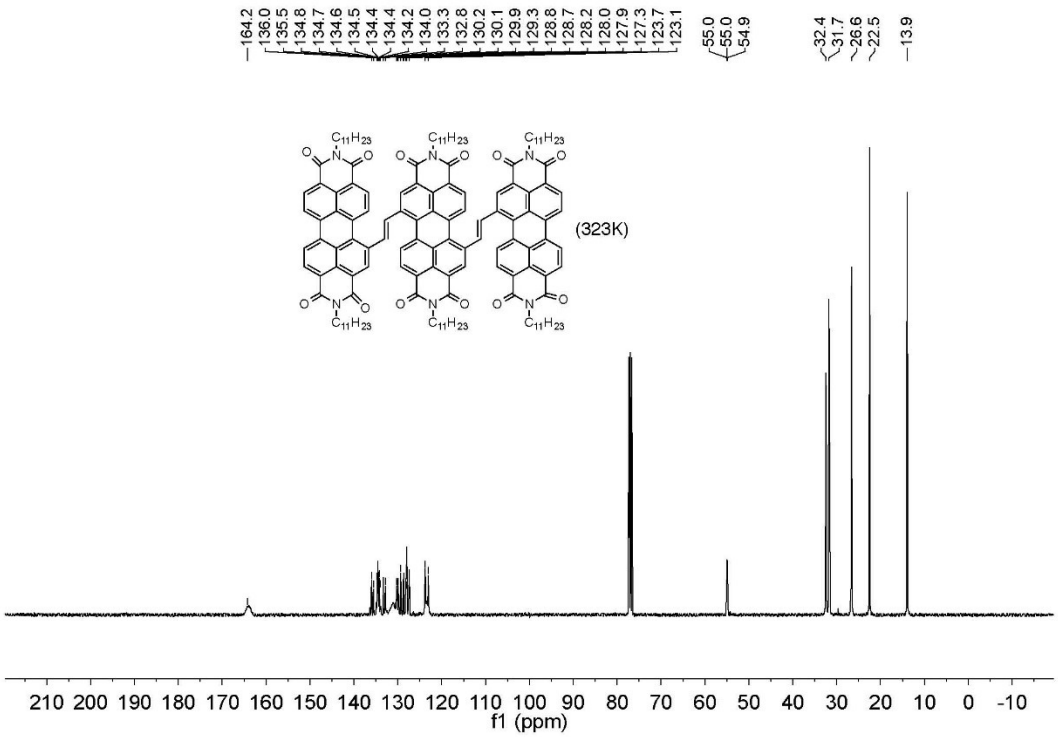
164.2
136.0
135.5
134.8
134.7
134.6
134.5
134.4
134.4
134.2
134.0
133.3
132.8
130.2
130.1
129.9
129.3
128.8
128.7
128.2
128.0
127.9
127.3
123.7
123.1
55.0
55.0
54.9
32.4
31.7
26.6
22.5
13.9
(323K)
210 200 190 180 170 160 150 140 130 120 110 100 90 80 70 60 50 40 30 20 10 0 -10
f1 (ppm)

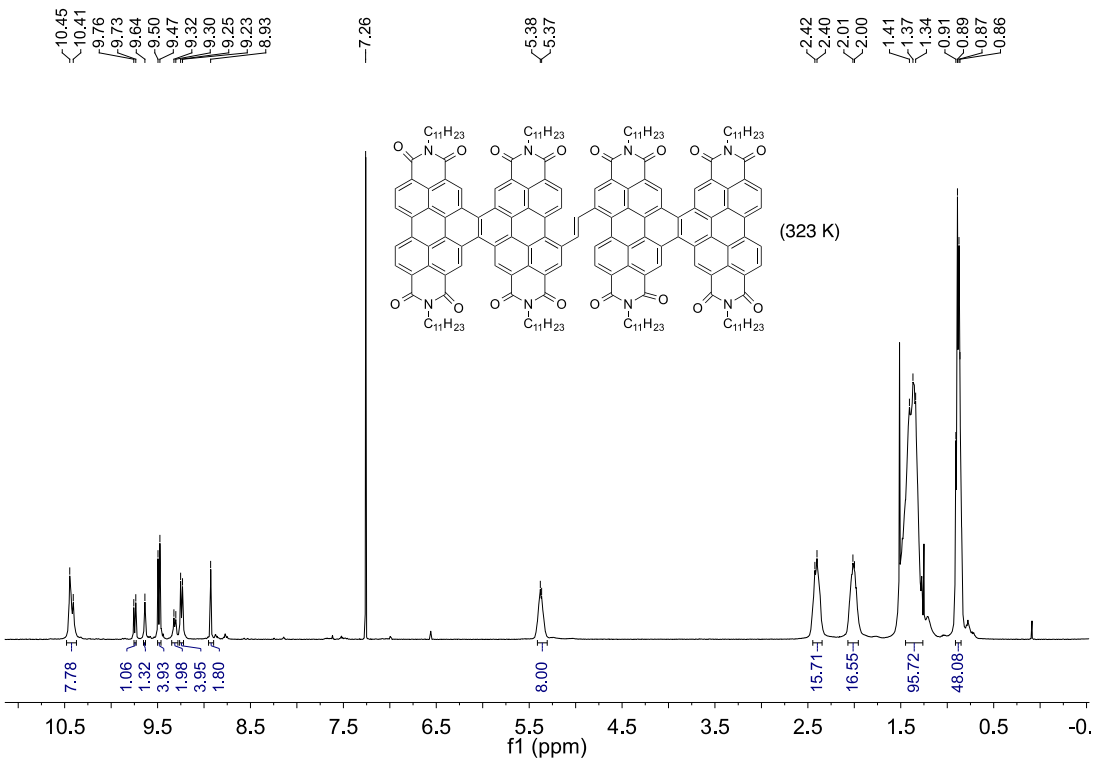
10.45
10.41
9.76
9.73
9.64
9.50
9.47
9.32
9.30
9.25
9.23
8.93
7.26
5.38
5.37
2.42
2.40
2.01
2.00
1.41
1.37
1.34
0.91
0.89
0.87
0.86
(323 K)
7.78
1.06
1.32
3.93
1.98
3.95
1.80
8.00
15.71
16.55
95.72
48.08
10.5 9.5 8.5 7.5 6.5 5.5 4.5 3.5 2.5 1.5 0.5 -0.
f1 (ppm)

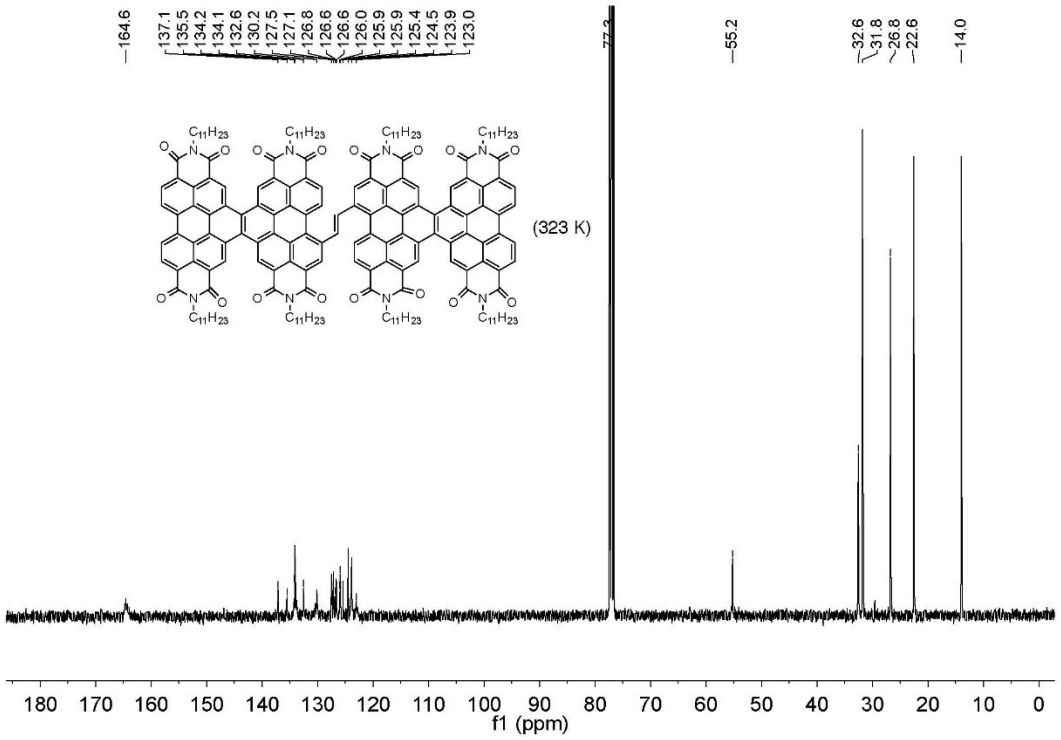
164.6
137.1
135.5
134.2
134.1
132.6
130.2
127.5
127.1
126.8
126.6
126.6
126.0
125.9
125.9
125.4
124.5
123.9
123.0
77.2
55.2
32.6
31.8
26.8
22.6
14.0
(323 K)
180 170 160 150 140 130 120 110 100 90 80 70 60 50 40 30 20 10 0
f1 (ppm)

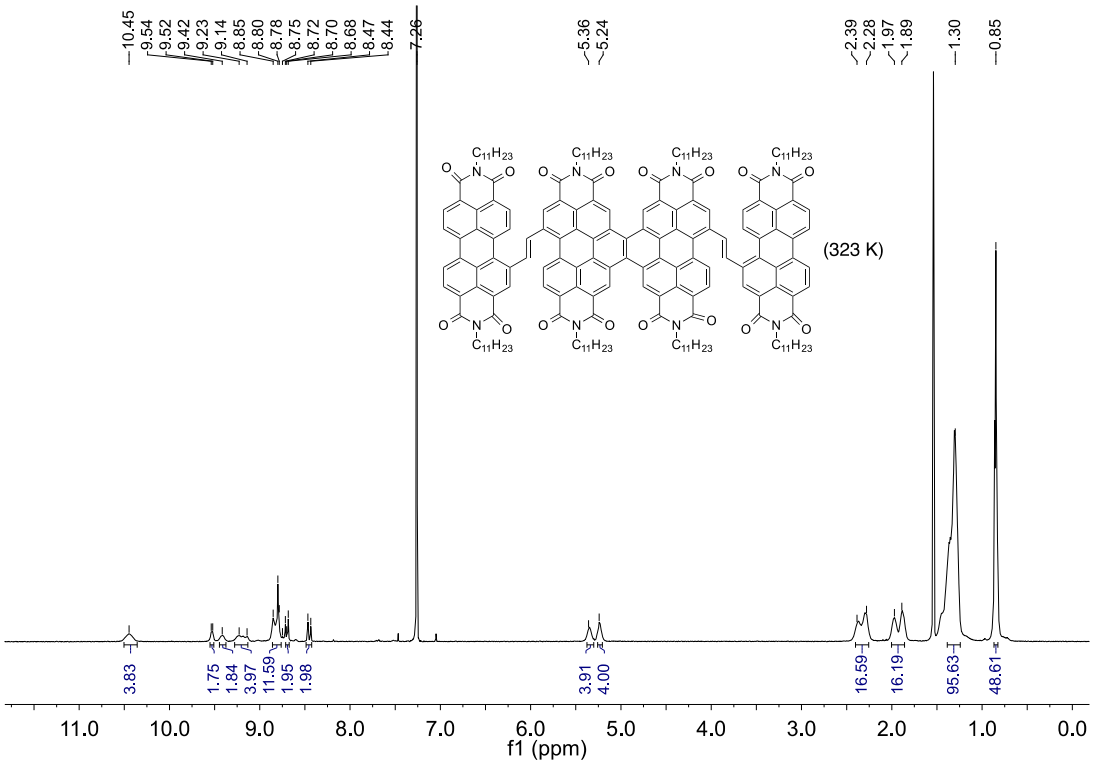
10.45
9.54
9.52
9.42
9.23
9.14
8.85
8.80
8.78
8.75
8.72
8.70
8.68
8.47
8.44
7.26
5.36
5.24
2.39
2.28
1.97
1.89
1.30
0.85
(323 K)
3.83
1.75
1.84
3.97
11.59
1.95
1.98
3.91
4.00
16.59
16.19
95.63
48.61
11.0 10.0 9.0 8.0 7.0 6.0 5.0 4.0 3.0 2.0 1.0 0.0
f1 (ppm)

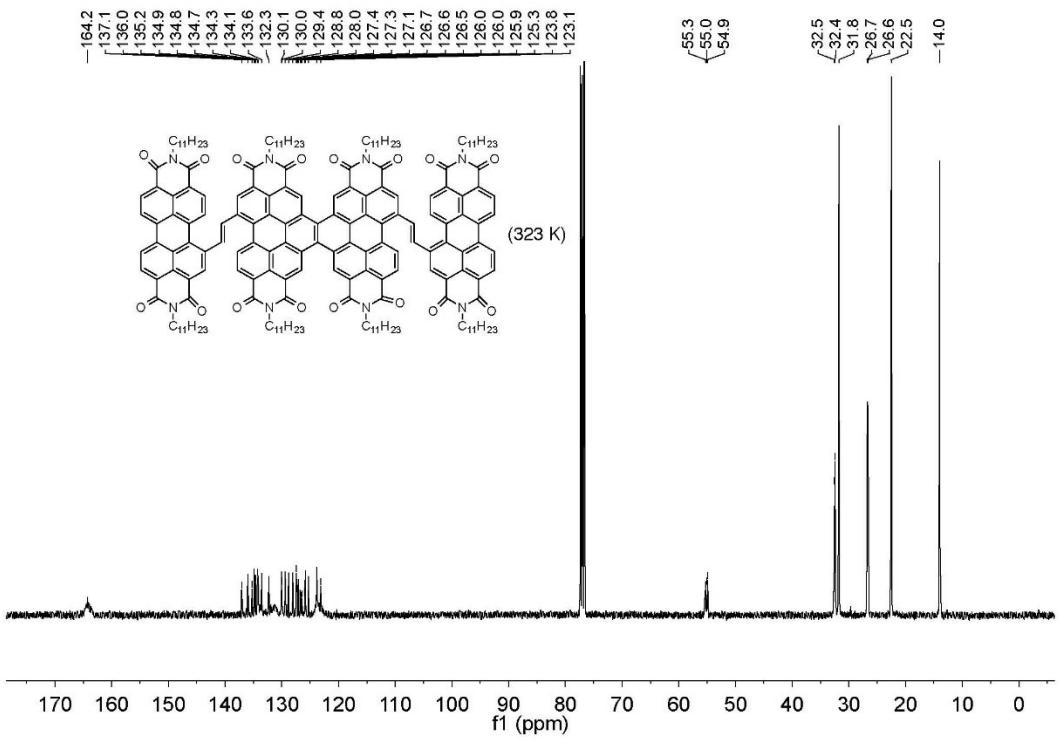
164.2
137.1
136.0
135.2
134.9
134.8
134.7
134.3
134.1
133.6
132.3
130.1
130.0
129.4
128.8
128.0
127.4
127.3
127.1
126.7
126.6
126.5
126.0
126.0
125.9
125.3
123.8
123.1
55.3
55.0
54.9
32.5
32.4
31.8
26.7
26.6
22.5
14.0
(323 K)
f1 (ppm)

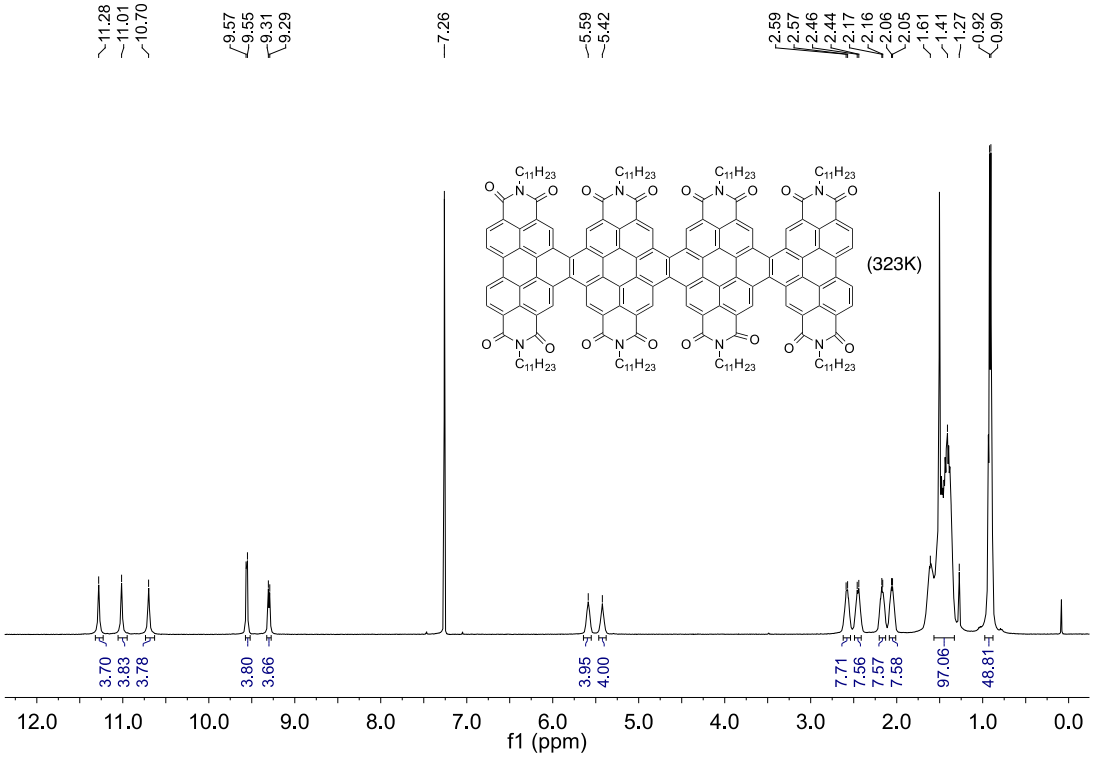
11.28
11.01
10.70
9.57
9.55
9.31
9.29
7.26
5.59
5.42
2.59
2.57
2.46
2.44
2.17
2.16
2.06
2.05
1.61
1.41
1.27
0.92
0.90
(323K)
3.70
3.83
3.78
3.80
3.66
3.95
4.00
7.71
7.56
7.57
7.58
97.06
48.81
f1 (ppm)

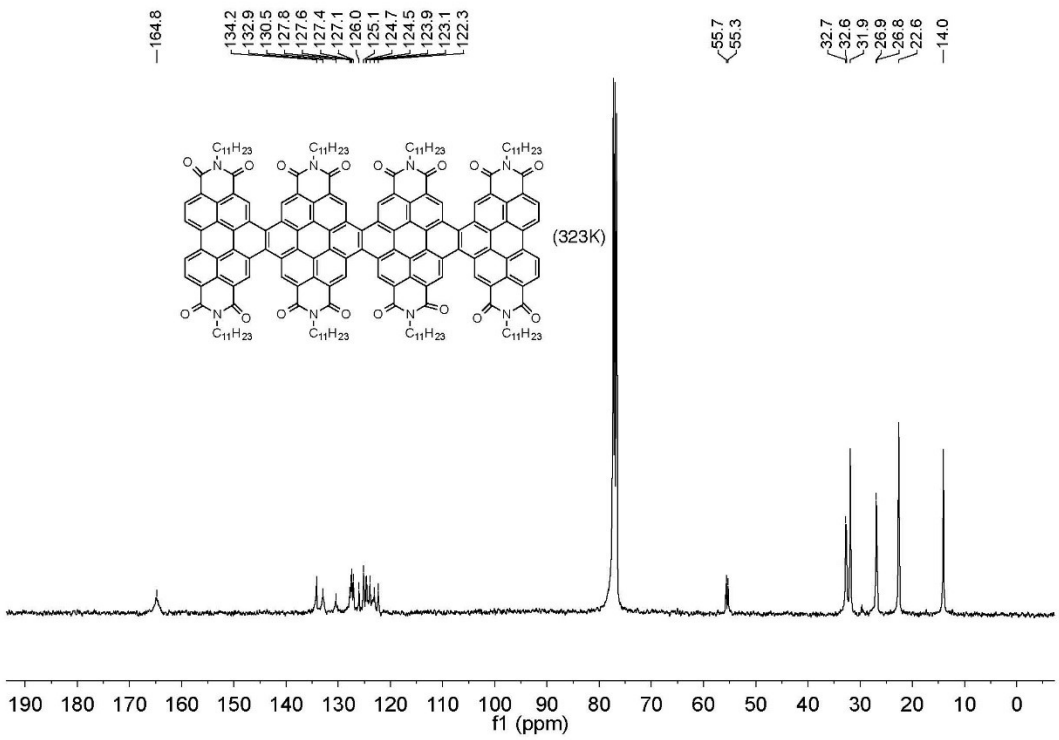
164.8
134.2
132.9
130.5
127.8
127.6
127.4
127.1
126.0
125.1
124.7
124.5
123.9
123.1
122.3
55.7
55.3
32.7
32.6
31.9
26.9
26.8
22.6
14.0
(323K)
190 180 170 160 150 140 130 120 110 100 90 80 70 60 50 40 30 20 10 0
f1 (ppm)

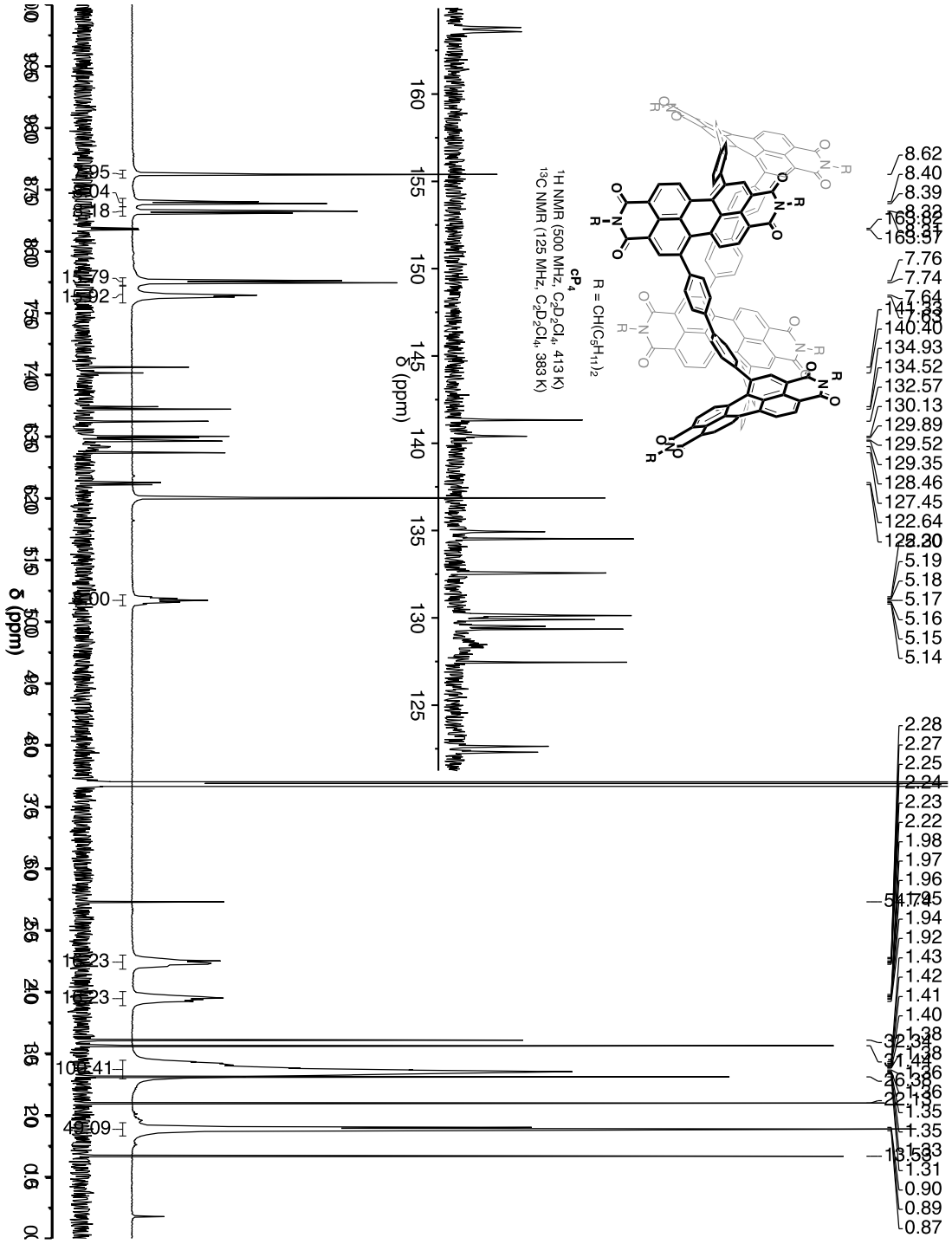
cP4
R = CH(C5H11)2
1H NMR (500 MHz, C2D2Cl4, 413 K)
13C NMR (125 MHz, C2D2Cl4, 383 K)
δ (ppm)

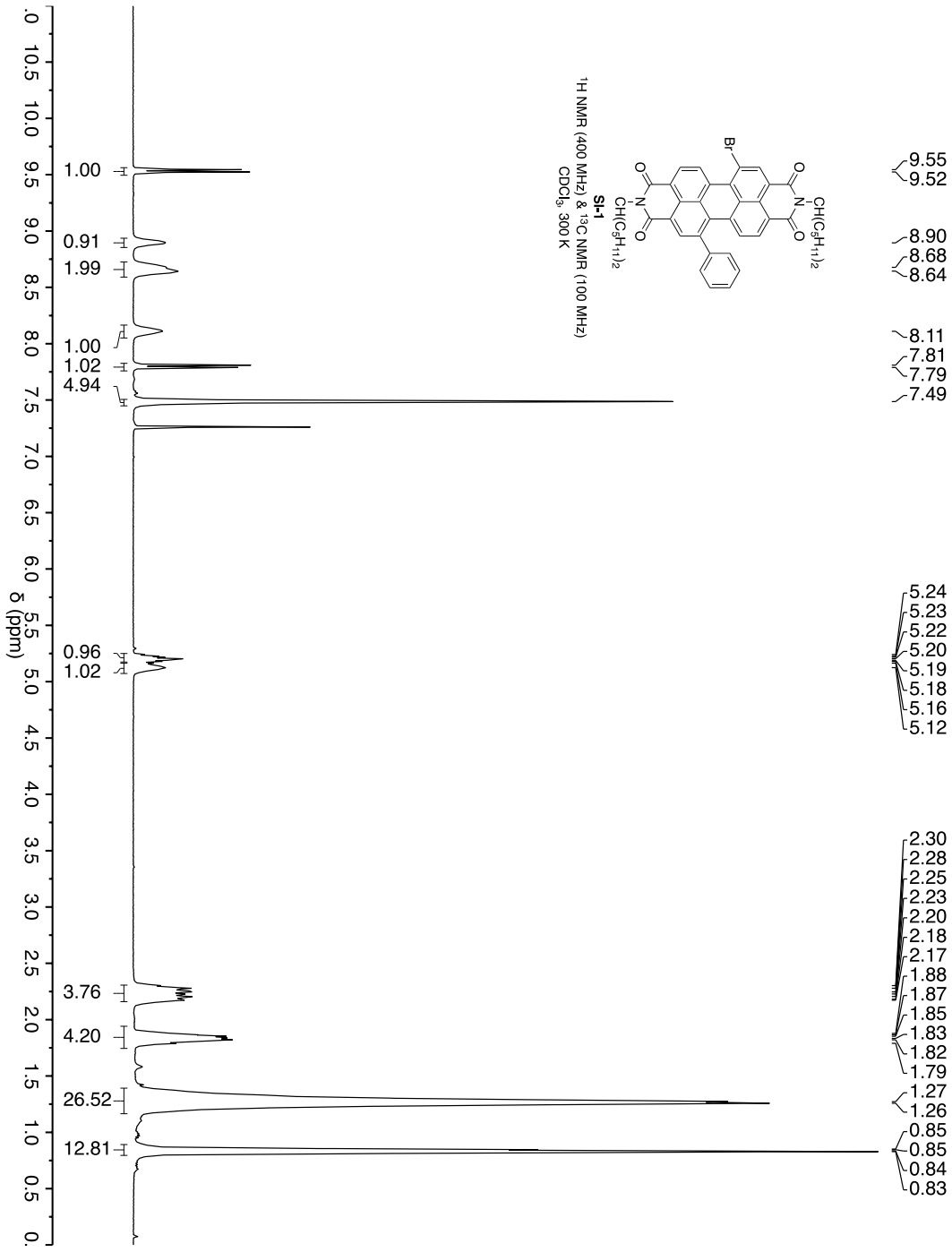
SI-1
^{1}H NMR (400 MHz) & ^{13}C NMR (100 MHz)
$CDCl_3$, 300 K
δ (ppm)
1.00
0.91
1.99
1.00
1.02
4.94
0.96
1.02
3.76
4.20
26.52
12.81
9.55
9.52
8.90
8.68
8.64
8.11
7.81
7.79
7.49
5.24
5.23
5.22
5.20
5.19
5.18
5.16
5.12
2.30
2.28
2.25
2.23
2.20
2.18
2.17
1.88
1.87
1.85
1.83
1.82
1.79
1.27
1.26
0.85
0.85
0.84
0.83

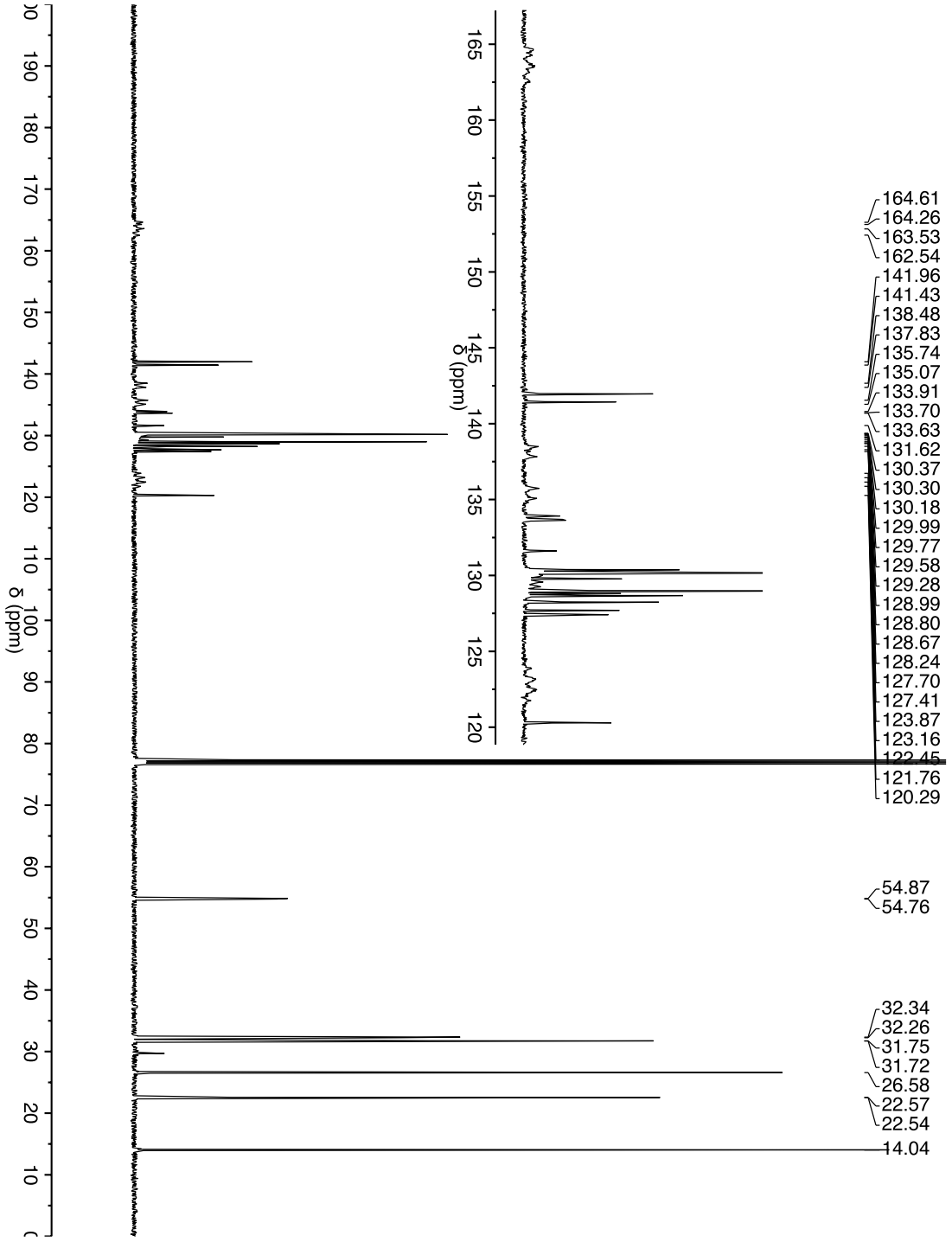
δ (ppm)
δ (ppm)
164.61
164.26
163.53
162.54
141.96
141.43
138.48
137.83
135.74
135.07
133.91
133.70
133.63
131.62
130.37
130.30
130.18
129.99
129.77
129.58
129.28
128.99
128.80
128.67
128.24
127.70
127.41
123.87
123.16
121.76
120.29
54.87
54.76
32.34
32.26
31.75
31.72
26.58
22.57
22.54
14.04

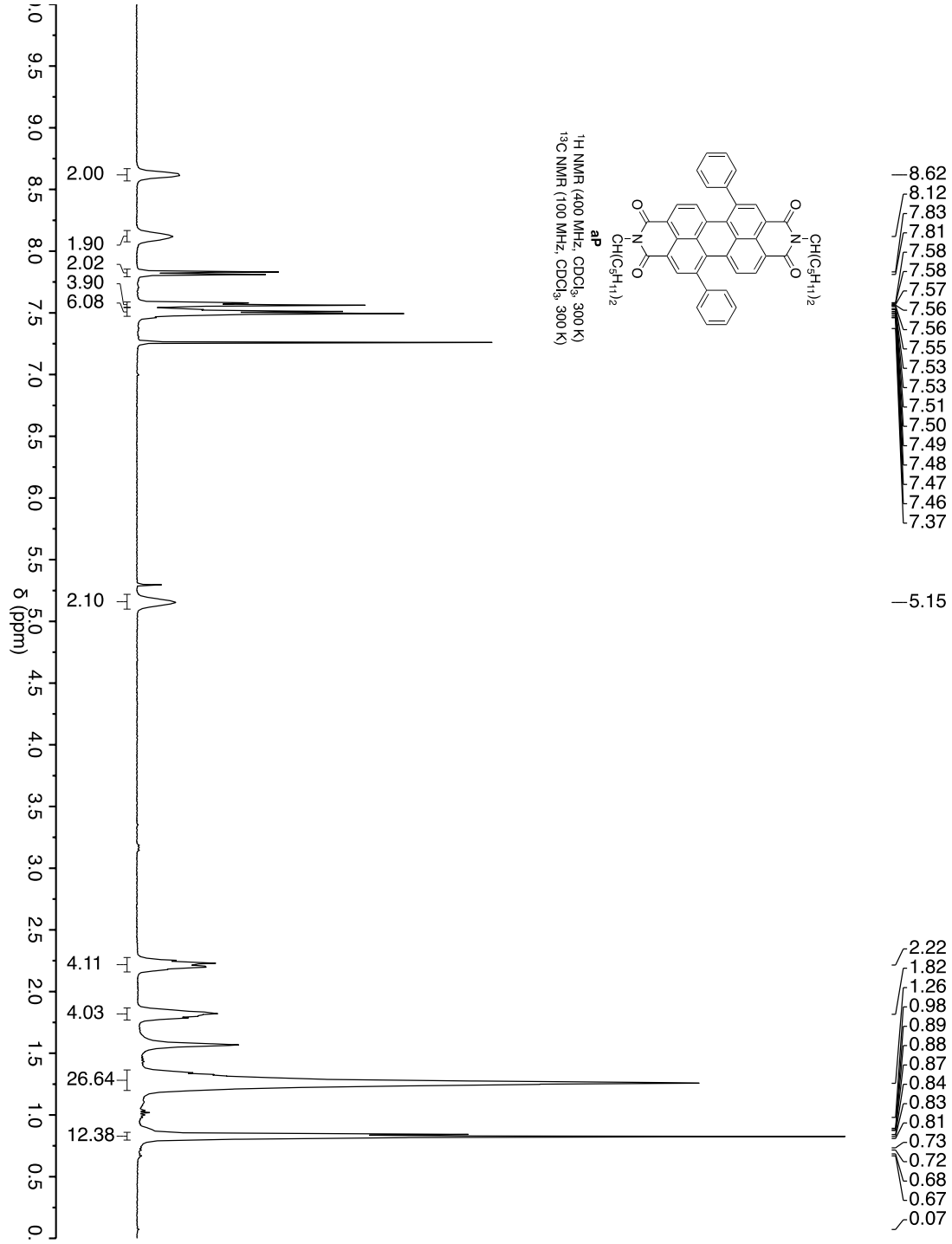
aP
^{1}H NMR (400 MHz, CDCl$_3$, 300 K)
^{13}C NMR (100 MHz, CDCl$_3$, 300 K)
CH(C$_5$H$_{11}$)$_2$
CH(C$_5$H$_{11}$)$_2$
δ (ppm)
2.00
1.90
2.02
3.90
6.08
2.10
4.11
4.03
26.64
12.38
8.62
8.12
7.83
7.81
7.58
7.58
7.57
7.56
7.56
7.55
7.53
7.53
7.51
7.50
7.49
7.48
7.47
7.46
7.37
5.15
2.22
1.82
1.26
0.98
0.89
0.88
0.87
0.84
0.83
0.81
0.73
0.72
0.68
0.67
0.07

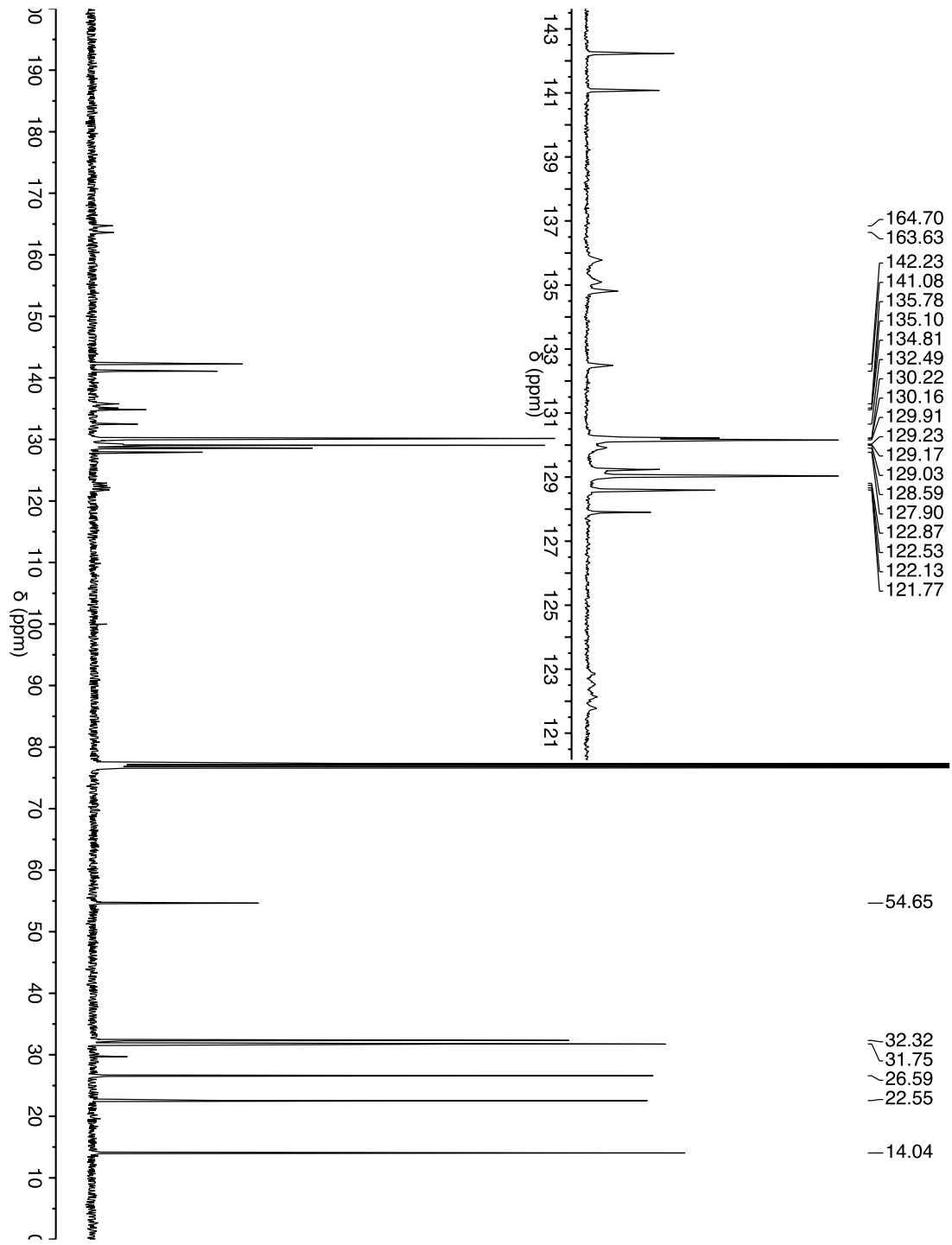
164.70
163.63
142.23
141.08
135.78
135.10
134.81
132.49
130.22
130.16
129.91
129.23
129.17
129.03
128.59
127.90
122.87
122.53
122.13
121.77
54.65
32.32
31.75
26.59
22.55
14.04
δ (ppm)

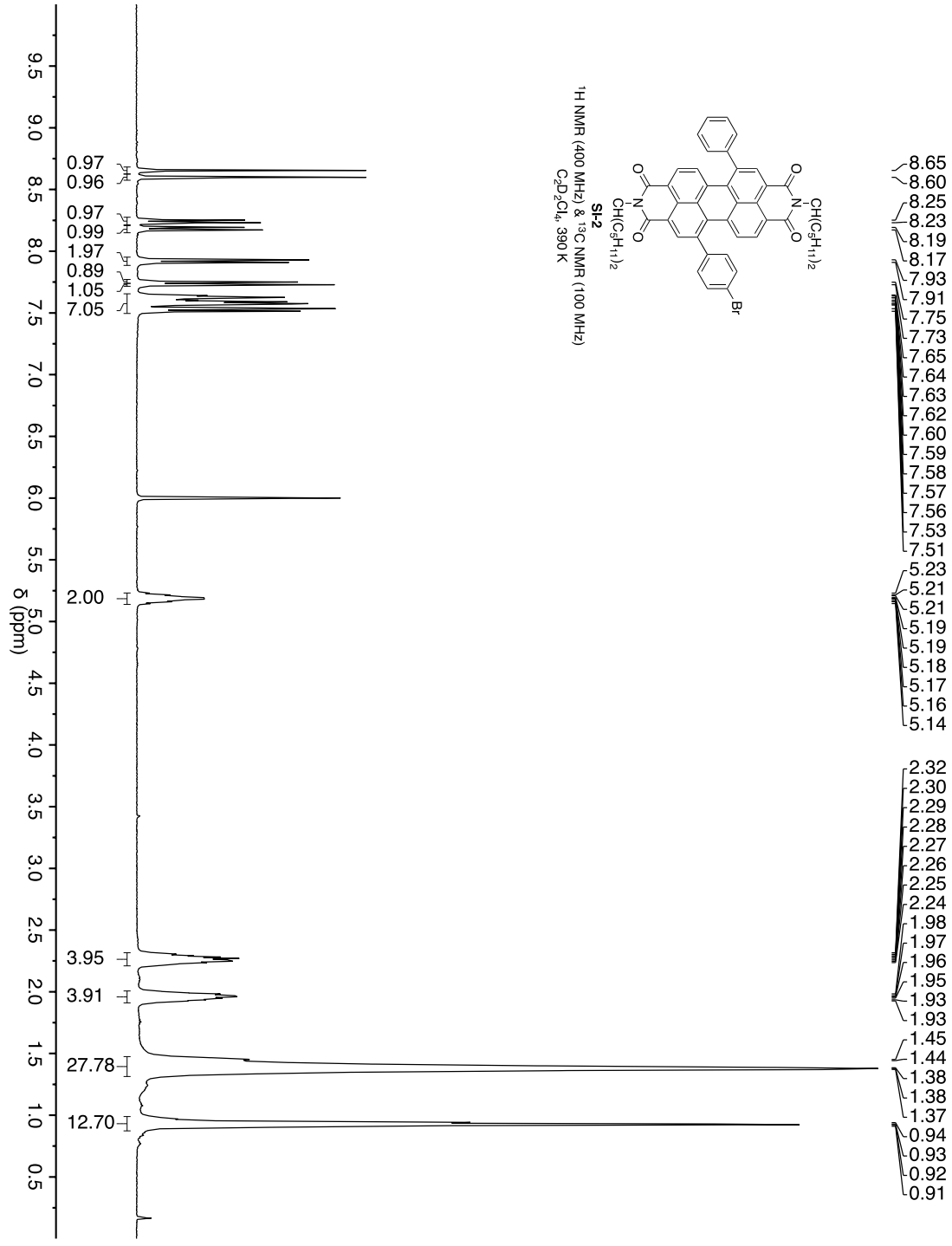
SI-2
^{1}H NMR (400 MHz) & ^{13}C NMR (100 MHz)
$C_2D_2Cl_4$, 390 K
CH(C$_5$H$_{11}$)$_2$
CH(C$_5$H$_{11}$)$_2$
Br
δ (ppm)
0.97
0.96
0.97
0.99
1.97
0.89
1.05
7.05
2.00
3.95
3.91
27.78
12.70
8.65
8.60
8.25
8.23
8.19
8.17
7.93
7.91
7.75
7.73
7.65
7.64
7.63
7.62
7.60
7.59
7.58
7.57
7.56
7.53
7.51
5.23
5.21
5.21
5.19
5.19
5.18
5.17
5.16
5.14
2.32
2.30
2.29
2.28
2.27
2.26
2.25
2.24
1.98
1.97
1.96
1.95
1.93
1.93
1.45
1.44
1.38
1.38
1.37
0.94
0.93
0.92
0.91

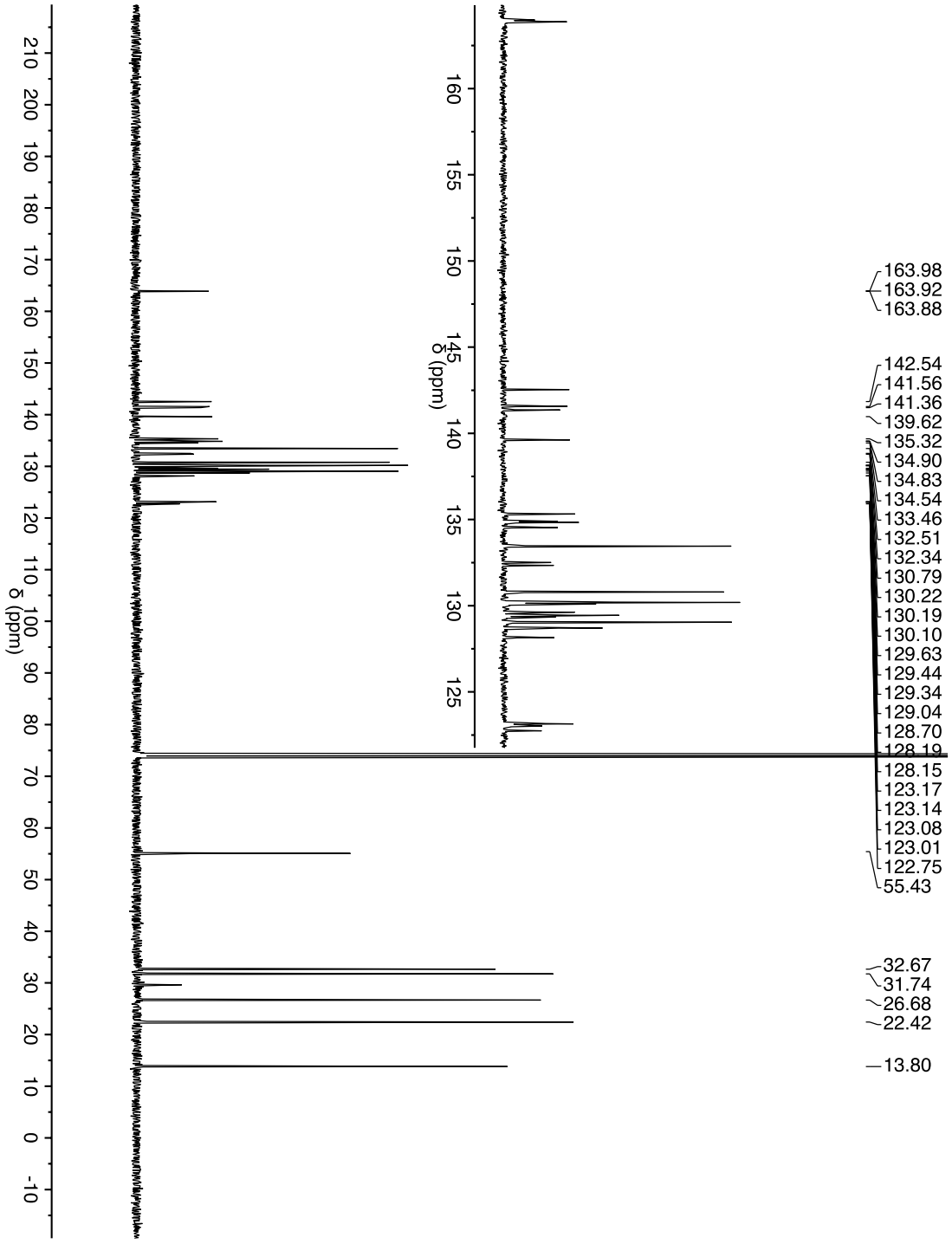
163.98
163.92
163.88
142.54
141.56
141.36
139.62
135.32
134.90
134.83
134.54
133.46
132.51
132.34
130.79
130.22
130.19
130.10
129.63
129.44
129.34
129.04
128.70
128.19
128.15
123.17
123.14
123.08
123.01
122.75
55.43
32.67
31.74
26.68
22.42
13.80
δ (ppm)
δ (ppm)

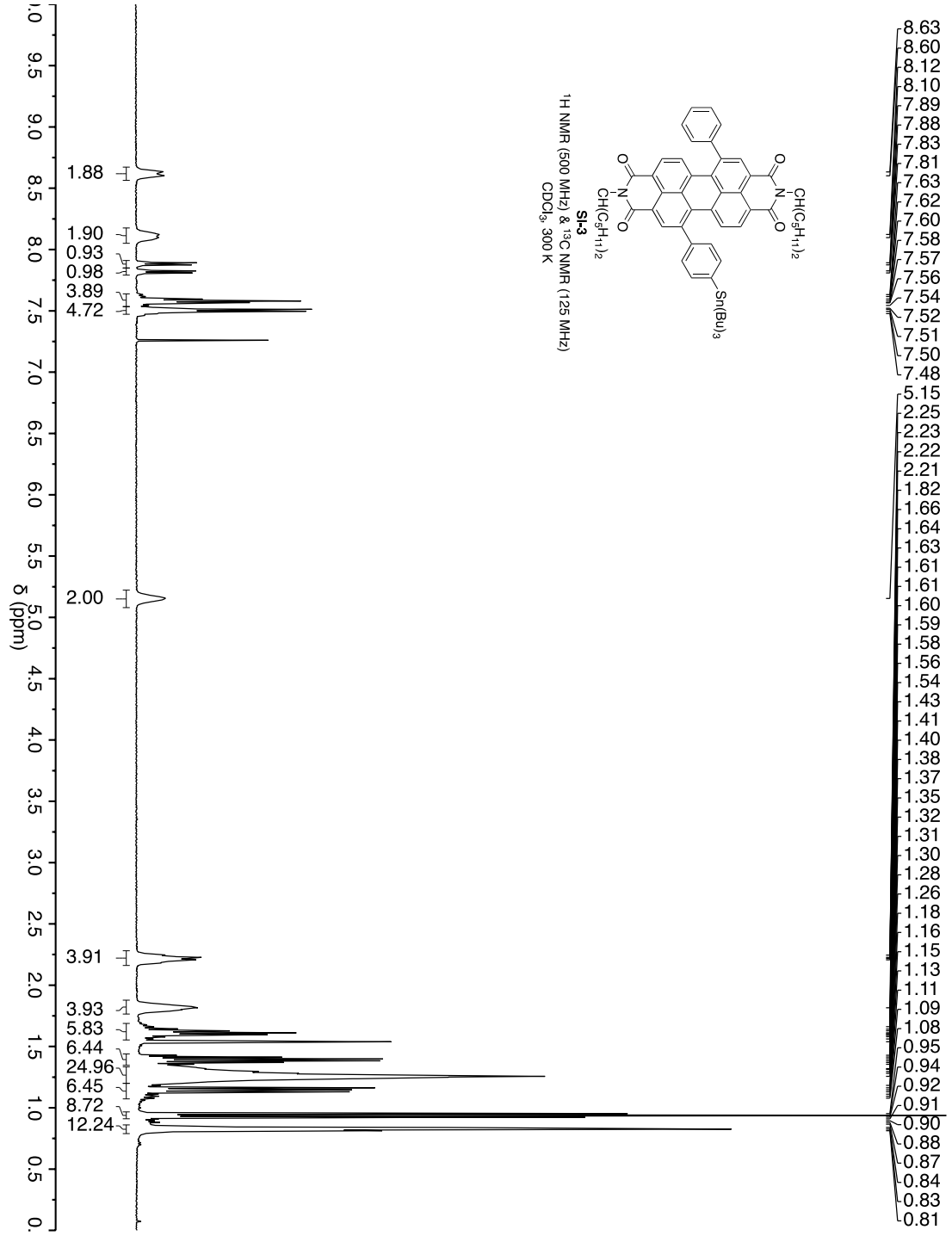
Si-3
^{1}H NMR (500 MHz) & ^{13}C NMR (125 MHz)
$CDCl_3$, 300 K
$CH(C_5H_{11})_2$
$Sn(Bu)_3$
δ (ppm)
1.88
1.90
0.93
0.98
3.89
4.72
2.00
3.91
3.93
5.83
6.44
24.96
6.45
8.72
12.24
8.63
8.60
8.12
8.10
7.89
7.88
7.83
7.81
7.63
7.62
7.60
7.58
7.57
7.56
7.54
7.52
7.51
7.50
7.48
5.15
2.25
2.23
2.22
2.21
1.82
1.66
1.64
1.63
1.61
1.61
1.60
1.59
1.58
1.56
1.54
1.43
1.41
1.40
1.38
1.37
1.35
1.32
1.31
1.30
1.28
1.26
1.18
1.16
1.15
1.13
1.11
1.09
1.08
0.95
0.94
0.92
0.91
0.90
0.88
0.87
0.84
0.83
0.81

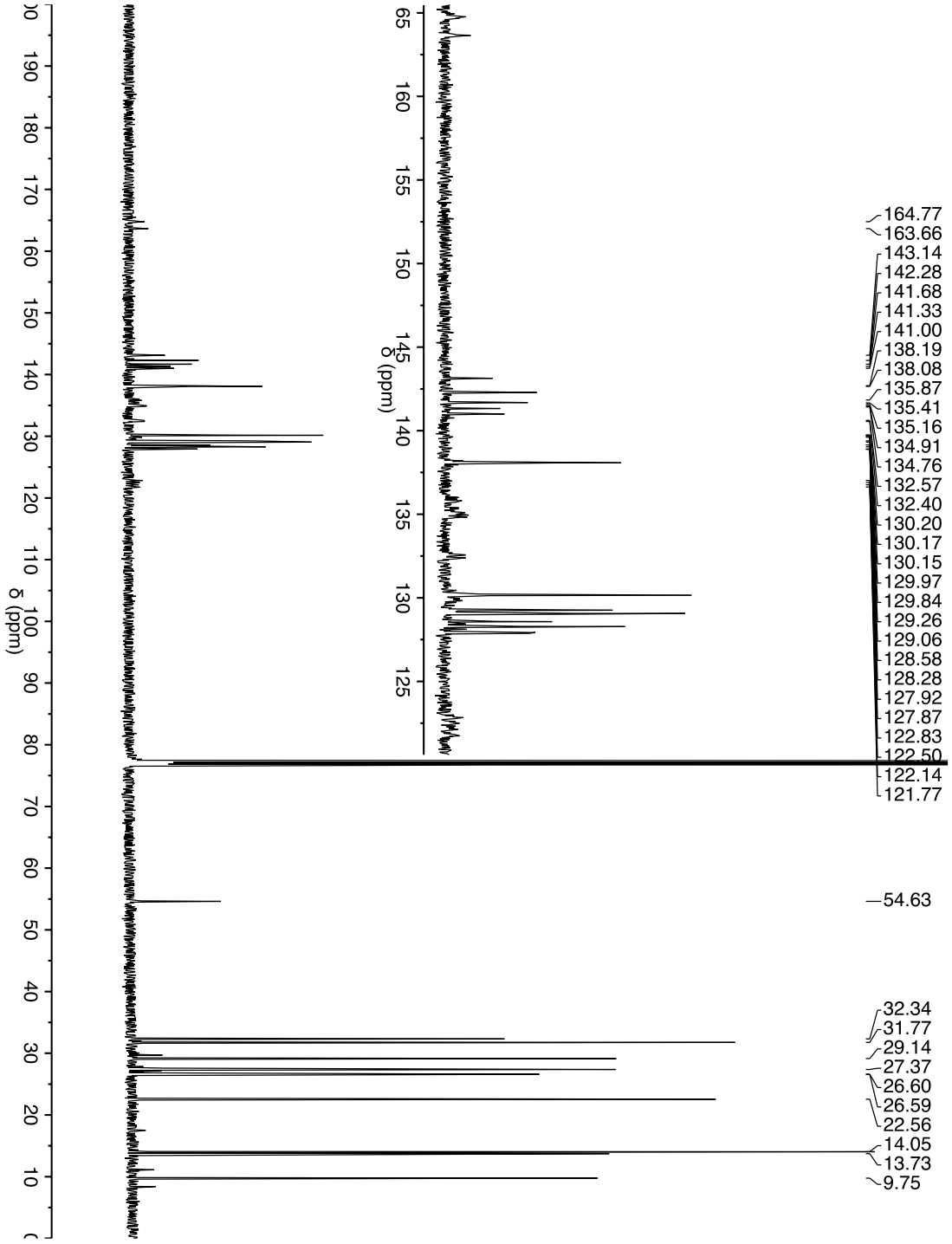
δ (ppm)
δ (ppm)
164.77
163.66
143.14
142.28
141.68
141.33
141.00
138.19
138.08
135.87
135.41
135.16
134.91
134.76
132.57
132.40
130.20
130.17
130.15
129.97
129.84
129.26
129.06
128.58
128.28
127.92
127.87
122.83
122.50
122.14
121.77
54.63
32.34
31.77
29.14
27.37
26.60
26.59
22.56
14.05
13.73
9.75

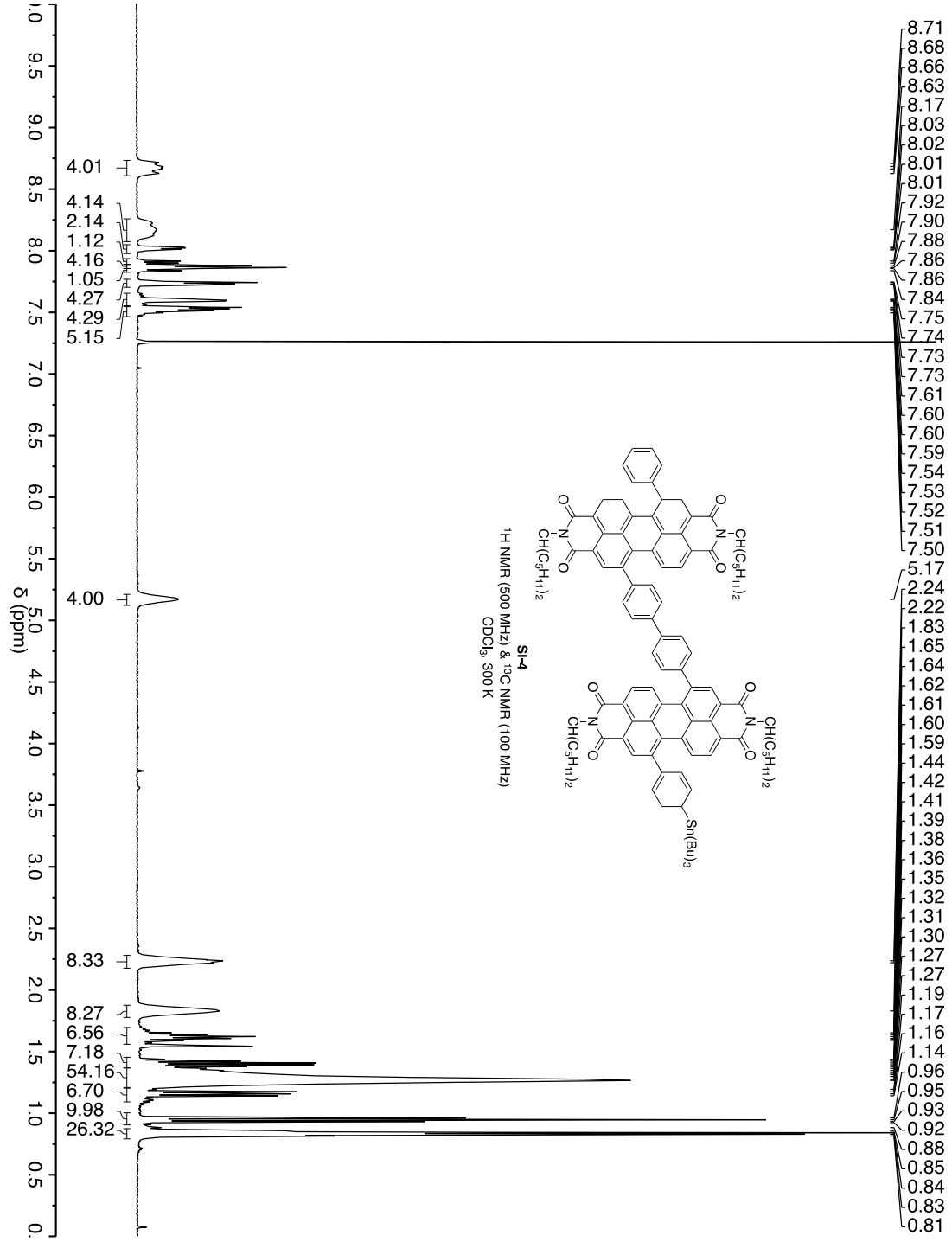
SI-4
^{1}H NMR (500 MHz) & ^{13}C NMR (100 MHz)
$CDCl_3$, 300 K
δ (ppm)
4.01
4.14
2.14
1.12
4.16
1.05
4.27
4.29
5.15
4.00
8.33
8.27
6.56
7.18
54.16
6.70
9.98
26.32
8.71
8.68
8.66
8.63
8.17
8.03
8.02
8.01
8.01
7.92
7.90
7.88
7.86
7.86
7.84
7.75
7.74
7.73
7.73
7.61
7.60
7.60
7.59
7.54
7.53
7.52
7.51
7.50
5.17
2.24
2.22
1.83
1.65
1.64
1.62
1.61
1.60
1.59
1.44
1.42
1.41
1.39
1.38
1.36
1.35
1.32
1.31
1.30
1.27
1.27
1.19
1.17
1.16
1.14
0.96
0.95
0.93
0.92
0.88
0.85
0.84
0.83
0.81

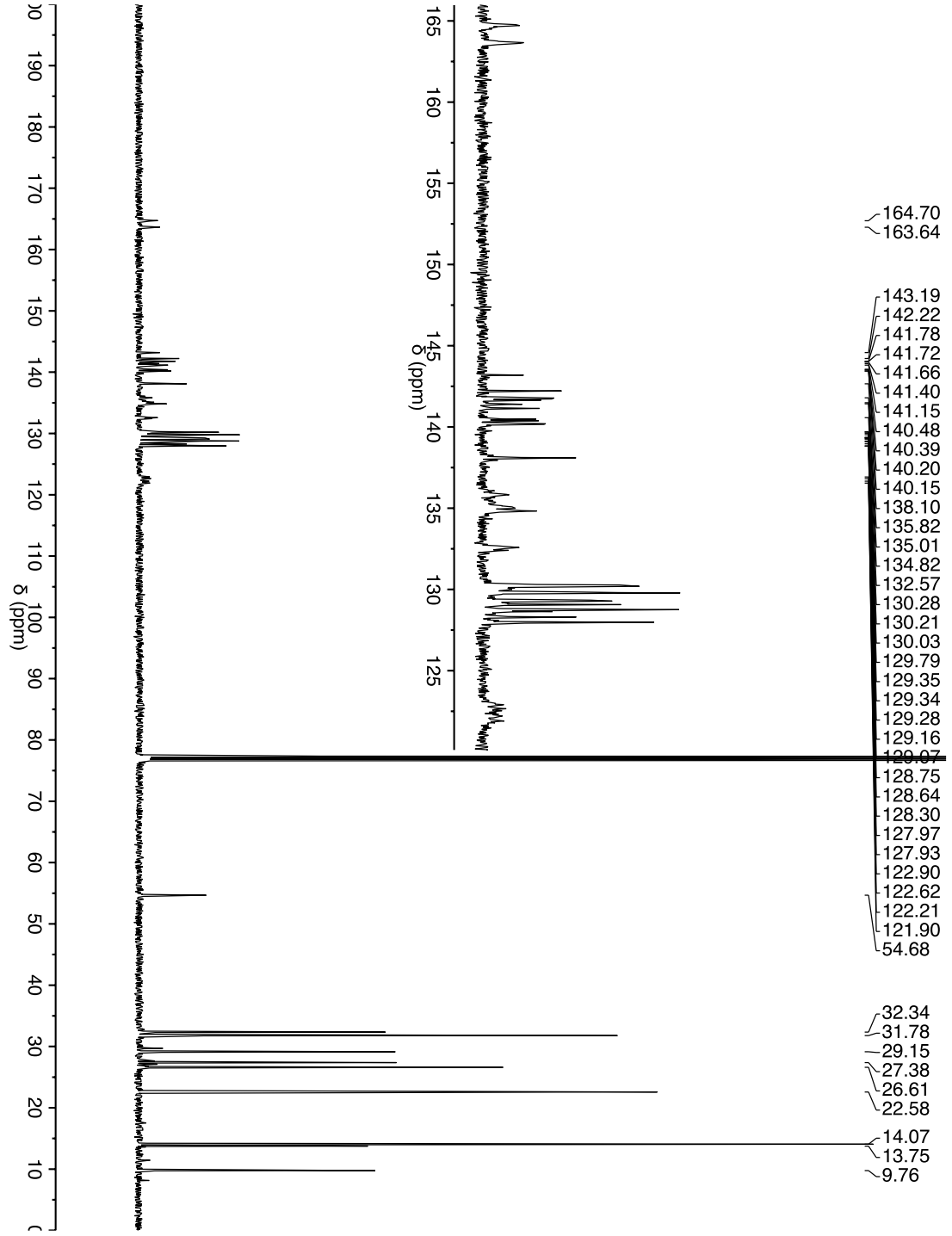
δ (ppm)
δ (ppm)
164.70
163.64
143.19
142.22
141.78
141.72
141.66
141.40
141.15
140.48
140.39
140.20
140.15
138.10
135.82
135.01
134.82
132.57
130.28
130.21
130.03
129.79
129.35
129.34
129.28
129.16
129.07
128.75
128.64
128.30
127.97
127.93
122.90
122.62
122.21
121.90
54.68
32.34
31.78
29.15
27.38
26.61
22.58
14.07
13.75
9.76

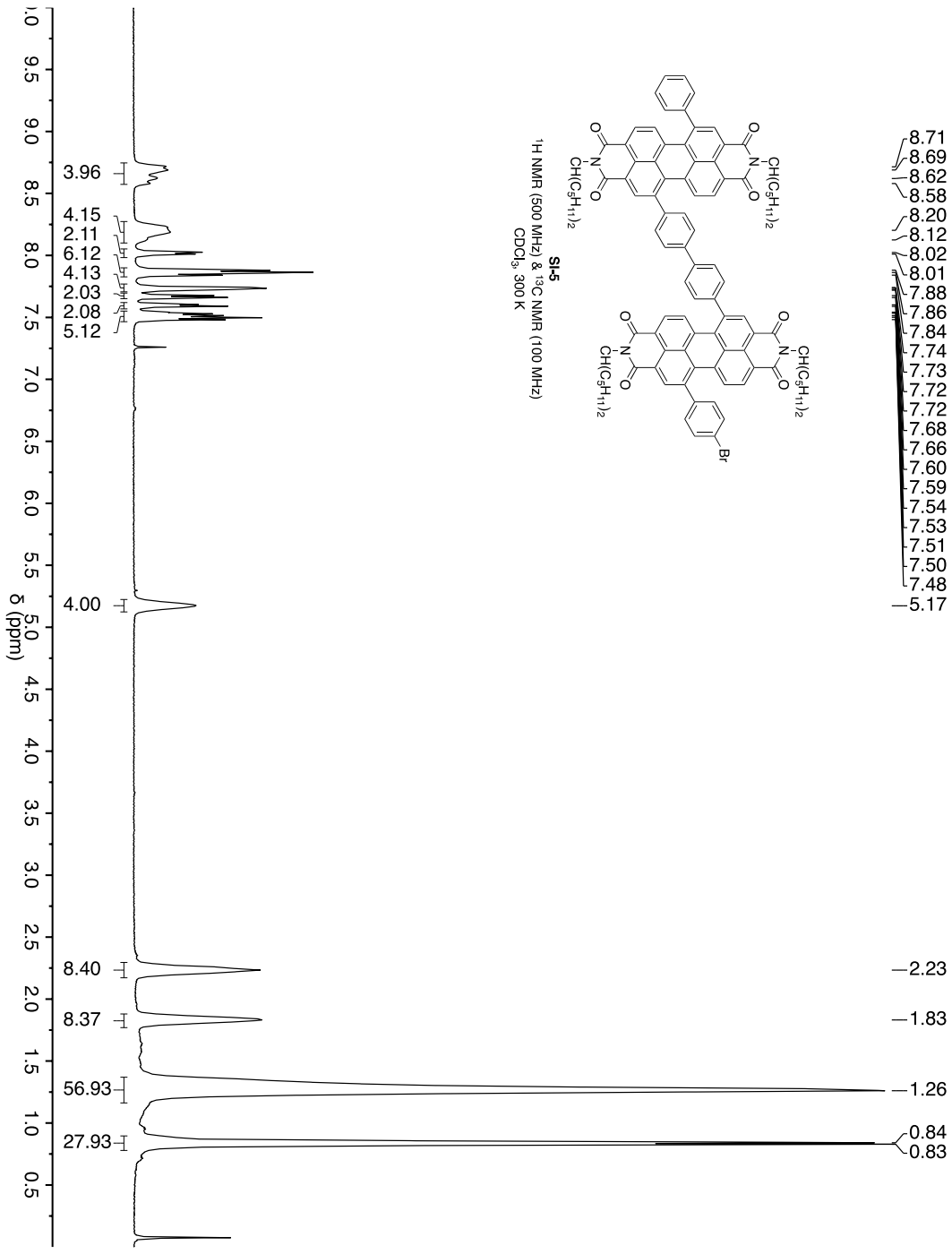
Si-5
¹H NMR (500 MHz) & ¹³C NMR (100 MHz)
CDCl₃, 300 K
δ (ppm)
3.96
4.15
2.11
6.12
4.13
2.03
2.08
5.12
4.00
8.40
8.37
56.93
27.93
8.71
8.69
8.62
8.58
8.20
8.12
8.02
8.01
7.88
7.86
7.84
7.74
7.73
7.72
7.72
7.68
7.66
7.60
7.59
7.54
7.53
7.51
7.50
7.48
5.17
2.23
1.83
1.26
0.84
0.83
Br

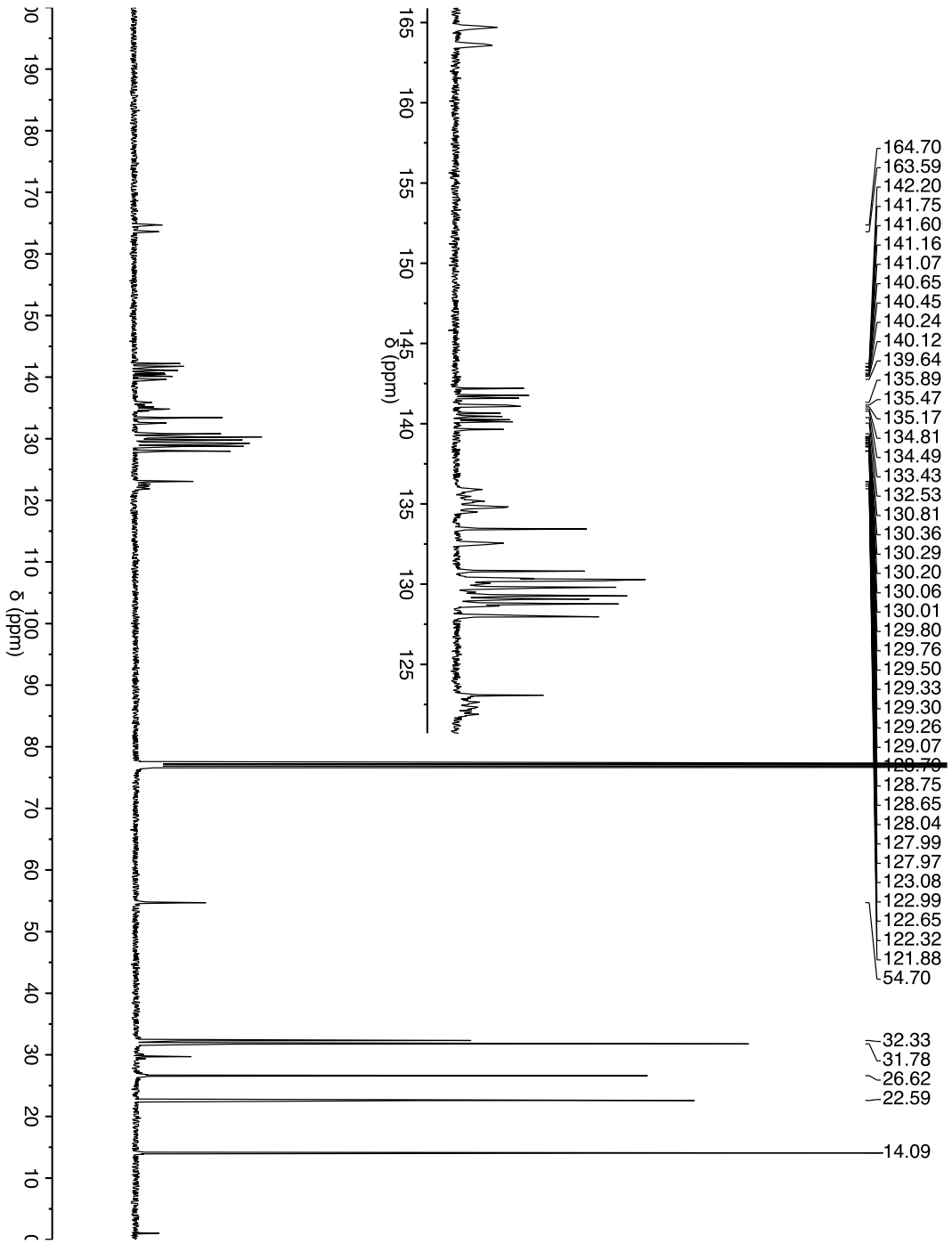
δ (ppm)
164.70
163.59
142.20
141.75
141.60
141.16
141.07
140.65
140.45
140.24
140.12
139.64
135.89
135.47
135.17
134.81
134.49
133.43
132.53
130.81
130.36
130.29
130.20
130.06
130.01
129.80
129.76
129.50
129.33
129.30
129.26
129.07
128.75
128.65
128.04
127.99
127.97
123.08
122.99
122.65
122.32
121.88
54.70
32.33
31.78
26.62
22.59
14.09

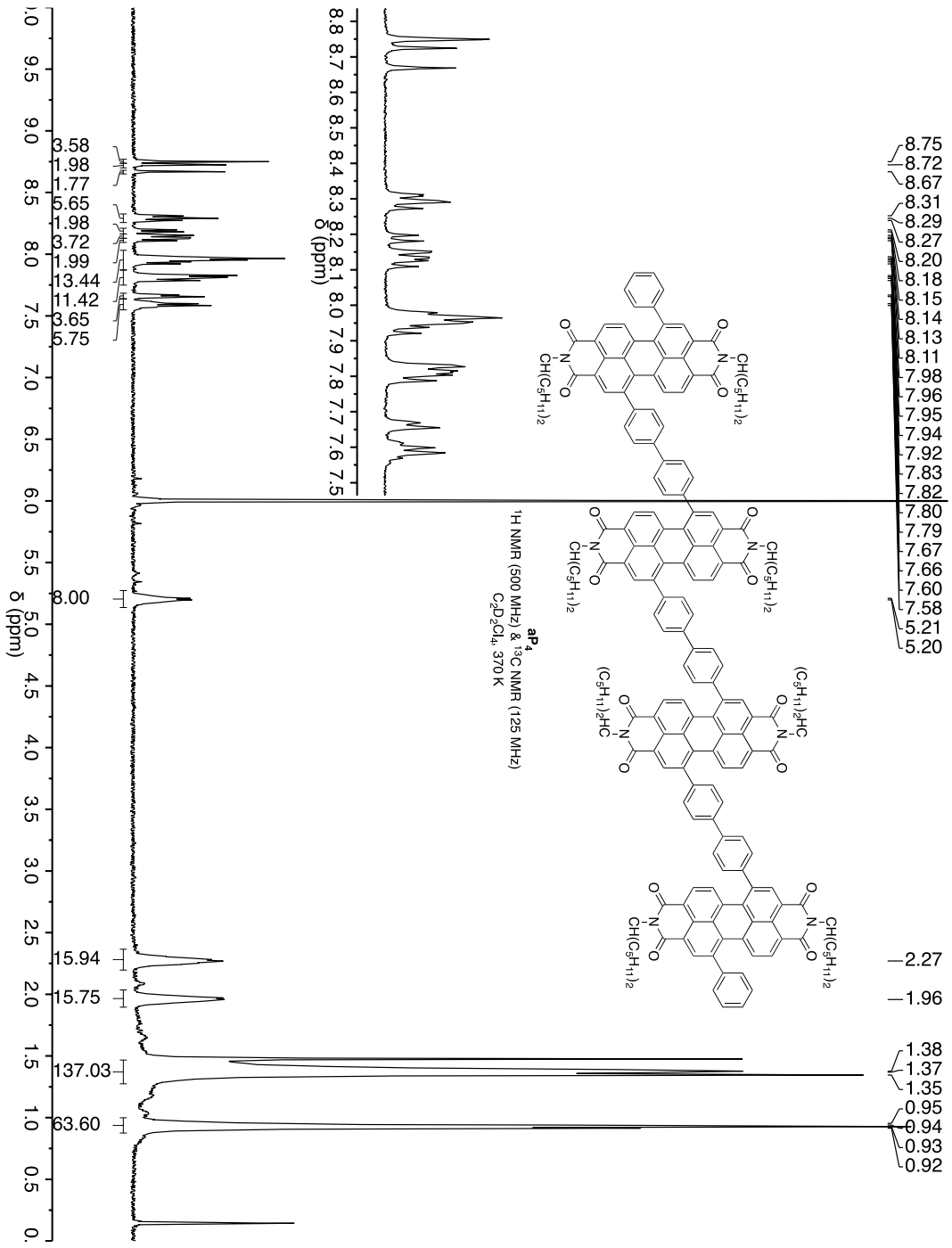
aP4
^{1}H NMR (500 MHz) & ^{13}C NMR (125 MHz)
$C_2D_2Cl_4$, 370 K
δ (ppm)
3.58
1.98
1.77
5.65
1.98
3.72
1.99
13.44
11.42
3.65
5.75
8.00
15.94
15.75
137.03
63.60
8.75
8.72
8.67
8.31
8.29
8.27
8.20
8.18
8.15
8.14
8.13
8.11
7.98
7.96
7.95
7.94
7.92
7.83
7.82
7.80
7.79
7.67
7.66
7.60
7.58
5.21
5.20
2.27
1.96
1.38
1.37
1.35
0.95
0.94
0.93
0.92

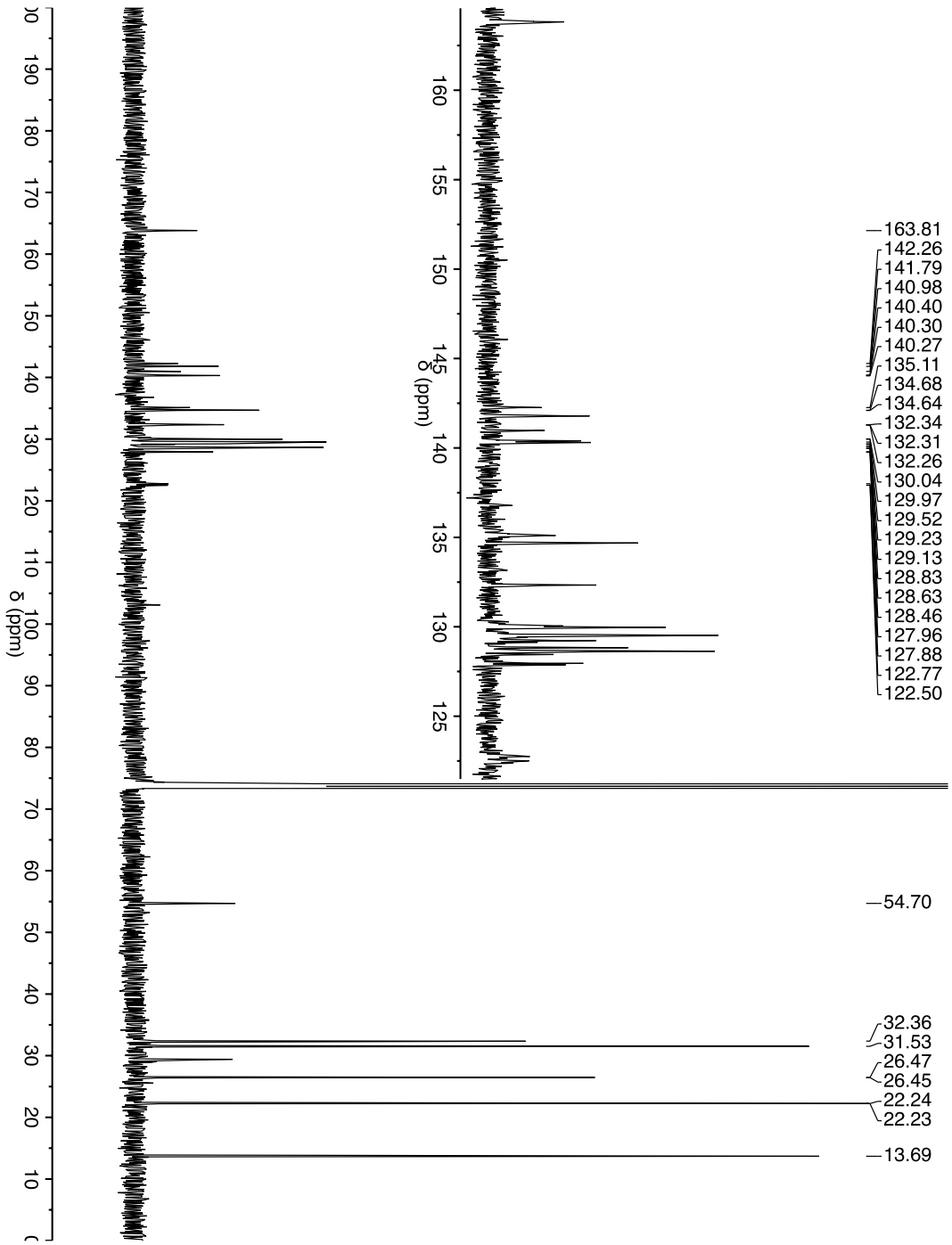
δ (ppm)
δ (ppm)
163.81
142.26
141.79
140.98
140.40
140.30
140.27
135.11
134.68
134.64
132.34
132.31
132.26
130.04
129.97
129.52
129.23
129.13
128.83
128.63
128.46
127.96
127.88
122.77
122.50
54.70
32.36
31.53
26.47
26.45
22.24
22.23
13.69

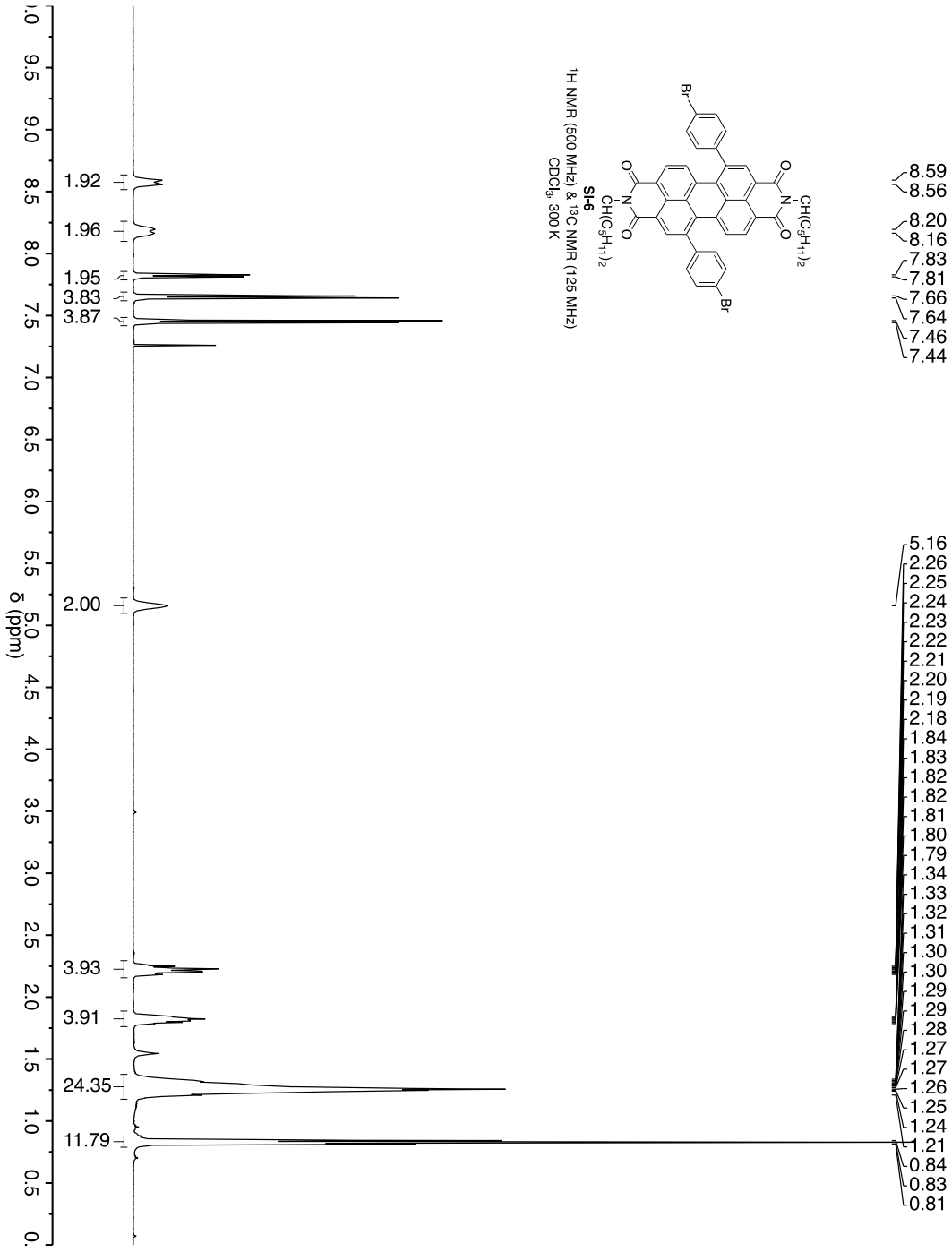
Si-6
^{1}H NMR (500 MHz) & ^{13}C NMR (125 MHz)
$CDCl_3$, 300 K
Br
Br
$CH(C_5H_{11})_2$
$CH(C_5H_{11})_2$
δ (ppm)
1.92
1.96
1.95
3.83
3.87
2.00
3.93
3.91
24.35
11.79
8.59
8.56
8.20
8.16
7.83
7.81
7.66
7.64
7.46
7.44
5.16
2.26
2.25
2.24
2.23
2.22
2.21
2.20
2.19
2.18
1.84
1.83
1.82
1.82
1.81
1.80
1.79
1.34
1.33
1.32
1.31
1.30
1.30
1.29
1.29
1.28
1.27
1.27
1.26
1.25
1.24
1.21
0.84
0.83
0.81

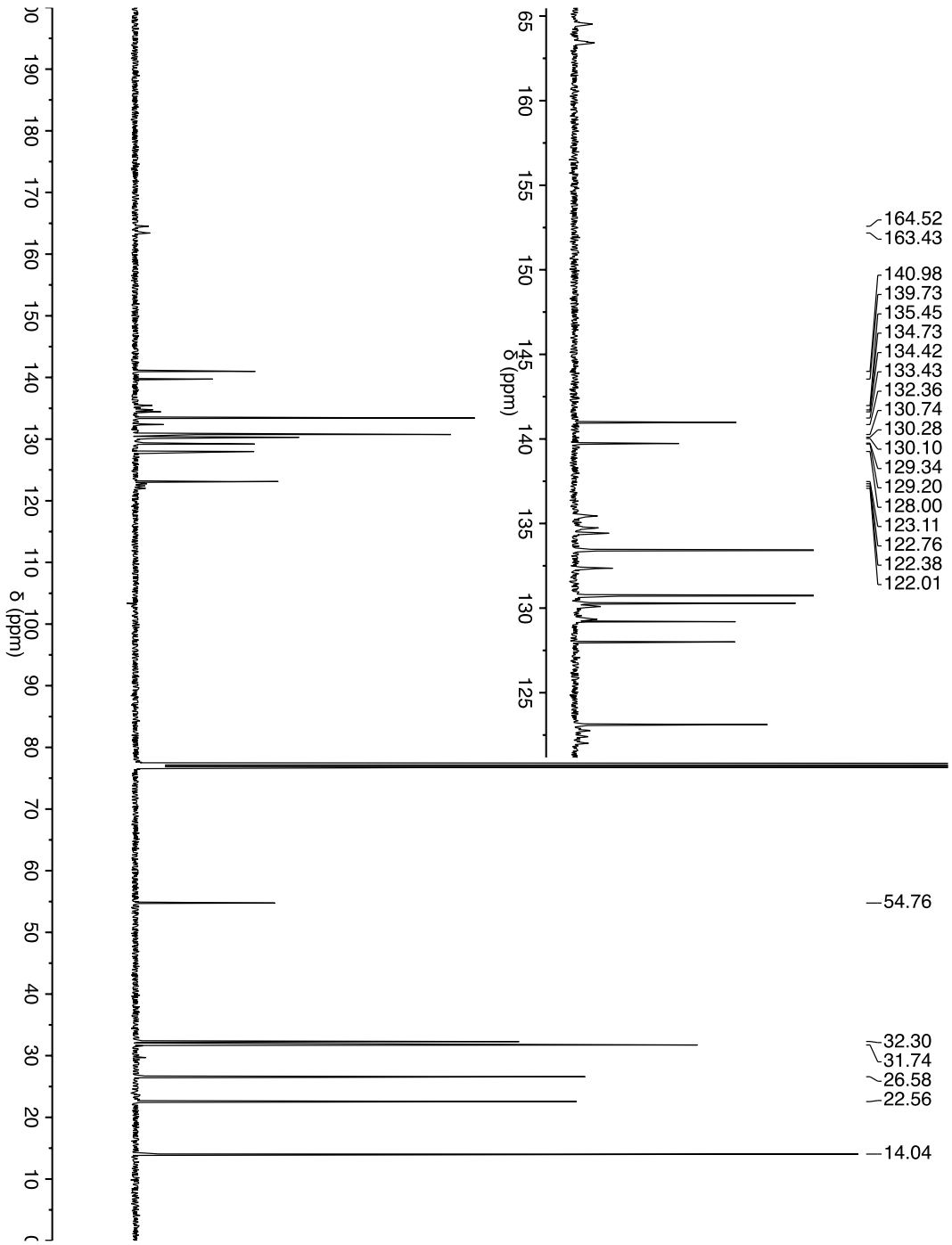
δ (ppm)
δ (ppm)
164.52
163.43
140.98
139.73
135.45
134.73
134.42
133.43
132.36
130.74
130.28
130.10
129.34
129.20
128.00
123.11
122.76
122.38
122.01
54.76
32.30
31.74
26.58
22.56
14.04

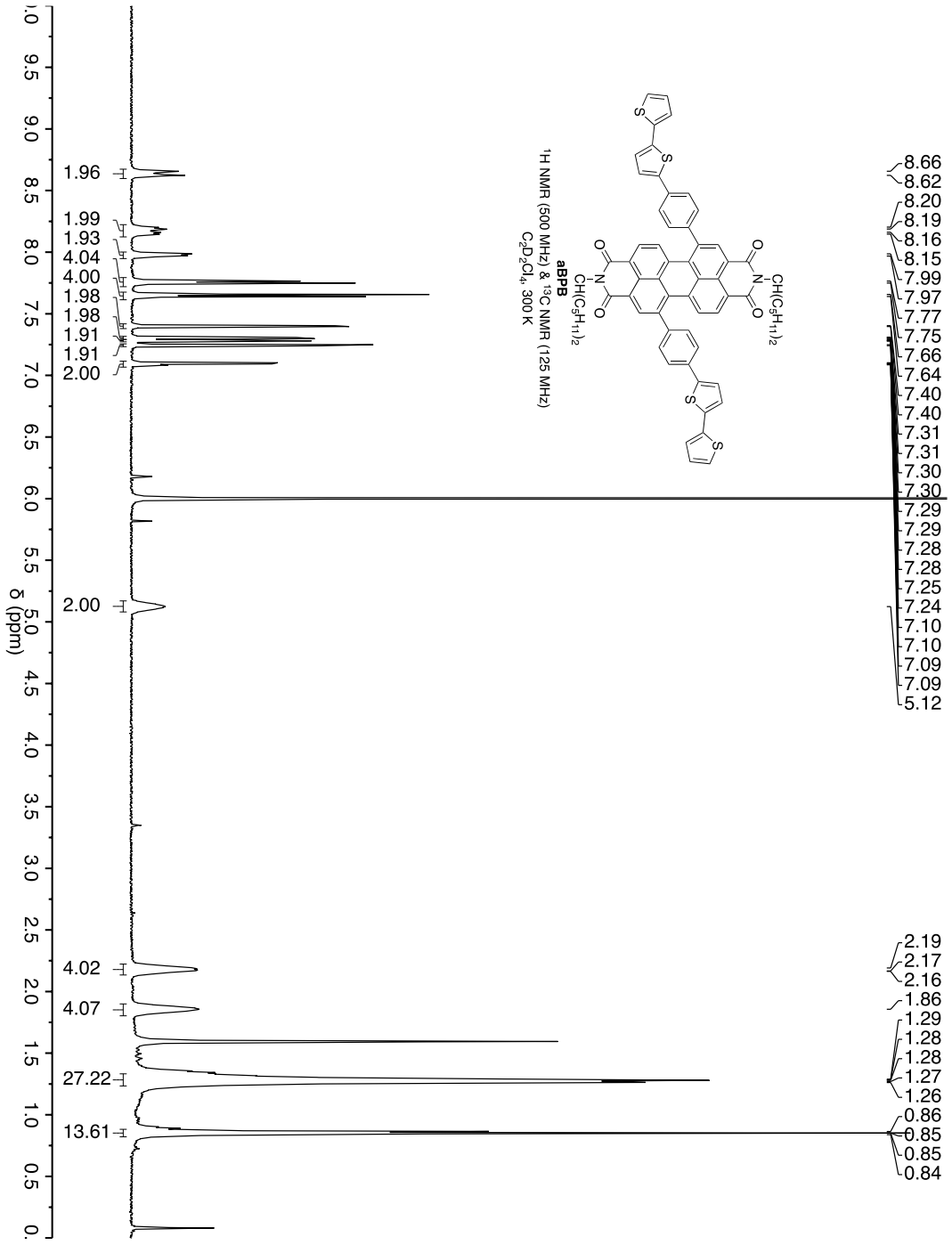
aBPP
^{1}H NMR (500 MHz) & ^{13}C NMR (125 MHz)
$C_2D_2Cl_4$, 300 K
δ (ppm)
1.96
1.99
1.93
4.04
4.00
1.98
1.98
1.91
1.91
2.00
2.00
4.02
4.07
27.22
13.61
8.66
8.62
8.20
8.19
8.16
8.15
7.99
7.97
7.77
7.75
7.66
7.64
7.40
7.40
7.31
7.31
7.30
7.30
7.29
7.29
7.28
7.28
7.25
7.24
7.10
7.10
7.09
7.09
5.12
2.19
2.17
2.16
1.86
1.29
1.28
1.28
1.27
1.26
0.86
0.85
0.85
0.84

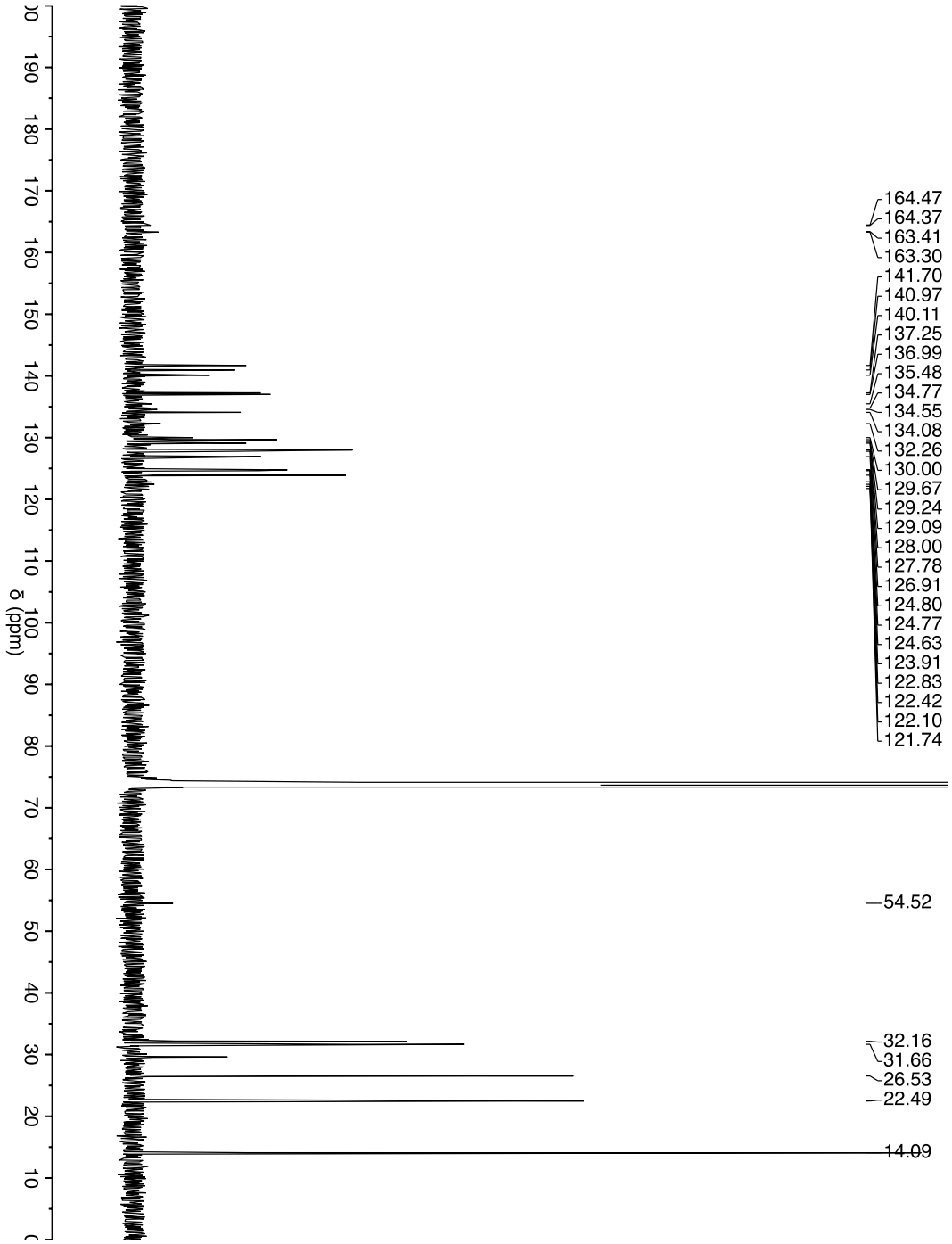
δ (ppm)
164.47
164.37
163.41
163.30
141.70
140.97
140.11
137.25
136.99
135.48
134.77
134.55
134.08
132.26
130.00
129.67
129.24
129.09
128.00
127.78
126.91
124.80
124.77
124.63
123.91
122.83
122.42
122.10
121.74
54.52
32.16
31.66
26.53
22.49
14.09

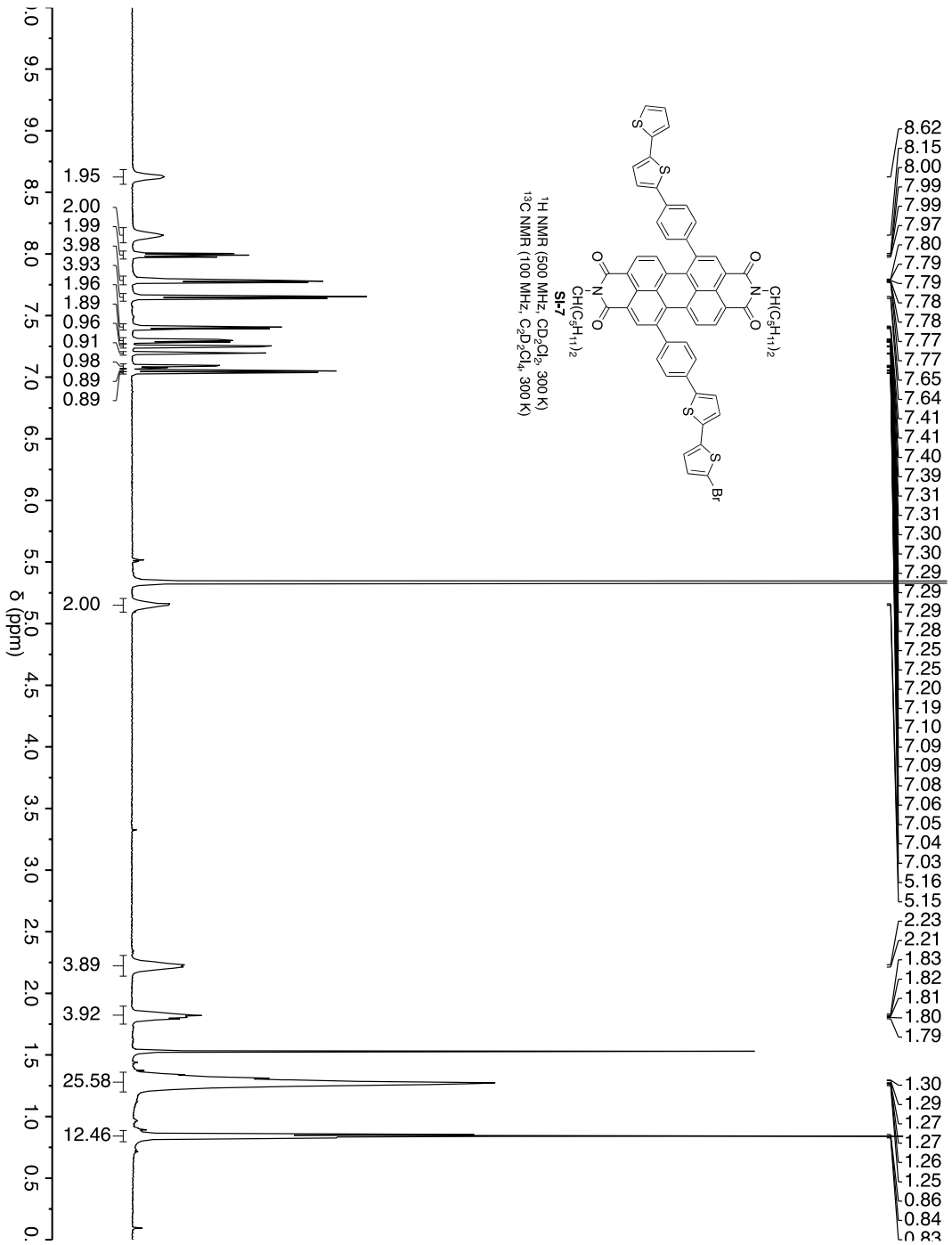
SI-7
^{1}H NMR (500 MHz, CD_2Cl_2, 300 K)
^{13}C NMR (100 MHz, $C_2D_2Cl_4$, 300 K)
CH(C$_5$H$_{11}$)$_2$
CH(C$_5$H$_{11}$)$_2$
δ (ppm)
1.95
2.00
1.99
3.98
3.93
1.96
1.89
0.96
0.91
0.98
0.89
0.89
2.00
3.89
3.92
25.58
12.46
8.62
8.15
8.00
7.99
7.99
7.97
7.80
7.79
7.79
7.78
7.78
7.77
7.77
7.65
7.64
7.41
7.41
7.40
7.39
7.31
7.31
7.30
7.30
7.29
7.29
7.29
7.28
7.25
7.25
7.20
7.19
7.10
7.09
7.09
7.08
7.06
7.05
7.04
7.03
5.16
5.15
2.23
2.21
1.83
1.82
1.81
1.80
1.79
1.30
1.29
1.27
1.27
1.26
1.25
0.86
0.84

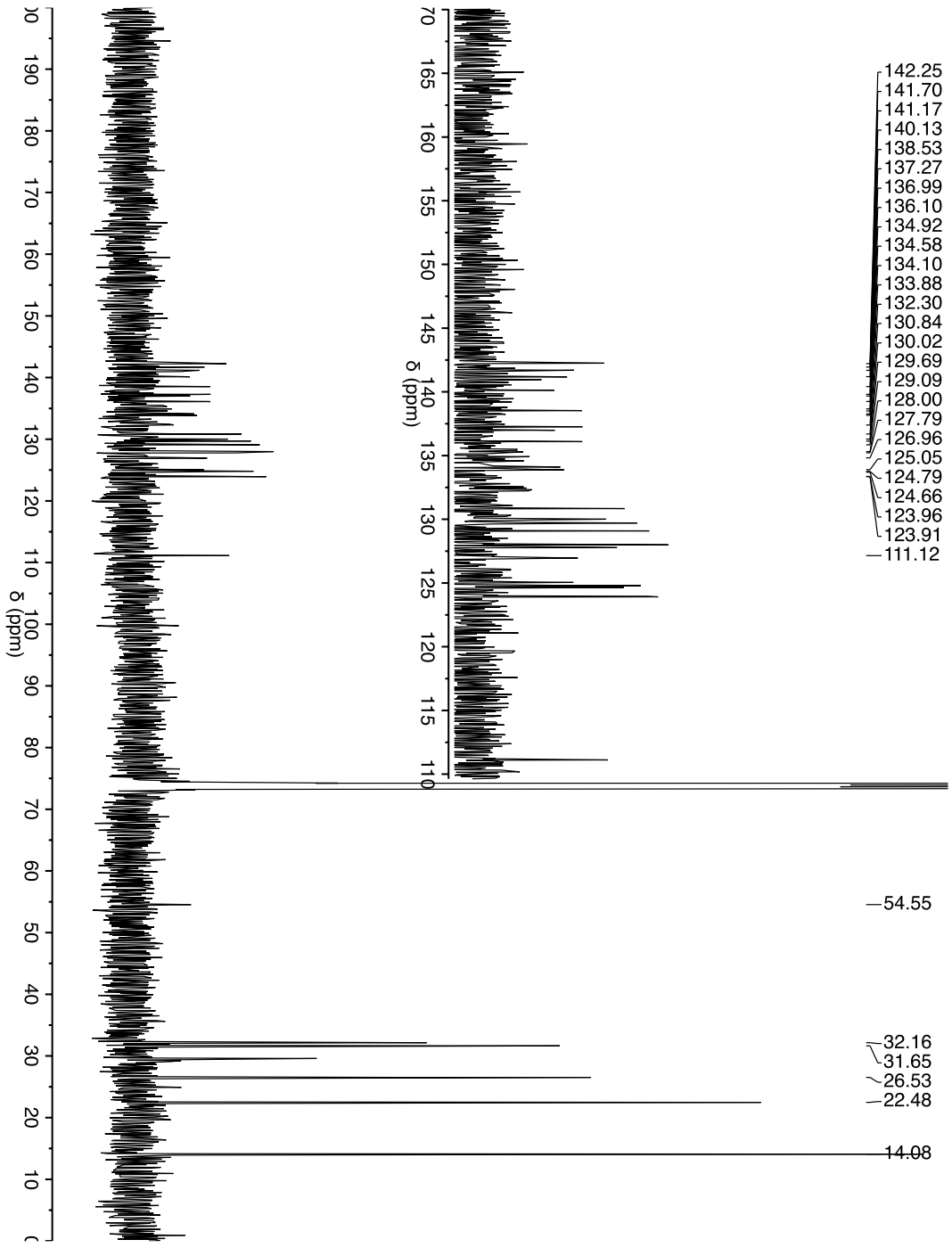
142.25
141.70
141.17
140.13
138.53
137.27
136.99
136.10
134.92
134.58
134.10
133.88
132.30
130.84
130.02
129.69
129.09
128.00
127.79
126.96
125.05
124.79
124.66
123.96
123.91
111.12
54.55
32.16
31.65
26.53
22.48
14.08
δ (ppm)

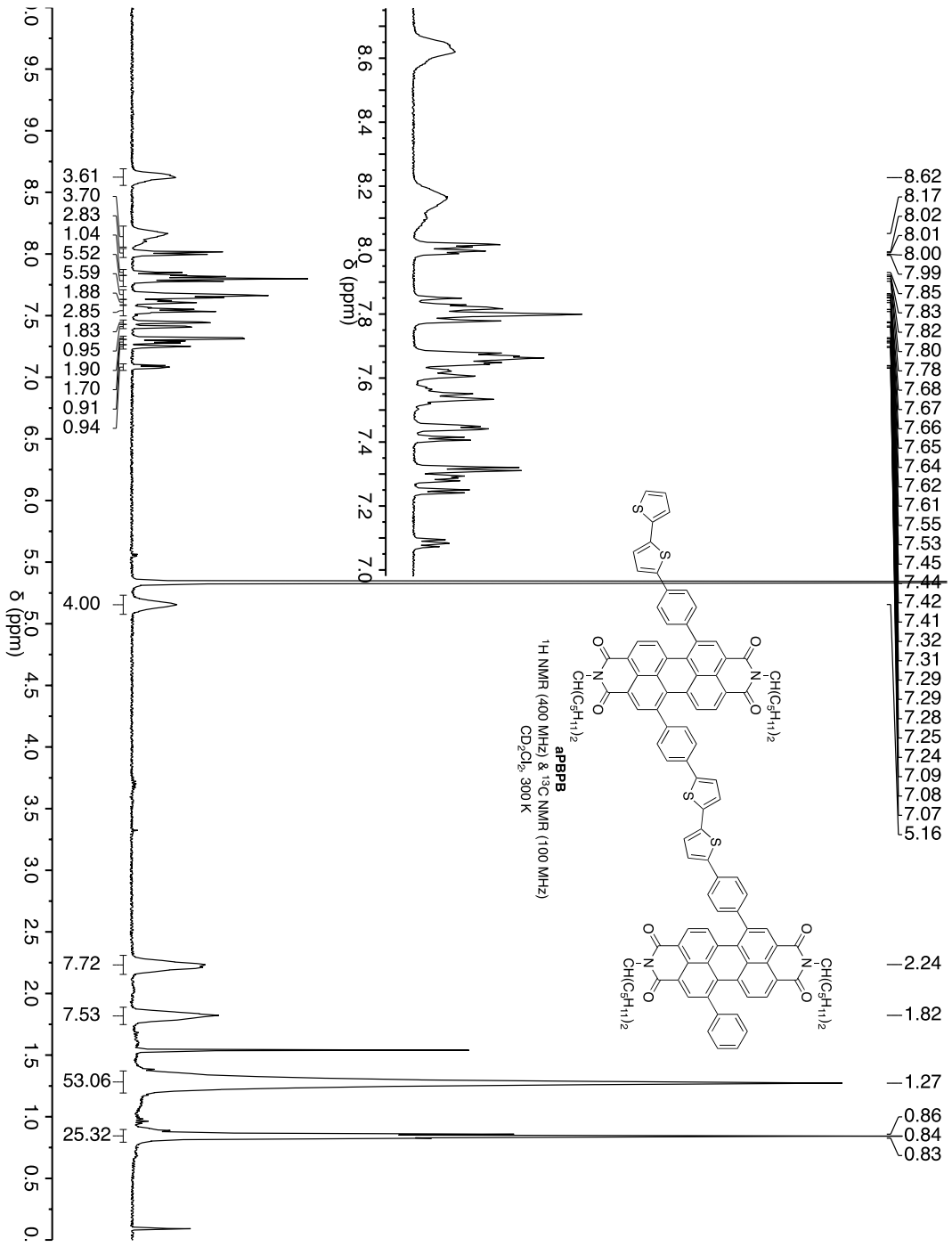
aPBPB
¹H NMR (400 MHz) & ¹³C NMR (100 MHz)
CD2Cl2, 300 K
δ (ppm)
3.61
3.70
2.83
1.04
5.52
5.59
1.88
2.85
1.83
0.95
1.90
1.70
0.91
0.94
4.00
7.72
7.53
53.06
25.32
8.62
8.17
8.02
8.01
8.00
7.99
7.85
7.83
7.82
7.80
7.78
7.68
7.67
7.66
7.65
7.64
7.62
7.61
7.55
7.53
7.45
7.44
7.42
7.41
7.32
7.31
7.29
7.29
7.28
7.25
7.24
7.09
7.08
7.07
5.16
2.24
1.82
1.27
0.86
0.84
0.83

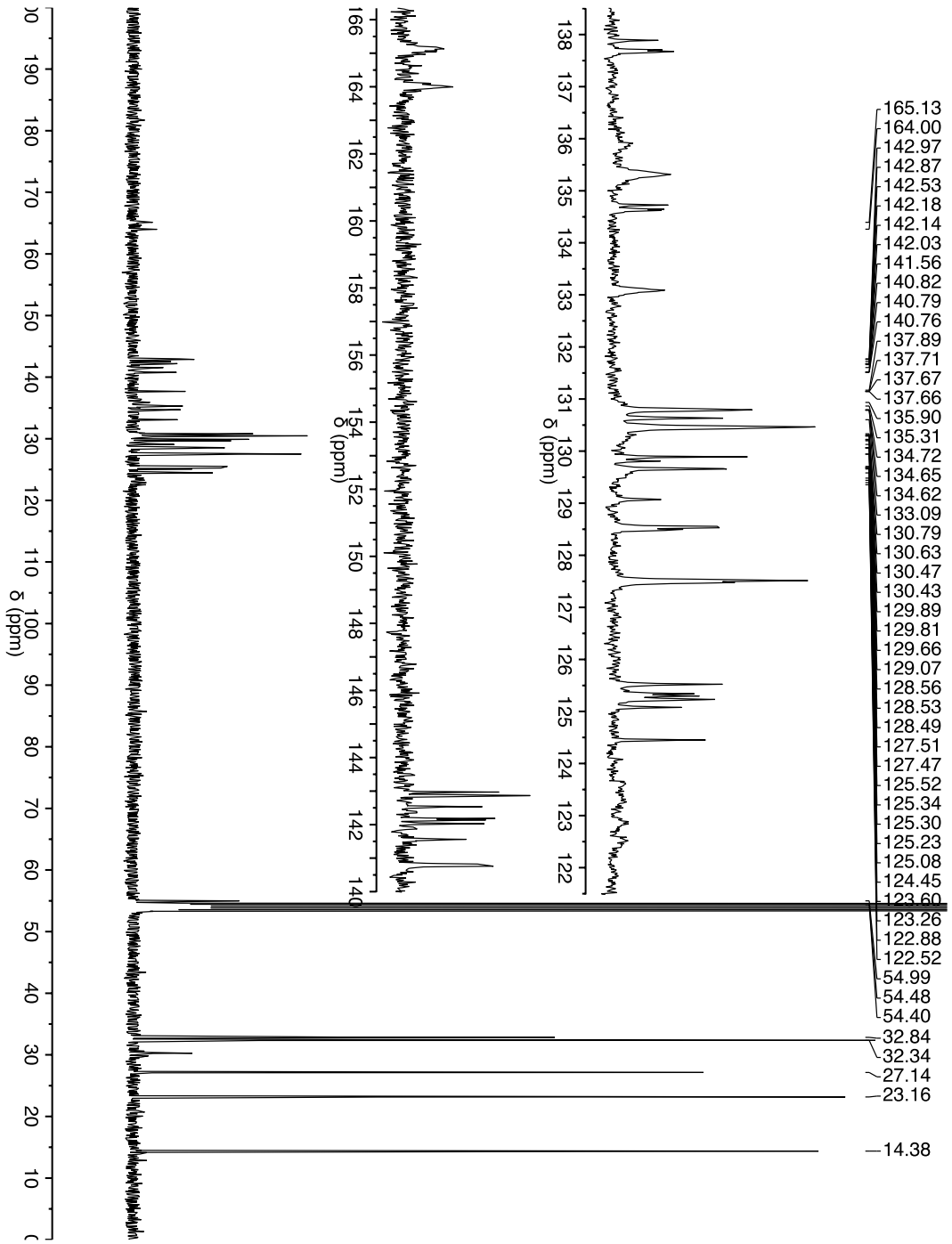
165.13
164.00
142.97
142.87
142.53
142.18
142.14
142.03
141.56
140.82
140.79
140.76
137.89
137.71
137.67
137.66
135.90
135.31
134.72
134.65
134.62
133.09
130.79
130.63
130.47
130.43
129.89
129.81
129.66
129.07
128.56
128.53
128.49
127.51
127.47
125.52
125.34
125.30
125.23
125.08
124.45
123.60
123.26
122.88
122.52
54.99
54.48
54.40
32.84
32.34
27.14
23.16
14.38
δ (ppm)

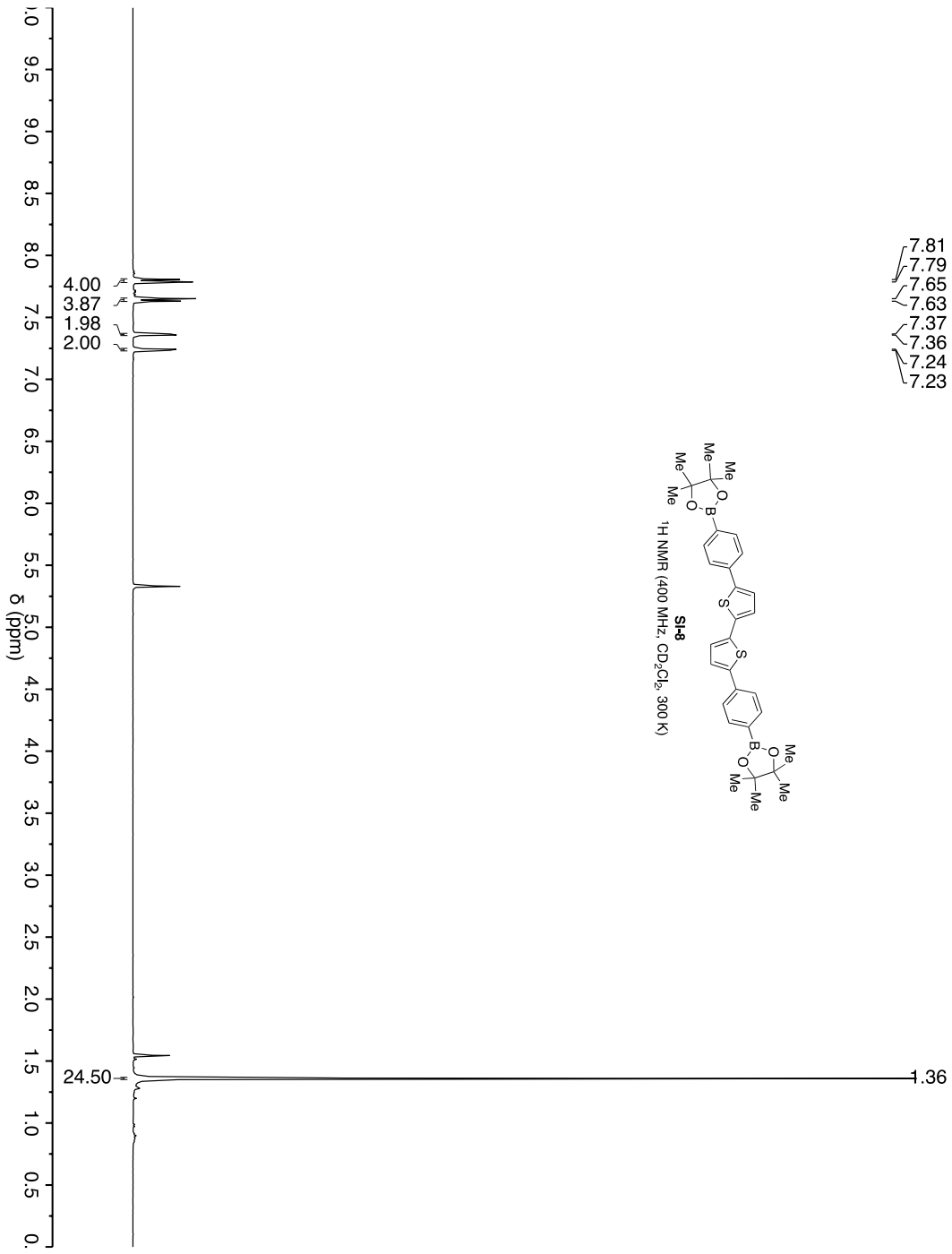
7.81
7.79
7.65
7.63
7.37
7.36
7.24
7.23
4.00
3.87
1.98
2.00
24.50
1.36
δ (ppm)
SI-8
1H NMR (400 MHz, CD2Cl2, 300 K)

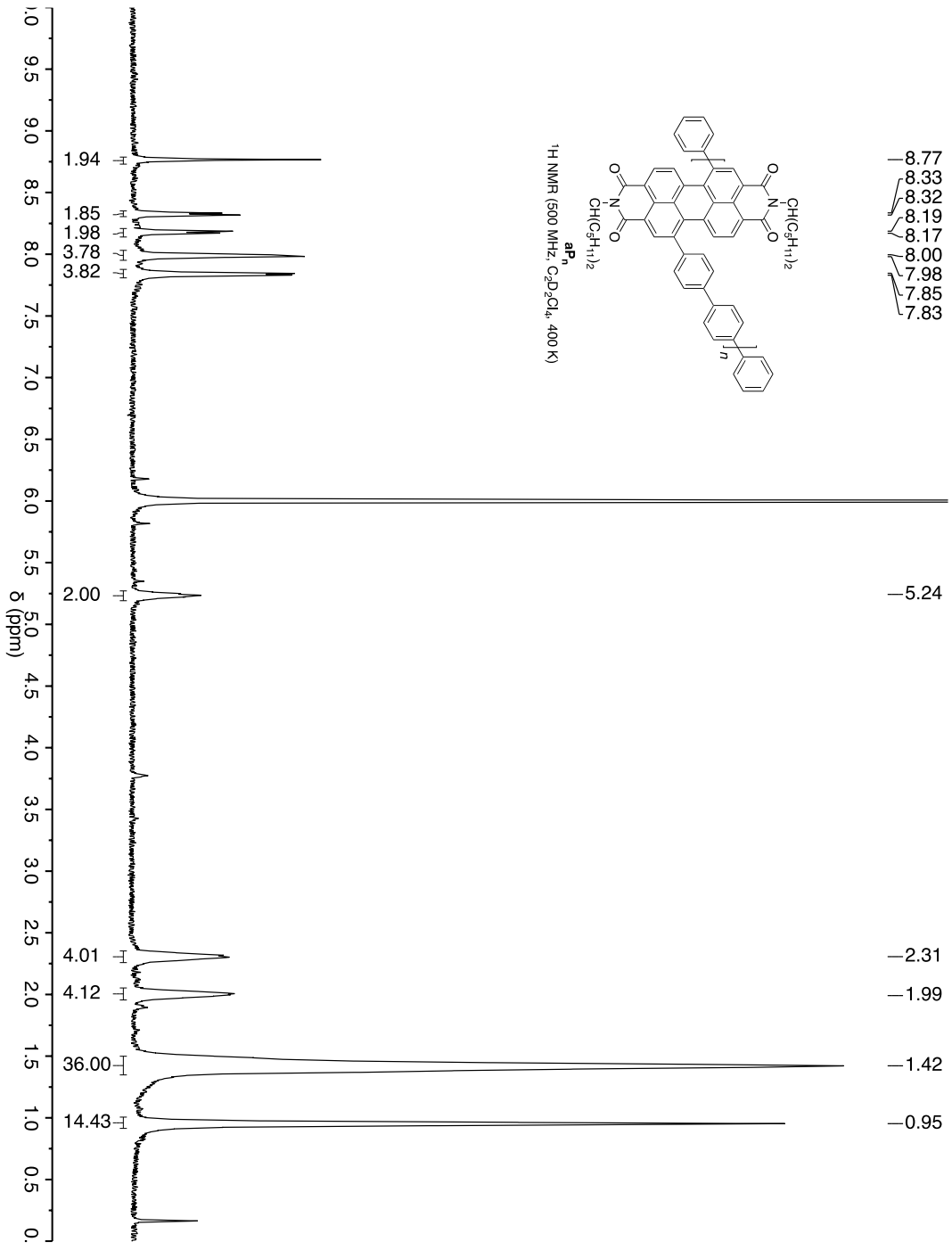
1H NMR (500 MHz, C2D2Cl4, 400 K)
aPn
1.94
1.85
1.98
3.78
3.82
2.00
4.01
4.12
36.00
14.43
8.77
8.33
8.32
8.19
8.17
8.00
7.98
7.85
7.83
5.24
2.31
1.99
1.42
0.95
δ (ppm)

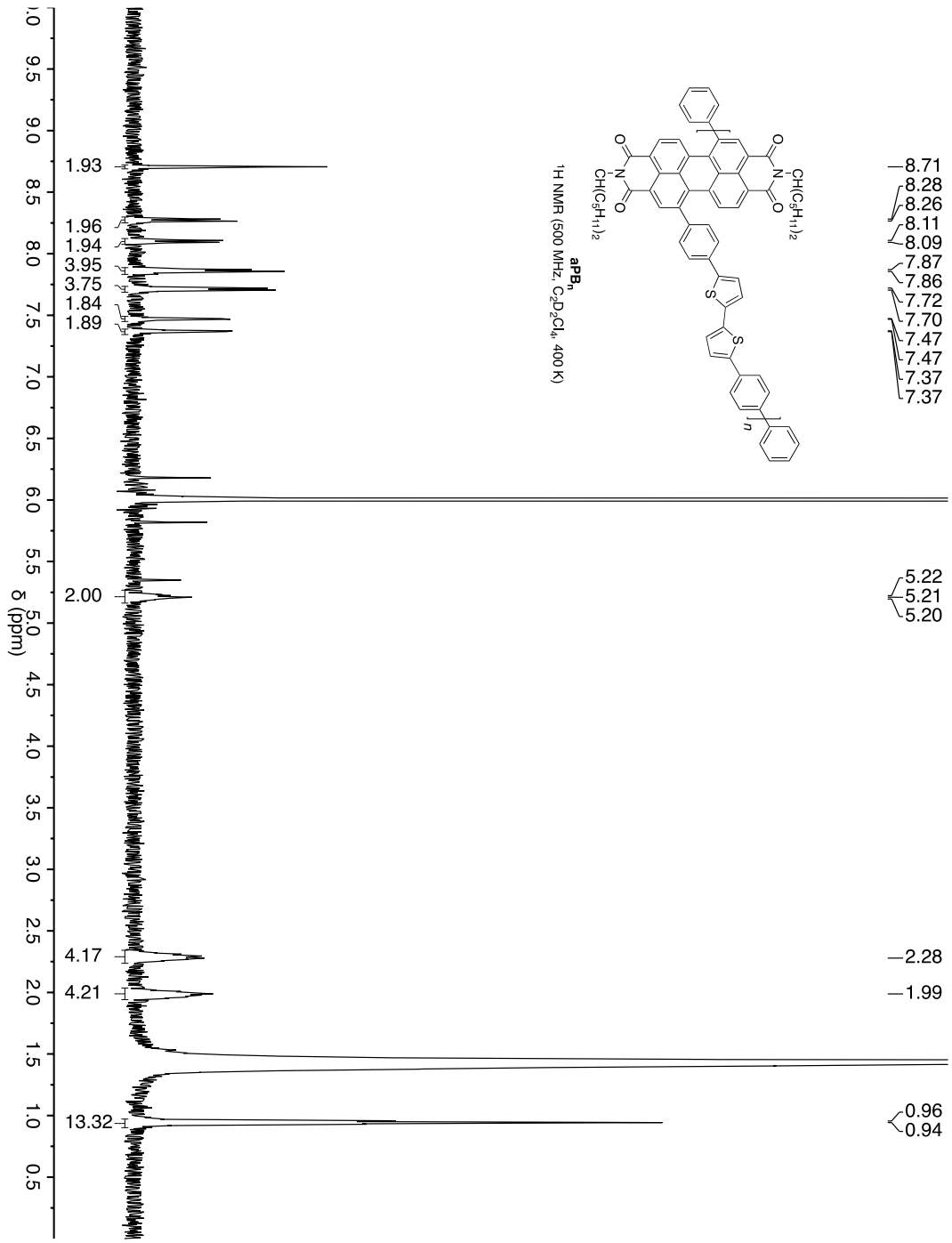
aPB$_n$
^{1}H NMR (500 MHz, $C_2D_2Cl_4$, 400 K)
δ (ppm)
1.93
1.96
1.94
3.95
3.75
1.84
1.89
2.00
4.17
4.21
13.32
8.71
8.28
8.26
8.11
8.09
7.87
7.86
7.72
7.70
7.47
7.47
7.37
7.37
5.22
5.21
5.20
2.28
1.99
0.96
0.94

Appendix B. DFT Computational details

PDI monomer **1**

B3LYP/6-31G** optimized geometry

Final total energy = -1331.141401 h

final geometry:

angstroms

atom	x	y	z
C1	0.0185172219	0.0014776359	-0.0312915642
C2	0.0313191055	-0.0389215840	1.3993347140
C3	1.2633450700	-0.0506666626	2.0576959137
C4	2.4742794465	-0.0377461647	1.3585623814
C5	2.4858541923	-0.0146995138	-0.0242538965
C6	1.2607104698	0.0058693035	-0.7415850508
C7	-1.2459772359	-0.0705242918	2.1277925666
H8	1.3033506382	-0.0683264975	3.1396538394
H9	3.4227113132	-0.0478037667	1.8847533085
C10	3.7846168913	-0.0085915886	-0.7421550589
C11	1.2635527157	0.0305213704	-2.1610343658
C12	0.0659788318	0.0509064564	-2.8521663476
C13	2.5404745053	0.0315461508	-2.9166945814
H14	0.0925023827	0.0653012390	-3.9363456323
C15	-1.1504640302	0.0551750741	-2.1626070128
C16	-1.2085237109	0.0370380427	-0.7676200227

H17	-2.0620695184	0.0706881098	-2.7458603519
C18	-2.4855822699	0.0534659620	-0.0376590467
N19	3.6918492966	0.0125912021	-2.1321430442
O20	4.8730069500	-0.0214473566	-0.1876317932
H21	4.5718408668	0.0148032587	-2.6361989424
C22	-2.4723987164	-0.0139718747	1.3919509732
C23	-3.7141859024	-0.0262582156	2.1021496834
C24	-4.9378769265	0.0446320180	1.3860104676
C25	-4.9269419851	0.1255750872	0.0051361977
C26	-3.7161736516	0.1282670499	-0.6941404867
C27	-3.7181703130	-0.1102182256	3.5195576308
C28	-6.2364874470	0.0351622124	2.1028193272
H29	-5.8752988387	0.1820836508	-0.5179710941
H30	-3.7548281677	0.1942194819	-1.7740748354
C31	-1.3048843053	-0.1550405625	3.5206732651
C32	-2.5214149682	-0.1765442659	4.2094567345
H33	-0.3930547877	-0.2122007724	4.1020863854
H34	-2.5490279136	-0.2445187083	5.2916571646
C35	-4.9957774920	-0.1309449768	4.2733624952
O36	2.6143642610	0.0478962667	-4.1359293095
N37	-6.1457055742	-0.0535960134	3.4904388871
O38	-7.3241178640	0.0976759258	1.5502148252
H39	-7.0260431481	-0.0653508171	3.9938686458

O40 -5.0711582587 -0.2094879266 5.4898475528

Excited State 1: 2.6994 eV 459.30 nm

orbitals in

excitation CI coeff.

---------- ---------

100 => 101 -0.96991

94 => 103 0.17508

Transition dipole moment (debye):

X= -8.6884 Y= 0.1302 Z= 4.8594 Tot= 9.9558

Oscillator strength, f= 1.0146

Excited State 2: 3.1251 eV 396.73 nm

orbitals in

excitation CI coeff.

---------- ---------

99 => 101 0.97083

98 => 102 -0.17960

Transition dipole moment (debye):

X= -0.0037 Y= -0.1387 Z= -0.0042 Tot= 0.1388

Oscillator strength, f= 0.0002

Excited State 3: 3.1289 eV 396.25 nm

orbitals in

excitation CI coeff.

---------- ---------

98 => 101 0.97062

99 => 102 -0.18054

Transition dipole moment (debye):

X= -0.0003 Y= 0.0266 Z= -0.0064 Tot= 0.0274

Oscillator strength, f= 0.0000

Excited State 4: 3.4294 eV 361.53 nm

orbitals in

excitation CI coeff.

---------- ---------

93 => 101 0.10618

94 => 101 -0.33554

97 => 101 -0.87400

100 => 104 -0.30823

Transition dipole moment (debye):

X= 0.0005 Y= 0.0283 Z= 0.0055 Tot= 0.0288

Oscillator strength, f= 0.0000

Excited State 5: 3.5705 eV 347.25 nm

orbitals in

excitation CI coeff.

---------- ---------

95 => 101 -0.66920

100 => 102 -0.73884

Transition dipole moment (debye):

X= -0.0001 Y= 0.0023 Z= 0.0090 Tot= 0.0092

Oscillator strength, f= 0.0000

Excited State 6: 3.6034 eV 344.08 nm

orbitals in

excitation CI coeff.

---------- ---------

94 => 101 0.76923

97 => 101 -0.24946

100 => 103 -0.55760

100 => 104 -0.16984

Transition dipole moment (debye):

X= -0.0019 Y= 0.0099 Z= -0.0018 Tot= 0.0102

Oscillator strength, f= 0.0000

Excited State 7: 3.6759 eV 337.29 nm

orbitals in

excitation CI coeff.

---------- ---------

96 => 101 -0.91942

95 => 104 0.12891

100 => 105 0.33428

Transition dipole moment (debye):

X= 0.8005 Y= -0.0292 Z= 1.4234 Tot= 1.6333

Oscillator strength, f= 0.0372

Excited State 8: 3.6998 eV 335.11 nm

orbitals in

excitation CI coeff.

--- ---

91 => 101 0.96630

90 => 102 0.18578

99 => 103 0.12397

Transition dipole moment (debye):

X= -0.0218 Y= 0.0001 Z= 0.0172 Tot= 0.0277

Oscillator strength, f= 0.0000

Excited State 9: 3.7118 eV 334.03 nm

orbitals in

excitation CI coeff.

--- ---

90 => 101 0.96495

91 => 102 0.18882

98 => 103 -0.12787

Transition dipole moment (debye):

X= 0.0016 Y= 0.0012 Z= 0.0054 Tot= 0.0058

Oscillator strength, f= 0.0000

Excited State 10: 3.7629 eV 329.49 nm

orbitals in

excitation CI coeff.

---

93 => 101 0.37506

94 => 101 -0.44178

100 => 103 -0.72690

100 => 104 0.33369

Transition dipole moment (debye):

X= -0.0121 Y= -0.0098 Z= -0.0175 Tot= 0.0234

Oscillator strength, f= 0.0000

Excited State 11: 4.0200 eV 308.42 nm

orbitals in

excitation CI coeff.

---

93 => 101 0.78458

97 => 101 0.25052

100 => 103 0.15046

100 => 104 -0.50766

Transition dipole moment (debye):

X= -0.1813 Y= 0.0257 Z= -0.3275 Tot= 0.3752

Oscillator strength, f= 0.0021

Excited State 12: 4.0292 eV 307.72 nm

orbitals in

excitation CI coeff.

--- ---

92 => 101 0.93624

96 => 101 -0.13340

100 => 105 -0.24551

Transition dipole moment (debye):

X= -0.9079 Y= 0.0326 Z= -1.6285 Tot= 1.8648

Oscillator strength, f= 0.0531

Excited State 13: 4.1583 eV 298.16 nm

orbitals in

excitation CI coeff.

--- ---

95 => 101 -0.70006

100 => 102 0.62703

88 => 103 -0.14929

96 => 104 -0.17088

97 => 105 0.14657

94 => 107 0.13788

Transition dipole moment (debye):

X= 0.0102 Y= -0.0172 Z= -0.0049 Tot= 0.0206

Oscillator strength, f= 0.0000

Excited State 14: 4.4661 eV 277.61 nm

orbitals in

excitation CI coeff.

---------- ---------

93 => 101 0.44307

94 => 101 0.26891

97 => 101 -0.25947

92 => 102 0.19753

96 => 102 0.17430

100 => 103 0.31572

100 => 104 0.66180

Transition dipole moment (debye):

X= -0.0002 Y= 0.1190 Z= -0.0065 Tot= 0.1192

Oscillator strength, f= 0.0002

Excited State 15: 4.7017 eV 263.70 nm

orbitals in

excitation CI coeff.

---------- ---------

98 => 101 -0.21387

98 => 102 0.18185

99 => 102 -0.91193

90 => 103 -0.14179

98 => 106 -0.21128

Transition dipole moment (debye):

X= -0.0017 Y= 0.0106 Z= -0.0018 Tot= 0.0109

Oscillator strength, f= 0.0000

Excited State 16: 4.7052 eV 263.51 nm

orbitals in

excitation CI coeff.

---------- ---------

99 => 101 0.21295

98 => 102 0.91154

99 => 102 0.18189

91 => 103 -0.14335

99 => 106 0.21258

90 => 107 0.10039

Transition dipole moment (debye):

X= 0.0003 Y= 0.0982 Z= -0.0026 Tot= 0.0983

Oscillator strength, f= 0.0002

Excited State 17: 4.8082 eV 257.86 nm

orbitals in

excitation CI coeff.

--- ---

92 => 101 -0.20936

96 => 101 -0.20822

93 => 102 -0.18566

94 => 102 0.12134

97 => 102 0.58777

100 => 105 -0.69665

Transition dipole moment (debye):

X= 1.1652 Y= -0.0437 Z= 2.0826 Tot= 2.3868

Oscillator strength, f= 0.1039

Excited State 18: 4.8671 eV 254.74 nm

orbitals in

excitation CI coeff.

---

91 => 101 -0.19217

90 => 102 0.24050

99 => 103 0.90199

98 => 107 0.23661

Transition dipole moment (debye):

X= -0.0229 Y= 0.0000 Z= 0.0088 Tot= 0.0246

Oscillator strength, f= 0.0000

Excited State 19: 4.8779 eV 254.17 nm

orbitals in

excitation CI coeff.

---

90 => 101 -0.19891

91 => 102 0.23515

98 => 103 -0.90769

99 => 107 -0.23612

Transition dipole moment (debye):

X= 0.0009 Y= 0.0007 Z= 0.0010 Tot= 0.0016

Oscillator strength, f= 0.0000

Excited State 20: 5.0342 eV 246.28 nm

orbitals in

excitation CI coeff.

---------- ---------

88 => 101 0.53597

94 => 102 0.28804

97 => 102 0.14531

95 => 103 0.30692

100 => 107 0.69716

Transition dipole moment (debye):

X= -0.4051 Y= 0.0155 Z= -0.6977 Tot= 0.8069

Oscillator strength, f= 0.0124

Excited State 21: 5.0778 eV 244.17 nm

orbitals in

excitation CI coeff.

---------- ---------

89 => 101 -0.37048

94 => 103 0.11237

97 => 103 -0.60853

94 => 104 -0.29175

100 => 106 -0.60576

Transition dipole moment (debye):

X= 0.7102 Y= -0.0103 Z= -0.3938 Tot= 0.8122

Oscillator strength, f= 0.0127

Excited State 22: 5.0966 eV 243.27 nm

orbitals in

excitation CI coeff.

---

88 => 101 0.14726

93 => 102 -0.12134

94 => 102 0.54485

97 => 102 -0.61016

95 => 103 0.20003

95 => 104 0.23557

100 => 105 -0.34724

100 => 107 -0.21208

Transition dipole moment (debye):

X= 0.8397 Y= -0.0315 Z= 1.5000 Tot= 1.7193

Oscillator strength, f= 0.0571

Excited State 23: 5.1922 eV 238.79 nm

orbitals in

excitation CI coeff.

---

89 => 101 0.49608

97 => 103 -0.66124

94 => 104 -0.22223

100 => 106 0.49674

Transition dipole moment (debye):

X= -0.8780 Y= 0.0121 Z= 0.5125 Tot= 1.0167

Oscillator strength, f= 0.0204

Excited State 24: 5.1959 eV 238.62 nm

orbitals in

excitation CI coeff.

--- ---

96 => 102 -0.95322

100 => 104 0.13413

95 => 105 -0.15722

Transition dipole moment (debye):

X= -0.0052 Y= 0.0393 Z= 0.0198 Tot= 0.0443

Oscillator strength, f= 0.0000

Excited State 25: 5.2268 eV 237.21 nm

orbitals in

excitation CI coeff.

--- ---

88 => 101 0.29874

94 => 102 -0.42619

97 => 102 -0.35410

95 => 103 -0.58462

95 => 104 0.23584

100 => 105 -0.22533

100 => 107 0.34411

Transition dipole moment (debye):

X= 0.6531 Y= -0.0240 Z= 1.1414 Tot= 1.3152

Oscillator strength, f= 0.0343

PDI closed-dimer **2**

B3LYP/6-31G** optimized geometry

Final total energy = -2736.131816 h

final geometry:

angstroms

atom	x	y	z
N1	0.2349333162	1.6389793712	0.0409466655
C2	0.2334069181	1.5981921712	1.4355274757
C3	1.5047901570	1.1444678691	2.0539894584
C4	2.5994238069	0.7666763869	1.2465945118
C5	2.5079912956	0.8083352577	-0.1771280618
C6	1.2671534861	1.3045999827	-0.8334696325
C7	3.5635893437	0.4143921410	-0.9603738609
C8	4.7970101149	-0.0277080397	-0.3980564232

C9	4.9391383031	0.0253106999	1.0130915353
C10	3.8277068703	0.3713609898	1.8484201867
C11	3.9338226828	0.3367998931	3.2728215766
C12	5.1971864528	-0.0901424325	3.8819351048
C13	6.3092108323	-0.3831708287	3.0354858573
C14	6.2026134778	-0.2804252773	1.6112656691
C15	7.3440738152	-0.4578506596	0.7902624109
C16	8.5472886716	-0.9146022551	1.4025707495
C17	8.6495795131	-1.0812589138	2.7603636849
C18	7.5476871331	-0.7793515357	3.6154495334
C19	5.3655070065	-0.2106735923	5.2692457843
C20	6.5774957563	-0.6098601963	5.8288385408
C21	7.6670834932	-0.8980753503	5.0162014441
C22	8.9438341849	-1.3431744640	5.6289427793
N23	9.9585714508	-1.6550272147	4.7241334676
C24	9.9258654933	-1.5899337896	3.3328108492
C25	1.6229845156	1.1109227567	3.4382832137
C26	2.8166654962	0.7095872774	4.0350829313
O27	10.8907421853	-1.9259181237	2.6653135176
O28	9.1236130507	-1.4511184630	6.8316339736
O29	-0.7557326426	1.9300317308	2.0695276972
O30	1.1284920228	1.4194355283	-2.0405185205
C31	7.2281355792	-0.3058765526	-0.6468999957

H32	9.4032362966	-1.1990218028	0.8052502831
H33	6.6933225181	-0.7056776430	6.9030451083
H34	4.5411657235	0.0041633103	5.9371893271
H35	10.8286687384	-1.9804163796	5.1312672091
H36	0.7689948983	1.4073466374	4.0378809066
H37	2.8687654168	0.6978736743	5.1167639618
H38	3.4418635835	0.5171575991	-2.0298261381
H39	-0.6221886868	1.9659724555	-0.3918864016
C40	5.9405481108	-0.3655511298	-1.2268789223
C41	8.3677420991	-0.0826535744	-1.5148409936
C42	9.5865977949	0.4719607736	-1.0257669727
C43	10.6466235664	0.7350115627	-1.8555484020
C44	10.5723297580	0.4394811257	-3.2493978838
C45	9.3535694827	-0.0640249628	-3.7856086629
C46	8.2364740681	-0.2725075989	-2.9139223789
C47	9.2644487374	-0.3495559289	-5.1821306904
C48	10.3911170359	-0.1148481129	-5.9846109597
C49	11.5760632118	0.3904689959	-5.4538837533
C50	11.6757428964	0.6723179212	-4.0969588373
C51	12.9376897309	1.2345062539	-3.5542170005
N52	12.9179576061	1.5270931747	-2.1906579879
C53	11.8749364337	1.3512007557	-1.2843251348
O54	11.9950654582	1.6843086392	-0.1163693738

H55	13.7685079436	1.9305798960	-1.8133652456
O56	13.9345967407	1.4497688951	-4.2252517895
H57	12.4377153848	0.5764723936	-6.0859479132
H58	10.3537859774	-0.3207844273	-7.0471933329
C59	8.0105529556	-0.8813909693	-5.7200501489
C60	6.8905399876	-1.0333103555	-4.8464658614
C61	6.9810046119	-0.6914440396	-3.4580662699
C62	5.8343578299	-0.7450851957	-2.6242280327
H63	9.6921666980	0.7610349791	0.0110815288
C64	4.6413447387	-1.3067530610	-3.1661675741
C65	4.5531306736	-1.6944955133	-4.4795274521
C66	5.6617172101	-1.5321106652	-5.3639130348
C67	5.5601075936	-1.8879616252	-6.7261251840
C68	6.6572161335	-1.7364935524	-7.5657397308
C69	7.8597933672	-1.2392417806	-7.0684287476
C70	3.2851257293	-2.2994617978	-4.9723618069
N71	3.2695830972	-2.5988240472	-6.3334255809
C72	4.2935190383	-2.4385242520	-7.2679849093
O73	2.3131098908	-2.5232620829	-4.2692406660
H74	2.4051894753	-2.9930765447	-6.6889096501
O75	4.1271729224	-2.7497958812	-8.4367158782
H76	6.5534083185	-2.0159852988	-8.6085717770
H77	8.6913976921	-1.1365328695	-7.7536831566

H78 3.7800143323 -1.4960353240 -2.5401249372

Excited State 1: 2.2459 eV 552.04 nm

orbitals in

excitation CI coeff.

---------- ---------

204 => 205 0.94595

203 => 206 -0.25816

202 => 207 -0.14262

Transition dipole moment (debye):

X= -4.9986 Y= -2.0531 Z= -2.5481 Tot= 5.9745

Oscillator strength, f= 0.3040

Excited State 2: 2.3921 eV 518.32 nm

orbitals in

excitation CI coeff.

---------- ---------

203 => 205 -0.73551

204 => 206 0.67292

Transition dipole moment (debye):

X= 0.0467 Y= -0.1478 Z= 0.0403 Tot= 0.1602

Oscillator strength, f= 0.0002

Excited State 3: 2.5355 eV 488.99 nm

orbitals in

excitation CI coeff.

---------- ---------

202 => 205 -0.92159

204 => 207 -0.35532

Transition dipole moment (debye):

X= 2.3655 Y= 0.2246 Z= -5.1217 Tot= 5.6461

Oscillator strength, f= 0.3065

Excited State 4: 2.8000 eV 442.80 nm

orbitals in

excitation CI coeff.

---------- ---------

203 => 205 0.65377

204 => 206 0.71643

Transition dipole moment (debye):

X= -1.3164 Y= 3.8626 Z= -0.3514 Tot= 4.0959

Oscillator strength, f= 0.1781

Excited State 5: 2.9259 eV 423.75 nm

orbitals in

excitation CI coeff.

---------- ---------

202 => 206 0.93544

203 => 207 0.30238

204 => 213 0.10395

Transition dipole moment (debye):

X= 0.0895 Y= 0.0938 Z= 0.0791 Tot= 0.1519

Oscillator strength, f= 0.0003

Excited State 6: 3.0005 eV 413.21 nm

orbitals in

excitation CI coeff.

---------- ---------

204 => 205 0.20254

203 => 206 0.93122

202 => 207 -0.19890

Transition dipole moment (debye):

X= -6.3342 Y= -2.5422 Z= -3.1479 Tot= 7.5162

Oscillator strength, f= 0.6428

Excited State 7: 3.1504 eV 393.55 nm

orbitals in

excitation CI coeff.

---------- ---------

199 => 205 0.16328

200 => 205 0.11905

201 => 205 -0.88240

198 => 206 0.10238

199 => 206 -0.19381

201 => 206 0.28037

Transition dipole moment (debye):

X= 0.1964 Y= 0.0468 Z= 0.0306 Tot= 0.2042

Oscillator strength, f= 0.0005

Excited State 8: 3.1544 eV 393.05 nm

orbitals in

excitation CI coeff.

---------- ---------

199 => 205 0.13056

200 => 205 0.89144

201 => 205 0.14577

198 => 206 0.26133

199 => 206 0.22180

200 => 208 0.10543

Transition dipole moment (debye):

X= 0.1452 Y= 0.0647 Z= -0.0509 Tot= 0.1669

Oscillator strength, f= 0.0003

Excited State 9: 3.1560 eV 392.85 nm

orbitals in

excitation CI coeff.

---------- ---------

198 => 205 -0.10418

199 => 205 -0.87844

200 => 205 0.15387

201 => 205 -0.13410

198 => 206 0.16857

199 => 206 -0.13848

200 => 206 -0.20543

201 => 206 -0.19977

198 => 208 -0.11149

Transition dipole moment (debye):

X= -0.1909 Y= -0.0976 Z= -0.1717 Tot= 0.2747

Oscillator strength, f= 0.0009

Excited State 10: 3.1614 eV 392.18 nm

orbitals in

excitation CI coeff.

---------- ---------

198 => 205 -0.89643

198 => 206 -0.12140

199 => 206 0.15259

200 => 206 -0.29390

199 => 208 -0.12576

Transition dipole moment (debye):

X= -0.0457 Y= -0.0028 Z= 0.0187 Tot= 0.0495

Oscillator strength, f= 0.0000

Excited State 11: 3.3458 eV 370.56 nm

orbitals in

excitation CI coeff.

--- ---

202 => 205 -0.32815

204 => 207 0.90642

204 => 209 0.15503

Transition dipole moment (debye):

X= 4.0379 Y= 0.4106 Z= -8.4040 Tot= 9.3328

Oscillator strength, f= 1.1051

Excited State 12: 3.4567 eV 358.68 nm

orbitals in

excitation CI coeff.

--- ---

189 => 205 0.10983

194 => 205 -0.36480

197 => 205 -0.84541

196 => 206 -0.20408

204 => 212 0.23144

Transition dipole moment (debye):

X= -1.0750 Y= -0.4387 Z= -0.5341 Tot= 1.2780

Oscillator strength, f= 0.0214

Excited State 13: 3.4683 eV 357.47 nm

orbitals in

excitation CI coeff.

---

191 => 205 0.17995

196 => 205 -0.92179

194 => 206 -0.20815

197 => 206 -0.12674

204 => 211 -0.15826

Transition dipole moment (debye):

X= -0.1082 Y= 0.0471 Z= -0.0006 Tot= 0.1180

Oscillator strength, f= 0.0002

Excited State 14: 3.5517 eV 349.09 nm

orbitals in

excitation CI coeff.

---------- ---------

188 => 205 -0.19468

192 => 205 -0.10544

195 => 205 -0.68082

202 => 206 0.20276

203 => 207 -0.63620

Transition dipole moment (debye):

X= -0.0270 Y= 0.0184 Z= 0.0251 Tot= 0.0412

Oscillator strength, f= 0.0000

Excited State 15: 3.5629 eV 347.99 nm

orbitals in

excitation CI coeff.

---------- ---------

194 => 205 0.82660

197 => 205 -0.36747

191 => 206 -0.10130

196 => 206 0.18333

204 => 210 -0.29873

203 => 211 0.10736

204 => 212 0.10991

Transition dipole moment (debye):

X= -0.5578 Y= -0.2167 Z= -0.2095 Tot= 0.6340

Oscillator strength, f= 0.0054

Excited State 16: 3.6147 eV 343.00 nm

orbitals in

excitation CI coeff.

--- ---

192 => 205 -0.56687

193 => 206 -0.15745

204 => 208 -0.78317

203 => 209 -0.13248

Transition dipole moment (debye):

X= -0.0331 Y= -0.0110 Z= 0.0916 Tot= 0.0980

Oscillator strength, f= 0.0001

Excited State 17: 3.6169 eV 342.79 nm

orbitals in

excitation CI coeff.

--- ---

193 => 205 -0.75407

203 => 208 -0.17339

204 => 209 -0.61170

Transition dipole moment (debye):

X= 0.4853 Y= 0.0367 Z= -1.0657 Tot= 1.1715

Oscillator strength, f= 0.0188

Excited State 18: 3.6723 eV 337.62 nm

orbitals in

excitation CI coeff.

--- ---

187 => 205 0.25015

199 => 205 -0.35569

198 => 206 -0.12149

199 => 206 0.29833

200 => 206 0.21985

201 => 206 0.77596

Transition dipole moment (debye):

X= 0.1326 Y= 0.0590 Z= 0.0802 Tot= 0.1658

Oscillator strength, f= 0.0004

Excited State 19: 3.6751 eV 337.36 nm

orbitals in

excitation CI coeff.

--- ---

186 => 205 -0.19656

201 => 205 -0.36435

198 => 206 -0.28487

199 => 206 0.74890

201 => 206 -0.35140

Transition dipole moment (debye):

X= -0.0958 Y= 0.0262 Z= 0.0650 Tot= 0.1187

Oscillator strength, f= 0.0002

Excited State 20: 3.6797 eV 336.94 nm

orbitals in

excitation CI coeff.

---------- ---------

184 => 205 -0.16958

198 => 205 0.37421

198 => 206 -0.12360

199 => 206 0.13028

200 => 206 -0.84371

201 => 206 0.17195

Transition dipole moment (debye):

X= -0.0278 Y= -0.0153 Z= -0.0066 Tot= 0.0324

Oscillator strength, f= 0.0000

PDI trimer - helix conformer **3**

B3LYP/6-31G** optimized geometry

Final total energy = -4141.118852 h

final geometry:

		angstroms	
atom	x	y	z
N1	0.0246020000	0.6836730000	-0.1424350000
C2	-0.0036890000	0.7390980000	1.2510380000
C3	1.3179540000	0.6018380000	1.9135880000
C4	2.4860730000	0.4005500000	1.1483740000
C5	2.4239170000	0.3211690000	-0.2755090000
C6	1.1249850000	0.5065690000	-0.9785840000
O7	0.9961430000	0.5032040000	-2.1917960000
O8	-1.0553380000	0.9011590000	1.8494710000
C9	1.4060120000	0.6880260000	3.2978400000
C10	2.6401100000	0.5807110000	3.9356520000
C11	3.8289880000	0.3910110000	3.2149910000
C12	3.7527270000	0.3046250000	1.7913150000
C13	4.9305570000	0.1223330000	0.9966440000
C14	4.8348920000	-0.0686670000	-0.4058600000
C15	3.5550720000	0.0858080000	-1.0155550000
C16	5.1349600000	0.2650580000	3.8657150000
C17	6.3029440000	0.1332020000	3.0557600000

C18	6.2137800000	0.1096560000	1.6268190000
C19	7.3873340000	0.0852380000	0.8311410000
C20	8.6382660000	-0.0867540000	1.4906470000
C21	8.7352640000	-0.1300660000	2.8570570000
C22	7.5782400000	0.0189330000	3.6777420000
C23	7.6853780000	0.0191410000	5.0841610000
C24	6.5413220000	0.1505780000	5.8613030000
C25	5.2909770000	0.2740690000	5.2595710000
C26	9.0087510000	-0.1381840000	5.7391070000
N27	10.0834980000	-0.3167620000	4.8673780000
C28	10.0698220000	-0.3509140000	3.4742450000
O29	11.0951400000	-0.5438320000	2.8408740000
O30	9.1788510000	-0.1297310000	6.9479450000
C31	6.0384160000	-0.2719830000	-1.1894730000
C32	7.2815500000	0.0741230000	-0.6135710000
C33	8.3984750000	0.3817680000	-1.4926510000
C34	9.5015200000	1.1756020000	-1.0790870000
C35	10.5444680000	1.4662330000	-1.9325520000
C36	10.5470640000	0.9809970000	-3.2650340000
C37	9.4324590000	0.2447260000	-3.7352320000
C38	8.3393170000	-0.0152630000	-2.8550230000
C39	9.4206570000	-0.2331180000	-5.0804340000
C40	10.4775470000	0.0940240000	-5.9715220000

C41	11.6041060000	0.7793270000	-5.4432550000
C42	11.6417000000	1.2131670000	-4.1360670000
C43	12.8475410000	1.9321610000	-3.6407800000
N44	12.7410180000	2.4271140000	-2.3408080000
O45	11.7246890000	2.8117670000	-0.3403400000
O46	13.8591630000	2.1076800000	-4.2991960000
C47	7.1848190000	-0.6951540000	-3.3503590000
C48	7.2066270000	-1.2387220000	-4.6694530000
C49	8.3333390000	-1.0461300000	-5.5247740000
C50	8.3853990000	-1.6662210000	-6.8019190000
C51	7.2265680000	-2.3528710000	-7.2537450000
C52	6.1192940000	-2.5145340000	-6.4492030000
C53	6.0979810000	-1.9879120000	-5.1326140000
C54	4.9943980000	-2.1986590000	-4.2684070000
C55	4.9666220000	-1.6372750000	-3.0110870000
C56	6.0303480000	-0.8285370000	-2.5320870000
C57	3.8502970000	-3.0370490000	-4.7145920000
N58	3.9214490000	-3.4695110000	-6.0397680000
C59	4.9390750000	-3.2577130000	-6.9708780000
O60	4.8440560000	-3.6788000000	-8.1116230000
O61	2.8994550000	-3.3300100000	-4.0090800000
C62	9.5557570000	-1.4661960000	-7.6421130000
C63	10.4360150000	-0.4026490000	-7.3370700000

C64	11.2609150000	0.1351930000	-8.4001640000
C65	11.4417320000	-0.6036870000	-9.5973190000
C66	12.2698510000	-0.0964780000	-10.6497690000
C67	12.5461890000	-0.8764910000	-11.8132570000
C68	13.3638430000	-0.3208700000	-12.8083380000
C69	13.8969380000	0.9604970000	-12.6898160000
C70	13.6334700000	1.7302340000	-11.5634790000
C71	14.1905830000	3.1021540000	-11.4629210000
N72	13.8248740000	3.8074210000	-10.3164780000
C73	13.0192020000	3.3830120000	-9.2616630000
O74	12.7591760000	4.1290140000	-8.3318650000
O75	14.9088730000	3.6110890000	-12.3082320000
C76	12.8274400000	1.2074660000	-10.5308160000
C77	12.5321860000	1.9827620000	-9.3698450000
C78	11.7876040000	1.4582630000	-8.3447160000
C79	9.8709000000	-2.3127620000	-8.7755780000
C80	10.8094680000	-1.8767640000	-9.7456700000
C81	11.1178050000	-2.6931450000	-10.8814630000
C82	11.9803980000	-2.2226290000	-11.9171730000
C83	12.2437530000	-3.0723240000	-13.0018620000
C84	11.6964940000	-4.3506880000	-13.0833090000
C85	10.8589690000	-4.8217730000	-12.0798480000
C86	10.5548620000	-3.9966800000	-10.9767710000

C87	9.7101600000	-4.4631810000	-9.9262440000
C88	9.3791140000	-3.6464710000	-8.8761150000
C89	9.1840080000	-5.8533690000	-9.9493920000
N90	9.5184570000	-6.5885450000	-11.0849120000
C91	10.3040620000	-6.1957660000	-12.1684880000
O92	10.5096400000	-6.9567530000	-13.1002440000
O93	8.5028500000	-6.3434010000	-9.0635890000
H94	-0.8701490000	0.7932950000	-0.6074180000
H95	0.4944660000	0.8423970000	3.8650070000
H96	2.6653420000	0.6517910000	5.0159730000
H97	4.4247130000	0.3721060000	5.9012630000
H98	6.6450930000	0.1500180000	6.9409420000
H99	10.9896410000	-0.4456170000	5.3044050000
H100	9.5475510000	-0.2515230000	0.9293620000
H101	3.4457930000	0.0849510000	-2.0918930000
H102	4.1185400000	-1.8791230000	-2.3859870000
H103	3.1285020000	-4.0091420000	-6.3699510000
H104	7.1598020000	-2.7379510000	-8.2618820000
H105	12.4908690000	0.9440580000	-6.0394140000
H106	13.5395150000	2.9537210000	-2.0031590000
H107	9.5391690000	1.6125650000	-0.0905820000
H108	8.7721420000	-4.0786270000	-8.0928110000
H109	11.5611820000	2.1156620000	-7.5160500000

H110 14.1827750000 4.7538620000 -10.2469840000

H111 14.5216940000 1.3812300000 -13.4702580000

H112 13.5937950000 -0.8890020000 -13.7013590000

H113 12.8922440000 -2.7428700000 -13.8043430000

H114 11.9147620000 -5.0008660000 -13.9236150000

H115 9.1489450000 -7.5322210000 -11.1258850000

C116 11.6816910000 2.2923270000 -1.4425770000

Excited State 1: 2.1607 eV 573.80 nm

orbitals in

excitation CI coeff.

---------- ---------

308 => 309 -0.96111

307 => 310 -0.13133

305 => 311 -0.11622

306 => 312 0.16131

Transition dipole moment (debye):

X= 4.1398 Y= 2.6279 Z= 1.3815 Tot= 5.0943

Oscillator strength, f= 0.2127

Excited State 2: 2.2574 eV 549.22 nm

orbitals in

excitation CI coeff.

---------- ---------

306 => 309 0.92715

307 => 309 -0.21264

308 => 312 0.23212

Transition dipole moment (debye):

X= -4.1943 Y= 1.2893 Z= 8.1235 Tot= 9.2329

Oscillator strength, f= 0.7298

Excited State 3: 2.2604 eV 548.52 nm

orbitals in

excitation CI coeff.

--- ---

306 => 309 -0.22629

307 => 309 -0.86782

308 => 310 -0.38284

307 => 311 0.18814

Transition dipole moment (debye):

X= 0.3697 Y= 0.7986 Z= -2.3454 Tot= 2.5050

Oscillator strength, f= 0.0538

Excited State 4: 2.4492 eV 506.22 nm

orbitals in

excitation CI coeff.

--- ---

307 => 309 0.34462

305 => 310 -0.25832

308 => 310 -0.86470

307 => 311 -0.18479

Transition dipole moment (debye):

X= 1.5997 Y= -3.1355 Z= 1.0903 Tot= 3.6850

Oscillator strength, f= 0.1261

Excited State 5: 2.5448 eV 487.21 nm

orbitals in

excitation CI coeff.

--- ---

305 => 309 0.72406

308 => 311 0.67836

Transition dipole moment (debye):

X= -0.7918 Y= -0.5654 Z= -0.3395 Tot= 1.0304

Oscillator strength, f= 0.0102

Excited State 6: 2.5555 eV 485.17 nm

orbitals in

excitation CI coeff.

--- ---

306 => 310 0.95062

307 => 312 -0.22207

308 => 313 0.15056

Transition dipole moment (debye):

X= 0.0721 Y= -0.1156 Z= 0.0486 Tot= 0.1446

Oscillator strength, f= 0.0002

Excited State 7: 2.6547 eV 467.04 nm

orbitals in

excitation CI coeff.

--- ---

305 => 309 -0.30730

307 => 310 0.85588

308 => 311 0.34337

306 => 312 0.19139

Transition dipole moment (debye):

X= 3.7519 Y= 2.4528 Z= 1.5102 Tot= 4.7301

Oscillator strength, f= 0.2252

Excited State 8: 2.7981 eV 443.10 nm

orbitals in

excitation CI coeff.

--- ---

306 => 311 -0.93353

305 => 312 0.24507

308 => 312 0.16063

Transition dipole moment (debye):

X= 0.7406 Y= -0.1403 Z= -1.2816 Tot= 1.4868

Oscillator strength, f= 0.0235

Excited State 9: 2.8331 eV 437.62 nm

orbitals in

excitation CI coeff.

--- ---

307 => 309 0.17599

305 => 310 -0.53148

307 => 311 0.81477

Transition dipole moment (debye):

X= 0.4678 Y= -1.4968 Z= 0.4661 Tot= 1.6360

Oscillator strength, f= 0.0288

Excited State 10: 2.8387 eV 436.76 nm

orbitals in

excitation CI coeff.

--- ---

305 => 309 -0.57496

308 => 309 0.10566

307 => 310 -0.45152

308 => 311 0.61583

Transition dipole moment (debye):

X= -2.7775 Y= -1.6950 Z= -1.1813 Tot= 3.4616

Oscillator strength, f= 0.1290

Excited State 11: 2.8630 eV 433.06 nm

orbitals in

excitation CI coeff.

--- ---

304 => 309 -0.90827

306 => 310 0.13145

307 => 312 0.29146

308 => 313 -0.21688

Transition dipole moment (debye):

X= 0.1011 Y= 0.0814 Z= 0.0067 Tot= 0.1300

Oscillator strength, f= 0.0002

Excited State 12: 2.9602 eV 418.84 nm

orbitals in

excitation CI coeff.

--- ---

307 => 309 -0.15068

305 => 310 -0.78977

308 => 310 0.24183

307 => 311 -0.48461

Transition dipole moment (debye):

X= -2.2617 Y= 4.3531 Z= -1.5051 Tot= 5.1313

Oscillator strength, f= 0.2956

Excited State 13: 3.0235 eV 410.07 nm

orbitals in

excitation CI coeff.

--- ---

306 => 309 0.23716

304 => 310 -0.40475

305 => 312 0.10282

308 => 312 -0.83794

307 => 313 0.18736

Transition dipole moment (debye):

X= -4.1735 Y= 0.9391 Z= 8.3939 Tot= 9.4212

Oscillator strength, f= 1.0177

Excited State 14: 3.1559 eV 392.87 nm

orbitals in

excitation CI coeff.

---

302 => 309 -0.13946

303 => 309 0.77402

303 => 310 -0.50995

303 => 311 0.19690

305 => 311 0.16944

301 => 315 0.11085

Transition dipole moment (debye):

X= 0.4019 Y= 0.1865 Z= 0.1023 Tot= 0.4548

Oscillator strength, f= 0.0025

Excited State 15: 3.1581 eV 392.59 nm

orbitals in

excitation CI coeff.

---

302 => 309 0.76508

303 => 309 0.16912

302 => 310 0.49872

302 => 311 0.19012

305 => 311 -0.14993

300 => 315 -0.11237

Transition dipole moment (debye):

X= -0.4619 Y= -0.2400 Z= 0.1828 Tot= 0.5517

Oscillator strength, f= 0.0036

Excited State 16: 3.1596 eV 392.40 nm

orbitals in

excitation CI coeff.

---

300 => 309 -0.17952

301 => 309 -0.76299

302 => 309 -0.10606

300 => 310 -0.25458

301 => 310 0.41939

304 => 310 0.18047

301 => 311 -0.18435

Transition dipole moment (debye):

X= -0.7828 Y= 0.2134 Z= 1.5698 Tot= 1.7671

Oscillator strength, f= 0.0374

Excited State 17: 3.1632 eV 391.96 nm

orbitals in

excitation CI coeff.

---

300 => 309 -0.77724

301 => 309 0.20750

300 => 310 -0.42485

301 => 310 -0.27669

300 => 311 -0.18871

302 => 315 0.10320

Transition dipole moment (debye):

X= -0.2435 Y= 0.1364 Z= 0.6755 Tot= 0.7309

Oscillator strength, f= 0.0064

Excited State 18: 3.1688 eV 391.27 nm

orbitals in

excitation CI coeff.

--- ---

302 => 309 -0.16950

303 => 309 0.12721

305 => 311 -0.84035

306 => 312 -0.44231

Transition dipole moment (debye):

X= -2.4886 Y= -1.5483 Z= -0.7633 Tot= 3.0287

Oscillator strength, f= 0.1102

Excited State 19: 3.1830 eV 389.53 nm

orbitals in

excitation CI coeff.

---------- ---------

299 => 309 -0.93247

299 => 311 0.29430

298 => 314 0.14017

Transition dipole moment (debye):

X= 0.1139 Y= 0.0234 Z= -0.2967 Tot= 0.3187

Oscillator strength, f= 0.0012

Excited State 20: 3.1914 eV 388.50 nm

orbitals in

excitation CI coeff.

---------- ---------

298 => 309 -0.89806

304 => 310 0.21914

298 => 311 0.27774

308 => 312 -0.13472

299 => 314 0.13536

Transition dipole moment (debye):

X= -1.2609 Y= 0.3372 Z= 2.6031 Tot= 2.9120

Oscillator strength, f= 0.1026

Excited State 21: 3.1970 eV 387.81 nm

orbitals in

excitation CI coeff.

---------- ---------

298 => 309 -0.24784

300 => 309 -0.11518

301 => 309 -0.15123

300 => 310 -0.10854

304 => 310 -0.78579

306 => 311 0.16808

305 => 312 0.14060

308 => 312 0.39216

307 => 313 0.11655

Transition dipole moment (debye):

X= 3.5845 Y= -0.9577 Z= -7.4024 Tot= 8.2802

Oscillator strength, f= 0.8312

Excited State 22: 3.2922 eV 376.61 nm

orbitals in

excitation CI coeff.

---------- ---------

304 => 309 0.24017

306 => 310 0.19058

304 => 311 -0.37659

307 => 312 0.83743

308 => 313 0.11242

Transition dipole moment (debye):

X= 0.0678 Y= -0.0762 Z= 0.0658 Tot= 0.1214

Oscillator strength, f= 0.0002

Excited State 23: 3.4551 eV 358.84 nm

orbitals in

excitation CI coeff.

--- ---

304 => 309 -0.10391

304 => 311 -0.87935

307 => 312 -0.35794

305 => 313 0.12746

308 => 313 -0.17330

Transition dipole moment (debye):

X= -0.0579 Y= 0.0140 Z= -0.0152 Tot= 0.0615

Oscillator strength, f= 0.0000

Excited State 24: 3.4624 eV 358.08 nm

orbitals in

excitation CI coeff.

--- ---

287 => 309 0.10848

295 => 309 -0.34382

297 => 309 0.80371

296 => 310 0.36160

308 => 320 0.15094

Transition dipole moment (debye):

X= 0.2606 Y= -0.5383 Z= 0.1899 Tot= 0.6274

Oscillator strength, f= 0.0052

Excited State 25: 3.5066 eV 353.57 nm

orbitals in

excitation CI coeff.

---------- ---------

285 => 309 -0.11925

293 => 309 0.57801

295 => 309 -0.68254

297 => 309 -0.22342

293 => 311 -0.14558

306 => 313 0.13417

308 => 318 -0.12190

Transition dipole moment (debye):

X= -0.2333 Y= 0.3348 Z= -0.1225 Tot= 0.4260

Oscillator strength, f= 0.0024

PDI trimer **3** waggle conformer

B3LYP/6-31G** optimized geometry

Final total energy = -4141.118908 h

final geometry:

		angstroms	
atom	x	y	z
C1	0.0142343905	0.8648555712	0.1211654257
C2	0.0167817853	0.5896757559	1.5831846265
C3	1.2475219074	0.4284654285	2.2692985920
C4	2.4898842716	0.4726747267	1.5873704942
C5	2.5256909385	0.7485790840	0.1281950866
N6	1.2761114013	0.9076029275	-0.4708669781
C7	1.2401298661	0.2863495627	3.6770829443
C8	2.4798613357	0.1540052022	4.3754188735
C9	3.7081358083	0.0636378550	3.6647470667
C10	3.6758900466	0.2883074701	2.2636758707
C11	2.4744051886	0.0829642623	5.8006302948
C12	1.2292032265	0.0663926143	6.4975401190
C13	-0.0073328932	0.2121168659	5.7995753868
C14	-0.0071523491	0.2778119656	4.3738461222
C15	3.7007535410	0.0699218849	6.5174322292
C16	3.6496435162	-0.1685603033	7.9156039775
C17	2.4512822939	-0.2509706955	8.5895944180

C18	1.2218269664	-0.0787667858	7.9052012178
C19	4.9522433544	-0.0995726332	4.4013007284
C20	4.9538364316	0.1677380661	5.7894162740
C21	6.1956018183	-0.5188377963	3.7838793134
C22	7.4251859379	-0.3156587345	4.4631469331
C23	7.4311920584	0.3023484048	5.7529191626
C24	6.2039598930	0.5418954931	6.4214164939
C25	8.6643123011	-0.7121912431	3.8639794170
C26	8.6475810320	-1.4178189500	2.6279931283
C27	7.3919847555	-1.7139803022	2.0182059263
C28	6.2184308709	-1.2681044898	2.5712286526
C29	7.3383124407	-2.5315127478	0.7755081267
N30	8.5795225492	-2.8935176294	0.2571405311
C31	9.8457449275	-2.6160090270	0.7713020358
C32	9.8568512064	-1.8436411526	2.0385505225
C33	9.9143611712	-0.4175568164	4.4881075995
C34	11.0909989760	-0.8497936475	3.8587744060
C35	11.0669872283	-1.5544695145	2.6574456664
C36	8.6767230953	0.6577827123	6.3639843653
C37	9.9217287667	0.3254120054	5.7498066818
C38	8.6720828672	1.3575488770	7.6034050430
C39	9.8885969760	1.7418539033	8.2058884595
C40	11.0942881071	1.4181300023	7.5951178019

C41	11.1061344700	0.7183357816	6.3906389339
C42	7.4214623204	1.6892927810	8.2045124668
C43	6.2397649155	1.2845468632	7.6380790727
C44	9.8905957421	2.5063836117	9.4782163164
N45	8.6289918000	2.8195495817	9.9840634090
C46	7.3816546582	2.4991035410	9.4528646521
C47	-0.0183744887	-0.1077212587	8.5906269668
C48	-0.0546106334	-0.3882864109	10.0493481109
N49	1.1942395891	-0.5673821659	10.6450550558
C50	2.4549463918	-0.5381658656	10.0476590659
C51	-1.2001696751	0.1050913490	7.9164022726
C52	-1.2273430993	0.3313236669	6.5153493139
C53	-1.1826068475	0.5203036896	2.2586792687
C54	-1.2383739401	0.3052558421	3.6612945464
O55	10.8516385527	-3.0057986031	0.2004732093
O56	6.3046950839	-2.8724741680	0.2243615891
O57	10.9032257411	2.8612782554	10.0597246285
O58	6.3539592178	2.8670674385	9.9976948563
O59	-1.0795876726	-0.4689153416	10.7050677937
O60	3.4634782304	-0.7419869789	10.7020536149
O61	3.5506569481	0.8417419274	-0.5259730980
O62	-0.9945673699	1.0504776117	-0.5383450510
H63	5.3292100603	1.6090988180	8.1224558526

H64	12.0172687578	1.7243412110	8.0751533381
H65	12.0653923480	0.4852031280	5.9465009832
H66	8.6185764578	3.3580148000	10.8435765980
H67	11.9838098936	-1.8920881269	2.1867933814
H68	12.0532193152	-0.6452552731	4.3105386156
H69	5.3009411033	-1.5686253029	2.0829913964
H70	8.5596914852	-3.4381658409	-0.5982212664
H71	1.1833082442	-0.7614784569	11.6405897930
H72	-2.1128686056	0.0357158135	8.4921026989
C73	-2.4648739069	0.5414705669	5.7852330812
H74	4.5502812054	-0.3407092306	8.4890848498
H75	1.2873233297	1.0959873324	-1.4675836057
H76	-2.0803409802	0.6902163247	1.6805116779
H77	4.5863074735	0.3742469928	1.6868948783
C78	-2.4931254658	0.2639860875	4.3987889470
C79	-3.6722931468	1.0264019738	6.4204867001
C80	-4.9211311231	0.8780030048	5.7674270848
C81	-3.6322020630	1.7813828516	7.6283935539
C82	-4.9768628773	0.2575250750	4.4807425931
C83	-3.7736697660	-0.0454594541	3.7896820574
C84	-6.2508679089	-0.0393450326	3.8969680642
C85	-3.8728553638	-0.7867750622	2.5754206677
C86	-7.4668094447	0.3485881322	4.5381731828

C87	-6.3045493104	-0.7410925337	2.6603076965
C88	-8.6814632269	0.0108885459	3.9243169595
C89	-7.4023154775	1.0858709962	5.8007555402
C90	-6.1275424124	1.3279462978	6.3941676695
C91	-8.5455072523	1.5585041396	6.4620904519
C92	-6.0528246281	2.0281017659	7.6307025952
C93	-5.0843972828	-1.1353267804	2.0340929081
H94	-2.9898224682	-1.1587651532	2.0746370018
C95	-5.1131061901	-1.9535542353	0.7906851026
C96	-7.5510272251	-1.0692106378	2.0869919569
C97	-4.7723096612	2.2739909854	8.2083130252
H98	-2.6916193303	2.0434746721	8.0939226313
C99	-4.6530658604	3.0847710774	9.4482985922
C100	-7.2283264266	2.4965628006	8.2536563853
C101	-8.7264768020	-0.6892065683	2.7216819601
C102	-7.6194330286	-1.8363720521	0.8199800924
H103	-9.6723910466	-0.9538628747	2.2617119246
H104	-9.6191819766	0.2879071926	4.3886853964
C105	-7.1545607784	3.2606155910	9.5239703384
C106	-8.4634569882	2.2549328626	7.6654403568
H107	-9.5265890450	1.3915461043	6.0361801626
H108	-9.3549872599	2.6227338638	8.1617725578
O109	-4.1181606524	-2.3783539696	0.2268217721

N110 -6.3861785810 -2.2119598822 0.2874098446

O111 -8.6606290157 -2.1445452485 0.2626279222

H112 -6.4213077169 -2.7576761126 -0.5667821128

O113 -3.5920825436 3.3859194519 9.9698623653

O114 -8.1296265748 3.6834799013 10.1240237607

N115 -5.8652170989 3.4884969034 10.0043940278

H116 -5.8018791503 4.0278902696 10.8609955804

Excited State 1: 2.1597 eV 574.07 nm

orbitals in

excitation CI coeff.

---------- ---------

308 => 309 0.96004

307 => 310 -0.13842

305 => 311 0.11731

306 => 312 0.15853

Transition dipole moment (debye):

X= -0.0056 Y= -1.3124 Z= -5.1641 Tot= 5.3282

Oscillator strength, f= 0.2325

Excited State 2: 2.2569 eV 549.36 nm

orbitals in

excitation CI coeff.

---------- ---------

306 => 309 -0.37136

307 => 309 0.82556

308 => 310 -0.35597

307 => 311 -0.17366

308 => 312 0.10104

Transition dipole moment (debye):

X= -3.9225 Y= 0.1791 Z= 0.0026 Tot= 3.9266

Oscillator strength, f= 0.1320

Excited State 3: 2.2619 eV 548.15 nm

orbitals in

excitation CI coeff.

---

306 => 309 -0.87795

307 => 309 -0.34107

308 => 310 0.17336

308 => 312 0.21926

Transition dipole moment (debye):

X= -8.5123 Y= 0.3892 Z= 0.0062 Tot= 8.5211

Oscillator strength, f= 0.6228

Excited State 4: 2.4469 eV 506.70 nm

orbitals in

excitation CI coeff.

---------- ---------

307 => 309 -0.34734

305 => 310 -0.25805

308 => 310 -0.86376

307 => 311 0.18357

Transition dipole moment (debye):

X= -0.2908 Y= 0.0061 Z= 0.0037 Tot= 0.2909

Oscillator strength, f= 0.0008

Excited State 5: 2.5452 eV 487.12 nm

orbitals in

excitation CI coeff.

---------- ---------

305 => 309 -0.72455

308 => 311 -0.67712

Transition dipole moment (debye):

X= 0.0312 Y= 0.2082 Z= 1.0800 Tot= 1.1003

Oscillator strength, f= 0.0117

Excited State 6: 2.5594 eV 484.43 nm

orbitals in

excitation CI coeff.

---------- ---------

306 => 310 0.94775

307 => 312 -0.22596

308 => 313 0.15383

Transition dipole moment (debye):

X= 0.0199 Y= 0.1618 Z= 0.2171 Tot= 0.2715

Oscillator strength, f= 0.0007

Excited State 7: 2.6572 eV 466.60 nm

orbitals in

excitation CI coeff.

---------- ---------

305 => 309 0.31688

307 => 310 0.84955

308 => 311 -0.34480

306 => 312 0.19044

Transition dipole moment (debye):

X= -0.0431 Y= -1.8039 Z= -4.9021 Tot= 5.2237

Oscillator strength, f= 0.2750

Excited State 8: 2.8089 eV 441.40 nm

orbitals in

excitation CI coeff.

---------- ---------

306 => 311 0.92742

305 => 312 0.25304

308 => 312 0.16498

Transition dipole moment (debye):

X= 1.5421 Y= -0.0701 Z= -0.0694 Tot= 1.5453

Oscillator strength, f= 0.0254

Excited State 9: 2.8349 eV 437.35 nm

orbitals in

excitation CI coeff.

---------- ---------

307 => 309 0.16970

305 => 310 0.55356

307 => 311 0.79976

Transition dipole moment (debye):

X= 0.1626 Y= 0.0956 Z= 0.0493 Tot= 0.1950

Oscillator strength, f= 0.0004

Excited State 10: 2.8491 eV 435.17 nm

orbitals in

excitation CI coeff.

---------- ---------

304 => 309 0.11365

305 => 309 0.56586

308 => 309 -0.10739

307 => 310 -0.45363

308 => 311 -0.61346

Transition dipole moment (debye):

X= 0.3396 Y= 5.3786 Z= 3.9954 Tot= 6.7088

Oscillator strength, f= 0.4863

Excited State 11: 2.8615 eV 433.28 nm

orbitals in

excitation CI coeff.

--- ---

304 => 309 -0.90097

306 => 310 0.13566

307 => 312 0.28529

308 => 313 -0.21481

Transition dipole moment (debye):

X= 0.0240 Y= 0.6559 Z= 0.4913 Tot= 0.8199

Oscillator strength, f= 0.0073

Excited State 12: 2.9594 eV 418.95 nm

orbitals in

excitation CI coeff.

---------- ---------

307 => 309 0.15383

305 => 310 -0.77491

308 => 310 0.23980

307 => 311 0.50713

Transition dipole moment (debye):

X= 0.3917 Y= -0.0354 Z= -0.0084 Tot= 0.3934

Oscillator strength, f= 0.0017

Excited State 13: 3.0201 eV 410.53 nm

orbitals in

excitation CI coeff.

---------- ---------

306 => 309 0.23967

304 => 310 -0.40881

305 => 312 -0.10519

308 => 312 0.83509

307 => 313 -0.18854

Transition dipole moment (debye):

X= 9.3422 Y= -0.4402 Z= -0.0055 Tot= 9.3525

Oscillator strength, f= 1.0018

Excited State 14: 3.1491 eV 393.71 nm

orbitals in

excitation CI coeff.

---------- ---------

301 => 309 0.12083

302 => 309 0.16152

303 => 309 0.76717

303 => 310 -0.51953

303 => 311 0.20009

301 => 315 0.11477

Transition dipole moment (debye):

X= 0.0307 Y= -0.0324 Z= -0.1095 Tot= 0.1182

Oscillator strength, f= 0.0002

Excited State 15: 3.1506 eV 393.52 nm

orbitals in

excitation CI coeff.

---------- ---------

302 => 309 -0.76835

303 => 309 0.17755

302 => 310 -0.51938

302 => 311 -0.19903

Transition dipole moment (debye):

X= -0.5508 Y= 0.0512 Z= 0.0930 Tot= 0.5609

Oscillator strength, f= 0.0038

Excited State 16: 3.1525 eV 393.29 nm

orbitals in

excitation CI coeff.

--- ---

300 => 309 0.18220

301 => 309 -0.75747

302 => 309 0.11830

300 => 310 0.14805

301 => 310 0.47967

304 => 310 -0.13505

301 => 311 -0.18762

303 => 315 -0.10445

Transition dipole moment (debye):

X= -1.3631 Y= 0.0520 Z= -0.0044 Tot= 1.3641

Oscillator strength, f= 0.0222

Excited State 17: 3.1544 eV 393.05 nm

orbitals in

excitation CI coeff.

--- ---

300 => 309 -0.77422

301 => 309 -0.19840

300 => 310 -0.48645

301 => 310 0.15306

300 => 311 -0.19091

Transition dipole moment (debye):

X= 0.7434 Y= -0.0193 Z= 0.0534 Tot= 0.7456

Oscillator strength, f= 0.0066

Excited State 18: 3.1737 eV 390.66 nm

orbitals in

excitation CI coeff.

--- ---

299 => 309 0.64096

299 => 311 -0.21435

305 => 311 -0.63160

306 => 312 0.31004

298 => 314 0.10865

Transition dipole moment (debye):

X= 0.0129 Y= -0.5551 Z= -2.4438 Tot= 2.5061

Oscillator strength, f= 0.0756

Excited State 19: 3.1816 eV 389.69 nm

orbitals in

excitation CI coeff.

---------- ---------

299 => 309 0.66654

299 => 311 -0.20767

305 => 311 0.59361

306 => 312 -0.33055

298 => 314 0.10774

Transition dipole moment (debye):

X= -0.0288 Y= 0.4903 Z= 2.1106 Tot= 2.1670

Oscillator strength, f= 0.0567

Excited State 20: 3.1859 eV 389.16 nm

orbitals in

excitation CI coeff.

---------- ---------

298 => 309 -0.92346

298 => 311 0.28818

299 => 314 -0.15205

Transition dipole moment (debye):

X= 0.0256 Y= -0.0240 Z= -0.0677 Tot= 0.0762

Oscillator strength, f= 0.0001

Excited State 21: 3.1973 eV 387.77 nm

orbitals in

excitation CI coeff.

---------- ---------

300 => 309 0.10308

301 => 309 -0.11416

304 => 310 0.82054

306 => 311 -0.18658

305 => 312 0.14692

308 => 312 0.42054

307 => 313 0.12429

Transition dipole moment (debye):

X= 8.9246 Y= -0.3930 Z= 0.0118 Tot= 8.9333

Oscillator strength, f= 0.9676

Excited State 22: 3.2909 eV 376.75 nm

orbitals in

excitation CI coeff.

---------- ---------

304 => 309 -0.23837

306 => 310 -0.19160

304 => 311 0.37228

307 => 312 -0.83891

308 => 313 -0.11376

Transition dipole moment (debye):

X= 0.0465 Y= -0.1242 Z= 0.0201 Tot= 0.1341

Oscillator strength, f= 0.0002

Excited State 23: 3.4596 eV 358.38 nm

orbitals in

excitation CI coeff.

--- ---

287 => 309 0.11582

295 => 309 0.35943

297 => 309 -0.79461

296 => 310 -0.36529

308 => 320 -0.15062

Transition dipole moment (debye):

X= -0.0381 Y= -0.0022 Z= -0.0154 Tot= 0.0412

Oscillator strength, f= 0.0000

Excited State 24: 3.4603 eV 358.30 nm

orbitals in

excitation CI coeff.

--- ---

304 => 311 0.87880

307 => 312 0.35222

305 => 313 -0.12818

308 => 313 0.18326

Transition dipole moment (debye):

X= 0.0002 Y= 0.0349 Z= 0.0151 Tot= 0.0381

Oscillator strength, f= 0.0000

Excited State 25: 3.5040 eV 353.84 nm

orbitals in

excitation CI coeff.

--- ---

285 => 309 0.13724

294 => 309 -0.62806

295 => 309 -0.62676

297 => 309 -0.22379

294 => 311 0.14688

306 => 313 -0.11792

308 => 318 -0.11328

Transition dipole moment (debye):

X= 0.0737 Y= -0.0149 Z= -0.2279 Tot= 0.2400

Oscillator strength, f= 0.0008

PDI tetramer **4** helix conformer

B3LYP/6-31G** optimized geometry

Final total energy = -5546.104789 h

final geometry:

angstroms

atom	x	y	z
C1	0.0000000000	0.0000000000	0.0000000000
C2	0.0000000000	0.0000000000	1.4828756752
C3	1.2150077252	0.0000000000	2.1987205553
C4	2.4663247596	-0.0014576416	1.5148931606
C5	2.5083071340	0.0703927335	0.0310461664
N6	1.2625683445	0.0431418259	-0.5926162032
C7	1.2065932086	0.0341436091	3.6205285402
C8	2.4509848239	0.0398616582	4.3291379082
C9	3.6783422955	-0.1021362720	3.6326931234
C10	3.6468930530	-0.0601448136	2.2090711798
C11	2.4545166875	0.1692667324	5.7516763725
C12	1.2129242904	0.1552450128	6.4656808616
C13	-0.0363597611	0.0863805013	5.7774875140
C14	-0.0397666012	0.0572302288	4.3149864909
C15	3.6859987030	0.3271964129	6.4391976466
C16	3.6591693704	0.3261229108	7.8640765864
C17	2.4824180837	0.2570147880	8.5647359513
C18	1.2277149185	0.2034562666	7.8871296359
C19	4.9260812958	-0.1482874591	4.3677559100

C20	4.9328896883	0.3263751314	5.7003884453
C21	6.1601849422	-0.6795248043	3.8068724496
C22	7.3889985015	-0.4210653794	4.4710741261
C23	7.4095055509	0.3974594696	5.6413999954
C24	6.1932664641	0.7861227850	6.2624100120
C25	8.6645540169	0.8133754210	6.1803057353
C26	9.8907154875	0.3080061257	5.6538323179
C27	9.8528879397	-0.6713688443	4.6162736508
C28	8.6108228497	-0.9751956436	3.9844260374
C29	11.0419073618	-1.3443794810	4.2296113558
C30	12.2746917452	-1.0636314104	4.9449941911
C31	12.3665619162	0.1481189457	5.6697061544
C32	11.1411516173	0.7638589442	6.1537153563
C33	13.6878893573	0.6881491462	5.9406635781
C34	14.8139328098	-0.1744016258	5.8706862180
C35	14.6476467280	-1.5399339651	5.4892646311
C36	13.3945088448	-1.9894073453	4.9885554709
C37	16.1177029303	0.3091391421	6.1919731557
C38	16.3014770722	1.6853221710	6.4661899624
C39	15.1845070548	2.5597865723	6.4136420283
C40	13.9193930328	2.0714550689	6.1654731787
C41	15.3728643775	4.0178094865	6.6479790900
N42	16.6678032072	4.3924095149	7.0073287073

C43	17.8008915297	3.5892765604	7.1414045289
C44	17.5974727521	2.1550151809	6.7972911785
C45	17.2336205464	-0.5796177386	6.2565167877
C46	18.5399902508	-0.0852016842	6.5155693197
C47	18.6752202538	1.2960300222	6.8195916676
C48	15.7482232397	-2.4396066153	5.6181439637
C49	17.0254407385	-1.9789559635	6.0615550332
C50	18.0796295383	-2.8978425006	6.3136056331
C51	19.3655450158	-2.3971646228	6.7790877529
C52	19.6502038701	-1.0216931622	6.6125858594
C53	15.5673156232	-3.8092888172	5.3126630155
C54	16.6588775073	-4.7008628134	5.4675712076
C55	17.8668591518	-4.2577208506	5.9638054533
C56	21.0386368538	-0.6067129192	6.5668092758
C57	22.0536235140	-1.4739718388	7.0454404058
C58	21.7014770098	-2.7660301676	7.5468399726
C59	20.3681444592	-3.2354574323	7.4110885880
C60	23.4244249277	-1.0574439215	7.0544952900
C61	23.7757478938	0.1963180805	6.4810843995
C62	22.7547337040	0.9932059886	5.8835835636
C63	21.4410775873	0.6043869348	5.9327303642
C64	24.4417327014	-1.8741141024	7.6343753534
C65	24.0673755747	-3.1576005303	8.2290042977

C66	22.7043449674	-3.5811435804	8.1668613536
C67	22.3340607208	-4.8330775551	8.7339787562
C68	20.9659878821	-5.2382614440	8.6862985240
C69	20.0295772048	-4.4683595656	8.0438440237
C70	23.3063197164	-5.6393513795	9.3627264907
C71	22.9263545892	-6.9298149962	9.9876581524
N72	21.5670912192	-7.2403750859	9.9258520156
C73	20.5355440193	-6.5001454744	9.3510442675
C74	24.6288689064	-5.2171383969	9.4140936979
C75	25.0008446575	-3.9978404986	8.8541412137
C76	25.1202735084	0.6226913264	6.4788559760
C77	26.1000835554	-0.1778502291	7.0527362246
C78	25.7638605705	-1.4039901231	7.6212270906
C79	23.1040077860	2.2613933419	5.1893680951
N80	24.4504489282	2.6151014180	5.2585213646
C81	25.4999859189	1.9142102229	5.8550331946
C82	13.2512183611	-3.3748545602	4.7060827542
C83	14.2986756075	-4.2570054641	4.8627918066
C84	14.0846518411	-5.6995615310	4.5657928055
N85	15.2198793740	-6.5002881265	4.6898909406
C86	16.5045889449	-6.1330261422	5.0923317417
C87	8.6914918206	1.7249258883	7.2621522235
C88	9.9439288262	2.1438145349	7.7804853160

C89	11.1238413106	1.6803331305	7.2396440724
C90	8.5905248849	-1.8528776715	2.8751030052
C91	9.8078666944	-2.4223313208	2.4187844378
C92	10.9907475268	-2.1838420017	3.0855899513
C93	6.2620738174	1.7215734836	7.3287702880
C94	7.4675230995	2.1907137601	7.8056975209
C95	7.4788582432	3.1931829368	8.9054972721
N96	8.7472004294	3.5334162387	9.3770831122
C97	9.9908364917	3.0794802274	8.9373479089
C98	7.3514040332	-2.1492662612	2.2533993129
C99	6.1803868310	-1.5791261915	2.7067106908
C100	7.3057722191	-3.0993803464	1.1083325831
N101	8.5495008629	-3.5677432865	0.6833083729
C102	9.8101373139	-3.3011673330	1.2180109204
C103	0.0159963884	0.1624214397	8.6080976897
C104	0.0218522683	0.1737243599	10.0907907997
N105	1.2875928220	0.1957069746	10.6780567068
C106	2.5315654123	0.2148190844	10.0497710821
C107	-1.1929736029	0.0926450786	7.9274978732
C108	-1.2163214901	0.0588962772	6.5357041385
C109	-1.2067434906	0.0147928559	2.1699899806
C110	-1.2225994843	0.0411333103	3.5618583950
O111	18.8647801193	4.0620693306	7.5036202639

O112	14.4822685310	4.8458510919	6.5587592583
O113	19.3801933534	-6.8899013690	9.4018646301
O114	23.7152136694	-7.6843565430	10.5344124565
O115	26.6376635667	2.3564258875	5.8353012589
O116	22.2986755224	2.9671627167	4.6035795260
O117	17.4065954232	-6.9523034121	5.1316203671
O118	13.0151298248	-6.1755662383	4.2241023029
O119	11.0200402448	3.4513937445	9.4755637863
O120	6.4764379702	3.6920089105	9.3881116014
O121	10.8159727811	-3.7800028621	0.7222429743
O122	6.2797545908	-3.4532617736	0.5525200869
O123	-0.9860128394	0.1537514008	10.7789356239
O124	3.5635008320	0.2019860440	10.7009284486
O125	3.5364306629	0.1402690523	-0.6221574248
O126	-1.0109988548	-0.0219832188	-0.6832594797
H127	21.2925705816	-8.1109866349	10.3680837758
H128	25.3573151528	-5.8558106882	9.9017650788
H129	26.0406987888	-3.7041156612	8.9150688958
H130	26.5563596099	-1.9981047076	8.0574633109
H131	27.1264686830	0.1728472659	7.0430238209
H132	24.7016955562	3.4894615618	4.8098106177
H133	20.7241909127	1.2328944500	5.4226735218
H134	19.0046687072	-4.8096096351	8.0863043219

H135	18.6670951141	-4.9825357546	6.0195171145
H136	15.0950799034	-7.4800656624	4.4589193432
H137	12.2984735137	-3.7939289881	4.4111790693
H138	13.1139390525	2.7919658602	6.1034492787
H139	16.8007533558	5.3777419083	7.2086724344
H140	19.6208145092	1.7123427348	7.1367265406
H141	11.8894464935	-2.6229722413	2.6731476321
H142	12.0366879953	1.9954423587	7.7248068982
H143	8.7671193363	4.1932856949	10.1472491471
H144	5.3662677001	2.1440560033	7.7625426335
H145	5.2672089818	-1.8961968726	2.2228160771
H146	8.5343882012	-4.1920688546	-0.1160588892
H147	1.3044591726	0.1825004286	11.6921036581
H148	-2.1107090943	0.0617967524	8.5047871048
H149	-2.1779152580	0.0051496107	6.0421877882
H150	4.5740867346	0.3116998028	8.4408765546
H151	1.2744980139	0.0684963620	-1.6064682479
H152	-2.1284551060	0.0098520772	1.5985291814
H153	-2.1831334092	0.0538865535	4.0604373137
H154	4.5600622195	-0.0171418599	1.6312201770

Excited State 1: 2.1261 eV 583.15 nm

orbitals in

excitation CI coeff.

---------- ---------

410 => 413 0.82665

412 => 413 -0.50150

408 => 414 -0.11447

412 => 417 0.13007

Transition dipole moment (debye):

X= 11.2912 Y= 0.4317 Z= 2.3541 Tot= 11.5420

Oscillator strength, f= 1.0741

Excited State 2: 2.1384 eV 579.79 nm

orbitals in

excitation CI coeff.

---------- ---------

410 => 413 0.49754

412 => 413 0.82776

410 => 417 -0.13255

Transition dipole moment (debye):

X= 4.7476 Y= -3.8320 Z= -1.4711 Tot= 6.2760

Oscillator strength, f= 0.3194

Excited State 3: 2.1967 eV 564.40 nm

orbitals in

excitation CI coeff.

---

411 => 413 0.95309

412 => 414 0.14298

411 => 415 0.19638

Transition dipole moment (debye):

X= 0.3736 Y= 1.3504 Z= -2.0788 Tot= 2.5069

Oscillator strength, f= 0.0524

Excited State 4: 2.3317 eV 531.74 nm

orbitals in

excitation CI coeff.

---

411 => 413 0.12158

409 => 414 -0.21204

412 => 414 -0.93315

407 => 415 0.11702

Transition dipole moment (debye):

X= 0.5299 Y= 1.9644 Z= -3.2511 Tot= 3.8353

Oscillator strength, f= 0.1301

Excited State 5: 2.3766 eV 521.68 nm

orbitals in

excitation CI coeff.

---

408 => 413 -0.10120

410 => 414 0.94342

411 => 417 -0.17660

412 => 418 -0.16153

Transition dipole moment (debye):

X= -0.1539 Y= -0.6355 Z= 1.0432 Tot= 1.2312

Oscillator strength, f= 0.0137

Excited State 6: 2.3975 eV 517.14 nm

orbitals in

excitation CI coeff.

---

409 => 413 0.81753

411 => 414 0.29093

412 => 415 -0.40991

411 => 416 0.24089

Transition dipole moment (debye):

X= 0.0140 Y= -0.6038 Z= -0.3844 Tot= 0.7159

Oscillator strength, f= 0.0047

Excited State 7: 2.4614 eV 503.72 nm

orbitals in

excitation CI coeff.

---------- ---------

409 => 413 0.30857

407 => 414 0.12222

411 => 414 -0.90533

409 => 415 -0.12522

411 => 416 -0.11349

410 => 417 -0.13471

Transition dipole moment (debye):

X= -0.7053 Y= -3.1195 Z= -1.9814 Tot= 3.7623

Oscillator strength, f= 0.1321

Excited State 8: 2.5670 eV 483.00 nm

orbitals in

excitation CI coeff.

---------- ---------

407 => 413 0.33029

408 => 413 -0.43499

411 => 413 -0.13752

409 => 414 0.52808

411 => 415 0.40855

412 => 416 -0.42899

Transition dipole moment (debye):

X= -0.1336 Y= -0.6496 Z= 1.0111 Tot= 1.2092

Oscillator strength, f= 0.0142

Excited State 9: 2.5737 eV 481.74 nm

orbitals in

excitation CI coeff.

--- ---

407 => 413 0.18605

408 => 413 0.82953

409 => 414 0.28510

410 => 414 0.14753

411 => 415 0.22328

412 => 416 -0.20131

411 => 417 0.14916

412 => 418 0.15371

Transition dipole moment (debye):

X= -0.0005 Y= 0.0165 Z= 0.0230 Tot= 0.0283

Oscillator strength, f= 0.0000

Excited State 10: 2.5759 eV 481.32 nm

orbitals in

excitation CI coeff.

--- ---

409 => 413 0.37927

407 => 414 -0.21681

409 => 415 0.25858

412 => 415 0.82193

410 => 417 -0.12630

Transition dipole moment (debye):

X= -0.1125 Y= -0.3532 Z= -0.3209 Tot= 0.4903

Oscillator strength, f= 0.0023

Excited State 11: 2.6027 eV 476.37 nm

orbitals in

excitation CI coeff.

---

408 => 414 0.14040

410 => 415 0.93759

409 => 417 0.19341

411 => 418 -0.10727

Transition dipole moment (debye):

X= -0.9608 Y= 0.0279 Z= -0.0898 Tot= 0.9654

Oscillator strength, f= 0.0092

Excited State 12: 2.6633 eV 465.52 nm

orbitals in

excitation CI coeff.

---------- ---------

407 => 413 -0.61829

409 => 414 0.48174

412 => 414 -0.18288

411 => 415 0.28711

409 => 416 0.17754

412 => 416 0.46335

Transition dipole moment (debye):

X= 0.1323 Y= 0.4806 Z= -0.7951 Tot= 0.9384

Oscillator strength, f= 0.0089

Excited State 13: 2.7366 eV 453.07 nm

orbitals in

excitation CI coeff.

---------- ---------

407 => 413 -0.29931

409 => 414 0.42248

411 => 415 -0.69612

410 => 416 0.13691

412 => 416 -0.42797

Transition dipole moment (debye):

X= 0.6395 Y= 2.1621 Z= -3.5765 Tot= 4.2279

Oscillator strength, f= 0.1855

Excited State 14: 2.7553 eV 449.98 nm

orbitals in

excitation CI coeff.

--- ---

408 => 415 -0.16616

411 => 415 0.13536

410 => 416 0.92271

407 => 417 0.19831

409 => 418 -0.13319

Transition dipole moment (debye):

X= -0.1181 Y= -0.2950 Z= 0.4768 Tot= 0.5729

Oscillator strength, f= 0.0034

Excited State 15: 2.7574 eV 449.63 nm

orbitals in

excitation CI coeff.

--- ---

406 => 413 0.12003

410 => 413 -0.17986

408 => 414 -0.87956

410 => 415 0.14497

412 => 417 0.27009

411 => 418 0.20779

Transition dipole moment (debye):

X= 1.1977 Y= -0.0280 Z= 0.2398 Tot= 1.2218

Oscillator strength, f= 0.0156

Excited State 16: 2.8229 eV 439.22 nm

orbitals in

excitation CI coeff.

--- ---

409 => 413 0.15397

407 => 414 -0.37493

411 => 414 0.10526

409 => 415 0.13868

412 => 415 -0.17040

411 => 416 -0.87350

Transition dipole moment (debye):

X= 0.2819 Y= 0.0951 Z= 0.1663 Tot= 0.3409

Oscillator strength, f= 0.0012

Excited State 17: 2.8635 eV 432.98 nm

orbitals in

excitation CI coeff.

---

407 => 413 0.57287

409 => 414 0.36230

412 => 414 -0.12110

411 => 415 -0.34366

412 => 416 0.57502

Transition dipole moment (debye):

X= 0.5232 Y= 2.4086 Z= -3.9686 Tot= 4.6718

Oscillator strength, f= 0.2370

Excited State 18: 2.9172 eV 425.02 nm

orbitals in

excitation CI coeff.

---

409 => 413 0.15507

411 => 414 0.11855

409 => 415 -0.89232

412 => 415 0.21866

411 => 416 -0.12377

410 => 417 0.20797

412 => 417 -0.12203

Transition dipole moment (debye):

X= 2.6403 Y= 2.7821 Z= 2.0855 Tot= 4.3659

Oscillator strength, f= 0.2109

Excited State 19: 2.9406 eV 421.63 nm

orbitals in

excitation CI coeff.

--- ---

407 => 414 -0.80693

411 => 414 -0.17234

412 => 415 -0.16322

411 => 416 0.32456

410 => 417 0.21017

412 => 417 -0.29229

Transition dipole moment (debye):

X= 4.1389 Y= -0.7814 Z= 0.2678 Tot= 4.2205

Oscillator strength, f= 0.1986

Excited State 20: 2.9533 eV 419.81 nm

orbitals in

excitation CI coeff.

--- ---

406 => 413 -0.22179

410 => 413 -0.11739

407 => 414 -0.27618

408 => 414 0.24289

409 => 415 -0.12659

410 => 415 -0.13640

409 => 417 0.16334

410 => 417 0.14798

412 => 417 0.81977

Transition dipole moment (debye):

X= -13.4736 Y= 1.9946 Z= -1.2566 Tot= 13.6783

Oscillator strength, f= 2.0954

Excited State 21: 2.9969 eV 413.71 nm

orbitals in

excitation CI coeff.

--- ---

406 => 414 -0.11861

410 => 414 0.15423

408 => 415 -0.86948

406 => 416 0.10677

410 => 416 -0.18247

407 => 417 0.10988

411 => 417 0.29418

409 => 418 -0.16493

Transition dipole moment (debye):

X= 0.1993 Y= -0.1027 Z= 0.2181 Tot= 0.3128

Oscillator strength, f= 0.0011

Excited State 22: 3.0616 eV 404.96 nm

orbitals in

excitation CI coeff.

--- ---

406 => 413 -0.87202

408 => 414 -0.26030

409 => 416 0.10380

409 => 417 0.19735

412 => 417 -0.20387

411 => 418 -0.17728

412 => 420 -0.10670

Transition dipole moment (debye):

X= 3.4826 Y= -0.4580 Z= 0.7516 Tot= 3.5921

Oscillator strength, f= 0.1498

Excited State 23: 3.0650 eV 404.52 nm

orbitals in

excitation CI coeff.

--- ---

409 => 416 0.93201

408 => 417 0.15073

410 => 418 0.19806

Transition dipole moment (debye):

X= -0.9362 Y= -1.7212 Z= 2.7931 Tot= 3.4118

Oscillator strength, f= 0.1353

Excited State 24: 3.1552 eV 392.95 nm

orbitals in

excitation CI coeff.

--- ---

408 => 413 0.13275

407 => 415 0.70169

408 => 415 -0.23682

411 => 417 -0.59386

410 => 418 0.10640

Transition dipole moment (debye):

X= -0.2490 Y= -0.5614 Z= 0.9772 Tot= 1.1541

Oscillator strength, f= 0.0159

Excited State 25: 3.1594 eV 392.43 nm

orbitals in

excitation CI coeff.

---------- ---------

408 => 413 0.14044

407 => 415 -0.64444

408 => 415 -0.22228

411 => 417 -0.66211

410 => 418 -0.11325

Transition dipole moment (debye):

X= 0.3412 Y= 1.2500 Z= -2.0024 Tot= 2.3851

Oscillator strength, f= 0.0682

PDI tetramer **4** waggle conformation

B3LYP/6-31G** optimized geometry

Final total energy = -5546.106252 h

final geometry:

angstroms

atom	x	y	z
N1	0.0000000000	0.0000000000	0.0000000000
C2	0.0000000000	0.0000000000	1.3956315049
C3	1.3486625677	0.0000000000	2.0213537256
C4	2.5091809223	0.0393942903	1.2076341044
C5	2.4234770373	0.0293593369	-0.2076176945
C6	1.0899221823	0.0300102163	-0.8710295654
C7	1.4496414837	-0.0157873935	3.3946040780
C8	2.7078524467	0.0176760832	4.0512715217

C9	3.8688584788	0.1943938044	3.2469572385
C10	3.7789236151	0.1578428595	1.8222789149
C11	5.1444267258	0.3807465679	3.8597031098
C12	5.2363994531	0.5344230485	5.2668712795
C13	4.0244291666	0.5359657859	6.0620922582
C14	2.8317106079	0.0259755405	5.4991534599
C15	3.9957882463	1.0481812858	7.4162919884
C16	2.9199257419	0.6911892234	8.2706054964
C17	1.8588768976	-0.1289379304	7.7796951998
C18	1.7958548530	-0.4615524891	6.3974989488
C19	2.9166252503	1.1136078603	9.6326582402
C20	1.9165529809	0.6495611919	10.5371789467
C21	0.8525568535	-0.1713454116	10.0515260843
C22	0.8502306116	-0.5824370136	8.6838268586
C23	4.9407526984	1.9960767272	7.8891404991
C24	4.9060913000	2.4629991803	9.1831575996
C25	3.9309954682	1.9873971946	10.0957566386
C26	3.9152378935	2.4110030522	11.4480292005
C27	4.8965820878	3.4264937307	11.9212648542
N28	5.8069807239	3.8587316122	10.9559764457
C29	5.8989216779	3.4814312001	9.6156451671
C30	2.0001703193	0.9655913712	11.9187625793
C31	2.9862329153	1.9022014846	12.3288439856

C32	-0.2089979154	-0.5473967742	10.9197413453
C33	-0.2056143229	-0.0732632257	12.2944763194
C34	1.0007566732	0.4353918003	12.8295352119
C35	-1.1587991755	-1.4865950796	10.4370087785
C36	-1.1384012489	-1.9327330033	9.1327768038
C37	-0.1661736606	-1.4520447504	8.2183603384
C38	-0.1482564082	-1.8727981448	6.8638354137
C39	0.7945737089	-1.3824028734	5.9863345591
C40	-1.1375567905	-2.8784457632	6.3849971066
N41	-2.0497150212	-3.3110203377	7.3485013339
C42	-2.1363452699	-2.9463784219	8.6925814035
C43	-1.3779050949	-0.0981939663	13.1468072447
C44	-1.2307809993	0.0403659644	14.5513170781
C45	0.0722847166	0.2064137967	15.1165886511
C46	1.1874959803	0.4032127738	14.2643918912
C47	0.2392396764	0.1921255162	16.5384612567
C48	1.5497970832	0.2733931039	17.0891607695
C49	2.6681838581	0.3498892080	16.2070461909
C50	2.4861703984	0.4207841511	14.8508141087
C51	-0.8864096469	0.0986282312	17.4110954168
C52	-2.2302339726	0.0291497193	16.8321731095
C53	-2.3748026225	-0.0048972753	15.4114852065
C54	-3.6763171859	-0.0863215076	14.8387618683

C55	-3.8089274890	-0.1032976604	13.4171249790
C56	-2.6994528002	-0.1164920992	12.6104081567
C57	-0.6545576879	0.0875970455	18.7946264542
C58	0.6314370348	0.1563665664	19.3261097773
C59	1.7353381158	0.2449960172	18.4871636562
C60	3.1011243619	0.2925606317	19.0688379102
N61	4.1400906377	0.3322008001	18.1384241324
C62	4.0538927008	0.3403245238	16.7472660255
C63	-4.8149289749	-0.1180062346	15.6710691529
C64	-4.6608756746	-0.0860824055	17.0518414566
C65	-3.3903563831	-0.0165812080	17.6192166280
C66	-5.1600397897	-0.0954669462	12.7903953721
N67	-6.2230823515	-0.1508848031	13.6896456000
C68	-6.1777133531	-0.1700382612	15.0837318718
C69	4.9515543690	0.2366558342	1.0088597999
C70	6.2255915305	0.4313678671	1.6256727492
C71	6.3176356346	0.4542332864	3.0494491553
C72	7.5868351561	0.5649703329	3.6678257484
C73	7.6705381796	0.5581070614	5.0832233858
C74	6.5298944871	0.5541058834	5.8538257732
C75	8.7482917478	0.6197070920	2.8573084489
C76	8.6431064654	0.6649913402	1.4841578088
C77	7.3843071862	0.6319156076	0.8271775544

C78	10.0970107947	0.6062184587	3.4887190584
N79	10.0923113891	0.5781602538	4.8840559939
C80	8.9990734527	0.5387572102	5.7508324321
C81	3.5648057253	0.0427874842	-0.9801178019
C82	4.8617282171	0.0890733880	-0.4014867446
O83	6.7407115416	3.9719698034	8.8816102714
O84	4.9271242999	3.8722114407	13.0561504568
O85	5.0597249042	0.3465542280	16.0561901566
O86	3.3340327679	0.2870699514	20.2672362192
O87	-7.2046270738	-0.2158754802	15.7422666592
O88	-5.3579960263	-0.0521863177	11.5869884647
O89	-1.1725827415	-3.3168467063	5.2473798118
O90	-2.9760954372	-3.4433241816	9.4245133537
O91	9.1581791166	0.4889594736	6.9592508060
O92	-1.0460599831	0.0034794840	2.0229837914
O93	11.1451145934	0.6121477933	2.8650091431
O94	0.9261031230	0.0597856437	-2.0793381676
H95	-2.8677208674	-0.0839433208	11.5420971429
H96	-5.5498328812	-0.1136879839	17.6727166028
H97	-3.3138527215	0.0060629855	18.6994631244
H98	-7.1499129441	-0.1655982058	13.2779211310
H99	0.7955953721	0.1385120139	20.3981879874
H100	-1.4866229255	0.0194327570	19.4837199623

H101	3.3763600438	0.4273741996	14.2379266372
H102	5.0783114619	0.3448554091	18.5237797911
H103	-2.7253321346	-4.0001475111	7.0359892579
H104	0.7758876334	-1.7794916267	4.9812528762
H105	-1.9011230503	-1.9204295787	11.0929033075
H106	6.4798519579	4.5519070569	11.2652657321
H107	5.6897373416	2.4163718220	7.2322035486
H108	3.0045931121	2.2908005041	13.3373356829
H109	6.6606067813	0.5171778624	6.9273669022
H110	0.5241539596	-0.0028489879	3.9527032079
H111	9.5675128081	0.6682537212	0.9239576463
C112	7.2580140523	0.6478457847	-0.6212846240
H113	3.4278644915	0.0748400999	-2.0519700217
H114	11.0051361043	0.5663701568	5.3263945577
H115	-0.9140976777	0.0003035022	-0.4397928718
C116	6.0771320217	0.1276305350	-1.2012071145
C117	8.2911047487	1.1605466205	-1.5004832958
C118	9.2614280781	2.1044111802	-1.0517200861
C119	10.2183624486	2.6165089599	-1.8899959472
C120	10.2871909700	2.2038739131	-3.2545842910
C121	9.3001522236	1.3089775259	-3.7572309859
C122	8.2727167107	0.8310434359	-2.8803741379
C123	9.3514576612	0.9013870861	-5.1251057668

C124	10.3806334675	1.4076623063	-5.9331424048
C125	11.3359963767	2.2914627009	-5.4366984525
C126	11.2973314999	2.6960694778	-4.1079860464
C127	12.3111164724	3.6557626795	-3.6018024737
N128	12.1550891575	4.0336710337	-2.2680816866
C129	11.1815129133	3.6215768882	-1.3604459499
O130	11.1544176859	4.0658590368	-0.2241428720
H131	12.8305662416	4.7041913346	-1.9175302245
O132	13.2207665051	4.1095386816	-4.2778809022
H133	12.1225348063	2.6812498970	-6.0738227999
H134	10.4467683331	1.1170331160	-6.9735654746
C135	8.3429190408	-0.0339040020	-5.6274070120
C136	7.2994358721	-0.4634887514	-4.7521246859
C137	7.2326900306	-0.0039707988	-3.3967667176
C138	6.1380617296	-0.3574348751	-2.5661569316
H139	9.2358842269	2.4944951752	-0.0438834448
C140	5.2022582144	-1.3090090949	-3.0662243721
C141	5.2840045259	-1.8047940201	-4.3415434374
C142	6.3094294798	-1.3667919290	-5.2317037883
C143	6.3687446467	-1.8453157107	-6.5575823528
C144	7.3869734753	-1.4164618385	-7.4004088122
C145	8.3541634635	-0.5242216903	-6.9422655263
C146	4.2941419348	-2.8240202267	-4.7806824965

N147 4.4136385727 -3.2202886392 -6.1115397841

C148 5.3613800632 -2.8177812441 -7.0531318363

O149 3.4269729080 -3.2934812719 -4.0615919702

H150 3.7344818041 -3.9020255872 -6.4321781292

O151 5.3413898028 -3.2623462952 -8.1899153144

H152 7.4115832862 -1.7956976143 -8.4163349359

H153 9.1314139280 -0.2159377238 -7.6303887428

H154 4.4308556965 -1.7216896208 -2.4313904503

Excited State 1: 2.1316 eV 581.65 nm

orbitals in

excitation CI coeff.

---------- ---------

410 => 413 -0.92718

411 => 413 0.11378

412 => 413 0.23816

408 => 414 -0.12587

412 => 417 0.15709

Transition dipole moment (debye):

X= 6.1371 Y= 0.6088 Z= -10.5502 Tot= 12.2206

Oscillator strength, f= 1.2072

Excited State 2: 2.1399 eV 579.40 nm

orbitals in

excitation CI coeff.

---

410 => 413 -0.23540

412 => 413 -0.93703

412 => 415 0.10115

410 => 417 -0.15341

Transition dipole moment (debye):

X= -3.1156 Y= -1.8068 Z= -4.5733 Tot= 5.8212

Oscillator strength, f= 0.2750

Excited State 3: 2.2019 eV 563.07 nm

orbitals in

excitation CI coeff.

---

410 => 413 0.11539

411 => 413 0.94788

412 => 414 0.14175

411 => 415 -0.19191

Transition dipole moment (debye):

X= -0.3255 Y= 0.1943 Z= 0.3644 Tot= 0.5258

Oscillator strength, f= 0.0023

Excited State 4: 2.3350 eV 530.98 nm

orbitals in

excitation CI coeff.

---------- ---------

411 => 413 -0.12110

409 => 414 0.21829

412 => 414 0.93766

407 => 415 0.11458

Transition dipole moment (debye):

X= 0.1832 Y= -0.3756 Z= -0.1626 Tot= 0.4484

Oscillator strength, f= 0.0018

Excited State 5: 2.3799 eV 520.97 nm

orbitals in

excitation CI coeff.

---------- ---------

408 => 413 0.10325

410 => 414 0.93692

411 => 414 -0.12305

411 => 417 0.18165

412 => 418 -0.16518

Transition dipole moment (debye):

X= 0.3355 Y= 0.0402 Z= 0.1424 Tot= 0.3667

Oscillator strength, f= 0.0012

Excited State 6: 2.4055 eV 515.42 nm

orbitals in

excitation CI coeff.

---

409 => 413 0.83346

411 => 414 0.24022

412 => 415 0.41378

411 => 416 0.22515

Transition dipole moment (debye):

X= 0.1708 Y= 0.0897 Z= 0.1430 Tot= 0.2402

Oscillator strength, f= 0.0005

Excited State 7: 2.4711 eV 501.74 nm

orbitals in

excitation CI coeff.

---

409 => 413 -0.26493

407 => 414 -0.12167

410 => 414 0.11041

411 => 414 0.91198

409 => 415 -0.12653

411 => 416 0.11790

410 => 417 -0.13894

Transition dipole moment (debye):

X= -4.4771 Y= -1.9163 Z= -2.0187 Tot= 5.2718

Oscillator strength, f= 0.2604

Excited State 8: 2.5720 eV 482.05 nm

orbitals in

excitation CI coeff.

--- ---

408 => 413 -0.92989

410 => 414 0.17640

411 => 417 -0.17374

412 => 418 0.17591

Transition dipole moment (debye):

X= -0.2147 Y= -0.0352 Z= -0.0409 Tot= 0.2214

Oscillator strength, f= 0.0005

Excited State 9: 2.5802 eV 480.52 nm

orbitals in

excitation CI coeff.

--- ---

407 => 413 -0.32574

409 => 413 -0.20632

411 => 413 0.12861

407 => 414 0.11123

409 => 414 -0.50386

409 => 415 0.13414

411 => 415 0.41280

412 => 415 0.43972

412 => 416 0.37770

Transition dipole moment (debye):

X= 0.5552 Y= 0.3073 Z= 0.1195 Tot= 0.6457

Oscillator strength, f= 0.0041

Excited State 10: 2.5829 eV 480.02 nm

orbitals in

excitation CI coeff.

---

407 => 413 0.20799

409 => 413 -0.32027

407 => 414 0.18124

409 => 414 0.31873

409 => 415 0.21794

411 => 415 -0.26590

412 => 415 0.69659

412 => 416 -0.24473

410 => 417 -0.11288

Transition dipole moment (debye):

X= 0.9479 Y= 0.3578 Z= 0.3187 Tot= 1.0622

Oscillator strength, f= 0.0111

Excited State 11: 2.6081 eV 475.38 nm

orbitals in

excitation CI coeff.

--- ---

408 => 414 -0.13961

410 => 415 -0.93369

409 => 417 -0.19327

411 => 418 -0.10682

Transition dipole moment (debye):

X= 0.2674 Y= 0.0265 Z= -0.9549 Tot= 0.9920

Oscillator strength, f= 0.0097

Excited State 12: 2.6764 eV 463.26 nm

orbitals in

excitation CI coeff.

--- ---

407 => 413 -0.64810

409 => 414 0.48947

412 => 414 -0.17855

411 => 415 -0.25477

409 => 416 0.17163

412 => 416 0.43982

Transition dipole moment (debye):

X= -0.0730 Y= 0.2896 Z= -0.1234 Tot= 0.3232

Oscillator strength, f= 0.0011

Excited State 13: 2.7489 eV 451.04 nm

orbitals in

excitation CI coeff.

--- ---

407 => 413 -0.24305

409 => 414 0.42938

411 => 415 0.71226

412 => 416 -0.44953

Transition dipole moment (debye):

X= -0.5642 Y= 1.3918 Z= 0.0157 Tot= 1.5019

Oscillator strength, f= 0.0235

Excited State 14: 2.7604 eV 449.15 nm

orbitals in

excitation CI coeff.

---------- ---------

406 => 413 -0.11596

410 => 413 -0.18372

408 => 414 0.87369

410 => 415 -0.13850

412 => 417 -0.28645

411 => 418 0.21324

Transition dipole moment (debye):

X= -0.3677 Y= -0.0035 Z= 0.7458 Tot= 0.8315

Oscillator strength, f= 0.0072

Excited State 15: 2.7750 eV 446.79 nm

orbitals in

excitation CI coeff.

---------- ---------

408 => 415 -0.17402

410 => 416 0.92175

411 => 416 -0.11412

407 => 417 -0.21013

409 => 418 -0.14140

Transition dipole moment (debye):

X= -0.0486 Y= -0.0821 Z= -0.0186 Tot= 0.0972

Oscillator strength, f= 0.0001

Excited State 16: 2.8454 eV 435.74 nm

orbitals in

excitation CI coeff.

---------- ---------

409 => 413 0.14389

407 => 414 -0.39934

409 => 415 -0.13693

412 => 415 0.17816

410 => 416 -0.10729

411 => 416 -0.85856

Transition dipole moment (debye):

X= -0.7609 Y= -0.3832 Z= -0.3098 Tot= 0.9065

Oscillator strength, f= 0.0089

Excited State 17: 2.8781 eV 430.78 nm

orbitals in

excitation CI coeff.

---------- ---------

407 => 413 0.56339

409 => 414 0.35212

412 => 414 -0.11901

411 => 415 0.32442

412 => 416 0.59915

Transition dipole moment (debye):

X= -1.3796 Y= 4.4626 Z= -0.9840 Tot= 4.7735

Oscillator strength, f= 0.2487

Excited State 18: 2.9275 eV 423.51 nm

orbitals in

excitation CI coeff.

--- ---

409 => 413 0.15695

411 => 414 0.10762

409 => 415 0.88979

412 => 415 -0.21074

411 => 416 -0.11886

410 => 417 -0.25589

Transition dipole moment (debye):

X= -5.4773 Y= -2.1107 Z= -1.4524 Tot= 6.0469

Oscillator strength, f= 0.4059

Excited State 19: 2.9434 eV 421.22 nm

orbitals in

excitation CI coeff.

--- ---

406 => 413 -0.22835

410 => 413 0.12548

408 => 414 0.26943

410 => 415 -0.15326

409 => 417 0.15443

412 => 417 0.87747

Transition dipole moment (debye):

X= -5.7088 Y= 0.1448 Z= 13.6071 Tot= 14.7568

Oscillator strength, f= 2.4307

Excited State 20: 2.9520 eV 420.01 nm

orbitals in

excitation CI coeff.

--- ---

407 => 414 -0.83674

411 => 414 -0.18240

412 => 415 0.15795

411 => 416 0.36521

410 => 417 -0.24557

Transition dipole moment (debye):

X= 2.9118 Y= 0.9737 Z= -0.0190 Tot= 3.0704

Oscillator strength, f= 0.1055

Excited State 21: 3.0029 eV 412.88 nm

orbitals in

excitation CI coeff.

---------- ---------

406 => 414 -0.11337

410 => 414 -0.15701

408 => 415 0.86317

410 => 416 0.18441

407 => 417 0.11495

411 => 417 0.31495

409 => 418 0.16925

Transition dipole moment (debye):

X= -0.1395 Y= -0.0027 Z= 0.1904 Tot= 0.2361

Oscillator strength, f= 0.0006

Excited State 22: 3.0645 eV 404.58 nm

orbitals in

excitation CI coeff.

---------- ---------

406 => 413 0.86911

408 => 414 0.26252

409 => 417 -0.21540

412 => 417 0.18449

411 => 418 -0.20015

412 => 420 -0.11625

Transition dipole moment (debye):

X= -1.4906 Y= -0.0322 Z= 3.2727 Tot= 3.5963

Oscillator strength, f= 0.1503

Excited State 23: 3.0881 eV 401.48 nm

orbitals in

excitation CI coeff.

--- ---

409 => 416 0.93932

408 => 417 0.15131

410 => 418 0.19430

Transition dipole moment (debye):

X= 0.0339 Y= 0.3106 Z= -0.3163 Tot= 0.4446

Oscillator strength, f= 0.0023

Excited State 24: 3.1529 eV 393.24 nm

orbitals in

excitation CI coeff.

--- ---

408 => 413 0.18763

408 => 415 0.33805

410 => 416 0.14025

411 => 417 -0.88421

Transition dipole moment (debye):

X= 0.0822 Y= -0.0424 Z= 0.1020 Tot= 0.1377

Oscillator strength, f= 0.0002

Excited State 25: 3.1693 eV 391.20 nm

orbitals in

excitation CI coeff.

--- ---

409 => 414 0.11020

407 => 415 -0.95457

409 => 416 -0.10488

408 => 417 0.12213

410 => 418 0.13490

Transition dipole moment (debye):

X= -0.0068 Y= 0.0823 Z= -0.0599 Tot= 0.1021

Oscillator strength, f= 0.0001

PDI tetramer **4** mixed conformation

B3LYP/6-31G** optimized geometry

Final total energy = -5546.104972 h

final geometry:

angstroms

atom	x	y	z
C1	0.0000000000	0.0000000000	0.0000000000
C2	0.0000000000	0.0000000000	1.4859940895
C3	1.2272646707	0.0000000000	2.1935974247
C4	2.4701357124	0.0705687493	1.5167680493
C5	2.5026913241	0.2249744459	0.0390584889
N6	1.2580392582	0.1448233635	-0.5865445396
C7	1.2118244843	-0.0763499798	3.6058866413
C8	-0.0408377033	-0.0845933692	4.2920488482
C9	-1.2614968033	0.0454194004	3.5754812783
C10	-1.2016717769	0.0093278654	2.1580180768
C11	-0.0575170390	-0.2127484548	5.7131260380
C12	-1.2968657463	-0.3370969020	6.4008980259
C13	-2.5426194713	-0.3510015624	5.6468889269
C14	-2.5213710918	0.0823778936	4.3010197076
C15	-3.7548209868	0.5643116194	3.7075442641
C16	-4.9973409903	0.2829679435	4.3318619012
C17	-5.0254613357	-0.4607761860	5.5529262182
C18	-3.8091909420	-0.7812060659	6.2113885239
C19	-3.8769462172	-1.6393881020	7.3482483142
C20	-5.0718809443	-2.0628223209	7.8703906036
C21	-6.3086060442	-1.6542473179	7.2903251925
C22	-6.2849106775	-0.8567541463	6.1117667369

C23	-5.0608035206	-2.9699621287	9.0508705177
N24	-6.3191226077	-3.2969600872	9.5511205738
C25	-7.5685801035	-2.9175297353	9.0617878177
C26	-7.5383190500	-2.0595233677	7.8510422832
C27	-7.5181575003	-0.4628628864	5.5100110546
C28	-8.7166948926	-0.8802680277	6.1081137712
C29	-8.7316220309	-1.6666803264	7.2574166320
C30	-6.2259645439	0.7235607739	3.7402891206
C31	-7.4877210096	0.3654000567	4.3040139899
C32	-6.1882635999	1.5270845365	2.5658169793
C33	-7.3877873390	1.9668694846	1.9677927940
C34	-8.6091114739	1.6032533867	2.5211765982
C35	-8.6543191838	0.8160559508	3.6687399452
C36	-4.9228576629	1.9076470779	2.0279476203
C37	-3.7590145886	1.4376023680	2.5796196643
C38	-7.3569285426	2.8277673940	0.7591698942
N39	-6.0828497165	3.1821351153	0.3160967994
C40	-4.8503244487	2.8291485027	0.8611430141
C41	3.6564549699	-0.0158188619	2.2090781809
C42	3.6843162655	-0.2028739541	3.6165159780
C43	2.4490911621	-0.1458636650	4.3168858525
C44	2.4363701842	-0.1633973551	5.7432956678
C45	1.1815380815	-0.2210827182	6.4268076947

C46	3.6613410907	-0.1113330414	6.4675137976
C47	4.9233223905	-0.0303359661	5.7444998111
C48	4.9267952803	-0.3237019798	4.3601793889
C49	-1.2667202361	-0.3036936363	7.8197017025
C50	-0.0798020288	-0.2837372117	8.5180214315
C51	1.1646750692	-0.2809123252	7.8397193838
C52	2.3929324050	-0.3371426562	8.5450582984
C53	3.5959827357	-0.2672700771	7.8780056328
C54	-0.1142775124	-0.2665852308	10.0039073969
N55	1.1317178005	-0.3878275072	10.6211113975
C56	2.3919358545	-0.4666294854	10.0261319983
C57	6.1721939250	-0.7319368178	3.7309040032
C58	7.4037497733	-0.5061564690	4.4025216839
C59	7.4089566740	0.0944173331	5.6969614087
C60	6.1818473356	0.3451058935	6.3739481937
C61	8.6444439645	-0.8398903551	3.7744535254
C62	8.6377190543	-1.4973460004	2.5207238506
C63	7.3960876657	-1.8559409349	1.9363659742
C64	6.2089611440	-1.4744632571	2.5199752917
C65	8.6595051920	0.4100434682	6.3134649141
C66	9.8993322709	0.0652644616	5.6920311652
C67	9.8924065478	-0.5179991026	4.3895989577
C68	9.8701842161	-1.8425105387	1.9118956124

C69	11.0661102982	-1.4599766569	2.4793749916
C70	11.1174867343	-0.7425874046	3.7033498610
C71	7.3679716256	-2.6720826196	0.6925794633
N72	8.6214140437	-2.9847448420	0.1675210507
C73	9.8817028036	-2.6534981923	0.6644329691
C74	8.6708463113	1.0720194457	7.5641373245
C75	7.4397549063	1.4488072756	8.1589143018
C76	6.2410794924	1.0869437194	7.5848005093
C77	9.9133720863	1.4031151713	8.1591411180
C78	11.0994149868	1.0021747200	7.5862175266
C79	11.1315137760	0.2743139691	6.3688932098
C80	7.4361605910	2.2676728486	9.4019421497
N81	8.6988347763	2.5647634289	9.9135866913
C82	9.9491129222	2.2174138653	9.4015194854
O83	-8.5940785462	-3.2906639156	9.6082830952
O84	-4.0467260353	-3.4055387261	9.5705028620
O85	-8.3540425281	3.2238824665	0.1774929496
O86	-3.8096610633	3.2523481339	0.3856389360
O87	3.5226366623	0.3863689162	-0.6089246625
O88	-1.1354207889	-0.1735025265	10.6632788870
O89	3.3971863271	-0.6071943351	10.7013617903
O90	10.8962091220	-3.0257869261	0.0994466051
O91	6.3466357508	-3.0600319722	0.1509910212

O92	6.4261571394	2.6706395145	9.9534900214
O93	10.9742538321	2.5800409148	9.9531533951
O94	-1.0047962329	-0.0947069576	-0.6837592460
H95	-6.3278817485	-3.8994803994	10.3669532369
H96	-9.6652583183	-1.9879436144	7.7059871340
H97	-9.6665077947	-0.5939706898	5.6750050871
H98	-9.6255634222	0.5563077433	4.0704213029
H99	-9.5189838824	1.9492032781	2.0428739730
H100	-6.0503606844	3.7887628695	-0.4961110610
H101	-2.8358663143	1.8062387815	2.1554448002
H102	-2.9812206355	-2.0318045206	7.8077139947
H103	-2.1753855232	-0.2441770744	8.4026368754
H104	1.1200740098	-0.4242479647	11.6348185480
H105	4.4894618383	-0.3745597680	8.4760462878
H106	4.5671422583	0.0987544812	1.6377140984
H107	1.2690058163	0.1956792043	-1.5995397126
H108	-2.0984501817	-0.0449544970	1.5570626875
H109	5.3439211814	1.4481606288	8.0667530824
H110	5.3010884236	-1.8153537188	2.0431699897
H111	8.6161140988	-3.5422307627	-0.6800180602
H112	11.9682444786	-1.7882404845	1.9824836404
C113	12.3777217601	-0.1226345412	5.7315290239
H114	12.0086101216	1.3245285924	8.0735727566

H115	8.7096876735	3.1235261840	10.7600960632
C116	12.3729091956	-0.3732373633	4.3401787497
C117	13.6256998312	-0.2663064695	6.4554904206
C118	13.6568289257	-0.4929265995	7.8621531026
C119	14.8348321889	-0.6660672690	8.5416376247
C120	16.0874668788	-0.6153196389	7.8620197695
C121	16.0973547544	-0.4540744352	6.4488926887
C122	14.8541112618	-0.3256665940	5.7475461163
C123	17.3455298097	-0.4276297936	5.7571950985
C124	18.5277003164	-0.5642811332	6.5007895445
C125	18.5092669156	-0.7292854432	7.8830429341
C126	17.3003975043	-0.7587286582	8.5676421057
C127	17.2970306166	-0.9613572859	10.0365793819
N128	16.0328044410	-1.0283761626	10.6228901630
C129	14.7879487627	-0.9242137655	10.0049951818
O130	13.7574298431	-1.0339629463	10.6486401394
H131	16.0173466543	-1.1860453825	11.6247081399
O132	18.3068013402	-1.0767763362	10.7123194719
H133	19.4274727259	-0.8412910546	8.4489605730
H134	19.4877219004	-0.5474674169	6.0017405599
C135	17.3464787479	-0.2480271581	4.3061604780
C136	16.0994628930	-0.1592224397	3.6176518092
C137	14.8540687799	-0.2397785328	4.3213729668

C138	13.6233924172	-0.2517676999	3.6147679763
H139	12.7445226716	-0.5983086807	8.4330632845
C140	13.6609688642	-0.0028438673	2.2111637041
C141	14.8430544580	0.1319264771	1.5293505795
C142	16.0932536713	0.0136640074	2.2057133394
C143	17.3097247232	0.0990279517	1.4974460886
C144	18.5171399827	0.0028341418	2.1774385460
C145	18.5302442950	-0.1681266096	3.5584776871
C146	14.8071792720	0.4176817636	0.0690387162
N147	16.0544157787	0.4635397617	-0.5495706750
C148	17.3135237479	0.3108552320	0.0308064234
O149	13.7826586091	0.5953689040	-0.5690508814
H150	16.0458233710	0.6369802739	-1.5488719809
O151	18.3263544912	0.3705293652	-0.6476935755
H152	19.4388949650	0.0691483042	1.6101571970
H153	19.4897063438	-0.2352266795	4.0544847900
H154	12.7508941905	0.1424887416	1.6457184441

Excited State 1: 2.1315 eV 581.69 nm

orbitals in

excitation	CI coeff.
410 => 413	0.14458
412 => 413	0.95650

412 => 415 -0.10069

410 => 417 0.15225

Transition dipole moment (debye):

X= 2.0375 Y= 0.0070 Z= -5.0340 Tot= 5.4307

Oscillator strength, f= 0.2384

Excited State 2: 2.1380 eV 579.92 nm

orbitals in

excitation CI coeff.

--- ---

410 => 413 0.95214

412 => 413 -0.14505

408 => 414 0.12884

412 => 417 -0.16189

Transition dipole moment (debye):

X= 12.3061 Y= -0.1577 Z= 0.8617 Tot= 12.3373

Oscillator strength, f= 1.2340

Excited State 3: 2.1932 eV 565.31 nm

orbitals in

excitation CI coeff.

--- ---

411 => 413 0.95377

412 => 414 -0.14652

411 => 415 -0.19261

Transition dipole moment (debye):

X= -0.1301 Y= -0.9709 Z= 0.0251 Tot= 0.9799

Oscillator strength, f= 0.0080

Excited State 4: 2.3274 eV 532.72 nm

orbitals in

excitation CI coeff.

--- ---

411 => 413 0.12657

409 => 414 0.21614

412 => 414 0.93706

407 => 415 0.11684

Transition dipole moment (debye):

X= -0.1318 Y= -1.5299 Z= -0.1743 Tot= 1.5454

Oscillator strength, f= 0.0211

Excited State 5: 2.3876 eV 519.28 nm

orbitals in

excitation CI coeff.

--- ---

408 => 413 -0.10955

410 => 414 -0.94152

411 => 417 0.18560

412 => 418 -0.16553

Transition dipole moment (debye):

X= -0.3881 Y= -0.0872 Z= 0.1065 Tot= 0.4118

Oscillator strength, f= 0.0015

Excited State 6: 2.3959 eV 517.48 nm

orbitals in

excitation CI coeff.

--- ---

409 => 413 0.82874

411 => 414 -0.25312

412 => 415 0.41162

411 => 416 -0.23060

Transition dipole moment (debye):

X= 0.0115 Y= -0.9215 Z= -0.2123 Tot= 0.9457

Oscillator strength, f= 0.0081

Excited State 7: 2.4627 eV 503.45 nm

orbitals in

excitation CI coeff.

--- ---

409 => 413 0.27202

407 => 414 0.12324

411 => 414 0.91550

409 => 415 0.12949

411 => 416 0.11892

410 => 417 0.13431

Transition dipole moment (debye):

X= 0.0949 Y= 1.0567 Z= -5.1162 Tot= 5.2250

Oscillator strength, f= 0.2550

Excited State 8: 2.5705 eV 482.33 nm

orbitals in

excitation CI coeff.

---------- ---------

407 => 413 -0.38773

409 => 413 -0.10342

411 => 413 -0.14730

409 => 414 -0.57563

411 => 415 -0.46391

412 => 415 0.18301

412 => 416 0.45449

Transition dipole moment (debye):

X= 0.0351 Y= 0.8571 Z= -0.0227 Tot= 0.8582

Oscillator strength, f= 0.0072

Excited State 9: 2.5749 eV 481.51 nm

orbitals in

excitation CI coeff.

--- ---

409 => 413 0.36975

407 => 414 -0.21352

409 => 414 -0.13924

409 => 415 -0.25095

411 => 415 -0.10639

412 => 415 -0.80608

412 => 416 0.10425

410 => 417 0.12534

Transition dipole moment (debye):

X= -0.1478 Y= -2.0075 Z= 1.0454 Tot= 2.2682

Oscillator strength, f= 0.0502

Excited State 10: 2.5792 eV 480.71 nm

orbitals in

excitation CI coeff.

--- ---

408 => 413 -0.93217

410 => 414 0.18301

411 => 417 0.17378

412 => 418 -0.17231

Transition dipole moment (debye):

X= 0.0613 Y= 0.1725 Z= -0.0370 Tot= 0.1867

Oscillator strength, f= 0.0003

Excited State 11: 2.6155 eV 474.04 nm

orbitals in

excitation CI coeff.

--- ---

408 => 414 -0.14213

410 => 415 -0.93716

409 => 417 -0.20034

411 => 418 -0.10419

Transition dipole moment (debye):

X= -1.1899 Y= 0.1044 Z= -0.0876 Tot= 1.1977

Oscillator strength, f= 0.0142

Excited State 12: 2.6656 eV 465.13 nm

orbitals in

excitation CI coeff.

---

407 => 413 0.63547

409 => 414 -0.49739

412 => 414 0.18162

411 => 415 -0.27205

409 => 416 -0.17321

412 => 416 -0.43715

Transition dipole moment (debye):

X= 0.0266 Y= -0.2899 Z= -0.1156 Tot= 0.3132

Oscillator strength, f= 0.0010

Excited State 13: 2.7402 eV 452.46 nm

orbitals in

excitation CI coeff.

---

407 => 413 0.25872

409 => 414 -0.42565

411 => 415 0.71493

412 => 416 0.44708

Transition dipole moment (debye):

X= -0.1121 Y= -1.2876 Z= -0.3996 Tot= 1.3528

Oscillator strength, f= 0.0190

Excited State 14: 2.7678 eV 447.94 nm

orbitals in

excitation CI coeff.

---------- ---------

406 => 413 0.11186

410 => 413 0.18691

408 => 414 -0.86819

410 => 415 0.13877

412 => 417 0.29549

411 => 418 -0.21287

Transition dipole moment (debye):

X= -0.5556 Y= 0.0134 Z= -0.0050 Tot= 0.5558

Oscillator strength, f= 0.0032

Excited State 15: 2.7774 eV 446.40 nm

orbitals in

excitation CI coeff.

---------- ---------

408 => 415 0.17313

410 => 416 -0.92835

407 => 417 0.20448

409 => 418 -0.13908

Transition dipole moment (debye):

X= -0.0609 Y= 0.0253 Z= -0.0400 Tot= 0.0771

Oscillator strength, f= 0.0001

Excited State 16: 2.8328 eV 437.67 nm

orbitals in

excitation CI coeff.

---

409 => 413 0.14919

407 => 414 -0.39681

409 => 415 -0.13258

412 => 415 0.17538

411 => 416 0.86659

Transition dipole moment (debye):

X= -0.0195 Y= -0.9173 Z= 0.9066 Tot= 1.2899

Oscillator strength, f= 0.0179

Excited State 17: 2.8654 eV 432.69 nm

orbitals in

excitation CI coeff.

---

407 => 413 -0.56553

409 => 414 -0.35742

412 => 414 0.11671

411 => 415 0.33419

412 => 416 -0.59225

Transition dipole moment (debye):

X= 0.1530 Y= -0.0273 Z= -0.9896 Tot= 1.0017

Oscillator strength, f= 0.0109

Excited State 18: 2.9228 eV 424.20 nm

orbitals in

excitation CI coeff.

--- ---

409 => 413 0.15310

411 => 414 -0.11274

409 => 415 0.89783

412 => 415 -0.21148

411 => 416 0.11215

410 => 417 -0.23726

Transition dipole moment (debye):

X= -0.6961 Y= -2.2428 Z= 5.8765 Tot= 6.3284

Oscillator strength, f= 0.4439

Excited State 19: 2.9427 eV 421.32 nm

orbitals in

excitation CI coeff.

---

406 => 413 -0.21274

410 => 413 0.12531

408 => 414 0.28339

410 => 415 -0.16349

409 => 417 0.16714

412 => 417 0.87650

Transition dipole moment (debye):

X= 15.0281 Y= -0.2618 Z= 0.3534 Tot= 15.0345

Oscillator strength, f= 2.5225

Excited State 20: 2.9445 eV 421.07 nm

orbitals in

excitation CI coeff.

---

407 => 414 0.84201

411 => 414 -0.18269

412 => 415 -0.16518

411 => 416 0.36667

410 => 417 0.23430

Transition dipole moment (debye):

X= -0.0178 Y= -2.8297 Z= 2.5788 Tot= 3.8285

Oscillator strength, f= 0.1637

Excited State 21: 3.0116 eV 411.68 nm

orbitals in

excitation CI coeff.

---------- ---------

406 => 414 -0.10929

410 => 414 -0.15891

408 => 415 0.85933

406 => 416 0.10409

410 => 416 0.18192

407 => 417 0.11497

411 => 417 -0.32726

409 => 418 -0.17027

Transition dipole moment (debye):

X= 0.0365 Y= -0.0566 Z= 0.0055 Tot= 0.0676

Oscillator strength, f= 0.0001

Excited State 22: 3.0765 eV 403.01 nm

orbitals in

excitation CI coeff.

---------- ---------

406 => 413 -0.27895

409 => 416 -0.89025

408 => 417 -0.14294

410 => 418 0.18337

Transition dipole moment (debye):

X= -0.9965 Y= 1.5624 Z= 0.0481 Tot= 1.8538

Oscillator strength, f= 0.0401

Excited State 23: 3.0777 eV 402.85 nm

orbitals in

excitation CI coeff.

--- ---

406 => 413 -0.82052

408 => 414 -0.24415

408 => 416 0.11610

409 => 416 0.30169

409 => 417 0.22423

412 => 417 -0.16274

411 => 418 0.17590

Transition dipole moment (debye):

X= -3.0069 Y= -0.4663 Z= -0.0009 Tot= 3.0428

Oscillator strength, f= 0.1081

Excited State 24: 3.1542 eV 393.07 nm

orbitals in

excitation CI coeff.

---------- ---------

408 => 413 -0.18567

408 => 415 -0.34722

410 => 416 -0.14053

411 => 417 -0.88293

Transition dipole moment (debye):

X= -0.0550 Y= -0.0248 Z= 0.0094 Tot= 0.0610

Oscillator strength, f= 0.0000

Excited State 25: 3.1609 eV 392.24 nm

orbitals in

excitation CI coeff.

---------- ---------

409 => 414 0.10678

407 => 415 -0.95348

408 => 417 0.12954

410 => 418 -0.14606

Transition dipole moment (debye):

X= -0.0249 Y= -1.0948 Z= 0.0177 Tot= 1.0952

Oscillator strength, f= 0.0144

Optimized Geometries for **cP4**

Compound (S,S,S,S)- **cP4**

Energy: -7482.6599 hartrees

	angstroms		
atom	x	y	z
H1	2.7686998882	-8.0253694187	0.2598638329
H2	4.9018944861	-8.3719335166	-3.4567220523
H3	6.1896179135	-6.3555320877	-2.9019171059
H4	4.1036255702	-6.0581716250	0.8376641613
H5	-4.1267948287	-8.7330185987	0.6211550990
H6	-1.8086546635	-9.5129992441	0.5698928093
C7	-7.8877905588	5.6704461128	-2.2642246602
C8	-7.6422905106	6.5665918956	-1.1289473997
C9	-6.4034143827	7.2811837858	-1.0568099399
C10	-5.8527544683	6.6097084927	-3.3689976368
C11	-8.6132930500	6.8026594881	-0.1504728318
C12	-7.1767480054	8.3270631966	1.0415704911
C13	-5.3995969668	7.1495806406	-2.0751084625
C14	-8.8964423203	4.6832334176	-2.2936085167
C15	-4.9061980964	8.7357571025	0.2228803614

C16	-7.0865353078	5.8794230699	-3.4312359044
C17	-3.8936187621	8.4337121737	-0.6603627793
C18	-7.2256547637	5.0540110217	-7.1620989744
C19	-8.3934935770	7.6814633973	0.9141335908
C20	-4.0890114143	7.6107024795	-1.7953240831
N21	-8.3884566640	4.2684877970	-7.1513004255
C22	-5.6127783605	6.3529808081	-5.7900909539
C23	-5.1580912900	6.8421900170	-4.5597806135
C24	-6.7654166766	5.5870987661	-5.8574554291
C25	-9.1303548244	3.9310849129	-6.0071151995
C26	-6.1681314961	8.1191930415	0.0727540123
C27	-6.9427836061	9.2383062637	2.1871155751
C28	2.0104939098	-11.8044279149	2.1819287283
C29	3.3894107671	-11.7703048668	2.4938307328
C30	2.2738047768	-9.2102591502	-3.4701063814
C31	-0.1943654187	6.1537691785	-2.9565893602
C32	-2.8226666175	7.1583501082	-2.4456489108
C33	-1.3214644574	5.3075712330	-2.9443676093
C34	3.5426107429	-7.6953058776	-0.4235271612
C35	-7.5008334227	5.3265292046	-4.6788321228
C36	-8.6506033055	4.5024681682	-4.7234655566
C37	-0.8231366284	-11.2379866790	-3.6025737596
C38	-5.4660033824	10.7447485794	3.4034239179

O39	-3.5341978987	10.1709791101	1.5297375318
C40	-9.2847845340	4.1541821255	-3.5475682708
N41	-0.3402103867	-10.3539658209	-5.8449103702
C42	-1.1899977171	-11.1276493217	-5.0351595682
H43	-5.0694852716	6.5557039104	-6.7066416167
C44	-4.6225665929	9.6350044060	1.3675758089
O45	-10.1167263629	3.2094087169	-6.0750336247
C46	-9.4465403841	3.9790360142	-1.0973215289
H47	-7.5118232541	3.7761883050	-0.1583912277
O48	-6.6431147478	5.2753422008	-8.2158612092
C49	0.8364342089	-9.7255244356	-5.4135089046
C50	2.4813932651	-10.7705404949	-0.0061283169
C51	-8.8267133894	3.7493163960	-8.4506507624
C52	-10.2684675889	1.9801629376	0.7559454467
C53	-1.3296657661	-12.0149520758	-1.3752547865
C54	-11.1950365114	2.5939173780	-0.0991484124
C55	3.8353982097	-10.7583571769	0.3434890808
C56	0.3614889412	-10.6412206443	-3.1156095029
C57	1.5268397336	-12.7609942119	4.4575893630
C58	-8.5509443482	3.4624678721	-0.1418330653
C59	4.2870710637	-11.2677706082	1.5664280306
C60	-1.6441426852	-11.9404290339	-2.7359572895
C61	-0.4344057992	7.5290221815	-2.8193610315

C62	5.4548153879	-6.7303679579	-2.1948460403
C63	-10.7873396999	3.5629654752	-1.0189396791
C64	-1.7157248162	8.0173149012	-2.5722263869
C65	-0.1733412517	-11.4261754999	-0.8529945438
C66	-8.9508203818	2.4726933764	0.7463582068
C67	2.6880363826	-9.3422944372	-2.1223442459
C68	1.1836335288	-9.8817234561	-3.9803221392
O69	-2.1802377138	-11.6722439507	-5.5045881911
O70	-7.7912758779	9.4716218528	3.0378328365
N71	-5.6817892669	9.8473349729	2.2643801251
O72	0.7570973395	-13.1598778654	5.3221484211
C73	-2.5761291814	-10.1546114584	0.9902936311
C74	5.2352107022	-6.0427584058	-0.9940933369
C75	3.8845457419	-12.2780282170	3.7968422392
C76	-4.5557481755	-11.7571568859	2.0942465241
N77	2.9106603904	-12.7658881753	4.6857405036
C78	-3.2336569911	-12.2071193332	2.0534546556
O79	1.5264969409	-9.0841706711	-6.1952154559
C80	3.7048693699	-8.3497791896	-1.6571115900
C81	-4.9085173555	-10.4898170835	1.6065262801
C82	3.3523670611	-13.2840198525	5.9842743881
C83	-2.5980886449	5.7915590760	-2.6889229414
O84	5.0724995334	-12.2852889487	4.0916249616

C85	-2.2143698772	-11.4120226544	1.5071172520
C86	-3.8859732868	-9.7062271828	1.0357688571
C87	4.2992322141	-6.5786356807	-0.0953042508
C88	4.7144337122	-7.8699681349	-2.5122664484
C89	1.5497318084	-11.3659931992	0.9063987553
C90	-0.7665402986	-11.7499502823	1.6068341619
H91	-9.1610344353	7.8649731337	1.6580962323
H92	-10.0824085750	3.4218532828	-3.6002623656
H93	-2.9066883116	8.8230135949	-0.4413546067
H94	-1.8454565540	9.0846887508	-2.4213318911
C95	0.1652334756	-11.4990961071	0.5738234586
C96	-0.2802303897	-12.1741964730	2.8651047683
C97	0.7384194343	-10.7831617404	-1.7495367017
H98	-8.2196015303	2.0418219748	1.4239998763
C99	1.0712995344	-12.2645536937	3.1354783187
H100	-1.1913040644	4.2423087008	-3.1045741066
C101	1.9915838412	-10.2555814894	-1.2946494500
H102	-3.4229804053	5.0909170503	-2.6166732197
H103	-0.9758942729	-12.4119827973	3.6626486575
H104	4.5594919194	-10.3525553803	-0.3488921830
H105	-12.2265976953	2.2527390308	-0.1078148107
H106	-2.5364333678	-12.4129981720	-3.1313990276
H107	-11.5143507344	3.9616511647	-1.7213195691

H108	0.3982599553	8.2266149145	-2.8349571999
H109	5.3428661999	-11.2665513780	1.8148493158
H110	2.8021353369	-8.5375778636	-4.1348350274
H111	-2.0002332994	-12.5454429804	-0.7139780219
H112	-2.9929018341	-13.1848322976	2.4625099763
H113	-5.3141969915	-12.3872614159	2.5506041295
C114	-0.6845222468	-10.2217987474	-7.2640753236
H115	-9.7403692272	3.1832612435	-8.2868090667
H116	-9.0021167831	4.5788240933	-9.1386927546
H117	-8.0508784226	3.1097866927	-8.8776006294
H118	-4.4989755360	11.2223091929	3.2677135043
H119	-6.2676370532	11.4837827712	3.4405850136
H120	-5.4782867644	10.1782301765	4.3379913209
H121	-0.3946818508	-9.2278179922	-7.6003934030
H122	4.4310918453	-13.4102252549	5.9403340059
H123	3.0919207863	-12.5838727156	6.7827135872
H124	2.8509474260	-14.2317980916	6.1815609732
H125	-1.7549391264	-10.3832028158	-7.3683236503
H126	-9.5668433162	6.2953578402	-0.2179045045
H127	-4.2445393488	7.4224429637	-4.5358301864
H128	-0.1484398136	-10.9653147601	-7.8623763813
H129	-7.7710608563	-6.8867708001	2.0971052126
H130	-9.5762866529	-10.6967515158	1.2606851976

H131	-7.3603264093	-11.7540390345	1.2902703184
H132	-5.5672058056	-7.9480551455	2.1663323474
H133	-8.9932943641	-0.3232980631	0.5368163439
H134	-9.3569408753	-2.4335128990	1.7399091749
C135	-10.2170435200	-5.0808627449	5.4532400377
C136	-9.7815468355	-6.1439185054	6.2784469807
C137	-10.7554025581	-8.2984438384	0.1552293286
C138	-7.6902047477	-7.9569369644	1.9353014636
C139	-12.9843664934	-5.3906593587	-0.4009530961
N140	-13.3495597782	-7.0367186695	-2.1875156889
C141	-13.6747906300	-5.7763558955	-1.6571191296
C142	-12.3923912432	-7.9147029483	-1.6596058879
C143	-10.2928358637	-6.6104314862	3.5254473782
C144	-12.5926329633	-3.7759651784	1.3531635447
C145	-9.8716892715	-7.6326107658	4.3811255186
C146	-12.0686720429	-6.2714096449	0.2210508226
C147	-10.0413130256	-3.5021721137	7.4161157155
C148	-9.6315153349	-7.4104591348	5.7407859632
C149	-13.2437844653	-4.1595468658	0.1753814135
C150	-7.4415010004	-10.6889931697	1.4889808991
C151	-11.6898820047	-4.6160939073	2.0112882176
C152	-10.1141320951	-7.9697357192	1.3697404860
C153	-11.7460594876	-7.5062801198	-0.3881750133

O154	-14.4921946360	-5.0517682920	-2.2088984401
O155	-10.1240048208	-2.3804859488	7.8996252139
C156	-9.9907013331	-1.5784454075	1.9546329244
C157	-6.2803282270	-9.9298827756	1.6978375873
C158	-9.4969971867	-5.9156058533	7.7150622452
C159	-11.6020994427	0.6254506915	2.4803806225
N160	-9.6589421250	-4.6075411447	8.1933202728
C161	-11.7858315182	-0.5648528092	3.1913319649
O162	-12.1269657480	-8.9633400807	-2.2330651346
C163	-8.8489354043	-8.7030694841	1.6591921864
C164	-10.5763924038	0.7467667466	1.5320432214
C165	-9.3739070550	-4.4008465543	9.6165017392
O166	-9.1392557835	-6.8072086304	8.4736310430
C167	-10.9819492252	-1.6872651089	2.9432492240
C168	-9.7812216435	-0.3845001293	1.2811229114
C169	-6.4411069192	-8.5560926113	1.9549555045
C170	-8.7005074139	-10.0861048403	1.4630854458
C171	-10.5298563712	-5.3093852366	4.0791533269
C172	-10.9732482917	-2.9220058214	3.7864260145
C173	-11.0458724126	-4.2386095284	3.2797084482
C174	-10.6598560353	-2.7260082294	5.1492744810
C175	-11.4509985901	-5.9181921131	1.4593649954
C176	-10.3373654048	-3.7758882495	5.9864900662

C177	-10.5799441646	-6.8532367372	2.1049192043
H178	-10.6416876768	-1.7209762342	5.5569600576
H179	-9.7267339145	-8.6294091178	3.9858745654
H180	-13.9559321711	-3.4991556202	-0.3071385364
H181	-9.3145706470	-8.2180842593	6.3915695918
H182	-10.4412659127	-9.1736007760	-0.4014230684
H183	-12.8114456201	-2.8020089853	1.7678379855
H184	-12.5566244255	-0.6149850340	3.9561115686
H185	-12.2357084412	1.4800490485	2.7001740169
C186	-14.0105512939	-7.4520793648	-3.4286700671
H187	-13.3641100585	-7.2640001555	-4.2913007901
H188	-8.3221475179	-4.6131364091	9.8233767768
H189	-9.6046397262	-3.3648820028	9.8512633501
H190	-9.9824504035	-5.0818540023	10.2142788634
H191	-14.9260750338	-6.8746228418	-3.5298500931
H192	-14.2161540115	-8.5204316125	-3.3761088170
H193	2.7692236027	2.7395096236	-1.9632960995
H194	4.3824697618	6.1541849295	-4.0123909599
H195	2.1641275120	7.1972976406	-4.0294348637
H196	0.5742919790	3.8041625770	-1.9177177127
H197	4.8622995173	-3.8716525222	-2.4972180485
H198	5.2575644365	-1.5274955406	-1.9049054766
C199	5.4585591546	1.9512549911	1.5530300386

C200	5.0288835747	3.1832186180	2.0970345840
C201	5.5833641225	3.5869848206	-4.4451618501
C202	2.6481898931	3.7229634873	-2.4043063402
C203	8.0917664566	0.8627903440	-4.2458315174
N204	8.1772762329	1.8826037310	-6.4815245122
C205	8.6897269164	0.9181472508	-5.6007387100
C206	7.1758208657	2.8171032603	-6.1690853097
C207	5.4171629821	2.9322631942	-0.7014573327
C208	7.9229098594	-0.1806097741	-2.0778045705
C209	4.9976538220	4.1335640405	-0.1230073742
C210	7.0902479598	1.7881938346	-3.8700739687
C211	5.3559919434	0.9137423231	3.8424435805
C212	4.8249376561	4.2671839143	1.2596997035
C213	8.5219610279	-0.0928224229	-3.3393866942
C214	2.2866276015	6.2270171268	-3.5569368504
C215	6.9160445454	0.7009237633	-1.6745205034
C216	5.0304452308	3.6022574617	-3.1444250382
C217	6.6223511850	2.7495769704	-4.7957847075
O218	9.5860147969	0.1680615020	-5.9639750935
O219	5.4417802442	-0.0478392949	4.5949825747
C220	5.6362091405	-2.3066202661	-1.2541405593
C221	1.1755202459	5.5766668574	-2.9942193716
C222	4.8069484451	3.3279320100	3.5562086436

C223	6.4743293277	-4.3410429277	0.4436230308
N224	5.0139177175	2.1787400125	4.3390695257
C225	6.7329450351	-3.0087260577	0.7635549749
O226	6.7878450064	3.6346682573	-6.9929589050
C227	3.7552863181	4.3598583661	-2.9884497781
C228	5.7766096308	-4.6789813574	-0.7224604197
C229	4.8029953841	2.2830305754	5.7861855130
O230	4.4676350141	4.3859270164	4.0679295023
C231	6.2725379855	-1.9584690635	-0.0492283588
C232	5.4092254132	-3.6352505372	-1.5892913172
C233	1.3970526051	4.3188008867	-2.4020998315
C234	3.5479818652	5.6286738083	-3.5559290995
C235	5.7268152557	1.8289903366	0.1588578620
C236	6.2283771176	-0.5516973618	0.4497001441
C237	6.2778275008	0.6103557408	-0.3548978888
C238	5.9227934943	-0.4000269658	1.8237046596
C239	6.5404860006	1.7658772089	-2.5566537449
C240	5.6123427053	0.8197408773	2.3846822578
C241	5.6155221957	2.7827049290	-2.1515074449
H242	5.9021556403	-1.2667642159	2.4734711948
H243	4.8008688348	4.9878328942	-0.7579233070
H244	9.3096461214	-0.7765475833	-3.6360772706
H245	4.5145253372	5.2102923009	1.6958587534

H246	5.1707825429	4.2317850114	-5.2131687926
H247	8.2468523447	-0.9580224583	-1.3992601000
H248	7.2723784567	-2.7848685080	1.6790119805
H249	6.7961386380	-5.1252612749	1.1226769586
C250	8.7658267217	1.9070118874	-7.8240982402
H251	8.2041883334	2.6245171726	-8.4170064432
H252	4.8805138004	3.3321878423	6.0604367850
H253	3.8123675878	1.9076999855	6.0600590512
H254	5.5546994044	1.6809141304	6.2951699058
H255	8.7126343048	0.9093776097	-8.2630326940
H256	9.8169567350	2.2008135132	-7.7690262555